

# **Comparative STM-based study of thermal evolution of Co and Ni germanide nanostructures on Ge(001)**

Von der Fakultät für Mathematik, Naturwissenschaften und Informatik  
der Brandenburgischen Technischen Universität Cottbus

zur Erlangung des akademischen Grades

Doktor der Naturwissenschaften

(Dr. rer. nat.)

genehmigte Dissertation

vorgelegt von

Master of Science Engineer

Tomasz Grzela

Geboren am 25. Oktober 1986 in Swiecie (Polen)

Gutachter: Prof. Dr. Thomas Schroeder

Gutachter: Prof. Dr. Giovanni Capellini

Gutachter: Prof. Dr. Ryszard Czajka

Tag der mündlichen Prüfung: 18. November 2015







# Acknowledgements

My PhD thesis would not exist without the assistance and support of many people. In consequence, before presenting my doctoral thesis, I wish to express my genuine gratitude to a number of people whose support made this thesis possible.

First of all, I would like to sincerely thank my supervisor Prof. Dr. Thomas Schroeder for his continuous support and guidance throughout the course of my research. For giving me the opportunity to work in the Materials Research Department at IHP, support and for sharing with me his knowledge and experience I sincerely thank him.

Special thanks belong to employees working in Solid State Spectroscopy Division at Poznan University of Technology. In particular deepest gratitude goes to Prof. Dr. Ryszard Czajka, Dr. Eng. Wojciech Koczorowski, Dr. Eng. Maciej Bazarnik and M.Sc. Eng. Adam Wykrota. These people introduced me into the fascinating world of scanning probe microscopy, and without their help the surface science laboratory at IHP would not work so well.

Similarly, I am deeply grateful to other researches involved in the project titled “International Network for Germanium Surface Science Research by Scanning Probe Microscopy”: Prof. Dr. Giovanni Capellini from University Roma Tre, Dr. Neil Curson and Dr. Steven Schofield from London Centre of Nanotechnology, Prof. Marian Radny from The University of Newcastle, Prof. Leszek Jurczyszyn from Wroclaw University, and Prof. Dr. Jens Falta, Dr. Thomas Schmidt and Dr. Jan Ingo Flege from University of Bremen. I strongly appreciate their support for common experiments, scientific discussions and advices.

I am also very indebted to Dr. Ioan Costina and Max Klingsporn for XPS measurements, Dr. Markus Andreas Schubert for (S)TEM-EDX measurements, Hans-Michael Krause for SEM measurements, and Dr. Peter Zaumseil for XRD results.

Many thanks to all my other colleagues from IHP: Jürgen Borngräber, Dr. Pauline Calka, Dr. Jarosław Dabrowski, Reinhard Dorn, Dr. Oksana Fursenko, Andrzej Gajda, Dr. Wolfgang Klesse, Dr. Dawid Kot, Dr. Grzegorz Kozłowski, Beate Kuck, Dr. Gunther Lippert, Dr. Mindaugas Lukosius, Dr. Grzegorz Lupina, Dr. Lidia Lupina, Dr. Gang Niu, Heike Silz, Dr. Oliver Skibitzki, Dr. Małgorzata Sowinska, Hans-Jürgen Thieme, Dr. Christian Walczyk, Dipl-Ing. Damian Walczyk, Dr. Christian Wenger, Dr. Yuji Yamamoto, Dr. Marvin Zöllner and Yvonne Heier, for friendly atmosphere and their personal and scientific support.

Further thanks are devoted to all students, who I had opportunity to supervise in the STM lab during their summer internship and M.Sc. course. These words are especially addressed to Katarzyna Domieracka, Julia Milosz and Filip Lisiecki.

W tym miejscu chciałbym również wyrazić gorące słowa podziękowania moim najbliższym, w szczególności rodzinie i przyjaciołom. Rodzicom, mojej siostrze Małgorzacie i jej mężowi Rafałowi, przyjacielowi Sebastianowi oraz cioci Urszuli wraz z mężem Bogdanem za realne wsparcie oraz za ich autentyczne zainteresowanie postępem moich badań. Nie mniej ważne są także szczere wyrazy wdzięczności dla najdroższej Moniki. Dziękuję wam wszystkim za wsparcie w tym ważnym a zarazem trudnym wyzwaniu, jakim niewątpliwie są studia doktoranckie.

# Abstract

Since 1947, when Bardeen and Brattain initiated the era of microelectronics by constructing the first Germanium (Ge) transistor, semiconductors have become the main material platform for advanced integrated circuit (IC) technologies. Later on, given in particular the electrical stability of its native oxide, IC technology shifted from Ge to Silicon (Si) substrates and the dominance of Si-based complementary metal oxide semiconductor (CMOS) microelectronics is today unquestionable (in particular high level of system complexity, high performance and cost effectiveness). However, as the semiconductor industry is approaching the limits of traditional Si CMOS scaling, the integration of new materials into Si micro- and nano-electronics is required to extend the performance and functionality of future CMOS-based IC technologies.

Recently, Ge due to its superior optoelectronic properties (high carrier concentration, high carrier mobility, band gap at 1.5  $\mu\text{m}$ ) and compatibility with conventional Si CMOS technology has re-emerged as an alternative semiconductor material on the mainstream Si technology platform. Therefore, nowadays Ge is under the spotlight in “More Moore” scaling research (e.g. Ge channels for p-MOSFETS) as well as functionalized “More than Moore” (e.g. Ge-based photonic modules for electronic-photonic integrated circuits (EPICs)) technologies. Many of the Ge integration challenges, such as e.g. doping, epitaxial quality etc., have been recently solved or minimized to an acceptable level. However, the fabrication of low resistance, thermally stable metal/Ge contacts is still one of the main barriers towards the full use of the potential offered by Ge. In particular, the formation of ohmic contacts is relevant for applications where high current densities are of importance (i.p. Ge p-MOSFET and Ge laser applications). In addition, it was shown that strong Fermi level pinning effect close to the valence band results in the formation of a large Schottky barrier between n-type Ge and the majority of metals, which complicates the preparation of ohmic contacts to n-type Ge surface. Consequently, intensive investigations of metal/Ge contacts are imperative for future applications of Ge.

Various metal/Ge contact systems were studied and demonstrated good thermal stability and promising electrical properties. However, given their widespread use in Si CMOS technologies in form of their respective silicides, Co- and Ni-germanides seem to be an obvious choice for electrical contacts in Ge-based devices. Both metal/Ge systems exhibit a complex bulk phase diagrams with a wide range of different physical properties. It is generally acknowledged that the stoichiometric  $\text{CoGe}_2$  and  $\text{NiGe}$  phases are best suited for ohmic metal contact formation, mainly due to their low resistivity. It is worth noting that the bulk phase diagram is limited in its use for nanoscience due to an increased surface/volume ratio as well as by the strong nanostructure/substrate interface influence. Please note that this statement is gaining more and more importance in the era of continuous device miniaturization where a good scalability of metal-germanide formation gets crucial with progress towards nano-scaled Ge devices i.e. in CMOS applications. In consequence, laterally averaging thin film characterization techniques without nano-scale resolution face severe limits to meet these high end materials characterization needs.

This PhD thesis sheds light on the formation process at the atomic level of Co and Ni germanide nanostructures on clean, reconstructed  $\text{Ge}(001)$  substrates. The main part of the presented research is based on *in-situ* scanning tunneling microscopy (STM) studies on the influence of subsequent, post-evaporation annealings at various temperatures in order to follow and investigate on the nano-scale the structural evolution of a few monolayers of Co and Ni metal (deposited at RT and in UHV conditions) on an atomically clean, reconstructed  $\text{Ge}(001)$  surface. Furthermore, additional techniques like LEED, (S)TEM-EDX and XPS were used to corroborate and complement the STM derived insights.

It was demonstrated that - for both investigated systems - room temperature deposition of a few metal monolayers on clean  $\text{Ge}(001)$  results in a Volmer Weber growth mode. Starting with annealing treatments at relatively low temperature ranges, the formation of a continuous  $\text{Metal}_x\text{Ge}_y$  wetting layer from as-deposited 3D metal clusters on  $\text{Ge}(001)$  was detected. It should be noted that a very flat wetting layer was observed for the  $\text{Co}/\text{Ge}(001)$  system, which is different for the  $\text{Ni}/\text{Ge}(001)$  system where inhomogeneous terraced domains were formed. Finally, the 2D wetting layer



gradually evolves with increasing temperature into well-ordered 3D  $\text{Metal}_x\text{Ge}_y$  nanostructures, surrounded by clean, reconstructed Ge(001). Analysis of these Co and Ni germanide nanostructures shows that the growth mechanism is different: in particular the Ni/Ge system is more reactive by means of Ni bulk diffusion and results in 3D Ni germanide nanostructures which show a strong tendency to be embedded into the Ge(001) substrate. In contrast, Co germanide nanostructures are situated initially on top of the Ge(001) substrate due to the fact that Ge diffusion dominates in the low temperature range. Only at higher annealing temperatures, Co diffusion into the bulk occurs and Co germanide nanostructures penetrate into the Ge substrate. For the Co- as well as Ni-Germanide system, the nanostructures undergo Ostwald ripening phenomena in the high temperature range. The present PhD thesis thus allows to understand on the nano-scale the main growth and reaction mechanisms of the Walser and Benè rule set up about 40 years ago to describe metal/semiconductor interface reaction on the macro-scale.

Finally, although this PhD thesis reveals important findings related with the growth mechanism and evolution process of Co and Ni germanide nanostructures on Ge(001), it does not yet explain all aspects of the growth process. In especial, the correlation of structural and chemical information on the nano-scale needs to be accomplished in future LEEM/PEEM studies at Synchrotron facilities. In consequence, further investigations and efforts are still needed in order to complete our understanding of the Co and Ni germanide nanostructures formation for future homogeneous metal germanide contacts to Ge-based devices in “More Moore” and “More than Moore” Si micro- and nanoelectronics.



# Zusammenfassung

Seit 1947 als Bardeen und Brattain die Ära der Mikroelektronik, durch die Konstruktion des ersten Germanium (Ge) Transistors, einleiteten, wurden Halbleiter zur Hauptgrundlage für fortschrittliche „integrated circuit“ (IC)-Technologien. Später wechselten IC-Technologien von Ge zu Silizium (Si)-Substraten, bedingt durch die elektrische Stabilität der natürlichen Oxide, wodurch die Dominanz von Si-basierten „complementary metal oxide semiconductor“ (CMOS) Mikroelektronik unangefochten wurde (insb. durch die hohe Komplexität, Leistung und Kosteneffektivität). Jedoch wird, durch die Annäherung an die Limitierung der traditionellen Si-CMOS-Skalierung, die Integration von neuen Materialien in die Si-Mikro- und Nanoelektronik notwendig, um die Leistung und Funktionalität von zukünftigen CMOS-basierten IC-Technologien weiter auszubauen.

Jüngst hat sich Ge, durch seine optoelektronische Eigenschaften (hohe Ladungsträgerdichte, hohe Ladungsträgermobilität und Bandlücke im 1.5  $\mu\text{m}$  Bereich) und Kompatibilität mit konventionellen Si-CMOS-Technologien, wieder als alternatives Halbleitermaterial auf einer Si-Technologieplattform hervorgerufen. Deshalb ist Ge heutzutage wieder im Rampenlicht von „More Moore“ Skalierungsforschung (z.B. als Ladungsträgerkanal in p-MOSFETS) als auch „More than Moore“ Funktionalisierung (z.B. für photonische Module in „electronic-photonic integrated circuit“ (EPIC) Technologien). Viele der Ge-Integrationsherausforderungen, wie z.B. Dotierung, epitaktische Qualität etc., wurden mittlerweile gelöst oder auf ein akzeptables Niveau reduziert. Jedoch ist die Herstellung von niederohmigen, thermisch stabilen Metall/Ge-Kontakten immer noch eine der Hauptbarrieren zur vollständigen Nutzung des Potentials von Ge. Die Bildung von ohmschen Kontakten ist insbesondere für Anwendungen mit hohen Stromdichten (z.B. Ge p-MOSFET und Ge-Laser) von großer Relevanz. Es wurde zudem gezeigt, dass starkes Fermi-Energie-Pinning nahe des Valenzbandes zu einer hohen Schottky-Barriere zwischen n-dotiertem Ge und der Mehrzahl von Metallen führt, was die Präparation von ohmschen Kontakten zu n-

dotierten Ge-Oberflächen verkompliziert. Entsprechend sind intensive Untersuchungen von Metall/Ge-Kontakten zwingend notwendig für zukünftige Anwendungen von Ge.

Es wurden diverse Metall/Ge-Systeme studiert, welche eine gute thermische Stabilität und vielversprechende elektrische Eigenschaften demonstrierten. Co- und Ni-Germanide, in Betracht ihrer weiten Verbreitung in CMOS-Technologien als entsprechende Silizide, scheinen offensichtlich eine gute Wahl für elektrische Kontakte in Ge-basierten Bauteilen zu sein. Beide Metall/Ge-Systeme weisen ein komplexes Volumenphasendiagramm, mit unterschiedlichsten physikalischen Eigenschaften, auf. Es ist allgemein anerkannt, dass die  $\text{CoGe}_2$ - und NiGe-Phase sich am besten als ohmsche Metallkontakte durch ihren geringen Widerstand eignen. Es sollte erwähnt werden, dass das Volumenphasendiagramm in der Anwendbarkeit in den Nanowissenschaften, durch die erhöhte Oberflächen/Volumen-Ratio genauso wie durch den starken Nanostruktur/Substrat-Einfluss, limitiert ist. Diese Aussage gewinnt zunehmend an Wichtigkeit in der Ära der kontinuierlichen Bauteilminiaturisierung, wo eine gute Skalierbarkeit der Metall-Germanid-Bildung mit dem Fortschreiten der nanoskalierten Bauteile, insb. CMOS-Anwendungen, entscheidend ist. Entsprechend sind lateral mittelnde Dünnschichtcharakterisierungsmethoden ohne nanoskalierte Auflösung strengen Beschränkungen ausgesetzt, um dieser High-End-Materialcharakterisierung gerecht zu werden.

Diese Dissertation soll die Bildungsprozesse von Co- und Ni-Germanidnanostrukturen auf sauberen, rekonstruierten Ge(001) Substraten auf einem atomistischen Niveau näher beleuchten. Der Hauptteil der hier präsentierten Forschung basiert auf *in-situ* „scanning tunneling microscopy“ (STM)-Studien, bezüglich des Einflusses von aufeinanderfolgenden Temperschritten bei unterschiedlichen Temperaturen, um die nanoskalierte, strukturelle Evolution von wenigen Monolagen Co- und Ni-Metall nach der Abscheidung (bei RT und unter UHV-Bedingungen) auf einer atomar reinen, rekonstruierten Ge(001)-Oberfläche zu verfolgen und zu untersuchen. Des Weiteren wurden zusätzliche Techniken wie LEED, (S)TEM-EDX, und XPS verwendet, um die mit STM erzielten Ergebnisse zu bekräftigen und zu vervollständigen.

Es wurde demonstriert, dass für die beiden untersuchten Systeme die Raumtemperatur-abscheidung von wenigen Monolagen Metall auf reinem Ge(001) in einem Volmer-Weber-Wachstumsmodus resultiert. Temperschritte bei relativ niedrigen Temperaturen führten anfangs zur Detektion von kontinuierlichen Metall<sub>x</sub>Ge<sub>y</sub> Benetzungsschichten ausgehend von den abgeschiedenen 3D Metallclustern auf Ge(001). Zu beachten ist, dass eine sehr flache Benetzungsschicht für das Co/Ge(001) beobachtet wurde, was sich zu dem Ni/Ge(001)-System unterscheidet, wo sich inhomogene Domänen mit Terrassen bildeten. Mit ansteigender Temperatur entwickelt sich die 2D Benetzungsschicht allmählich zu wohlgeordneten 3D Metall<sub>x</sub>Ge<sub>y</sub> Nanostrukturen umgeben von sauberen, rekonstruierten Ge(001)-Flächen. Eine genaue Analyse dieser Co- und Ni-Germanid-Nanostrukturen zeigt, dass ihre Wachstumsmechanismen unterschiedlich sind. So ist das Ni/Ge-System reaktiver, was sich durch eine erhöhte Ni-Volumendiffusion andeutet, wodurch sich eine starke Tendenz zu in Ge(001) eingebetteten 3D Ni-Germanid-Nanostrukturen ergibt. Im Gegensatz dazu befinden sich Co-Germanid-Nanostrukturen anfänglich auf dem Ge(001)-Substrat, da die Germaniumdiffusion bei niedrigen Temperaturen dominiert. Nur bei höheren Temperaturen tritt eine Co-Diffusion auf und die Co-Nanostrukturen dringen in das Ge-Substrat ein. Sowohl für das Co- sowie auch das Ni-Germanid-System vollziehen die Nanostrukturen einen Ostwald-Reifungsprozess bei hohen Temperaturen. Die vorliegende Dissertation erlaubt so Einblicke in das Verständnis von nanoskalierten Wachstums- und Reaktionsmechanismen der Walser und Benè Regeln, die schon vor 40 Jahren aufgesetzt wurden, um die Metall/Halbleiter-Grenzflächenreaktion auf einer makroskopischen Skala zu beschreiben.

Obwohl diese Dissertation wichtige Erkenntnisse bezüglich des Wachstumsmechanismus und des Evolutionsprozess von Co- und Ni-Germanid-Nanostrukturen enthüllt, erklären diese nicht alle Aspekte des gesamten Wachstumsprozess. Insbesondere muss die Korrelation von strukturellen und chemischen Informationen auf der Nanoskala in Zukunft mittels LEEM/PEEM-Studien an Synchrotroneinrichtungen vervollständigt werden. Als Konsequenz sind weitere Untersuchungen und Bemühungen notwendig, um das vollständige Verständnis von Co-

und Ni-Germanid-Kontakten für Ge-basierte Bauteile in der „More Moore“ und „More than Moore“ Si-Mikro- und Nanoelektronik zu erlangen.

# Contents

1. Introduction .....	1
1.1. Electronic-Photonic group IV ICs .....	2
1.1.1. “More Moore” and “More than Moore” approaches .....	2
1.1.2. High mobility Ge channels for CMOS .....	5
1.2. High quality Ge modules for Si photonics .....	8
1.2.1. Optical Modulator .....	10
1.2.2. Photodetector .....	13
1.2.3. Light Source .....	16
1.3. Ge integration challenges .....	20
1.3.1. Epitaxial quality .....	20
1.3.2. Doping .....	21
1.3.3. Strain engineering .....	21
1.3.4. Metal contacts .....	22
1.4. The Schottky and Ohmic contacts .....	22
1.4.1. Schottky contact .....	24
1.4.2. Ohmic contact .....	34
1.5. Motivation and organization of the thesis .....	36
1.5.1. Structure of the thesis .....	39
2. Experimental background .....	41
2.1. Characterization techniques .....	41
2.1.1. Scanning Tunneling Microscopy .....	41
2.1.2. Other techniques .....	50

2.2.	Substrate preparation and thin film deposition.....	57
2.2.1.	Substrate properties and cleaning methods.....	57
2.2.2.	E-beam evaporation.....	61
2.3.	Thin film growth theory .....	63
3.	Results and discussion .....	67
3.1.	The pristine Ge(001) surface .....	68
3.2.	Cobalt germanide nanostructures on Ge(001) surface.....	70
3.3.	Nickel germanide nanostructures on Ge(001) surface.....	96
4.	Summary and Outlook .....	119
4.1.	Summary .....	119
4.2.	Thermal evolution of Co and Ni germanides .....	121
4.2.1.	Walser and Benè rule .....	121
4.2.2.	Growth scenarios of Co/Ge(001) and Ni/Ge(001) .....	124
4.3.	Outlook.....	128
5.	Scientific visibility during the PhD .....	131
5.1.	Publications in peer-reviewed journals .....	131
5.2.	Presentations at conferences and courses.....	132
6.	Tunneling theory.....	135
7.	Abbreviations .....	141
8.	Glossary of symbols.....	145
9.	Bibliography .....	149



# Chapter 1

## Introduction

This doctoral thesis was realized at IHP, the Leibniz institute for innovative microelectronics in Frankfurt Oder (Germany). IHP is a well known science centre for Silicon-Germanium (SiGe) technologies. It is focused on innovative solutions for application areas such as wireless and broadband communication, security, medical technology, aerospace, automotive industry and industrial automation [1]. In order to achieve these goals, IHP's strategy is not based on miniaturization of existing technology solutions (known as "More Moore" approach), but in functional diversification of the existing technology platform (known as "More than Moore" approach). Therefore, this introductory chapter starts with a general description of both "More Moore" and "More than Moore" strategies. Next subchapter (1.1.2) presents a brief characterization of Germanium (Ge) and its potential applications in future microelectronic industry as high mobility material. In the 21st century, which is believed to be dominated by photonics, Ge seems to be a remarkable candidate to replace Silicon (Si) in photonic modules. For that reason, Section 1.2 introduces the reader to the topics related with photonics and photonic devices, with particular emphasis on the usage of Ge in this field. Chapter 1.3 gives a short description of Ge integration challenges. Continuing this issue, in view of the fact that one of the major barriers towards the full use of Ge in future technologies is the development of reliable, low resistance metal contacts, in Section 1.4 the theory of Schottky and Ohmic contacts is briefly presented. At the end (Chapter 1.5), motivation and main goals of this doctoral thesis are described, and finally the organization of each chapter is shortly presented.

## 1.1. Electronic-Photonic group IV ICs

### 1.1.1. “More Moore” and “More than Moore” approaches

In 1965 Gordon E. Moore, the director of Research and Development Laboratories of Fairchild Semiconductor, observed that between 1959 and 1964, the number of transistors - the fundamental building blocks of electronic devices in today’s complementary metal-oxide semiconductor technology (CMOS) - on electronic chips increased exponentially and doubled approximately every two years. In addition, he postulated that the rate of increase would not substantially change within next few years [2]. This historical hypothesis has become known as Moore’s Law. The history has proven that due to consistent improvement in Si technology, based mainly on aggressive and continuous device miniaturization, the Moore’s Law was correct during the next 50 years. In order to ensure the continued development and to clarify the main technological requirements and needs of integrated circuit technology, the International Technology Roadmap for Semiconductors (ITRS) was designed [3].

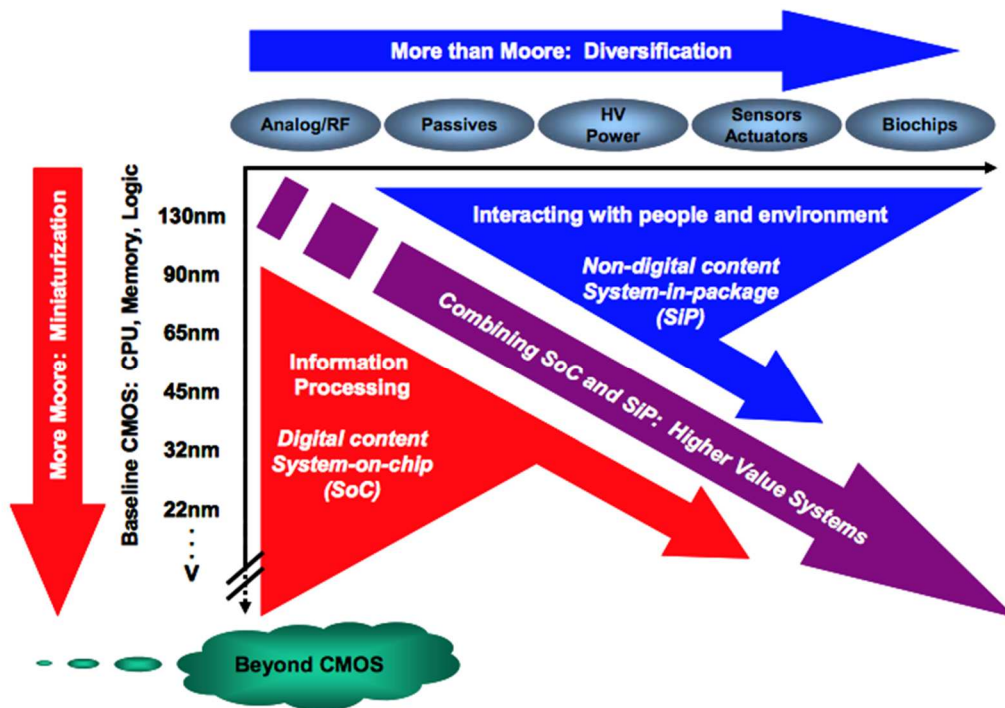


Figure 1.1 Two approaches in today’s microelectronic industry: miniaturization of digital functions (“More Moore”) and functional diversification (“More than Moore”) (from [4]).

As shown in Figure 1.1, ITRS is based today on two main approaches: “More Moore” and “More than Moore”. “More Moore” approach refers to the further miniaturization of the Si CMOS baseline technology and is represented on the vertical axis in Figure 1.1. From the physical point of view, this strategy will finally reach miniaturization limits at the atomic scale. However, not negligible will be also economic limitations. The costs of R&D, maintaining fabrication facilities, testing etc. in Si CMOS technology aimed at further shrinking of the dimensions of devices, increases exponentially – known as Moore's Second Law [5]. Consequently, alternative paths of technology development are searched. Such an alternative is represented by the “More than Moore” approach, depicted on the horizontal axis in ITRS. The “More than Moore” strategy is focused on functional diversification rather than miniaturization of the existing CMOS technology platform. Certainly, this approach can extend the functionality of electronic devices by adding non-digital modules to digital components in one product. The following list presents only a few selected examples for module groups in focus of the “More than Moore” approach (based on IHP’s activity).

- **Radio frequency (RF)**

SiGe hetero-bipolar transistors (HBT) and Graphene base transistor (GBT), also antennas, modulators, demodulators etc. [6] [7] [8] [9] [10]

- **Sensors / Biochips / Biomedical**

Glucose Bio-Micro-Electro-Mechanical System (BioMEMS) sensors and Surface Acoustic Wave (SAW) filters [11] [12]

- **Photonics**

Waveguides, modulators, photodiodes, light-emitting diodes (LEDs) and lasers [13] [14] [15] [16]

Generally, the migration of non-digital modules in the “More than Moore” approach to the existing Si CMOS baseline can be realised by two main ways (illustrated schematically in Figure 1.2): System-On-Chip (SOC) or System-In-Package (SIP).

**System-On-Chip (SOC):** It is a system integration concept, in which all digital (i.e. processor, memory) and analog (i.e. antenna, filter) components are monolithically integrated into a single chip. It is realized via heteroepitaxy, wafer bonding or

nanostructure printing. SOC designs are usually characterized by less power consumption, less board area, higher reliability and higher security - major advantages of this architecture for industrial mass-production. However, challenges like integration complexities and high costs (due to integration of various devices) are significant drawbacks and must be taken into account during the design of electronic circuits [17]. A perfect example of SOC architecture are modern multiple core processors.

**System-In-Package (SIP):** In this integration concept, a number of integrated circuits are combined in a single package (module). Basically, SIP consists of two or more vertically stacked dies (containing integrated circuits and/or other components (i.e. antennas, filters)) assembled on the same substrate and connected to each other. Connections between dices and components are realized by wire bonds, solder bumps or through Silicon Via (TSV) technologies. The main advantage of SIP concept is the fact that each chip can be built separately with its own dedicated technology. Furthermore, SIP is very flexible: the whole package can be easily modified by changing the design of single building blocks, depending on customer needs. Therefore, it is considered that the SIP concept will be strongly developed in the near future [18].

Summarizing, without doubt further development of today's microelectronics will continue on the basis of scaling. However, successful integration of high performance modules with different functions to existing platform brings new opportunities. At this point, it is be emphasized that "More Moore" and "More than Moore" are complementary approaches and a fruitful interaction will determine the future of micro and nanoelectronics.

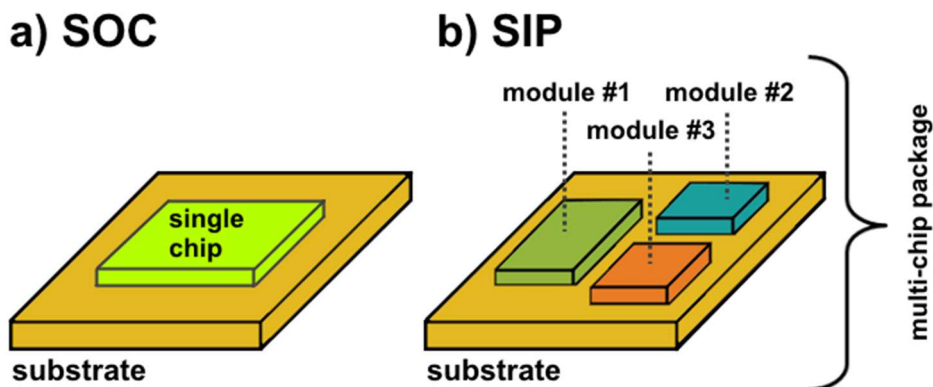


Figure 1.2 Schematic representation of the modern system integration concepts: a) System-On-Chip (SOC), b) System-In-Package (SIP).

### 1.1.2. High mobility Ge channels for CMOS

Despite the fact that the first transistor, invented at Bell Labs in 1947 by J. Bardeen and W. H. Brattain (honoured with the Nobel Prize for Physics in 1956), was fabricated using Ge [19], this material was abandoned in favor of Si in semiconductor technology already in the middle of 1960's. Since that time, for over 50 years, Si became the main material platform for advanced CMOS based micro- and nano-electronics, achieving a high level of system complexity. The main reason of the Si dominance was the economy of scale. Development of technological infrastructure, continuous cost-effective miniaturization of Si transistors and ceaseless improvement in circuit performance caused that Si is now the cheapest technology for integrated circuits. Due to aggressive miniaturization process, transistor sizes approach nanometer scale. This has undeniable advantages like larger operation frequency, but also new challenges have emerged (e.g. energy dissipation by gate leakage currents etc.). In this case, further miniaturization and evolution of transistors requires new approaches, like for example 3D transistor technologies (FinFETs) and the replacement of the Si by higher mobility channel materials (e.g. indium gallium arsenide (InGaAs) and Ge) [20] [21].

Table 1 depicts selected physical properties of Ge in comparison with Si. Bulk Ge is characterized by smaller effective mass for electrons and smaller effective mass in the heavy hole (hh) and light hole (lh) bands compared to Si. A small effective mass of carriers leads to high carrier mobility. It is worth to point out that Ge has the highest hole mobility of all known semiconductor materials. Ge offers nearly two times higher electron mobility than Si, but it is still a relatively small value compared to other materials e.g. III-V materials (InSb, InAs etc.). However, in case of Ge, electron and hole mobility is more balanced, which is a significant advantage for current state-of-the-art logic designs in CMOS based on symmetric configuration of both n- and p-type transistors [22]. Another crucial parameter is the material's bandgap. In comparison to Si, the minimum indirect energy gap of Ge is much smaller (0.66 eV). This parameter influences the scalability of electronic devices (e.g. metal-oxide semiconductor field-effect transistors (MOSFET's)) by affecting the threshold voltages and consequently driving voltages of device. Performance of nanoelectronic devices based on Ge, which

is characterized by low thermal noise at a low supply voltage of about 0.5 V was already successfully demonstrated [23] [24]. Since in this subsection the basic physical properties of Ge are presented, it should be also pointed out that Ge, mainly due to its small band gap, has become a promising material for monolithic integration in Si-based group IV photonics. These issues are described in detail in Chapter 1.2.

Despite promising physical properties of Ge and its enormous potential for further applications in microelectronic, there are still significant barriers towards the full, effective Ge integration processes into the Si-based platform. These aspects are also briefly described in this thesis in Chapter 1.3.

Table 1 Selected physical properties of Ge and Si [25]. Indexes of effective mass data: l - longitudinal effective mass, t - transverse effective mass, lh - light hole effective mass, hh - heavy hole effective mass.

Property	Ge	Si	
Number density [atoms/cm <sup>3</sup> ]	$4.42 \cdot 10^{22}$	$5.0 \cdot 10^{22}$	
Atomic Weight [u]	72.6	28.08	
Density [g/cm <sup>3</sup> ]	5.3267	2.328	
Crystal structure	diamond	diamond	
Lattice constant at 27 °C [Å]	5.64613	5.43102	
Linear coefficient of thermal expansion $\Delta L/(L\Delta T)$ [°C <sup>-1</sup> ]	$5.8 \cdot 10^{-6}$	$2.6 \cdot 10^{-6}$	
Melting point [°C]	937	1420	
Effective mass $m^*/m_0$	(electrons)	$1.64^l, 0.082^t$	$0.98^l, 0.19^t$
	(holes)	$0.04^{lh}, 0.28^{hh}$	$0.16^{lh}, 0.49^{hh}$
Mobility (drift) $\mu$ [cm <sup>2</sup> /(Vs)]	(electrons)	3900	1450
	(holes)	1900	500
Energy gap at 27 °C [eV]	0.66	1.12	
Vapour pressure (torr)	$10^{-3}$ at 1270 °C	$10^{-3}$ at 1600 °C	
	$10^{-8}$ at 800 °C	$10^{-8}$ at 930 °C	

Despite all these challenges of Ge, ITRS has acknowledged in 2009 the great potential of Ge and suggested it as a promising candidate for further integration to the existing Si platform. Taking into account the above considerations we can conclude that nowadays Ge is considered as a “hot candidate” for scaled “More Moore” (e.g., alternative high mobility channel semiconductors for n- and p- MOSFETS [26] [27]) as

well as functionalized “More than Moore” technologies (e.g., Ge-based photonic modules like modulators [28] [29], photodetectors [30] [31], and lasers [32]).

It is also worth to mention, that recently researchers from Purdue University reached a significant milestone in Ge-based microelectronics. During the 2014 IEEE International Electron Devices Meeting on Dec. 15-17 in San Francisco, the group of Professor Peide Ye demonstrated the first modern CMOS device, in which Ge was used as the semiconductor channel material instead of Si. This new concept allows the construction of Ge p-type, as well as n-type transistors, which has so far been a challenge (Figure 1.3). More information can be found in the press release published by Purdue University [33].

In summary, this is only one of many examples, which shows that research in the field of Ge-based materials and technologies on the mainstream Si platform has experienced a renaissance. Consequently, intensified work in both industrial and scientific laboratories is carried out in order to solve the outstanding hurdles, preventing up to today the full exploitation of Ge in microelectronic industry.

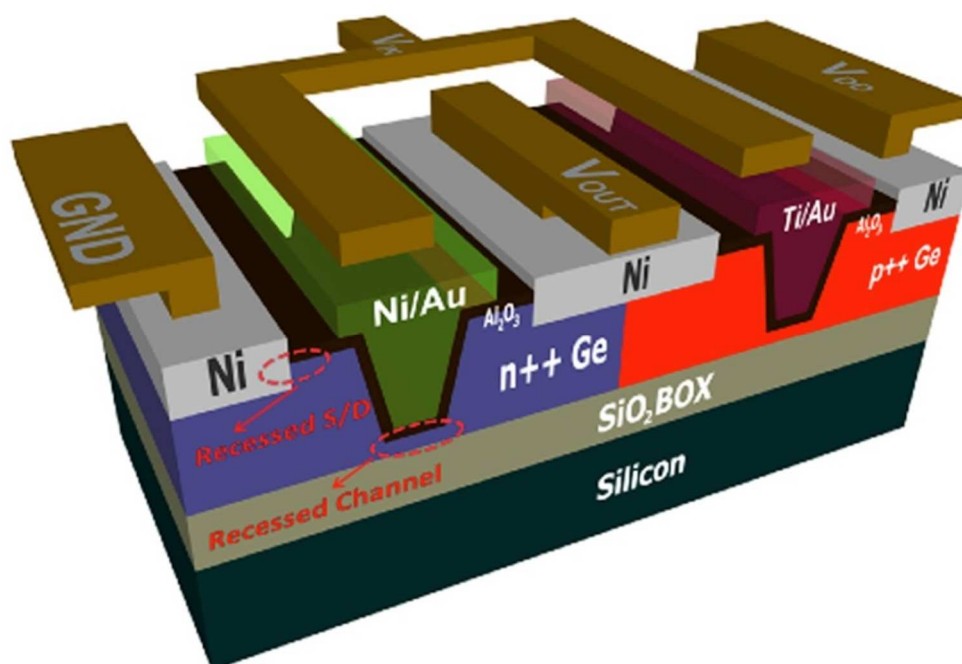


Figure 1.3 This graphic depicts a new electronic device created at Purdue that uses Ge as the semiconductor channel material instead of Si. Image: Purdue University (from [33]).

## 1.2. High quality Ge modules for Si photonics

Photonics is a young branch of science and technology associated with signal generation, processing, transmission and detection, where the signal is carried by photons (i.e., light). If the last century is considered as the era of microelectronics, photonics is believed to prevail in technology in the twenty-first century [34]. The ceaseless miniaturization of microprocessor sizes caused that the further improvement in integrated circuits performance is based not only on individual device efficiency (e.g. transistor gate delay), but is also more and more limited by the ability to get signals in and out of the microprocessor. This phenomenon, known as an “interconnect bottleneck”, is an increasing problem in high-performance microelectronic systems (Figure 1.4) [35] [36]. With continued increase in functionality of a Si circuit, the rate of data transfer on a Si chip is getting larger. Nowadays metal wiring used as interconnects greatly limits the data bandwidth. To overcome bandwidth limitations of classic electrical interconnects, a new concept of on-chip optical interconnects, which offers a much higher transfer bandwidth and low demand of energy, was recently proposed [37].

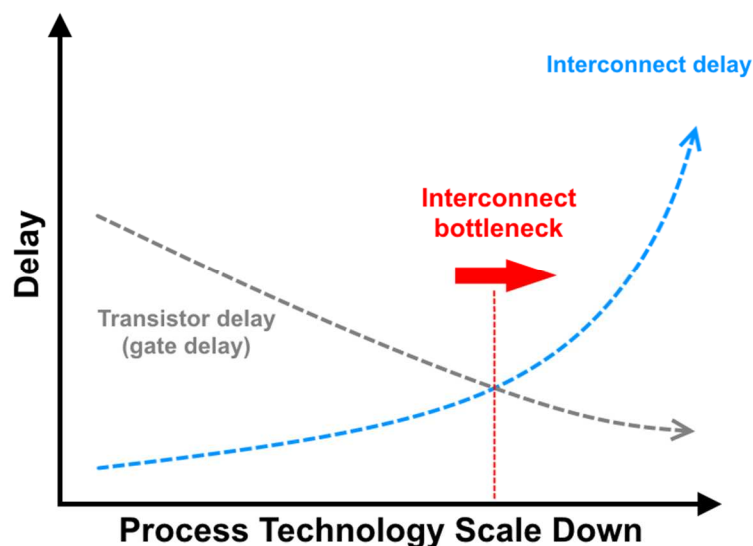


Figure 1.4 Trends in transistor gate delay (switching time) and interconnect delay in current IC fabrication technology. The crossover point represents the start of the 'interconnect bottleneck', where photonic technology could reduce this problem.



Optical interconnects demand the development of principal photonic modules like:

- i) active components: modulators, amplifiers, detectors; lasers, LED diodes;
- ii) passive components: waveguides, filters, polarizers, optical fibers.

In parallel to the further development of individual photonic modules, challenges related with their integration on Si CMOS technology (like material basis, fabrication compatibility, and packaging into single IC) are undertaken. Figure 1.5 depicts a schematic illustration of an optical system integrated with Si-BiCMOS platform, an electronic-photonic integrated circuit (EPIC), with basic photonic modules.

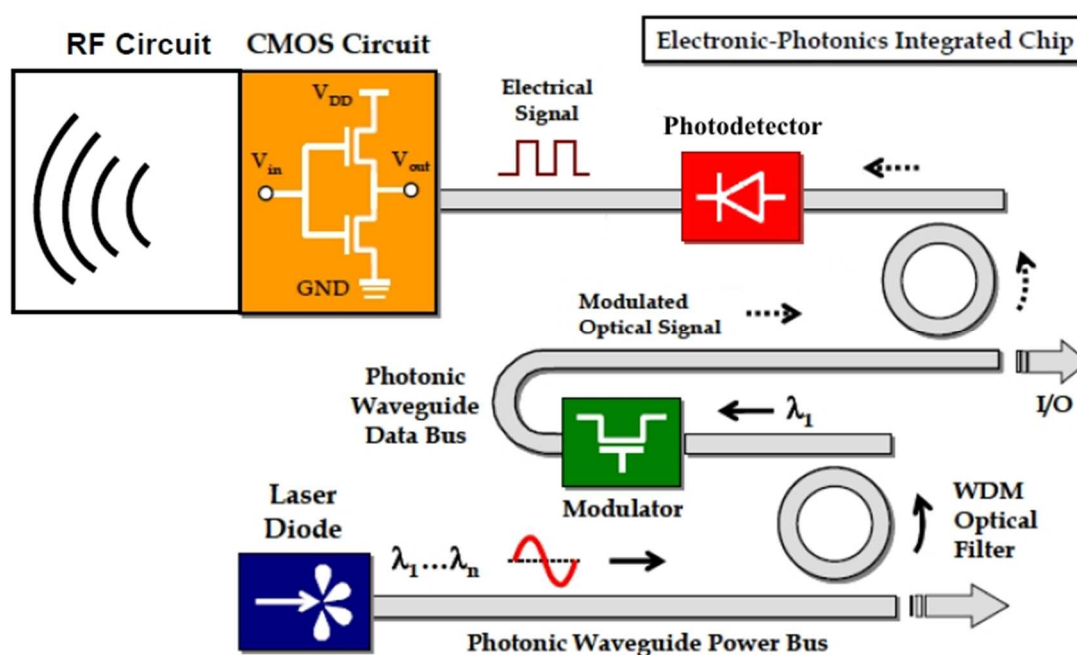


Figure 1.5 Schematic illustration of Electronic-Photonic Integrated Circuit (EPIC) concept. Electronics integrated circuit (BiCMOS) can be interconnected via Si photonics platform. Basic photonic modules are: light source (laser, diode), photodetector, modulator, filter, waveguide (after [38]).

Si is an indirect band gap semiconductor, which makes it a poor light emitter. In consequence, other materials are needed to build up light source modules. Currently, III-V materials (e.g. InSb [39], GaAs [40], InP [41]), which are characterized by direct band gap and superb optical properties, are the dominating players in the field of photonic light emitters. However, the most significant drawback is at present the fact that these materials are not compatible with Si-based technology platform and cannot be easily and cheaply integrated with Si-CMOS circuits. Due to the above mentioned

reasons, it is believed that the construction of Si-based light emitters, in particular Si-CMOS compatible laser is a milestone in the further EPIC development and is considered as a “holy grail” [42]. Other electronic properties of Si like a rather weak electro-optic effect and low absorption coefficient in the range of wavelengths commonly used in optical communication, (1.3–1.55)  $\mu\text{m}$  (transmission window of  $\text{SiO}_2$  optical fibers) further limit the use of Si materials.

It is clear that despite the importance of Si in EPIC technologies, new materials must be considered to replace Si. Here, particular attention is focused on group IV semiconductor like for example SiGeSn or Ge. As was mentioned in previous sub-chapter, Ge due to its promising optoelectronic properties experienced a renaissance as a semiconductor material for EPIC technologies. The band gap of Ge (at 1.5  $\mu\text{m}$ ) fits to the telecommunications wavelength (i.e. wavelengths of 1.3  $\mu\text{m}$  and 1.55  $\mu\text{m}$ ) and causes that this material is extensively researched for monolithic integration in Si- based group IV photonics. For example, recently Ge-based optoelectronic devices such as photodetectors [43] and electro-optic modulators [29] have been successfully integrated in Si-CMOS ICs. To describe this topic in more detail, in the following subsections the most important modern EPIC modules, which are based on utilization of Ge, are briefly characterized.

### 1.2.1. Optical Modulator

Photons, which were generated in typical photonic light sources, do not carry any logical information and therefore the electric signal in form of 0s and 1s must be properly encoded into the light beam. This is realized by optical modulators. Main types of optical modulators are:

- i)* ring resonators [44];
- ii)* Mach-Zehnder interferometers [45];
- iii)* electro-absorption (EA) modulators, which are directly integrated into a waveguide [29].

In general, the modulation of light consists of changing electromagnetic wave parameters in time. It is implemented by using the so-called electro-optic effect, which

---

means the change of refractive index of the material, through which light passes, by applying an external electric field  $E$ . Being more precise, the electro-optic effect can be further distinguished into electro-refraction or electro-absorption when, respectively, real or imaginary part of the refractive index is adapted. Thereby, modulation may be imposed on the phase, frequency, amplitude or polarization of the light beam. Basic physical phenomena by which mentioned above types of modulation are possible, are Pockels, Kerr, Franz-Keldysh and quantum confined Stark effects.

The *Pockels effect*, or linear electro-optic phenomenon, causes birefringence in an optical medium by a change in the real part of refractive index proportionally to the external electric field. The Pockels effect typically only occurs in crystals that lack inversion symmetry, such as lithium niobate ( $\text{LiNbO}_3$ ) or III-V materials (GaAs, InP) and in other non-centrosymmetric media like polymers or glasses. The Pockels effect was discovered by Friedrich Carl Alwin Pockels in 1893.

The *Kerr effect*, also called the quadratic or second order electro-optic effect, is a change in the real part of refractive index of a material in response to an applied electric field. The change of refractive index is proportional to the square of the external electric field, instead to the linear proportionality of in the Pockels effect. All materials show a Kerr effect, however it is generally masked by the much stronger linear effect. The Kerr effect plays a dominant role thus in centrosymmetric materials (e.g. Si, Ge). The Kerr effect was discovered in 1875 by Scottish physicist John Kerr.

The *Franz-Keldysh effect* is an electric field-induced change in the optical absorption spectrum of semiconductors. When an external electric field is applied, energy bands of the semiconductor bend and the expansion of electron and hole wavefunction into the bandgap is modified. In consequence, it influences absorption processes assisted by a photon with energy smaller than the bulk band gap, and leads to changes in the shape of the fundamental absorption edge of a semiconductor towards longer wavelength values. In contrast to Pockels and Kerr effects, the Franz-Keldysh effect is based on the change in both real and imaginary part of refractive index. The Franz-Keldysh effect was independently discovered by Walter Franz and Leonid Keldysh in 1958. The Franz-Keldysh effect occurs in uniform, bulk semiconductor materials, but usually requires strong electric fields (hundreds of volts/cm), which limits

its usefulness with conventional electronics. It was shown that Si possesses a weak electro-optic effect [46]. However, unlike Si, bulk Ge shows a significant Franz-Keldysh effect [47], which gave this material a clear perspective to be used as light modulator in EPIC. Recently, it was reported that the strong electro-optic effect for Ge can be further improved by tensile strain engineering, so that its strength of refractive index change starts to be comparable to InP and LiNbO<sub>3</sub> [48]. A successful monolithic integration of Ge-based modulator into a Si waveguide on SOI (silicon-on-insulator) wafer was demonstrated just a few years ago by Liu *et al.* [29] and Lim *et al.* [49] (Figure 1.6). In both works, fully functional, novel Ge electro-absorption modulators of high efficiency, RF signal modulation and low power consumption were presented. In addition, it was shown that the efficiency of novel Ge modules is fully comparable to existing Si microring resonator and Mach-Zehnder interferometers.

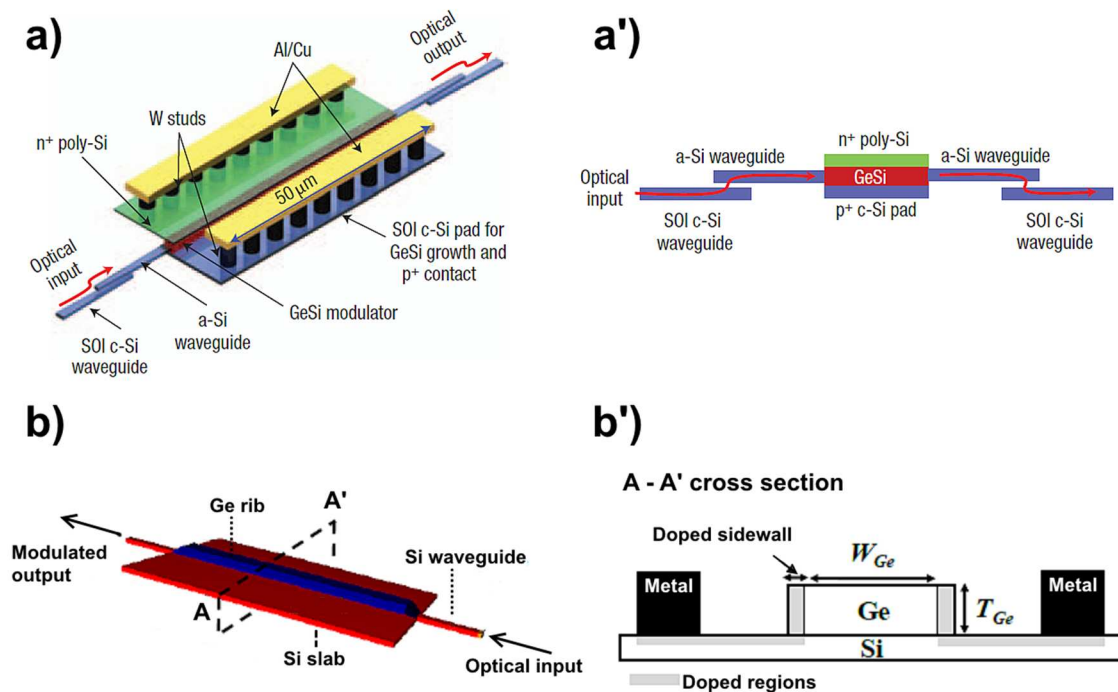


Figure 1.6 Two examples of modern Ge-based modulators located in the waveguide and monolithically integrated into Si-photonic circuits: a) and a') modulator based on tensile strained GeSi, a 3D schematic of the device and longitudinal cross-section of the device, taken parallel to the direction of light propagation, b) and b') schematic and cross-section cut of the Ge modulator (from [29] and [49], respectively).

---

*Quantum confined Stark effect* (QCSE) is a similar phenomenon to the Franz-Keldysh effect, but which is observed in multi quantum wells (MQW). Electrons and holes within the quantum well only occupy states within a discrete set of energies. In consequence, only a discrete set of frequencies of light is absorbed or emitted by the MQW system. This situation is changed when an external electric field is applied. Electrons and holes are pulled towards opposite sides of each quantum well, for example the electron states shift to lower energies, while the hole states shift to higher energies. In consequence, the permitted light absorption and emission frequency changes, as a result of decrease in wavefunction overlapping [50]. As regards the potential further application of Ge, QCSE effect was demonstrated for Ge quantum wells [51] and Ge/SiGe superlattices [52].

### 1.2.2. Photodetector

The main aim of photodetectors is the conversion of a light signal back into an electrical signal at the end of the optical bus. An efficient photodetector is characterized by high sensitivity at operating wavelengths, high response speed and high signal-to-noise ratio. So far Si photodetectors have been widely used as optical receivers. The most effective Si photodetectors were demonstrated to operate in the wavelength range  $\sim 850$  mbar [31]. However, due to relatively large band gap of Si (1.12 eV), which simultaneously determines an absorption cut-off wavelength around  $1.1 \mu\text{m}$ , higher wavelengths are not available for this material. For wavelengths longer than this value, the light will not be detected efficiently due to very small absorption coefficients. In order to increase the range of light detection, particularly in the range typical for telecommunication ( $1.3 \mu\text{m}$ – $1.5 \mu\text{m}$ ), other materials must be used.

Among many prospective candidates, III-V compound semiconductors nowadays prevail in the market of photodetectors. This choice seems obvious because these materials are characterized by high absorption efficiency and high carrier drift velocity required for fast response time. However, the integration of III-V materials into Si-CMOS technology, and in future EPIC systems, is still difficult. Most important issues related with III-V integration into Si-CMOS platform are: the complexity of integration

process, high costs and the possibility of doping contaminations into Si devices since III-V materials act also as dopants for group IV materials (and vice versa).

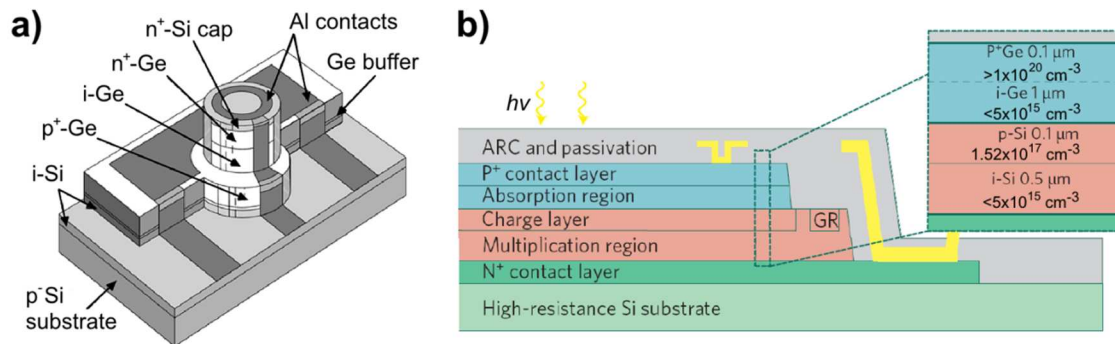


Figure 1.7 Examples of Ge photodetectors: a) 3D view of the PIN Ge photodiode, b) Schematic cross-section of a Ge/Si APD (APD - avalanche photodiode, ARC - anti-reflection coating). From [53] [54].

Here, Ge again can be a natural alternative for III-V materials. Ge is characterized by a relatively small band gap (indirect band gap 0.66 eV, direct band gap 0.8 eV) which results in a much higher absorption coefficient than Si in the typical telecommunication technologies wavelength range (1.3  $\mu\text{m}$ –1.5  $\mu\text{m}$ ). In addition, Ge integration on the Si platform does not cause cross contamination issue. In favor of Ge also points that recently many issues associated with the monolithic integration process into Si platform, like epitaxial quality, doping etc., are not fully solved but achieved a satisfying level.

Many structure types of Ge-based photodetectors were demonstrated over the last years (e.g. Figure 1.7). As an example, the simplest and most commonly used type of photodetector is a *pin diode*, operating in reverse bias. The pin diode is a special case of the p-n junction with an intrinsic layer (i) between the p- and n-region. Due to applied external reverse bias, the intrinsic layer is depleted and has a high resistivity. An electron-hole pair is created after light absorption and then carriers are separated by a built-in electric field - and the external field - inside the junction and contribute to the current flow in the external circuit [25]. As mentioned, the intrinsic layer is characterized by high resistivity, which means that the voltage drop takes place mainly in this region, consequently this promotes the excitation and collection of electron-hole pairs. In addition the intrinsic layer is usually thicker than the doped region for effective

collection of electron-hole pairs. The main advantage of the pin diode is the fact that by adjusting the thickness of intrinsic layers, the quantum efficiency and response time can be optimized [31]. In current Ge pin photodetectors (Figure 1.7 a)), the intrinsic layer is made of Ge for effective absorption around 1.55  $\mu\text{m}$ . However, highly doped p-, n- regions (because they are usually used as ohmic contacts) can be realized by implantation [55], *in-situ* doping [56] or by using p<sup>+</sup>/n<sup>+</sup> single crystalline Si substrates or Si heterojunctions [57].

***Metal-semiconductor-metal (MSM) photodiode*** is another class of photodetectors. MSM photodetector consists of back-to-back Schottky diodes that use an interdigitated electrode configuration on top of an active light absorption layer. In contrast to pin diode, MSM photodiode operates in a photoconductive mode which means that the resistivity of the device changes, due to exposition to light. Therefore, MSM photodetectors are only functional under non-zero external bias. There are three different operation modes of MSM photodiode, depending on the photon energy ( $h\nu$ ) and the applied bias. If the photon energy is smaller than the energy gap of the semiconductor  $E_g$ , photoexcited electrons in the metal can overcome the Schottky barrier and be collected by the semiconductor. This process is called internal photoemission. If photon energy is higher than the semiconductor energy gap, the light beam creates electron-hole pairs in the semiconductor, and the MSM device behaves similar to pin diodes. And finally if the applied voltage is comparable to the avalanche breakdown voltage, MSM diodes can operate in the avalanche mode. One speaks then of an ***avalanche photodiode (APD)***. APD operates at high reverse bias which is necessary for avalanche multiplication. The multiplication gives rise to high internal current gain. Therefore, APD gives opportunity for detection of lower power signals. In consequence, APDs have much higher sensitivity than standard pin or MSM diodes. One of the parameter that testifies to efficiency of the APD (signal-to-noise ratio) is the so-called effective ionization ratio  $k$ , where  $k$  is usually defined as the ratio of the ionization coefficient of one type of carriers to the ionization coefficient of the second type of carriers [25]. Small  $k$  values indicate noise decrease, and in consequence increase of device performance [58]. It was shown that Si offers much better multiplication properties than typical III-V compounds [43] [54].

Here, once again it turned out that the use of Ge in MSM photodiodes and APDs causes the increase in devices performance, however it appeared that construction of efficient diodes based on Ge was more challenging as expected. The small band gap of Ge results in high absorption in telecommunication wavelengths, however in this case the small band gap leads to small Schottky barriers and in consequence large dark currents of MSM detectors. In more detail, the high current of Ge-based MSM diodes is affected by the narrow bandgap and strong Fermi level pinning of the metal/Ge interface at valence band and hole injection over the Schottky Barrier Height [31]. Recently, it was shown that application of dopant segregation technique [59] or asymmetric electrodes [60] can substantially reduce the dark current. In summary, by using a combination of Ge (high absorption) and Si (efficient carrier multiplication) leads to fabrication of a high performance Ge/Si APDs, which can compete with traditional group III-V APDs. This concept was demonstrated by Kang *et al.* in 2008 [54]. A schematic cross-section of their concept of Ge/Si APD with additional anti-reflection coating (ARC) is presented in Figure 1.7 b). Furthermore, recently the successful integration of Ge photodetectors on silicon waveguides was reported [61].

### 1.2.3. Light Source

#### A. Laser Diode

As shown in previous subchapters, efficient optoelectronic devices in which Ge was used, such as electro-optic modulators and photodetectors have been recently successfully integrated with electronic circuitry in a Si CMOS environment. However, the last building block which is crucial for the EPIC systems is an integrated, efficient light source on the Si platform. Many research groups showed electroluminescence phenomena, in the range from 1.1  $\mu\text{m}$  to 2.2  $\mu\text{m}$ , from LEDs made from Ge, Si and SiGe compound [62] [63] [64] [65] [66]. However, the “holy grail” of Si photonics is the construction of a monolithically integrated laser (acronym from “light amplification by stimulated emission of radiation”) with high quantum efficiency.

Ge is an indirect bandgap semiconductor material with a conduction band minimum at L-point, as shown in Figure 1.8 a). In order to obtain light emission by radiative



processes from the  $\Gamma$ -point, high charge carrier population across the direct bandgap is needed. This in turn requires a population inversion at the  $\Gamma$ -point in the conduction band. In consequence, the radiative processes are competing with non-radiative processes, which occur with high probability in indirect semiconductors, thereby greatly reducing the light emission efficiency [67]. Among non-radiative, processes the following loss mechanisms are crucial: Auger recombination (i.e. energy transfer from electron-hole pair recombination in favor of third carrier, which results in excitation to a higher energy level), free-carrier absorption (i.e. excitation of conduction band electrons as a result of photon absorption), phonons generation (i.e. lattice vibrations), or Shockley-Read-Hall recombination (SRH, also called trap-assisted recombination, which means electron transition between energy bands by using localized state created within the band gap by an impurity in the lattice).

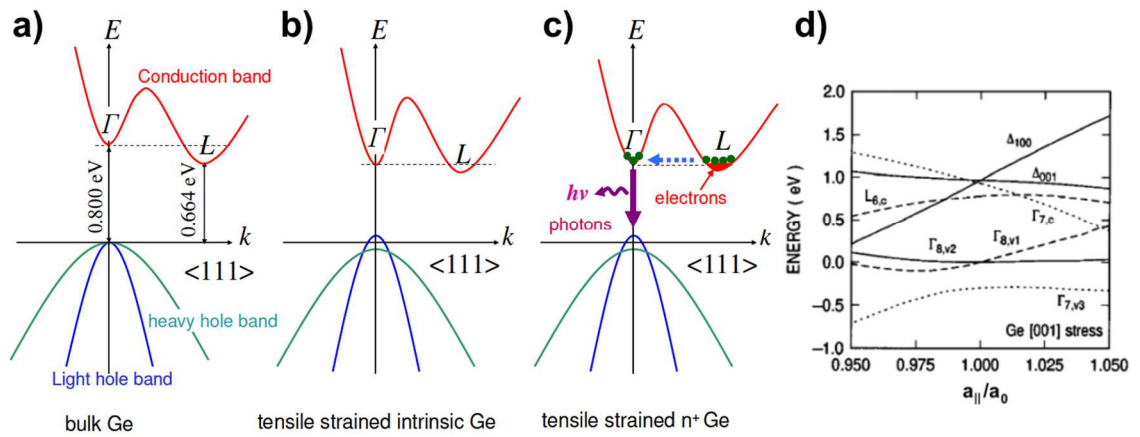


Figure 1.8 Schematic band structure of bulk and strained Ge: a) unstrained band structure of bulk Ge with 0.136 eV difference between the direct and the indirect gap, b) decrease of difference between direct-indirect gap due to applied tensile strain, and c) implementation of heavy n doping for further compensation of the gap difference (from [68]). Additionally, figure d) shows the calculated valence and conduction band shifts at various symmetry points in Ge as a function of in-plane biaxial strain  $a_{||}/a_0 - 1$  (from [69]).

In Ge, the difference between direct band gap at the  $\Gamma$ -point and indirect band gap at the L-point is only 136 meV (Figure 1.8 a)). It was predicted and shown that local band edges in Ge band structure can be controlled by strain, which is called band gap engineering [69] [70]. Introducing strain influences the position of band minima for the  $\Gamma$ -point and L-point, by shifting them upwards or downwards in the energy scale. Moreover, the impact of strain is different for different bands as illustrated in Figure

1.8 d). The lowering of  $\Gamma$  is more pronounced than the lowering of L band in case of tensile strain. As shown in Figure 1.8 b), an implemented tensile strain in the range between 1.7%– 2% into bulk Ge causes the transformation of Ge from an indirect to a direct band gap material [67]. As result of the decrease of the direct energy gap, a shift of the emitted spectra towards longer wavelengths will however be observed. Realization of stress implementation into Ge can be realized in various ways e.g. stressed Ge nanomembranes [71],  $\text{Si}_3\text{N}_4$  stressor layers [72] or by Ge  $\mu$ -bridges approach [73]. Finally, to improve light emission from the direct gap transition of Ge, n-type doping is applied, which is also called band filling (Figure 1.8 c)). It compensates the remaining energy difference between direct and indirect gaps in case not enough tensile strain can be applied to achieve a truly direct Ge semiconductor. N-type doping increases the fraction of the injected electrons into the direct  $\Gamma$ -valley without adding holes, thereby minimizing non-radiative processes. However, an optimization strategy will be needed to minimize for free carrier absorption.

In conclusion, combined techniques of band gap engineering and band filling (electron doping) give an opportunity for Ge as optical gain material for construction of a Si-CMOS compatible laser. Following these approaches in 2012, Camacho-Aguilera *et al.* from Massachusetts Institute of Technology showed electrically pumped lasing from Germanium-on-Silicon pnn heterojunction diode structures at room temperature [32]. This device was based on a small biaxial tensile strain  $\sim 0.24\%$  and moderate level of phosphorous doping at a concentration around  $4 \times 10^{19} \text{ cm}^{-3}$ . However, it turned out that this device is not yet suitable for mass production, and device concepts need to be further developed: The main issues were a high threshold current ( $\sim 280 \text{ kA/cm}^2$ ) and small output signal power around 1 mW, for drive current of  $350 \text{ kA/cm}^2$ . As a result improvement of the Ge laser efficiency requires further work towards doping levels and strain optimization, however it is also clear that ohmic contacts to Ge surface are needed for high electrical pumping power for achieving stable lasing. It is still an unresolved issue, which is also extensively studied, and will be described in Chapter 1.4.

It should be also mentioned that recently a new idea of band-engineering, without tensile-stresses, appeared. Incorporation of tin atoms (Sn) into Ge can reduce the gap at the  $\Gamma$ -point even below that of the L-valley for suitable Sn concentration. In 1987

Jenkins *et al.* predicted that the indirect-to-direct transition for relaxed GeSn occurs at around 20% Sn concentration [74]. However, more recent calculations indicate much lower Sn concentrations in the range of 6.5%–11.0% [75] [76]. For Ge-Sn binary system, realization of GeSn alloys with relatively low Sn concentration is very difficult. It is caused by a low equilibrium solubility of Sn in Ge. In addition, lattice mismatch of ~15% between Ge and  $\alpha$ -Sn poses a challenge for heteroepitaxial quality (e.g. presence of biaxial compressive strain for GeSn grown on Ge substrates, number of defects). Despite these significant barriers, in 2015 Wirths *et al.* demonstrated optically pumped lasing in a direct-bandgap GeSn alloy grown on Si [77].

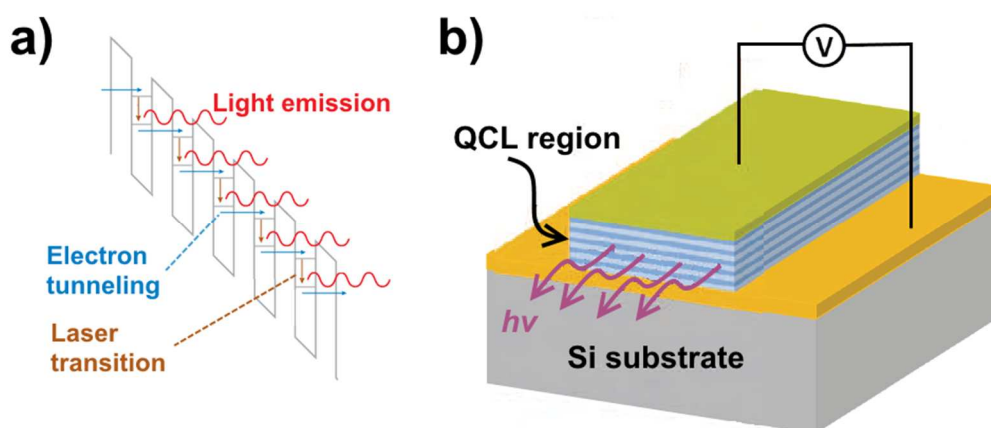


Figure 1.9 Quantum Cascade Laser. In part a) a schematic of the gain region of a quantum cascade laser is shown. Photons are emitted as a result of cascade electron tunneling through a series of quantum wells. Part b) depicts a schematic construction of QCL sandwiched between two metal layers.

## B. Quantum Cascade Laser

At this point, another way of laser light beam generation should be also mentioned, namely quantum cascade lasers (QCLs). The concept of QCLs was originally proposed by Kazarinov and Suris in 1971 [78], however, a first QCL was demonstrated in 1994 using III-V compounds (GaInAs and AlInAs) [79]. In contrast to typical semiconductor laser, QCL is a unipolar device, which means that the source of radiation is based only on one type of carriers, namely often electrons. QCL consists of a repeated stack of semiconductor multiple quantum well heterostructures. Laser emission is achieved through the use of intersubband transitions. Electron radiates a photon on an intersubband transition during the tunneling from one quantum well to the next one,

which is schematically illustrated in Figure 1.9 a). Quantum cascade lasing can be achieved for direct as well as indirect band gap materials. Recently, QCLs based on Si/SiGe [80] and Ge/SiGe [81] structures were shown. In contrast to the archetype of QCL made of III-V materials, Si/SiGe and Ge/SiGe QCLs offer additional advantages. They can be easily and cheaply integrated with Si technology and they lack polar optical phonon scattering [42]. A schematic illustration of a typical QCL structure is depicted in Figure 1.9 b). QCLs are important sources in the mid- and far-infrared, including the terahertz band. However, the main advantage of the QCL concept is the fact that wavelength of the emitted light can be further tuned by strain, composition and thickness of quantum wells [82].

### 1.3. Ge integration challenges

Despite the wide range of advantages of Ge over Si presented in previous chapters, there yet remain a number of critical issues, which need to be solved towards the full integration of Ge into classical Si-CMOS technology, within the meaning of scaled “More Moore” (e.g. Ge high mobility channel semiconductor) as well as functionalized “More than More” (e.g. Ge-based photonic modules) approaches. Here, a short description of main Ge integration challenges is given.

#### 1.3.1. Epitaxial quality

The greatest challenge in effective Ge integration processes into the Si-based platform is related to the large lattice parameter difference (around 4.2%) between Ge and Si. The heteroepitaxial growth for Si-Ge system is realized by a complex Stranski-Krastanov growth mode, which leads to high surface roughness and high threading dislocations density (TDD). The most frequently used Ge growth techniques on Si substrates are: direct growth on Si(001) [83], methods involving SiGe buffers [84], methods involving oxide buffers [85] and nanoheteroepitaxy [86]. Recently, epitaxial Ge layer growth of low TDD ( $\sim 10^6/\text{cm}^2$ ) and low surface roughness on Si surface was

---

successfully demonstrated [83] [87]. However, future “More Moore” as well as “More than Moore” technologies might require TDD levels below  $10^5/\text{cm}^2$ .

### 1.3.2. Doping

In modern CMOS technology, it is necessary to control the doping level as well as dopants diffusion in semiconductors. It was shown that Ge exhibits a dramatically different behaviour of both p- and n-type dopants than Si and dopant-defect interactions are less understood as compared to the mainstream material Si. In case of Ge, high active carrier densities for p-type dopants have been successfully demonstrated. However for n-type dopants, achieving high doping levels is more challenging. This is connected with the fact that the diffusion of any dopant in Ge significantly depends on the dopant concentration itself. Contemporary theoretical models supported by measurements show that diffusion of n-type dopants in Ge is mainly vacancy assisted, where substitutional dopant atoms exchange lattice positions with vacancies. More information about dopant diffusion and doping issues in Ge can be found in Refs. [88] and [89]. Today, doping levels of active n dopants about  $5 \times 10^{19}/\text{cm}^3$  can be achieved for example by  $\delta$ -layer doping techniques [90].

### 1.3.3. Strain engineering

The term “strain engineering” represents a general strategy employed in semiconductor manufacturing to enhance device performance. As was mentioned in previous chapters, Ge properties can be modified in a certain extent by induced strain. However, strain engineering was known much earlier and this concept applies not only to Ge. For example, induced strain into a modern silicided sub-micrometre transistor can influence carrier mobility (improvement as well as deterioration) depending on the type of channel material (n- or p-type) and the direction of applied strain. Currently, starting from 90 nm node CMOS technology, strain engineering is widely used in mass production of transistors [42]. The main challenges related with strain engineering for Ge devices are related with the method of stress implementation. Usually, stress

engineered devices require a “virtual” substrate with an adjustable lattice constant to provide the appropriate misfit strain to achieve specific properties. As was also mentioned previously, in case of Ge-based devices stress implementation is realized in other ways e.g. stressed Ge nanomembranes,  $\text{Si}_3\text{N}_4$  stressor layers or by a Ge  $\mu$ -bridge approach. However, proposed methods rely either on non CMOS-qualified materials or require complex fabrication schemes like for example lithography of complex shapes, which prevents their easy integration within standard fabrication processes.

#### 1.3.4. Metal contacts

Last point discussed in this sub-chapter refers to ohmic contact formation on Ge. Achieving a low resistivity, thermally stable Ge contact module is very important for “More Moore” applications such as Ge channel MOSFET. Moreover, low resistance ohmic contacts on Ge are of paramount importance in the booming field of integrated silicon photonics (e.g. Ge-based laser). This is especially relevant for n-type doped Ge(001). It was shown that due to interface states, Fermi level pinning at the interface between n-Ge and most metals results in the formation of a Schottky barrier, which shows only a weak dependence on the metal work function. It was demonstrated that the pinning factor  $S$  for n-type Ge may have a very small value of 0.05 [91], which suggest strong Fermi level pinning close to the Bardeen limit. In consequence, the formation of ohmic metal contacts on n-type Ge is quite challenging. In the next chapter, the basic theories of Schottky contact and Ohmic contact formation are given, however more information about Fermi level pinning in Ge can be found in Refs. [91] [92] [93].

### 1.4. The Schottky and Ohmic contacts

The physical and chemical properties of metal-semiconductor (MS) interfaces have a significant importance for electronic devices. Starting from the nineteenth century MS interfaces were, and surprisingly still are extensively studied, both for their basic physical properties and for their technological importance in microelectronics [94]. The first systematic study on MS interfaces is deemed to Ferdinand Braun, who in 1874

---

discovered and investigated an unipolar conduction of metal-semiconductor junctions [95]. He observed rectifying characteristics of MS interfaces, which means that the electrical current flowing across the MS interface is non-linear against the applied bias voltage.

It took more than sixty years after Braun's discovery until in 1939 Walter Schottky presented a semiconductor theory, based on the band theory of solids, which well explains the physics of MS junctions [96]. The Schottky theory is quite simple, but it describes only few limiting cases. However, contribution of Schottky's work to the understanding of MS interfaces was significant, and it was the prelude to more complex theories. When a metal is making close contact with a semiconductor, a potential barrier will be formed at the MS interface. This barrier, known as Schottky barrier height (SBH), has a major impact on current flowing across an MS interface. Therefore, SBH is clearly an important property of the MS contact, which decides its electrical characteristic. Consequently, knowledge of MS interface formation, discovering all physical and chemical issues related with this process, is crucial in terms of applications of MS interfaces in microelectronic devices (in particular, the most relevant for the performance, reliability and stability of devices) [94].

Despite decades of intensive investigations, a coherent unifying model of SBH formation for any metal-semiconductor system is still missing. Interestingly, a quick review into recent literature related to Schottky and Ohmic contacts shows a wide spectrum of different, sometimes conflicting opinions and models [97]. In particular, it was shown that basic hypotheses in simple models are often inconsistent with what *ab initio* calculations revealed about real MS interfaces [94]. The above statements just confirm how complex, difficult and demanding further research on the nature of MS interfaces is. However, recent experiments have shown that the properties of MS junctions strongly depend on the interface atomic structure, and the atomic inhomogeneities of MS interfaces. This has suggested that any complete and realistic theory of MS interfaces must be built on the rigor of quantum mechanics with atomic MS structure input. Some researchers suggest that fundamental principles of MS interface formation can be already described by quantum-mechanics-based models. However, it should be noted that proper and complete quantum-mechanic description of

MS interfaces should consider such aspects like: quantum theory of solids, chemical bond formation, quantum transport, etc., which consequently suggest that quantum description of the MS interface in general cannot be formulated into simple analytic equations valid in a unifying way for all types of MS systems.

It should be also mentioned, that the physics and chemistry of the MS interfaces constitutes only a small, albeit very important, part of a much broader problem related to interfaces and alignment of electronic band structures between different materials [97]. Just for example, recently, scientists and device engineers focus their attention on the study of interfaces between such systems like: semiconductor-semiconductor (e.g. band offset at the interface influencing the electrical and optical properties in quantum wells for LEDs [98]) or metal-oxide (e.g. interface chemical reactivity causing changes in the SBH upon electrical pulses in resistive random-access memory (RRAM) [99]).

#### 1.4.1. Schottky contact

MS junctions can present rectifying or non-rectifying behaviour. When the electrical current flowing across the MS interface is non-linear against the applied voltage, the MS junction is known as Schottky contact (or alternatively: Schottky diode, Schottky barrier, Schottky junction, etc.). The rectifying character of MS contact results from the discontinuity on the energy scale of the electronic states responsible for conduction in these junction materials. Electrical conduction in the metal is related with the delocalized electronic states around the Fermi level ( $E_F$ ).

However, as depicted in Figure 1.10 these states are not coupled to any delocalized electronic states in the semiconductor drawn on the right. In the case of electrical conduction in the semiconductor, it depends on the doping type of the semiconductor. Electrons near semiconductor conduction band minimum ( $E_C$ ) and holes near the valence band maximum ( $E_V$ ) are responsible for electrical conduction for n-type and for p-type semiconductors, respectively. As shown in Figure 1.10, due to the existence of the fundamental band gap, the lowest-lying states for n-type semiconductor are shifted above the metal Fermi level by  $\phi_{B,n}$ , which is called n-type Schottky barrier height (SBH). By analogy, p-type SBH ( $\phi_{B,p}$ ) is defined as the difference between metal  $E_F$



and semiconductor  $E_V$ . This simple band structure MS junction model, can easily explain that the presence of the SBH in both cases leads to rectifying behaviour of Schottky contact (e.g. in case of n-type semiconductor in Figure 1.10, electrons can easier flow from the semiconductor to the metal than in the opposite direction).

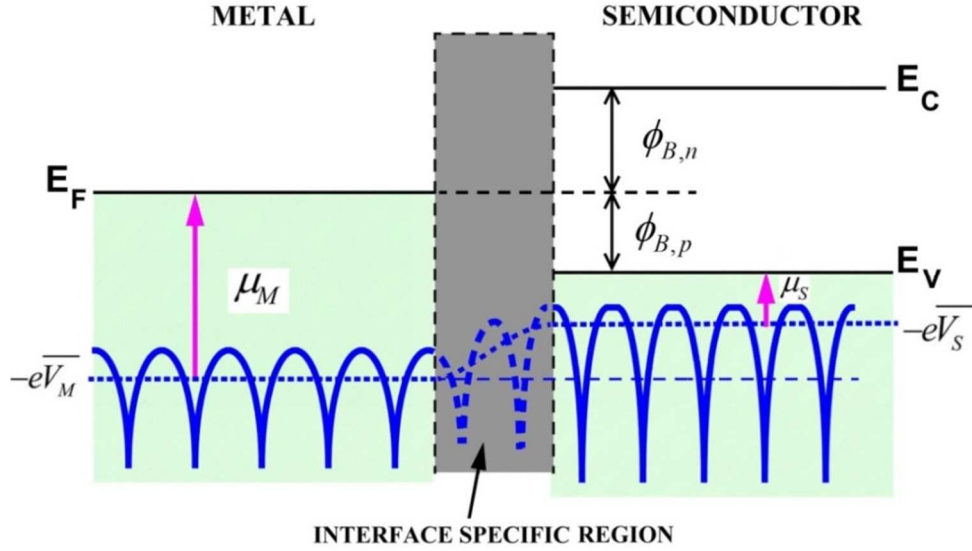


Figure 1.10 Schematic metal-semiconductor interface band diagram. Blue curve lines represent the electrostatic potential energy and dotted lines indicate average electrostatic potential. Description of all symbols in text. Figure after [97].

To supplement this model, here metal Fermi level is defined by Eq. (1.1), where:  $-e\bar{V}_M$  is referenced to the vacuum, average electrostatic potential energy per unit cell of the metal;  $\mu_M$  is the internal chemical potential. The chemical potential is a pure bulk quantity, independent of external factors, which is in contrast to the average electrostatic potential which may be affected by the structure of the crystal surface or Coulomb interaction.

$$E_F = -e\bar{V}_M + \mu_M \quad (1.1)$$

By analogy, the position of  $E_V$  of the semiconductor can be defined as the sum of the average electrostatic potential energy of the crystal  $-e\bar{V}_S$ , and its internal chemical potential  $\mu_S$  (see Eq. (1.2)).

$$E_V = -e\bar{V}_S + \mu_S \quad (1.2)$$

### Schottky-Mott rule

One of the most important parameter describing the Schottky contact applies to pinpoint the value of SBH. The formation of ideal Schottky contact between metal and n-type semiconductor, which means achievement of thermal equilibrium and the absence of surface states, is presented in Figure 1.11. First, the metal and the semiconductor are isolated (Figure 1.11 a)). In this case, the position of the crystal internal energy bands can be referenced to the vacuum level. As example, the metal work function  $\phi_M$  is the energy difference between the vacuum level and  $E_F$ . For the semiconductor, the work function can be defined in the same way, however more practical is to determine the position of  $E_C$  band as shifted below the vacuum level by the electron affinity of the semiconductor  $\chi_s$ . When metal and semiconductor are electrically connected, electrons pass from the semiconductor to the metal, achieving thermal equilibrium. The Fermi levels on both materials line up, which means that in the described case the  $E_F$  in the semiconductor is lowered, relative to the metal  $E_F$ , by an amount equal to the difference between the two work functions (Figure 1.11 b)). Due to the flow of the electrons, negative charge is built up at the metal surface and consequently equal, positive charge is formed in the semiconductor. The built-up of this dipole field counteracts the further flow of electrons from the semiconductor to the metal. As the gap distance  $\delta$  decreases, the metal and semiconductor finally touch, the gap becomes transparent and the only barrier seen by the electrons is the resulting band bending in the semiconductor (Figure 1.11 c)).

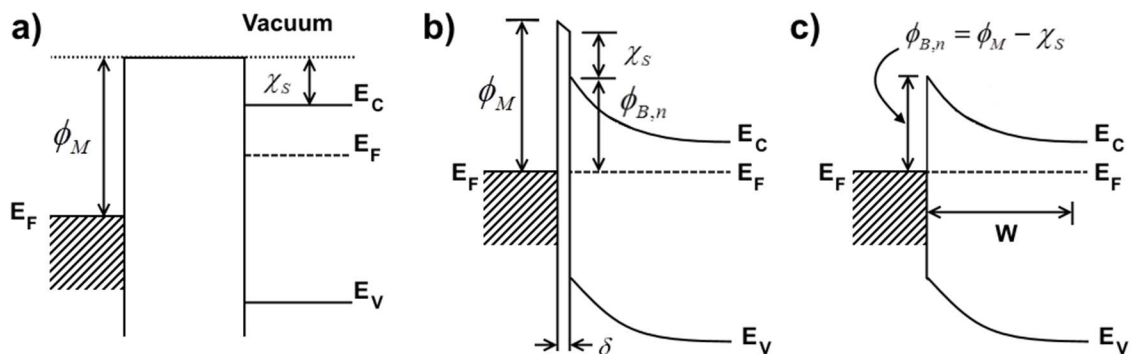


Figure 1.11 An example of energy band diagrams of metal and n-type semiconductor contact: a) metal and semiconductor are isolated, b) metal and semiconductor are electrically connected and separated by a narrow gap  $\delta$ , and c) perfect contact when gap  $\delta$  becomes zero.

It should be noted that the depletion width ( $W$ ) plays in this case also an important role in the current transport mechanism. For a narrow depletion width (high doping level) the tunneling process will dominate in the current transport, thus reducing the MS contact resistance (described in more detail in Chapter 1.4.2).

The Schottky-Mott model assumes that the alignment condition for the energy bands when the two crystals are isolated retain over the intimate MS interface formation between these two crystals [96] [100]. In consequence, according to Schottky-Mott rule, the n-type SBH of MS contact presented in Figure 1.11 c) is simply equal to the difference between the metal work function and the electron affinity of a semiconductor, which can be written as Eq. (1.3).

$$\phi_{B,n} = \phi_M - \chi_S \quad (1.3)$$

Equivalently, using Schottky-Mott assumptions, the p-type SBH is given by Eq. (1.4), where  $E_g$  is semiconductor band gap and for a given semiconductor, the band gap  $E_g$  is equal to the sum of n-type and p-type Schottky barrier height (Eq. (1.5)).

$$\phi_{B,p} = E_g - \phi_{B,n} = E_g - (\phi_M - \chi_S) \quad (1.4)$$

$$\phi_{B,n} + \phi_{B,p} = E_g \quad (1.5)$$

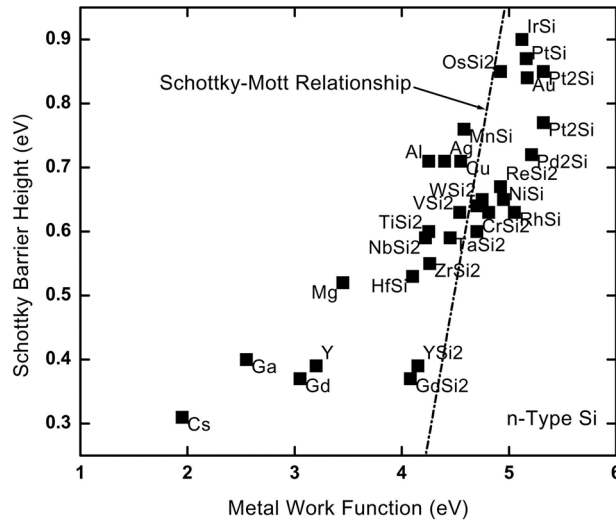


Figure 1.12 Experimentally measured Schottky-barrier heights on n-type Si. The straight line marks the prediction of the Schottky-Mott rule (from [101]).

Experimentally measured values of SBH (e.g. Figure 1.12) have however shown that the Schottky-Mott Rule has very limited relevance for real MS interfaces, and in

consequence, it also revealed that the main principle of this model based on simple superposition of electrostatic potentials for isolated crystals is insufficient. This leads to the conclusion that states, which are related to the surface of the two crystals, will not survive the formation of the MS interface, at least not without serious modifications. This means that new interface states dependent on interface atomic structure will appear and for their proper model description the interface chemistry as well as charge rearrangement and atomic relaxation must also be considered. In order to underline the meticulous character of this thesis, it should be mentioned that the direct correspondence of vacuum work function to interface barrier heights is proven to be incorrect.

### **Fermi level pinning at MS interfaces**

As shown in Figure 1.12 there is no clear dependence of the SBH on the metal work function as would be expected from Eq. (1.3) or Eq. (1.4). The presented example relates to different metals on n-type Si, however the absence of a strong dependence of the SBH on the metal work function was observed for various semiconductors. This phenomenon was named “Fermi level pinning at MS interfaces”. For scientists, it soon became obvious that the Schottky-Mott model – idealistic, non-interacting concept of the MS interface – is erroneous and incomplete. Consequently, the expression for SBH should be supplemented by an additional parameter. In the general description, a parameter called interface dipole  $eD_{int}$  is introduced as shown in Eq. (1.6). There are many definitions of interface dipole parameter, depending on which model was used for the description of the MS interface formation. However, in many models  $eD_{int}$  refers to a transfer of charge between the metal and the semiconductor, as for example results by the formation of chemical bonds in the MS interface or enforced by the so-called inhomogeneous barrier phenomena in SBH.

$$\phi_{B,n} = \phi_M - \chi_S + eD_{int} \quad (1.6)$$

In a more practical way, the description of the “pinning strength” of the given semiconductor is commonly represented by the so called S-parameter. The S-parameter, also called interface behaviour parameter, shows the ability of a semiconductor surface to screen out external (metallic) influence, and is defined as a slope of SBH against

metal work function (Eq. (1.7)). If for given MS system no scatter of SBH from the Schottky-Mott rule is observed ( $eD_{\text{int}} = 0$ ), we deduce that the semiconductor shows no pinning effect and S-parameter equals 1. In contrast, small value of S-parameter ( $\ll 1$ ) implies “strong pinning effect” for given semiconductor in MS interface.

$$S = \frac{\partial \phi_{B,n}}{\partial \phi_M} = 1 + \frac{e \partial D_{\text{int}}}{\partial \phi_M} \quad (1.7)$$

A bunch of studies revealed that S-parameter for different semiconductors correlate with specific properties, such as the ionicity, the polarizability or the dielectric constant [102] [103] [104]. However, those dependencies must be interpreted with caution, because it was shown that SBH measured at the same type of MS interface quite often exhibited very significant variations as a result of sample preparation conditions, sample treatment and measurement technique [97] so that more parameters actually vary SBH, than just those are plotted.

### **Fermi level pinning in the band gap – Bardeen model**

To shed more light on the interface state issue on the semiconductor surface in interaction with metal, John Bardeen in 1947 proposed a model, in which it was suggested that the work function difference between a metal and a semiconductor with surface states could be compensated by an exchange of charge between the metal and the semiconductor surface states [105]. His model was thus a natural extension of the research, carried out at the same time, on the overall neutrality of the semiconductor free versus adsorbate-covered surfaces. The presence of the semiconductor surface disrupts the periodic structure of a crystal, and leads to the creation of new electronic states particularly related to the surface - called also surface states. It turned out that the Fermi level for the semiconductor surface should always be positioned such that, just when all electronic states below the Fermi level are occupied, the surface is electrically neutral. In these considerations, a new phrase called the charge neutrality level (CNL) of electronic states in the surface region was introduced. CNL is the Fermi level for the surface. It was shown that for the majority of semiconductor surfaces the CNL is located in the gap of the bulk band structure, thus effectively “pinning” the surface Fermi level inside the band gap [97]. This phenomenon is called - unfortunately by the

similar nickname as the previous described phenomenon - Fermi level pinning in the band gap. Few years later, Bardeen's model has been expanded and supplemented by contributions from Cowley *et al.* [106].

As shown in Figure 1.13 metal and semiconductor are separated by a thin dielectric layer. This layer does not affect neither the surface states of the semiconductor nor the metal, which release this model from the problem that the electronic structure of both the metal and the semiconductor should be significantly modified upon contact and simultaneously allows for the consideration of chemistry expected at MS interface i.e., the charge exchange. According to this model, the n-type SBH is given by Eq. (1.8), where:  $\phi_{CNL}$  is the energy of the CNL measured with respect to the  $E_V$ ,  $S_{GS}$  is a constant,  $D_{GS}$  is the density of semiconductor surface states,  $\delta_{gap}$  is the dielectric gap thickness and  $\epsilon_{int}$  is the dielectric constant of the gap material.

$$\phi_{B,n} = S_{GS} (\phi_M - \chi_S) + (1 - S_{GS}) (E_g - \phi_{CNL}) \quad (1.8)$$

$$S_{GS} = \left( 1 + \frac{e^2 \delta_{gap} D_{GS}}{\epsilon_{int}} \right)^{-1} < 1 \quad (1.9)$$

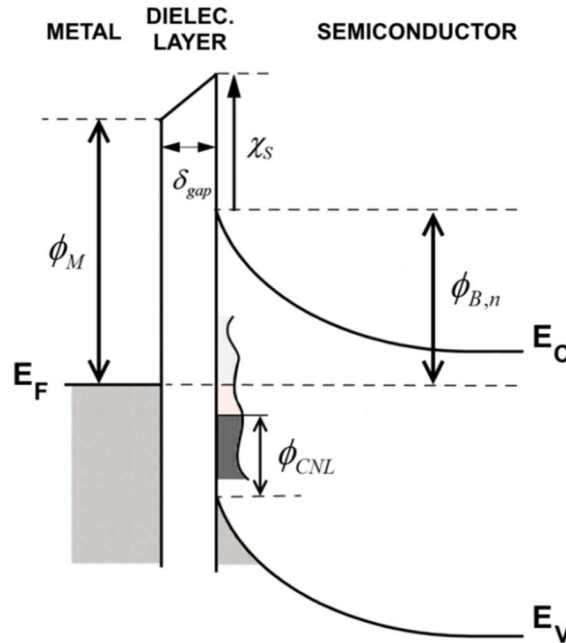


Figure 1.13 The Fermi level pinning in the band gap effect (the fixed separation model for SBH formation). Surface electronic states (CNL), with a characteristic density, are placed on the semiconductor surface, which is held at a fixed distance from the metal.

---

Based on equations (1.8) and (1.9) it is clear that the dependence of SBH on the metal work function is reduced by a factor of  $S_{GS}$ , which could be a large number for a significant density of surface states. Consequently, the Fermi level is expected to be strongly pinned near the position of the CNL, as a result of high density of surface states. The semiconductor's bands in such a case would be aligned to a location relative to the surface states which are in turn pinned to the Fermi level, all without strong influence from the metal. It appeared that for many commercially important semiconductors (Si, Ge, GaAs) the Fermi level pinning effect in the band gap is strong and therefore the design of semiconductor devices with i.e. appropriate electrical contacts, can be difficult.

### **Modification of SBH**

As already established, SBH formation in MS interfaces is a complex problem, which requires consideration of many important aspects from physics and chemistry, like for example atomic structure of MS interface or chemical bond formation etc., for a more accurate understanding of it. Moreover, no general rule exists and the interplay between charge and atomic rearrangement during interface formation needs to be considered for each individual case. Nevertheless, recently much attention was focussed on the possibility of SBH modification in a controlled way. In some cases, during the MS-type device fabrication, it turned out that no appropriate metals exist with high or low enough work function, or other process requirements like e.g. temperature, cost etc., restrict the choice of metals which can be used. In this context, it is important to be able to modify or tune the effective SBH without changing the metal used. For example, for most technological applications the ohmic contact formation, or the SBH value of the MS junction, plays the most important role. In contrast, for other devices, such as field-effect devices or rectifying diodes, not only the value of SBH, but also the uniformity of the interface is crucial. Here, a list of possible ways to modify the SBH in a controlled way is briefly presented. However, interestingly the common denominator of all mentioned techniques is concentrated around the electron transport mechanisms at an inhomogeneous MS interface near a so-called “saddle point potential” - which

represents the local changes in the potential energy “landscape” distribution “seen” by the charge (Figure 1.14).

SBH modification strategies:

*i)*     **SBH modification in heteroepitaxial systems.** Main basic models of SBH formation are based on ideal, homogeneous MS interfaces. However, in most real cases MS interfaces are heteroepitaxial systems. Between metal and semiconductor is an identifiable compound phase, with a structure/composition neither that of the metal nor that of the semiconductor. The current transport across this identifiable compound phase layer may affect the SBH. If the thick phase is metallic, such as metal silicides, germanides (often the case for Si and Ge contacts), this metallic compounds will control the carrier transport and thermionic-emission currents dominate in the overall current transport. In contrast, if this interface phase has more insulating behaviour, the transport across such a junction would be dominated by tunneling effects. It is also very important that real heteroepitaxial MS systems may be characterized by defects like threading dislocation in the MS interface. Of course, the presence of such defects and point defects does not remain unnoticed for the band bending conditions in MS interface and consequently may affect the value of SBH and its homogeneity. More detailed discussion on this topic can be found in Sec. III E of Ref. [97].

*ii)*     **SBH modification by using molecular dipoles.** This strategy is based on the introduction in the MS interface of a new, thin material, which is itself a dipole. In this field, organic molecules in form of self-assembled monolayers (SAM) or Langmuir-Blodgett films seem to offer the ability to tune SBHs [107] [108].

*iii)*     **SBH modification with thin layers of insulating material.** It was shown that thick enough insulating interlayers between metal and semiconductor strongly influence the potential distribution and the electron transport across the entire “stack”, which from now on should be considered more properly as a metal-interlayer-semiconductor (MIS) stack. Please note that insulating interlayers can be understood more broadly, because different materials e.g. inorganic materials (oxides), organic material (polymer, molecules) or even semiconducting



material with different band gap, are commonly employed as the insulating interlayer. A great example of this approach was given for SBH modification for n-type Ge. It was shown that various materials ( $\text{GeO}_x$  [109],  $\text{Ge}_3\text{N}_4$  [110], TaN [111] etc.) inserted as the interlayer between metal and n-type Ge reduce the strong pinning effect and lower the SBH.

*iv)* **Controlled introduction of impurities (such as metals, dopants, semiconducting and isolating elements) to the MS interface.** Here, it is clear that each of these inclusions can directly affect the magnitude of the local SBH, but in the case of a high inclusion density the global SBH will be also influenced. As for example shown in Figure 1.14, dopants can strongly modify the potential distribution in the MS interface. As a good example, Mueller *et al.* have shown studies on effective SBH modifications as a function of the implantation dose of As in NiGe/Ge(001) contacts [112].

*v)* **SBH modification with adsorbate-terminated semiconductor surface (ATS).** In this technique, ATSs are carefully covered by metal layer in such a way that the adsorbate induced different reconstruction (from the typical semiconductor surface) may survive the metallization process. Different types of semiconductor surface reconstruction induce different interface dipoles, which mean that also the SBH is affected. Ref. [113] presents the changes in measured SBH on ATS Si surfaces.

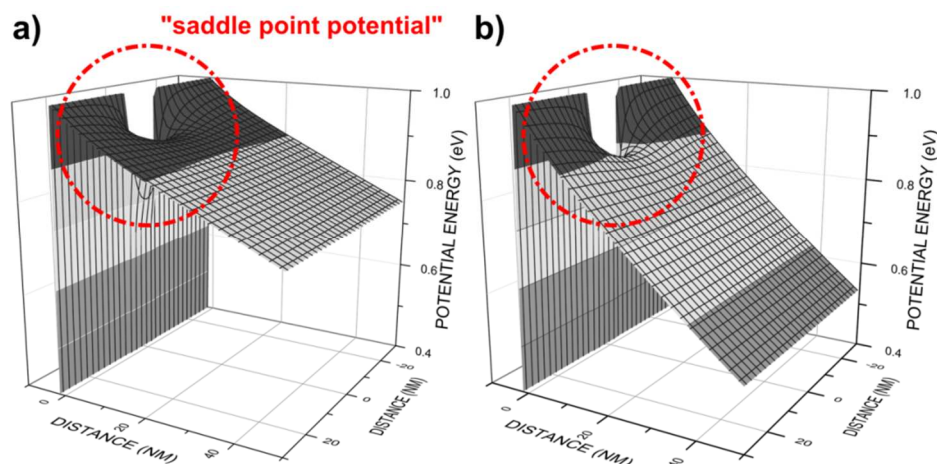


Figure 1.14 An example of theoretical calculations of potential distribution in front of a low-SBH patch for lightly and more heavily doped semiconductor- a) and b), respectively. Red-dashed circle specifies the area called “saddle-point potential”. This term is commonly used in the consideration of inhomogeneous SBHs (figure after [97]).

It should be noted that local SBH modifications may proceed also in “an uncontrolled way”, which is mostly related with the presence of impurities or structural defects at MS interface. The fabrication of real MS junctions requires special equipment, tight process control, and technological “know-how”. Despite the best willingness, small variations in the Schottky barrier manufacturing process, like less-than-ideal vacuum and surface cleaning conditions, may result in local impurities or structural defects at MS interface. This undoubtedly affects local SBHs by introduction of local charges, which reduce the saddle point potential further and result in substantial current crowding effects (e.g. impurities), or in general causing interface inhomogeneities with different SBHs (e.g. structural defects).

#### 1.4.2. Ohmic contact

Of course, it is also important, in the context of the above considerations on metal-semiconductor junctions to define the ohmic contact. A MS contact is considered to have an ohmic characteristic, when it presents non-rectifying behaviour and has negligible junction resistance contributing to the total resistance of the semiconductor device, i.e. bulk or spreading resistance of the semiconductor. The contact resistance ( $R_C$ ) is the macroscopic parameter describing ohmic contacts and is defined as the reciprocal of the derivative of the current density ( $J$ ), with respect to the voltage across the interface ( $V$ ). When evaluated at zero bias the contact resistance is given by Eq. (1.10). An acceptable ohmic contact should not significantly disrupt device performance, and it can supply the required current with a voltage drop that is sufficiently small compared to the drop across the active area of the device [25]. This prevents resistive heating of MS contact area and potential device failure.

$$R_C = \left( \frac{\partial J}{\partial V} \right)_{V=0}^{-1} \quad (1.10)$$

As shown in Figure 1.15, ohmic contacts can be realized in two ways: based on low barrier height (Figure 1.15 a)) or high doping concentration in the semiconductor (Figure 1.15 b)). For low doping concentrations in semiconductor and/or moderately high temperatures, the thermionic-emission current dominates in the current transport so

that contact resistance is given by equation (1.11), where:  $k_B$  - Boltzmann constant,  $kT$  - thermal energy,  $q\phi_B$  - Schottky barrier height and  $A^*$  - effective Richardson constant for thermionic emission. In this approximation, the small voltage dependence of the barrier height was neglected, since only a small applied voltage is relevant. Based on equation (1.11), it is evident that a low barrier height is mandatory to obtain small contact resistance. For M-S junction with n-type semiconductor, the metal work function must be smaller than that of the semiconductor to reach the ohmic contact condition (for p-type semiconductor situation is reversed).

$$R_c = \frac{k_B}{qA^*T} \exp\left(\frac{q\phi_B}{kT}\right) \quad (1.11)$$

For a higher doping level, the tunneling process will dominate, and the  $R_C$  can be described by Eq. (1.12),

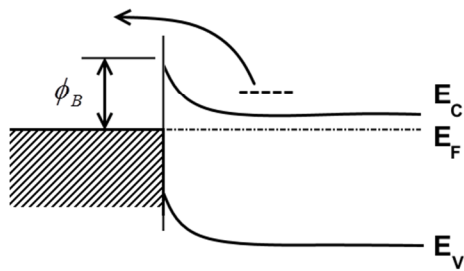
$$R_C \sim \exp\left(\frac{q\phi_{Bn}}{E_{00}}\right) = \exp\left[\frac{2\sqrt{\epsilon_s m^*}}{\hbar} \left(\frac{\phi_{Bn}}{\sqrt{N}}\right)\right] \quad (1.12)$$

where:  $E_{00}$  is a parameter related with doping and defined by equation (1.13) ( $\hbar$  - reduced Planck constant,  $N$  - doping concentration,  $\epsilon_s$  - permittivity of semiconductor, and  $m^*$  - effective mass).

$$E_{00} = \frac{q\hbar}{2} \sqrt{\frac{N}{\epsilon_s m^*}} \quad (1.13)$$

Equation (1.12) shows that  $R_C$  strongly depends on doping concentration and varies exponentially with the factor  $(\phi_{Bn} / \sqrt{N})$ . Theoretical calculation and experiments depict that the doping density necessary to achieve ohmic contact based on tunneling effect should be  $10^{19} \text{ cm}^{-3}$  or higher [114] [115]. In summary, it is obvious that high doping concentration, low barrier height, or both must be used to achieve low values of  $R_C$ . Currently, these two approaches are used for fabrication of electrical contacts in microelectronic devices [116] [117].

a) Low barrier height



b) High doping

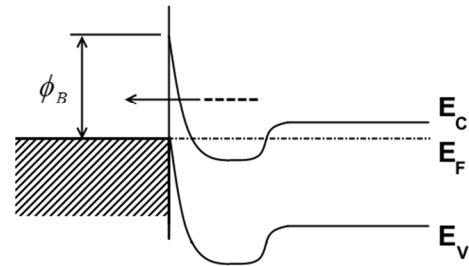


Figure 1.15 Energy band diagrams of ohmic contacts: a) with low barrier height and b) with high doping of the top semiconductor surface layers.

The second issue related with ohmic contacts, which should be mentioned here is progressive miniaturization of CMOS devices. As shown for the simplest case, which means uniform current density across the whole contact area, total contact resistance  $R$  is a function of contact resistance  $R_C$  and contact area  $A$  according to Eq. (1.14).

$$R = \frac{R_C}{A} \quad (1.14)$$

Since CMOS devices were typically scaled more and more aggressively, the device current density usually increases. This demands not only smaller ohmic resistance but also a smaller contact area. As consequence the formation of contacts for nano-CMOS applications with low resistance becomes more challenging [118]. More information about metal contact formation in CMOS devices can be found in Refs. [119] [120].

## 1.5. Motivation and organization of the thesis

Extending the performance of existing Si microelectronics beyond the limits faced by either miniaturization (“More Moore”) or available functions (“More than Moore”) requires the integration of new materials. Ge, due to its superior physical properties with respect to Si in terms of optoelectronics and its CMOS processing compatibility, has gained a lot of attention for its potential application as an integrated alternative semiconductor material on the mainstream Si technology platform.

Among various integration challenges for reliable integration processes (such as doping, epitaxial quality etc.), low resistance metal/Ge contacts are of special importance. As was mentioned in previous chapters, the formation of the SBH is a complex problem, which requires an individual quantum-mechanics-based approach for each type of MS system. In addition, it was proven that interface properties are strongly affected by atomic interface rearrangements (the atomic structure of the MS interface). It can be briefly pointed out that in terms of materials science the most important issues required to produce high quality ohmic contacts are related with:

- **controlled growth of correct phase with low resistance and thermal stability** - as is shown later in this dissertation, investigated systems exhibit a complex phase diagrams with a wide range of different physical properties;
- **single phase growth instead of phase fluctuation in the contact area** - for example crystalline quality, grain size, grain boundaries etc. lead to structural inhomogeneity of MS interfaces;
- and finally **homogenous, defect free atomic MS interface structure** - here it is important to achieve defect free and impurity free MS interfaces.

Nowadays, Co and Ni metal silicides are the most employed contact material in state-of-the-art Si CMOS devices. Obviously, due to similar cleanroom processing techniques, the corresponding low resistance Co and Ni germanides are an obvious choice for electrical contacts in Ge-based devices.

This dissertation is aimed to shed more light on the formation process of Co and Ni germanides on a Ge(001) substrate on the nano-scale. The main part of research was based on *in-situ* scanning tunneling microscopy (STM) studies, with the nano-scale spatial resolution, on the influence of subsequent, post-evaporation annealings at various temperatures in order to follow the structural evolution of a few monolayers of Co and Ni metal (deposited at room temperature (RT) in ultra-high vacuum (UHV)) on an atomically clean Ge(001) surface. Furthermore, additional techniques like LEED, (S)TEM-EDX and XPS were used to corroborate and complement the STM derived insights. I believe that findings presented in this thesis and associated with the investigated epitaxial Co-Ge and Ni-Ge systems, will allow to correlate experiment

and theory for advancing the understanding of SBH behaviour. It turned out in the past that studying the SBH of epitaxial systems with high quality MS interfaces and similar lattice parameters resulted in a good agreement between theory and experiment, as a result of the reduction of the parameters which may affect the SBH (mainly interface inhomogeneity). As an example, studies on NiSi<sub>2</sub>/Si(111) or CoSi<sub>2</sub>/Si(100) epitaxial systems may be cited here [121] [122], which substantially advanced our understanding of SBH formation on an atomic-scale. Certainly, epitaxial (model) systems like in the present thesis are of high value to deduce theoretical insights, as these systems can be well described by theory and thus correlated with experimental results.

Current theoretical models supported by experiments clearly show that the atomic structure at MS interface is a central factor contributing to the SBH formation. It is clear that many of the factors contributing to the formation of real MS interfaces like crystalline quality, grain size, stoichiometry, defect and dopant density, contamination etc. lead to structural inhomogeneities. The structural inhomogeneity affects the nominal SBH at the interface and in consequence the transport phenomenon across the interface. Therefore, an example of nano-scale STM study approaches as applied in this work, are well suited to unveil materials properties with respect to structural properties including inhomogeneities like defects and impurities and give thus basic research insight for overall electrical contact behaviour in future Ge devices.

It is worthwhile to reiterate that in the era of continuous microelectronic device miniaturization, researches on nano-scale contacts are particularly relevant. As for example in case of future Ge-based nanodevices, well-defined and homogeneous SBH behaviour of metal contacts are needed for advanced FinFet CMOS technologies as well as for micro-scale photonic devices to avoid e.g. contact burning by current crowding effects.

### 1.5.1. Structure of the thesis

In this doctoral thesis a systematic and comparative surface science study of the formation process on the nano-scale of Co- and Ni-germanides on Ge(001) substrate is presented. The dissertation is organized as follows:

In **Chapter 1** a brief historical overview of the microelectronic industry and its trends over the last years, with particular emphasis on the likely promising directions of development, are given. As a second part of introduction, the in depth theoretical background of Schottky and Ohmic contacts is briefly presented.

After presenting the abstract and the introduction, **Chapter 2** comprises a detailed description of used experimental methods and hardware setups. Given that the main part of presented research was based on *in-situ* STM studies, and the fact that samples were prepared in STM hardware system, the STM setup is precisely described. This includes a description of the UHV chambers, the sample preparation procedure and the "extended basics" of the STM technique applied in this study.

**Chapter 3** consists of the main part of this thesis. Here, results of comprehensive multi-technique studies on the formation and thermal evolution of metal germanide nanostructures on Ge(001) together with a detailed discussion are given. Subsections present the results, obtained from various experimental methods, separately for clean Ge(001) surface, Co-Ge(001) and Ni-Ge(001) systems, respectively.

Finally, **Chapter 4** provides the comparative discussion about these two investigated, Co- and Ni-Ge systems, detailing the most important common features and differences, in view of their possible applications in microelectronics. This chapter closes this dissertation with a summary, conclusions and outlines open questions.

**Chapter 5** presents the publication list and scientific visibility of the author of this dissertation. In addition, a description of the quantum mechanical tunneling process is given in **Appendix A**. Furthermore, lists of the most widely used acronyms and symbols in the field of surface science are given.





# Chapter 2

## Experimental background

### 2.1. Characterization techniques

In this doctoral thesis a number of different characterization techniques were used for investigation of the prepared and processed samples. In the following sections, the experimental setup and a concise theoretical introduction of each method is presented.

#### 2.1.1. Scanning Tunneling Microscopy

*HISTORY:* In 1978 scientists at IBM Zurich Research Laboratory began the study of an apparatus, which could allow real space imaging of solid surfaces with real atomic-scale without illuminating light lenses. In 1981 G. Binnig, H. Rohrer, Ch. Gerber and E. Weibel observed vacuum tunneling of electrons between a sharp tungsten tip and a platinum sample, the Scanning Tunneling Microscope (STM) was invented [123] [124] [125] [126]. This invention played a significant role in the development of surface science, and therefore Binnig and Rohrer received the Nobel Prize in Physics „for their design of the scanning tunneling microscope” just five years later (see Figure 2.1) [127].

STM was the pioneering method for a very extensive group of research techniques, which is today called scanning probe microscopy (SPM). The general principle of operation of all scanning probe microscopies is surprisingly simple: All SPMs are based upon scanning a probe just above a surface whilst monitoring some interaction between the probe and the surface. In the case of STM, the crucial interaction between probe and the specimen is based on the quantum mechanical tunneling phenomenon, namely the

tunneling of electrons through the potential barrier higher than the energy of the particles. A detailed description of the quantum mechanical tunneling process is given in Appendix A, so that the description in the following chapter is restricted to typical hardware and experimental aspects, including the most important criteria in the construction and efficient operation of STM.

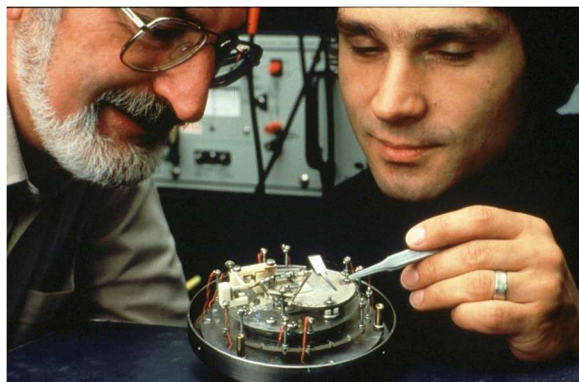


Figure 2.1 Nobel laureates Heinrich Rohrer (left) and Gerd Binnig (right) of IBM's Zurich Research Laboratory, shown here in 1981 with a first-generation scanning tunneling microscope (from [128]).

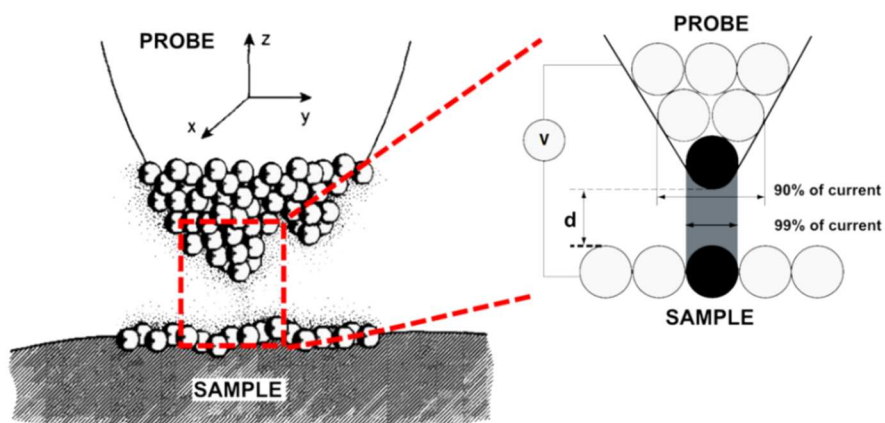


Figure 2.2 A schematic diagram of the probe-sample interaction in STM. The exponential dependence of the tunnel current on the gap separation selects the most protuberant atom on the probe tip for tunneling to the flat sample, giving rise to the atomic resolution of the tunneling microscope (after [129]).

*QUANTUM MECHANICS OF TUNNELING:* Figure 2.2 shows a scheme of interaction between tip and sample during the standard operation mode. A sharp conducting tip is brought very close to the surface of the sample, a distance of a few Å<sup>1</sup>. A bias voltage applied between the tip and the sample results in electrical current flow. Electrons can

<sup>1</sup> The Ångström unit (Å),  $1 \text{ Å} = 10^{-10} \text{ m}$ . Unit of length which is often used in SPM research community because it is the most appropriate length scale for dealing with structures on an atomic scale.

quantum mechanically tunnel across the gap. The direction of electron tunneling across the gap depends on the sign of the bias voltage. By analysing quantum tunneling through potential barriers it can be shown that the tunneling current strongly depends on the distance between tip and surface (barrier width). There are a number of theoretical models, which describe the tunneling phenomenon between the STM tip and the sample surface (see also Appendix A). Here, for example, the most important conclusions of the Tersoff and Hamann model (one of the first and simplest model) are provided [130].

$$I \propto \int_0^{eU} \rho_s(E) T(E, eU) dE \quad (2.1)$$

$$T(E, eU) \approx e^{-2\kappa s} \quad (2.2)$$

Assuming a point-like tip, equation (2.1) shows that the tunneling current  $I$  directly depends on the density of states of the sample ( $\rho_s(E)$ ) and the so called transmission coefficient ( $T(E, eU)$ ), which describes the probability of electron transition through the barrier (electron with energy  $E$  and applied bias voltage  $U$ ). It is seen that the transmission coefficient decreases exponentially with increasing the barrier width (distance sample-tip) named here -  $s$  (Eq. (2.2)). In case of a 10% change of barrier width, the tunneling current will change ten times. This “physics behind” is a key element in STM for its high resolution capability in the direction perpendicular to the sample surface.

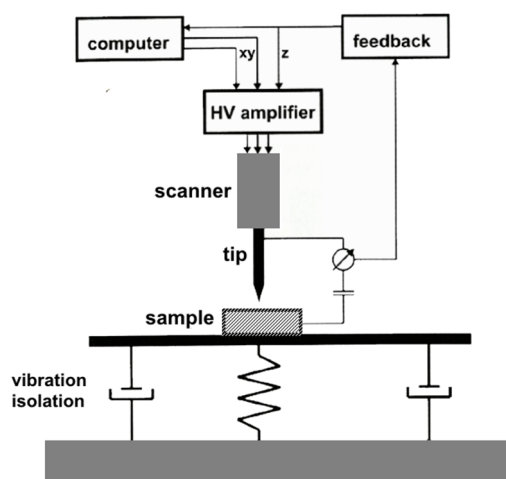


Figure 2.3 Schematic diagram of the construction of a typical scanning tunneling microscope, which shows the most important components. Detailed description is given in the text.

*STM HARDWARE:* The experimental arrangement is shown in Figure 2.3. A scanning tunneling microscope consists of four basic elements: 1) approach mechanism that enables the tip to be positioned within tunneling distance with respect to the sample surface (not included in Figure), 2) ultra-sharp tip which is mounted to high precision scanning mechanism allowing for three-dimensional tip motion, 3) electronics with computer system responsible for feedback loop and data acquisition, and finally 4) an isolation mechanism to protect the microscope from ambient noise and vibrations.

The coarse motion device, which brings the tip and sample into tunneling range, as well as high precision scanning mechanism are nowadays based mainly on piezoelectric transducers (piezoelectric transducers expand or contract upon applying a voltage). However, various types of construction design can be found. For example, an approach mechanism may be based on: piezoelectric walker [123], an inchworm (Inchworm is a registered trademark of Burleigh Instruments, Inc.) [131], a vacuum compatible stepper motor [132], or an inertial stepper [133] [134]. In the tunneling range, the scanning motion of the probe tip with respect to the sample is also controlled by piezoelectric elements, but here just two technical solutions are dominating: tripod scanners and piezoelectric tube scanners. A piezodriven tripod consists of three individual, mutually perpendicular piezoelectric transducers ( $x$ ,  $y$ ,  $z$ ), which need to be glued or screwed together. By applying a sawtooth voltage on the  $x$  piezo and a voltage ramp on the  $y$  piezo, the tip scans in the  $xy$  plane of the sample. Piezoelectric tube scanners have four electrodes placed into four equal segments of the tube. The movement in the  $xy$  directions is realized by applying differential scan signals to the electrode segments located on opposite sides of the tube, whereas common mode signals applied to the electrodes, or additional electrodes in the interior of the scanner tube, allows for extension in the  $z$  direction [135] [136] [137]. A typical piezoelectric ceramic used in STM scanners is PZT-5H (lead zirconate titanate), which offers large piezoelectric response ( $\sim 6 \text{ \AA/V}$ ) [138].

STM can work in different modes:

- *Scanning Tunneling Microscopy:* For imaging the topography of the sample, two basic modes are used: constant height- or constant current mode. In constant-height mode, the tip moves in a horizontal plane above the sample at a constant

---

height. The tunneling current varies as a function of the surface topography and the local surface electronic states of the sample, thus topographic images are formed from a set of tunneling current measurements at each point on the sample surface. Constant height mode is commonly used for investigations of relatively smooth surfaces, where the risk of tip damage is relatively small. In constant-current mode, the STM uses a negative feedback loop to provide a constant tunneling current value by adjusting the height of the scanner at each measurement point. When an increase in tunneling current occurs, the feedback system adjusts the voltage applied to the piezoelectric scanner to increase the distance between tip and sample. The scanner moves away from the sample, so that the tunneling current value reaches the set value. Therefore, in this mode the topographic image is created on the basis of the motion of the scanner data set. It should be clearly emphasized that in both working modes described above, the STM measures the electronic density of the sample surface at the tip position, which then may be interpreted as the morphology of the sample surface.

- *Scanning Tunneling Spectroscopy*: The ability of the STM to probe the local electronic structure of a surface, in principle with atomic resolution, leads to perform Scanning Tunneling Spectroscopy (STS). In this mode, the local electronic structure of the sample surface is examined by the measurement of local current-voltage characteristics ( $I/V$ ) – the dependence of the tunneling current as a function of bias voltage between tip and sample. Additionally, STM can collect  $I/V$  characteristics at each pixel of the standard topographic image, providing a three-dimensional map of electronic structure. This technique of STS is called current imaging tunneling spectroscopy (CITS). Extending STS measurements by adding a lock-in amplifier allows directly collecting information about samples electrical conductivity ( $dI/dV$ ), local density of states ( $d^2I/dV^2$ ), and work function ( $dI/dz$ ). In comparison with other surface analytical spectroscopies, where measured data are collected from relatively large areas (micrometres, millimetres), STS is emerging as extremely powerful technique to study surface electronic properties of a material with near atomic resolution [139].

*TIP PREPARATION:* Key issue of a productive STM imaging is the quality of the probe tip. In an ideal situation the tip should be ended by a single atom, from which electrons are tunneling to the surface (and vice versa). Various materials and techniques were used to check their ability to create ultra-sharp stable probe tips, however nowadays STM probe tips are typically made from either tungsten (W) or platinum-iridium (Pt-Ir) wires. Probe tips are usually fabricated by electrochemical etching of a small diameter wires. However, in the case of Pt-Ir, the tip can be fabricated in an easier way: cutting the wire with sharp scissors at an angle of 45°. Previously wire and scissors should be thoroughly cleaned in acetone or isopropyl alcohol using an ultrasonic bath. Cutting process should be made by one precise movement taken in a wire axes direction. But returning to the most popular methods: two different electrochemical etching techniques are used for forming the probe tip - alternating current (AC) self-termination method and direct current (DC) drop-off technique. Both techniques yield ultra-sharp probe tips with radii of curvature of 1000-1500 Å and 10° cone angle for AC self-termination technique, and sharper tips with radii of curvature of 500 Å and 6° cone angle for DC drop-off technique [140]. A few examples of different electrochemical etching recipes collected from literature are given in Table 2.

Table 2 Examples of electrochemical etching procedures for various tip materials to obtain ultra-sharp tips [141] [142] [143] [144].

Tip material	Polishing solution	Procedure
Molybdenum	KOH	5- 10 V AC or DC
	8NH <sub>4</sub> OH + 2KOH	3-6 V AC
	20% KCN	1-5 V AC
Platinum/alloys	20% KCN	3-15 V AC
	Molten 4NaNO <sub>3</sub> + NaCl	1-5 V DC
Tantalum	2HF (48%) + 0.5CH <sub>3</sub> COOH + H <sub>3</sub> PO <sub>4</sub> + H <sub>2</sub> SO <sub>4</sub>	5-15 V DC
Tungsten	KOH	1- 10 V AC or DC

*VIBRATION ISOLATION:* Finally, to obtain atomic resolution, vibration isolation is essential. For high-resolution applications, the distance between the probe tip and sample must be maintained with an accuracy of better than 0.01 Å [145]. Effective

microscope-vibration isolation systems should suppress external vibrations as well as noise from internal driving signals to less than desired tip-sample gap accuracy throughout the bandwidth of the instrument. A prominent example of typical external noise is building oscillations. Typical building vibrations fall in the 1-20 Hz range, depending on size and design. Additionally any motors, transformers and air-condition ducts in the STM laboratory, or in its neighbourhood, can occur as additional vibration noise around 60 Hz. These examples just show how important appropriate planning of SPM laboratory construction is. Laboratories, where STM measurements are performed, should be placed in the basement of the building, which are situated far away from any traffic. Furthermore, STM systems should be located on a separated foundation, which has no contact to the main building walls. However, such procedures are not sufficient and additional active and/or passive anti-dumping systems must be used. For example, the first STM system was isolated by magnetic levitation techniques. Its creators used magnetic levitation on a superconducting bowl of lead combined with eddy-current damping. However, the solution worked only at liquid helium temperatures. Modern SPM microscopes usually use suspension spring systems in addition with eddy-current dumping. Additionally, if STM is a part of a complex vacuum system, commercially available pneumatic feet can be used.

In summary, STM is a powerful tool which provides local information, ultimately with atomic resolution of samples directly in real-space. However, some main disadvantages of the STM technique are given: due to the fact that the measured signal is a tunneling current, only conductive samples can be investigated. STM as progenitor of SPM had thus a great impact on science development to overcome these limits. Nowadays, different SPM techniques are commonly used by interdisciplinary research groups in many different scientific disciplines like condensed matter physics, chemistry and biology.

### **STM experimental system**

The main experiments, including sample preparation and *in-situ* measurements, reported in this thesis were performed in an Omicron ultra-high vacuum (UHV) system, with a base pressure of  $8 \times 10^{-11}$  mbar. In this section, a compact description of the system is

given. Figure 2.4 depicts an overview of the instrument. This system consists of three main parts: 1) analysis chamber (ACh), 2) preparation chamber (PCh), and 3) load lock chamber (LL), shown in the image by grey dashed lines.

- 1) Analysis chamber, the main chamber of the system, was designed and used only for *in-situ* studies. ACh is equipped with a four-grid LEED optics which can also serve as a retarding field analyser for AES. In ACh is located the main measuring device SPM manufactured by Omicron (VT-AFM XA model). This model is equipped with cooling/heating stage which offers a variable temperature range from -220 °C to 380 °C. For the entire system (heating stages in manipulator, microscope stage) standard Omicron sample plates, made from Mo, Ta or stainless steel are used. Maximum sample size is 11 mm x 11 mm.
- 2) All sample preparation procedures, including surface cleaning, metal deposition with subsequent annealing steps at various temperatures, were performed in the preparation chamber (PCh). PCh is equipped with e-beam evaporator (not shown in Figure 2.4), ion sputtering gun with dosing valve and x-y-z manipulator with sample heating stage. Sample annealing treatments can be realized in two ways: in radiative heating (RH) mode and direct heating (DH) mode. In radiative heating, the sample is heated by thermal radiation from the outer heater hidden in the manipulator heating stage. In older manipulator designs, the heater is a tungsten wire dragged through ceramic tubes, in newest versions PBN (pyrolytic boron nitride) or PG (pyrolytic graphite) heaters are used. In direct heating mode, a current flows through the sample and in accordance with the sample resistance heat is generated. Annealing temperatures can be measured by means of a thermocouple type K and/or an infrared pyrometer (above 500 °C range) with an accuracy of  $\pm 10$  °C and  $\pm 5$  °C, respectively. The manipulator has proper electrical feedthroughs to connect heaters and thermocouple. Please note that exactly this same type of manipulator is located in ACh, however in this case the manipulator was used only to position and to ground the sample during LEED/AES measurements. To transfer the sample between the different chambers, magnetic transfer rods were used.



- 3) The last chamber is the load lock which is equipped with a fast entry gate and a separate high vacuum pumping system. LL was used to transfer the samples between the vacuum-air interface.

Blue description shown in Figure 2.4 refers to the pumping systems and pressure measurement setup. ACh and PCh have a separated UHV system, consisting of ion getter pump and titanium sublimation pump. In both chambers, pressure is controlled by Bayard-Alpert hot-cathode ionization gauges. These chambers can be separated by manual gate valve (MV). High vacuum pumping system for LL and PCh is similar and consists of turbomolecular pumps and rotary vane pumps. These pumps were used to pump also the LL for sample transfers and pump out the whole system after venting. In LL, the pressure is controlled by cold-cathode ionization gauge (inverted magnetron), whereas in the pre-vacuum, systems pressure control is realized by Pirani gauges. ACh and PCh are also equipped with residual gas analysers for potential system leak tests (not shown in Figure). Interlock systems control the chamber pressure and in any case of a sudden pressure increase or turbomolecular pump failure, which is added to PCh, it will immediately turn off all filaments in all chambers and close pneumatic valve (PV).

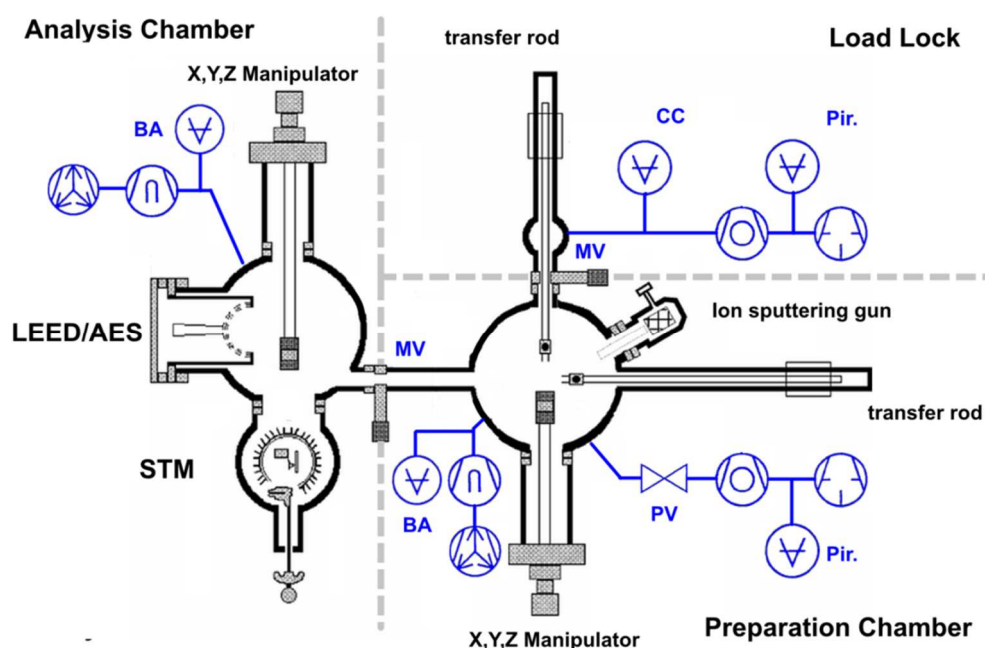


Figure 2.4 Schematic view of Omicron STM system. Key elements are named directly. Grey dashed lines represent the sections of the system consisting of load lock, preparation and analysis chambers. Blue items represent pumping systems and pressure measurement setup (MV - manual valve, PV - pneumatic valve, Pir. - Pirani gauge, BA - Bayard-Alpert gauge, CC - cold-cathode gauge). Detailed description of instrument is given in the text.

## 2.1.2. Other techniques

### A. Low Energy Electron Diffraction

In accordance with L. de Broglie's hypothesis of the wave nature of matter, a flux of particles moving with velocity  $v$  and having mass  $m$  can be considered as wave with a wavelength  $\lambda$  according to the formula ( $h$  – Planck's constant) [146] [147]:

$$\lambda = h/mv \quad (2.3)$$

In 1927 de Broglie's hypothesis has been confirmed by Davisson and Germer, who accidentally observed diffraction of electron with energy around 370 eV by a crystal of nickel [148]. In Low Energy Electron Diffraction (LEED) technique a low-energy beam of electrons (between 10 eV and 500 eV) is incident normal to a surface and diffracted. According to the formula (2.3) the wavelength for 100 eV electrons is about 1 Å, therefore the interference between electron beam and periodic crystal lattice is to be expected in case of a coherent excitation source.

Figure 2.5 a) presents a typical schematic diagram of a LEED device construction with three grids [149]. The electron beam emitted by the electron gun passes through energy selection in the Wehnelt cylinder and after appropriate focusing by electrostatic lenses is incident normal to the sample. Electrons are accelerated on the path between cathode and lenses to the selected energy (up to 500 eV). Lenses B and C have an intermediate potential, and are used to focus the electron beam. A fluorescent screen (collector) has a positive voltage of several kV (usually 5-7 kV) and works as an accelerating electrode for deflected electrons, which can be now observed on it. On the sample surface, inelastically scattered electrons can also occur. However, the central grid (suppressor) has a negative bias respect to the cathode, in consequence inelastically scattered electrons are mostly suppressed and do not reach the screen.

LEED is one of the most common methods in surface science to study the structure of surface, due to fact that the obtained results relate to the first few surface layers of the sample. This technique can be used e.g. for: assessment of the surface cleanliness of the sample; obtaining information about surface reconstructions; obtaining information about distances between molecules adsorbed on the surface or to define the amplitude of

vibration of atoms on the crystal surface [150] [151]. More information about LEED and diffraction physics can be found in Ref. [152] [153].

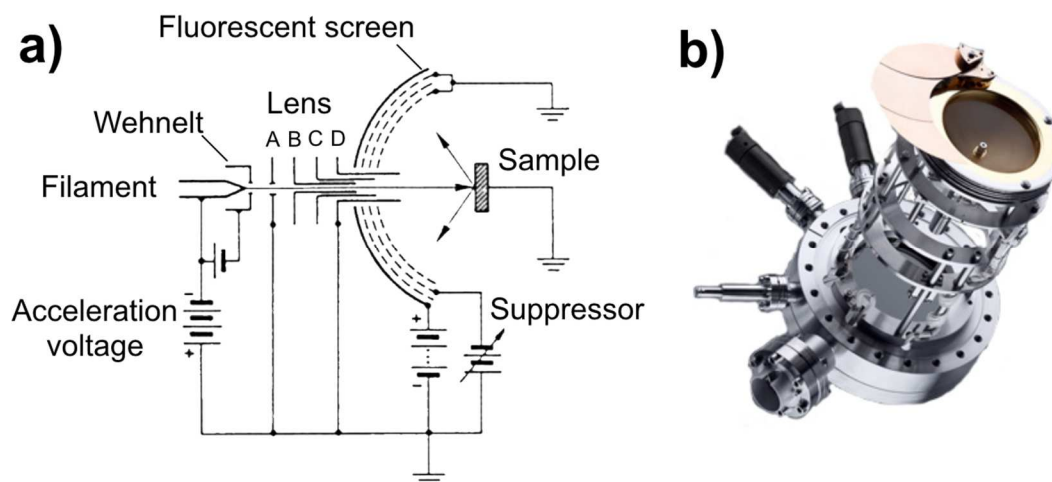


Figure 2.5 LEED measurements: a) Schematic diagram of LEED device with three-grid optics (after [149]), b) Photograph of ErLEED 150 unit equipped with optional shutter (from [154]).

### Experimental Setup

Figure 2.5 b) presents a general view of an ErLEED 150 device produced by SPECS GmbH, which was used for electron diffraction experiments in this PhD thesis. Such device (version without the shutter) is added to the analysis chamber in the UHV system from Omicron, which is described in the previous chapter (2.1.1.). In addition, the ErLEED 150 is equipped with 4-grid optics which can be used as an electron energy analyzer. This offers the possibility of recording Auger electron spectra (AES) (see Chapter 2.1.2. B: X-ray Photoelectron Spectroscopy). By changing the voltages applied to the electron gun, the grids and collector, it is possible to switch in an easy way from LEED to AES work mode. In this case, LEED circuits acts as a retarding field analyser (RFA), which means that electrons coming from the sample have to overcome a retarding field before they reach the collector screen. More precise explanation for RFA, as well as example of its use in LEED devices can be found in Refs. [155] [156] [157].

## B. X-ray Photoelectron Spectroscopy

X-ray Photoelectron Spectroscopy (XPS), also called Electron Spectroscopy for Chemical Analysis (ESCA), has been established as one of the most important and widely used surface analysis technique [158]. XPS is based on the photoelectric effect, which was discovered in 1905 by Albert Einstein (where a hypothesis of the quantum nature of light was postulated, and won him the Nobel Prize in Physics in 1921) [159]. When a surface is irradiated by a light source (photons), the photoelectric effect may occur, in which the incident photon is absorbed and its energy is fully transferred to an orbital electron, resulting in photoelectron emission. In accordance with equation (2.4) the maximum kinetic energy ( $E_{kin}$ ) of photoemitted electron is related to the energy of the incident light ( $h\nu_0$ ) and the work function ( $e\phi$ ), which describes the minimum energy required to remove electron from surface atoms towards the vacuum level.

$$E_{kin} = h\nu_0 - e\phi \quad (2.4)$$

Kai Siegbahn (Nobel Prize in Physics in 1981) showed that based on photoemission phenomena caused by X-ray radiation sources, in combination with high resolution electron energy spectrometry, it is possible to detect photoelectron spectra, in which photoemission from specific atomic orbitals is recorded in well resolved photoelectron peaks [160].

A typical XPS process is presented in Figure 2.6. An incident monochromatic photon beam causes the ejection of an electron in the solid. Then the photoelectron may travel to the surface, where it can emitted to the vacuum. However, only those photoelectrons emitted from the surface area that have suffered no energy loss contribute to the photoemission peak. On the other hand the photoelectrons emitted from the surface zone that have lost some energy due to inelastic interactions contribute to the scattering background. Typically inelastic interactions are quantified by the inelastic mean free path (IMFP), which is defined as the average distance in which an electron travel through a solid before it is inelastically scattered.

The essence of XPS technique is the analysis of the kinetic energy of the electrons that escape from the sample by the energy analyzer. Energy transfer between photon and electron can be described, in the simplest case, by equation (2.5) where:  $E_{Kin}$  is the

measured kinetic energy,  $h\nu$  is X-ray energy,  $\phi$  is the spectrometer work function and  $E_B$  is the binding energy of orbitals from which photoemission occurs (referenced to the Fermi level) of an appropriate material.

$$E_{kin} = h\nu - \phi - E_B \quad (2.5)$$

It should be noted that the photoemission process will only occur if the energy of incoming X-rays is higher than the binding energy of the irradiated electron. Because the binding energy of each core-level electron is characteristic of the atom and specific orbital to which it belongs, therefore XPS provides chemical identification of sample. Additionally, atomic orbitals from atoms of the same element in different chemical environments result in slightly different binding energies within the range 0.1–10 eV. Thus, small shift in peak position of the analysed elements gives information not only about the elements themselves but also about the chemical state of these elements e.g. state of oxidation [161].

The intensity of photoelectrons ( $I_{XPS}$ ) emitted from all depths greater than  $x$  in a direction normal to the surface is given by the Beer-Lambert relationship (2.6),

$$I_{XPS} = I_0 \exp(-x/\lambda) \quad (2.6)$$

where:  $I_0$  is the intensity from an infinitely thick, uniform substrate and  $\lambda$  is the inelastic mean free path. If  $x = 3\lambda$  then 95% of the XPS signal comes from the surface layer with a thickness  $x$ , and it is called sampling depth.

XPS due to the short inelastic mean free path (IMFP) of the photoelectrons is however a surface sensitive technique. More information about XPS can be found in Refs. [162] [163].

In addition, two other measurement techniques which are inevitably associated with XPS should be mentioned in this paragraph. A competitive process to the photoelectric effect is the emission of Auger electrons. The creation process of Auger electrons is shown in Figure 2.6 – middle panel. Photons or electrons from the incident beam remove a core electron, leaving a vacancy in the inner shell. Electrons from higher, outer level may relax into the vacancy, resulting in a release of energy. This energy can be transferred to another electron, which is ejected from the atom and called an Auger electron. This phenomenon was discovered independently by two researchers Lise

Meitner and Pierre Victor Auger [164] [165], and is commonly used in Auger Electron Spectroscopy (AES). It is worth to mention that during a typical XPS measurement peaks originating from Auger electrons are simultaneously observed. To be able to analyse photoemission from the valence band, with high sensitivity ultraviolet light for photoexcitation instead of X-rays is often used. The idea of such measurements is depicted in Figure 2.6 – right panel. The first such type of measurements was done in the 1960s by Spicer [166]. This work introduced a new tool, Ultraviolet Photoelectron Spectroscopy (UPS), to the family of experimental methods for surface science.

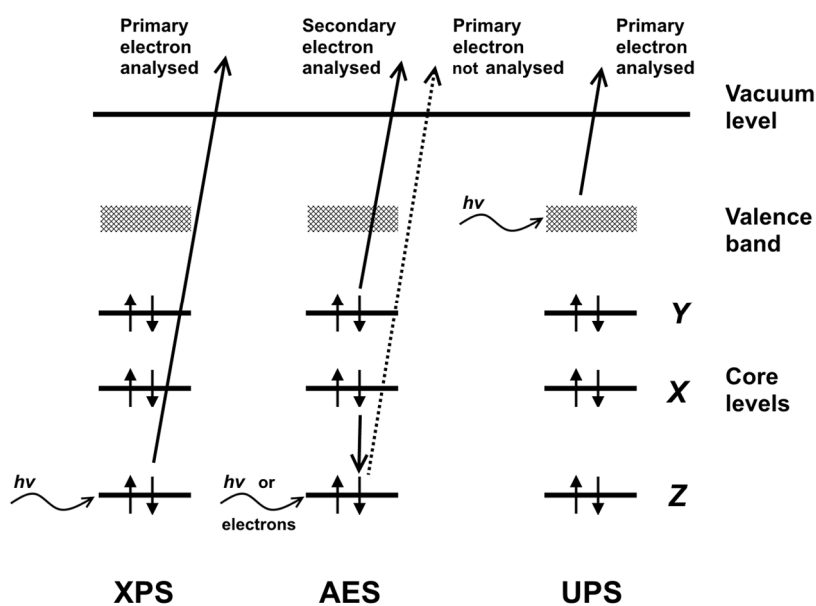


Figure 2.6 XPS-, AES- and UPS process schemes.

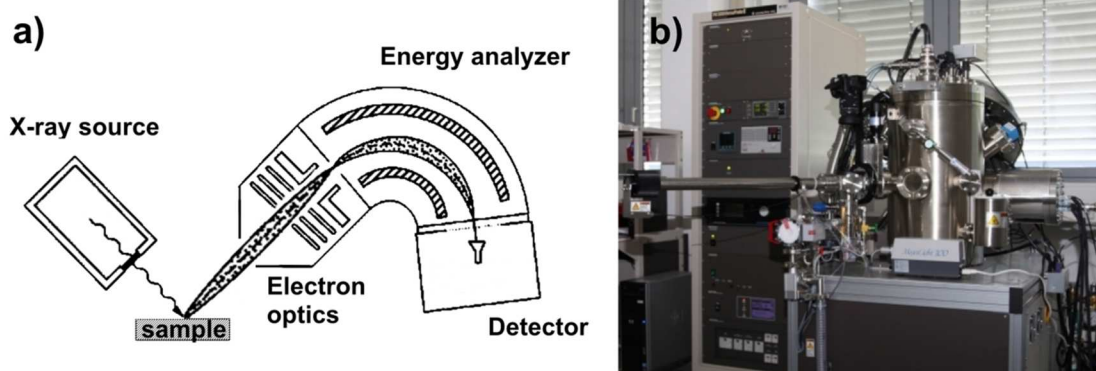


Figure 2.7 XPS hardware: a) Schematic of the basic apparatus used in X-ray photoelectron spectroscopy, b) Photograph of PHI Versa Probe II Scanning XPS Microprobe UHV system.

Finally Figure 2.7 a) depicts a sketch of the typical instrumentation used in XPS, which consist of X-ray source and concentric hemispheric electron energy analyzer, which offers a high energy resolution. X-rays are generated by accelerating electrons from the filament toward the high voltage potential of the anode ( $\sim 10$  kV). As an anode material Mg and/or Al are used, which give  $K_{\alpha}$  1253.6 eV and 1486.6 eV X-ray lines, respectively. Nowadays, multichannel plates are commonly used as electron detectors.

### **XPS experimental Setup**

XPS investigations presented in this thesis were performed using a PHI Versa Probe II Scanning XPS Microprobe UHV system (Figure 2.7 b)). XPS spectra were recorded using a hemispherical analyzer with monochromatic  $AlK_{\alpha}$  source. Binding energy was calibrated to the Fermi level of Au calibration samples. In addition, the sample holder for the PHI Versa Probe II system can be heated (up to 500 °C), which is realized by radiative heating. The heater filament and thermocouple are permanently built into the holder. This technological solution allows for temperature dependent XPS measurements.

## **C. Transmission Electron Microscopy**

A prominent tool in materials science for imaging of internal microstructures of ultrathin samples is Transmission Electron Microscopy (TEM) [167]. Figure 2.8 a) shows that in a sample exposed to the high energy electron radiation ( $\sim$ several 100 keV), several phenomena may occur. For instance: elastically (back-scattered electrons (BSE)) and inelastically (secondary electrons (SE)) scattered electrons, X-ray emission etc. In TEM method the transmitted electrons are measured, however the transmission decreases rapidly with sample thickness, therefore the sample thickness (also called specimen or lamella) has to be very limited ( $\sim 100$  nm). TEM offers much higher spatial resolution than classical light microscopy, since electrons have in this energy range a small de Broglie wavelength in the scale of Å.

The basic TEM design is depicted in Figure 2.8 b) [168]. The electron emitter, usually thermionic tungsten or  $LaB_6$ , is an electron source. Using a series of electromagnetic lenses (anode, condenser lenses) electrons from the emitter are

accelerated and tuned into a monochromatic electron beam, which is focused on the thin sample to uniformly illuminate it. Keeping with the concept outlined in Figure 2.8 a), the electrons exiting the material are either backward or forward scattered. The first group includes BSE and SE, which are important for Scanning Electron Microscopy – SEM (this technique is not described in this thesis). While the second group, either inelastically or elastically forward scattered electrons, is used in TEM method. Both techniques are able to image the sample in many different modes, more details can be found in Ref. [167]. A microscope combining the principles used by both TEM and SEM is usually referred to as scanning transmission electron microscopy (S)TEM. Finally, detectors in form of fluorescent screens, photo-active films or charge-coupled device (CCD) cameras are used. The whole machine is connected to the pumping system, because TEM is operating only in the UHV regime. Additionally, TEM microscopes may be equipped with an additional energy dispersive x-ray spectroscopy detector (TEM-EDX). Incident beams of high energy electrons remove electrons from inner shells in the sample atoms, creating electronic hole states. Electrons from higher energy shells, after a very short period, fill the holes emitting simultaneously X-rays of specific energies related to each element (X-ray fluorescence). This physical phenomenon allows for a determination of the chemical composition of the sample with high lateral resolution [169].

Summarizing, the combined (S)TEM-EDX is a powerful technique which allows to gather information about sample morphology, crystal phases, defects etc. However, it should be noted this technique is time consuming and destructive, due to the lamella preparation process.

### **TEM experimental Setup**

The (S)TEM-EDX results presented in this work were conducted by a FEI Tecnai Osiris microscope. Minimum point resolution for this microscope is 0.26 nm, at the maximum applicable voltage of 200 kV. In addition, Tecnai Osiris is equipped with high angle annular dark field (HAADF) detector which provides a material contrast.



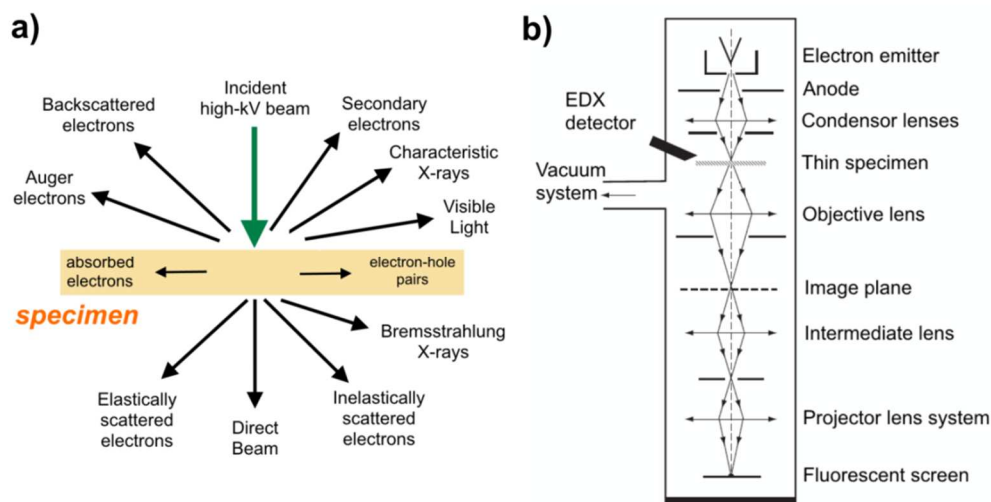


Figure 2.8 TEM - Principle of operation: a) Signals originating from a specimen exposed to a high energy electron beam (after [167]), b) Schematic diagram of the TEM (after [168]).

## 2.2. Substrate preparation and thin film deposition

During the discussion outlined in Chapter 1 about strategies for further development in microelectronic industry, Ge has been mentioned as a promising candidate to be used in novel device concepts. Basic information of Ge was already presented there, therefore in this section attention will be focused to present the Ge(001) surface and its properties. In addition, a detailed description of the sample preparation process and the thin film deposition method, used in this PhD thesis, are presented.

### 2.2.1. Substrate properties and cleaning methods

#### Ge(001) surface

In several aspects, the Ge(001) surface is quite similar to the technologically most important and well-studied Si(001) surface [170]. Figure 2.9 a) shows schematically that each surface atom is left with two dangling-bond  $sp^3$ -hybrid orbitals per surface atom, by cutting a germanium crystal to expose a (001) face. Ge(001) surface atoms dimerise, resulting in a dominating  $p(2 \times 1)$  surface reconstruction. As shown in Figure 2.9 b) this type of surface reconstruction consists of rows of dimers (pair of surface

atoms) running along the bulk unit cell [110] crystallographic directions. The driving force for this dimerization is the reduction in the number of dangling bonds from two to one per surface atom between the unreconstructed and reconstructed surfaces. This dimerization idea was proposed by Schlier and Farnsworth in the late 1950s and it was verified few years later based on investigations on Si(001) and Ge(001) surfaces by using different surface science techniques [171]. The Ge(001) surface was investigated over the years by means of many different surface science techniques like for example LEED (Bayliss *et al.* in 1976 [172]); however, first STM measurements showing p(2 x 1) surface reconstruction were performed by Kubby *et al.* not earlier than in 1987 [173]. Separation along the [110] crystallographic directions between dimer rows was measured and was determined to be 8 Å. This value correspond to the expected doubling of the unreconstructed lattice constant of  $a_0 / \sqrt{2} = 4$  Å, where  $a_0$  is the bulk lattice constant of Ge (5.66 Å). In addition, the orientation of the p(2 x 1) reconstruction is found to be rotated by 90°, when passing between monoatomic height (2 x 1) terraces. This is certainly the result of the diamond crystal structure of Ge, because tetrahedral dangling-bonds on the second layer atoms are rotated by 90° with respect to the top layer tetrahedral bonds around the surface normal.

In contrast to Si, room-temperature LEED studies on Ge(001) show that in addition to the half-order LEED spots expected for 90° rotated p(2 x 1) domains, a weak quarter-order LEED spots also occur, which proves the existence of higher order reconstructions [174] [175] [176]. In 1979, Chadi proposed a new structural model for (001) surfaces, which describes the formation of various higher order reconstructions, as a results of the fact that single surface dimer could be buckled (i.e. tilted) [177]. The buckling opens a gap between occupied and unoccupied surface states lowering thus the energy of the dimers. Neighbouring dimers along one dimer row always buckle in opposite directions. The different arrangements of the asymmetric buckled dimers between neighbouring dimer rows lead to local c(4 x 2) or p(2 x 2) structures (respectively Figure 2.9 c) and d)) besides the basic p(2 x 1) structure. In-phase buckling of adjacent dimer rows leads to a p(2 x 2) reconstruction (looking like asymmetric zig-zag for neighbouring dimer rows), whereas out-of-phase buckling results in a c(4 x 2) reconstruction (symmetric zig-zag for neighbouring dimer rows). It

has been shown by *ab-initio* calculation methods that small energy differences, of about 0.7 eV per dimer, between these reconstructions occur [178]. All discussed reconstructions can be simultaneously observed locally at room temperature by means of STM [170]. However, at lower temperatures the occurrence of higher order surface reconstructions increases, which was observed e.g. by Kevan or Culbertson *et al.* in temperature dependent LEED and high-resolution angle-resolved photoemission studies [179] [180].

Finally, on Ge(001) most of the defects that remain fall in the category of dimer vacancy (DV) defects. DVs can be in the form of A-type (isolated single missing dimer), B-type (pairs of dimer vacancies including more complicated structures such as the (1+2) vacancies) or C-type (most often associated with water absorption) which is occurring quite rarely on Ge(001) in comparison to Si(001). In general, dimer vacancy concentration (DVC) on Ge(001) is much less than on Si(001) [145].

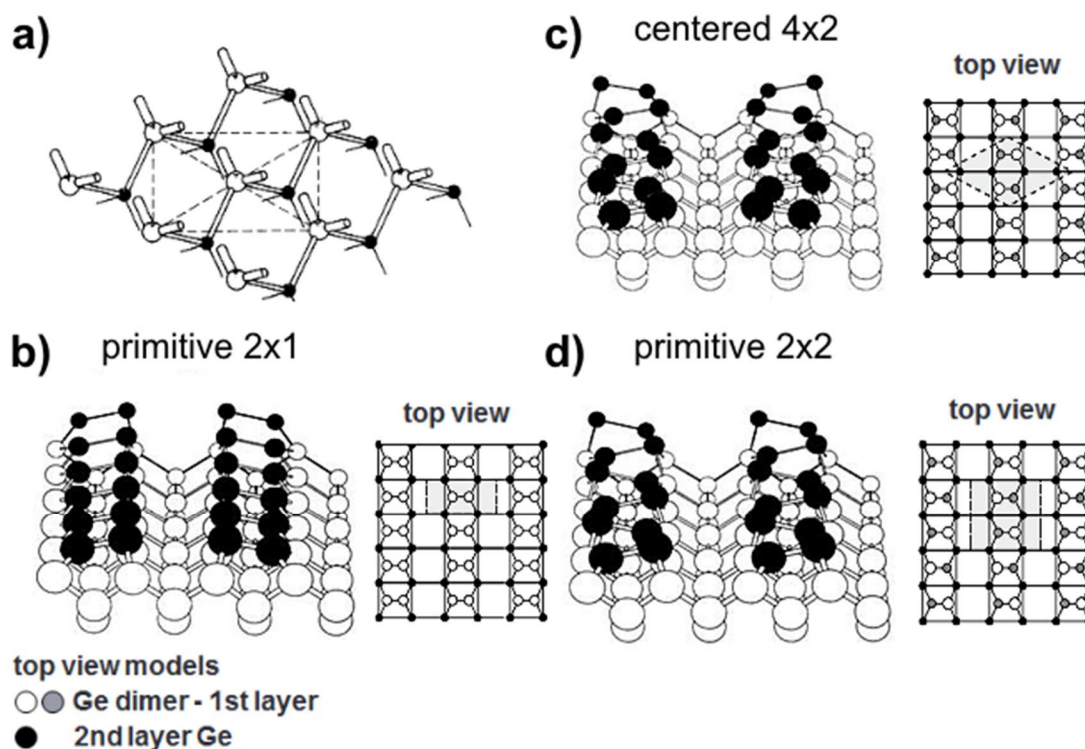


Figure 2.9 Ge(001) surface: a) plan view of the bulk terminated (001) surface, open circles with broken bond are atoms in the first layer; b) - d) perspective (left side) and top view (right side) of dimer models for (001) surface (after [140] [178]).

## Ge cleaning methods

Despite many crystallographic similarities between Ge and Si, the surface chemistry is rather different and the surface cleaning procedures thus differ substantially. A clean Si surface is typically prepared by rapid or flash heating in vacuum at 1200 °C and slow cooling to room temperature [181]. As the melting point of Ge is relatively low (938.2 °C), it is not possible to get a clean and flat Ge surfaces by flash annealing only. There are two main methods of Ge surface cleaning:

- 1) based on *in-situ* ion sputtering/annealing cycles,
- 2) based on *ex-situ* wet etching followed by *in-situ* annealing and possible buffer layer growth.

In the first group, all phases of cleaning procedure are realized under UHV conditions, and typically these steps are: degasing after introduction to UHV chamber by annealing at around 500 °C, and several cycles of ion sputtering followed by thermal treatment at higher temperatures, around 700 °C. As seen, there are many variable parameters, and therefore development of a correct cleaning procedure for the specific UHV system can be time consuming. Below are listed just a few variations of procedure parameters, which were used by different research groups:

- Ne<sup>+</sup> ion sputtering (5μA/cm<sup>2</sup>, 10 min) and annealing at 520 °C for 5 min [179],
- ion sputtering of Ar<sup>+</sup>, or Ne<sup>+</sup> ions with energy 1 keV and a dose of 100 ions per surface atom, and annealing at (795 ÷ 845) °C for 1 ÷ 20 min [173],
- several cycles of ion sputtering (Ar<sup>+</sup> ions, energy 1 keV for 20 min, sample kept at 425 °C), and subsequent annealing at 625 °C for 10 min [182],
- heating the sample to 525 °C for 24 h, followed by several cycles of 800 eV Ar<sup>+</sup> ion sputtering and subsequent annealing at 825 °C, samples were slowly cooled to room temperature (rate 1 °C/s) [183],

Further detailed descriptions of the various cleaning procedures can be found for example in the Refs. [184] [185] or [186].

The second group of cleaning methods is based mainly on repeated *ex-situ* wet chemical/oxidation to create GeO<sub>x</sub> or other passivation layers which can be then easily thermally desorbed by *in-situ* annealing treatments (examples can be found in [187]

---

[188] [189] [190] [191] [192] and [193]). Despite the high diversity of available Ge surface cleaning methods, the majority of atomic-scale STM studies on the Ge(001) are based on ion-sputtering cleaning processes [170].

### **Sample preparation**

Samples were cut into 10 mm x 4 mm pieces from Sb-doped, n-type Ge(001) 2" wafers with a resistivity of  $\rho_{\text{bulk}} \approx 1\text{-}10 \text{ }\Omega\text{cm}$  (supplied by GMaterials company) and mounted on standard molybdenum direct-heating microscope holders. In this type of holder construction, sample annealing can be realized by current flow through the sample, thus in accordance with Joule's law heat is generated. The simultaneous use of materials with high melting point (such as Mo) in carrier construction, allows to achieve high temperatures during sample treatment. Among many available methods for Ge surface cleaning presented in the previous chapter, standard cleaning procedure consisting of several cycles of argon ion sputtering followed by thermal treatment at UHV conditions was chosen. The whole procedure was carried out in the preparation chamber of the Omicron UHV system described in Chapter 2.1.1. Usual parameters for sputtering were: Ar pressure in the range of  $1 \times 10^{-5}$  mbar, beam energy (0.7-1) keV, emission current 10 mA, sputtering for 30 min. After sputtering, annealing treatments were realized by DH mode in the temperatures range of 700 °C-750 °C for 30 min. Such prepared clean Ge samples, as well as samples with deposited metal and after subsequent annealing steps, were studied *in-situ* by LEED and STM techniques. In addition, some samples were prepared exactly in the same way (like for LEED & STM measurements) and then transferred out of the Omicron tool to perform additional measurements with supplementary techniques. To summarize this part, it should be noted that sample preparation under UHV conditions is very delicate and time consuming, but the here presented process allows to obtain atomically clean Ge(001) surfaces.

### 2.2.2. E-beam evaporation

Electron Beam Evaporation (EBE), also known as Electron Beam Physical Vapour Deposition (EBPVD), is one of the most popular and commonly used methods of thin film deposition. Figure 2.10 a) depicts a construction of a typical UHV evaporator,

which consists mainly of the outer flange with electrical feedthroughs, cooling shroud, shutter and flux loop. Inside the water-cooled shroud are located the filament and evaporant, which may take a rod form or in powder form mounted in a special crucible – Figure 2.10 b). The electron beam, generated by thermionic emission from the filament (FV), is accelerated to high kinetic energies towards the evaporant as a result of applied high voltage between filament and evaporant (HV). As a result of collision, the kinetic energy of accelerated electrons is converted into thermal energy of the evaporant. The thermal energy heats thus up the evaporant causing it to melt or to sublime. When temperature and vacuum level are sufficiently high, vapour from the melt or solid evaporates. After opening the shutter, vaporized material in gaseous form flows in sample direction. Note, about 2-5% of the evaporated atoms are ionized, allowing calibration measurements by measuring the ion current at the exit (see FLUX loop in Figure 2.10 b)), which is proportional the total flux.

EBE has many advantages compared to other thin film deposition like: coverage from a few monolayers to real sub-monolayer atomic films can be realized, flexible deposition rates can be adjusted, relatively inexpensive techniques for new materials science studies. However, the main disadvantage of EBE is the fact that it requires a high or ultrahigh vacuum environment (below  $1 \times 10^{-6}$  mbar range), thus the method is rather of academic and not industrial interest [194] [195].

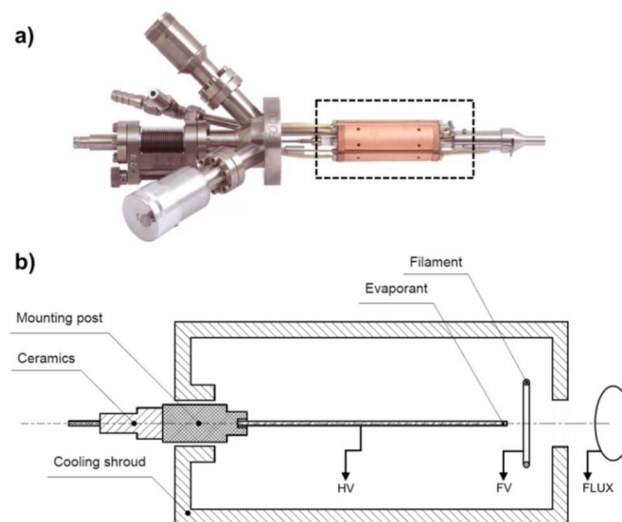


Figure 2.10 Construction of the EFM3 evaporator: a) Photography of EFM3 showing a general view with marked cooling shroud (dashed-line rectangle), b) Schematic cross section through the cooling shroud to illustrate the principles of evaporator operation, where: HV - high voltage, FV - filament voltage, FLUX - loop for measuring the flux current (after [196]).

### **Metal deposition Setup**

In the present work, all investigated metals were deposited at room temperature by the EBE method using an Omicron NanoTechnology EFM3 evaporator (Figure 2.10 a)). As a source of evaporated substances, high purity materials were used: Co rod 99.99 %, Ni rod 99.999 % both from MaTecK GmbH. During the metal deposition process, the evaporator parameters were maintained at constant levels (e.g. for Co:  $I_{\text{Emission}} = \sim 12$  mA,  $U_{\text{HV}} = \sim 800$  V,  $I_{\text{FLUX}} = \sim 20$  nA), while the total amount of deposited material was monitored by the time of evaporation. The number of deposited metal monolayers was estimated from STM measurements for low coverage and extrapolated towards high coverage. In addition other techniques like high resolution TEM or angle-resolved XPS study were used to find nominal thickness of evaporated metal layer. The evaporation chamber pressure was maintained below  $5 \times 10^{-10}$  mbar during deposition.

## **2.3. Thin film growth theory**

One of the basic information, which can be obtained by UHV STM measurements, is the growth study of thin films and/or nanostructures. In connection with this, basic concepts and processes involved in heteroepitaxial growth are briefly presented in this section.

### **Atomistic processes on surfaces**

During epitaxial growth several individual atomic processes responsible for adsorption and crystal growth on surfaces and determining the surface morphology of the growing film may occur. It is schematically illustrated in Figure 2.11. Atoms are deposited onto a perfect clean substrate surface with known deposition rate (process (a)). These single atoms may then diffuse over the surface until they are lost by one of several processes like re-evaporation, nucleation of 2D or 3D clusters, capture the existing clusters etc. (processes (b)-(i), accurate description in the figure caption). All these processes compete with each other. Each of these processes will be governed by characteristic times, which themselves will depend on the single-atom concentration and/or coverage. In addition if such processes are thermally activated its occurrence may take place with

a certain probability per unit time  $\nu$ , depending on the characteristic activation energy ( $E_a$ ) and substrate temperature  $T_s$  – equation (2.7) where  $k_B$  is the Boltzmann constant.

$$\nu \propto \exp(E_a / k_B T_s) \quad (2.7)$$

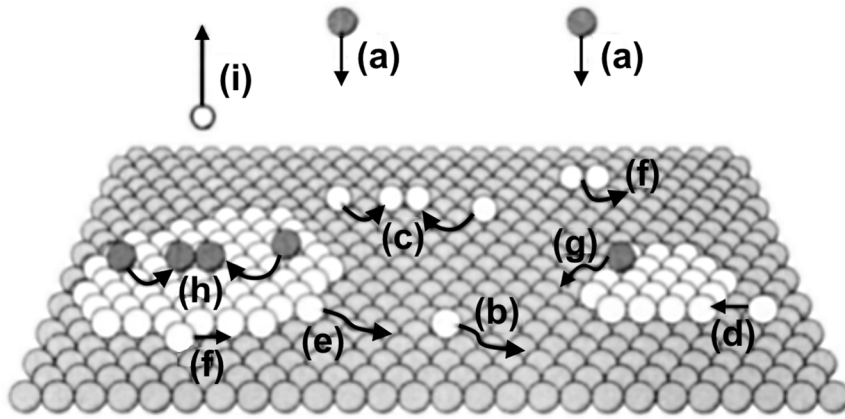


Figure 2.11 Main surface processes occurring during epitaxial growth: (a) atoms deposition on the terrace, (b) diffusion on the surface as adatoms, (c) island nucleation, (d) attachment of adatoms to existing islands, (e) atoms detachment from island, (f) atom diffusion along the island edge, (g) (h) deposition of adatoms on top of islands and the corresponding processes, (i) re-evaporation (after [197]).

In the thermodynamic equilibrium, all atomistic processes on surfaces run in two opposite directions at equal rates (e.g. island nucleation - island decay). A delicate balance is formed between all adsorption and desorption processes, therefore thin film growth is clearly a thermodynamic non-equilibrium process.

In contrast real surfaces, even very clean ones, may be far from perfect. Very often a distribution of ledges, dislocations and point defects are located on the surface in addition to the perfect terraces. These faults on substrate surfaces can certainly influence individual atomic processes like adsorption, diffusion and nucleation behaviour. More information about discussed growth issues can be found in Refs. [198] [199].

### Thin film growth mode

Epitaxial thin film growth at a crystal surface or interface can be described in principle by the three primary growth modes, which are shown in Figure 2.12. Following Bauer, film growth may be classified in either of the following schemes: island growth (Volmer-Weber (VW)), layer-by-layer growth (Frank van der Merwe (FM)) or layer-



plus-island growth (Stranski-Krastanov (SK)) [200]. A simple distinction between these three modes can be done on the basis of energy balances between interactions of film and substrate. During VW growth (Figure 2.12 a)) small clusters are directly nucleated on the substrate surface and then grow into three-dimensional (3D) structures. In a broad sense, the presence of a VW suggests a weak interaction between film and substrate. Atoms (or molecules) of deposited material are more strongly bound to each other than to the substrate. This mode is displayed by many systems of metals growing on insulators [198]. Layer-by-layer growth (Figure 2.12 b)) presents the opposite characteristic. The interactions between neighbouring atoms of deposited material in thin film are weaker than that with the atoms of the substrate. In consequence, atoms of deposited material attempt to close a complete monolayer on the surface, before the next layer starts to grow. FM growth mode was observed in cases such as: semiconductor growth on semiconductors, adsorbed gases on graphite and on several metals, in some metal-metal systems [198]. Finally Stranski-Krastanov growth mode (Figure 2.12 c)), presents an intermediate case. The SK growth mode is a 3D growth mode on an initial 2D overlayer of the film. During growth the first monolayer, or a few monolayers, form initially a 2D overlayer, but subsequent layer growth mode is unfavourable and further growth is realized by the formation of 3D islands. There are many possible reasons for this mode to occur, but a lattice mismatch between the film and the substrate is one of the frequent cases. There are now many examples of its occurrence in existing systems [198].

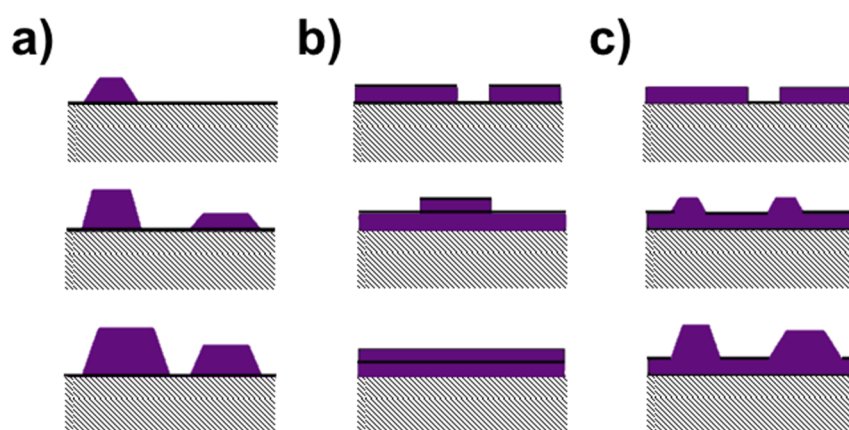


Figure 2.12 Schematic view of thin film growth modes: a) Volmer-Weber (island growth), b) Frank van der Merwe (layer-by-layer growth), c) Stranski-Krastanov growth (layer-plus-island growth).

It is noted that this classification is based on chemically non-active film - substrate interfaces. In case of the occurrence of chemical film - substrate reactions, like in the presented thesis, the growth scenario becomes more complex.

### **Ostwald ripening**

Ostwald ripening is the phenomena, observed in solid solutions or liquid sols, in which larger particles grow in favour of smaller particles in order to achieve a more thermodynamically stable state. The final state is characterized by a size distribution of the ensemble of particles. This phenomena was first described by Wilhelm Ostwald in 1896 [201]. Initially, the Ostwald ripening process was observed and theoretically described only in case of bulk materials (solid solutions, liquids). However, a similar phenomenon was also observed in several cases of epitaxial growth of nanocrystals on solids surface [202]. Driving force of Ostwald ripening is Gibbs-Thomson effect, which describes variations in vapour pressure or chemical potential across a curved surface or interface [203] [204]. In this sense, the vapour pressure for small particles/islands with high curvature is higher than for large particles/island with smoother curvature, resulting in higher stability of the latter ones. In case of epitaxial growth, nanoislands of the growing material will nucleate on the substrate if the distance between nanoislands is larger than the atom diffusion length. The surface is out of equilibrium since the step edges of the nanoislands cost free energy. The driving force of Ostwald ripening depends on the mean radius of curvature of the nanoislands: atoms flow from islands with high curvature to islands with low curvature. Therefore, for a fixed amount of material, the consumption of the smallest nanoislands in favor of the larger ones can be observed. More information, including also theoretical models of the phenomenon described above, can be found in Refs. [205] [206] [207].

# Chapter 3

## Results and discussion

After the theoretical introduction concerning different aspects of the possible development of microelectronic industry and a short presentation of the experimental setup, a detailed study of experimental results and discussion is given here.

This chapter begins with a brief presentation of the clean Ge(001) surface. Bearing in mind that obtaining a clean Ge(001) surface is extremely important, especially for nano-scale spatial resolution STM investigations, this short sub-chapter is focused on the description of Ge surface cleaning procedure. Presented results show that the mentioned cleaning technique results in an atomically clean Ge(001) substrate.

Afterwards, next two sub-chapters present a detailed structural, morphological, and compositional study on the growth and evolution of  $\text{Co}_x\text{Ge}_y$  and  $\text{Ni}_x\text{Ge}_y$  nanostructures, respectively, as a function of subsequent annealing treatments at increasing temperature. The main part of this study was based on an *in-situ* STM study of the morphological evolution of a thin metal layer deposited at RT on Ge(001) and then subsequent annealing treatments were carried out, thus mimicking the typical cleanroom process for metal contact formation in Si microelectronics. Additional measurements ((S)TEM-EDX, XPS) gave an opportunity to complete the findings from STM and allowed to monitor the reaction between metal and Ge in the formation process of germanide nanostructures. Both chapters were arranged in the same way (sequence of measurement techniques, the same size of scan area in STM for most cases etc.), thereby the reader can easily compare the two investigated systems. At the end of each section, a short summary of the key results is presented.

It should be noted, that results and discussions presented in this chapter are in a certain extent covered by work published in peer-reviewed journals. A detailed publication list of the author of this dissertation is given in the section: “Scientific visibility during the PhD thesis”.

### 3.1. The pristine Ge(001) surface

As the detailed description of the Ge(001) surface, its properties and the main types of Ge surface cleaning methods were given in Chapter 2.2.1, here attention was focused on a more precise description of the chosen cleaning method, including also the technical details. Then, based on STM, the effectiveness of the used cleaning method was presented.

The Ge samples were cleaved from an Sb-doped, n-type Ge(001) wafer with a resistivity of  $\rho_{\text{bulk}} \approx 1\text{-}10 \text{ }\Omega\text{cm}$ , mounted on standard molybdenum direct-current heating sample holders and introduced to the STM UHV system. From many different Ge(001) cleaning procedures (please see Chapter 2.2.1), a cleaning method consisting of several cycles of argon ion sputtering followed by thermal treatment at UHV conditions was chosen and the process parameters were optimized for the given STM UHV system.

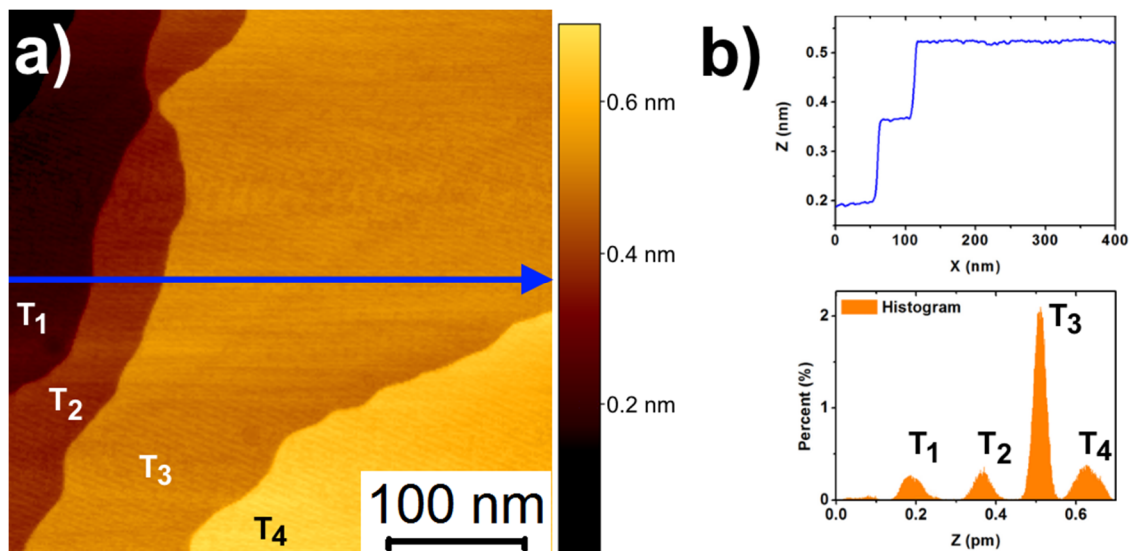


Figure 3.1 STM images of Ge(001) surface after cleaning procedure containing 5 cycles of sputtering and annealing: a)  $400 \times 400 \text{ nm}^2$ ,  $V_s = -2 \text{ V}$ ,  $I = 80 \text{ pA}$ ; b) height profile along blue line and histogram.

The cleaning procedure began with the degassing of the sample at around 500 °C in DH mode for 1 h-2 h, depending on the vacuum conditions ( $< 5 \times 10^{-10}$  mbar). Then the sample was processed by several cycles of argon ion sputtering followed by thermal treatment. Standard parameters for argon ion sputtering were: beam energy (0.7-1) keV, Ar pressure  $\sim 1 \times 10^{-5}$  mbar, and time 30 min. The thermal annealing at UHV conditions were realized at (700-750) °C for (10-30) min. Please note that during this procedure the vacuum pressure was an important parameter (should not reach above  $1 \times 10^{-9}$  mbar). In addition, the next cycle could start when the sample was cooled to below 50 °C. As standard, 5 to 7 of such cycles were typically carried out.

This procedure allowed to achieve an atomically clean, reconstructed Ge(001) surface. As shown in Figure 3.1, a clean Ge(001) surface featuring wide monoatomic terraces (typical width  $\sim 250$  nm) was obtained. The measured step height between monoatomic terraces of 0.15(2) nm by means of a height profiles and/or a histogram, is in agreement with earlier Ge(001) STM studies [173]. A detailed analysis of the surface geometry shows that both the  $p(2 \times 1)$  and  $c(4 \times 2)$  surface reconstructions were the dominant Ge(001) surface phases at RT, with a low dimer vacancy concentration (DVC) value of  $\sim 2\%$ . As expected, the  $p(2 \times 2)$  domains were visible only occasionally [170]. Examples of all these types of Ge(001) surface reconstruction are illustrated in Figure 3.2. The dashed white lines in Figure 3.2 b) aim to help to distinguish between  $c(4 \times 2)$  (symmetric rows) and  $p(2 \times 2)$  (asymmetric rows) surface reconstruction domains.

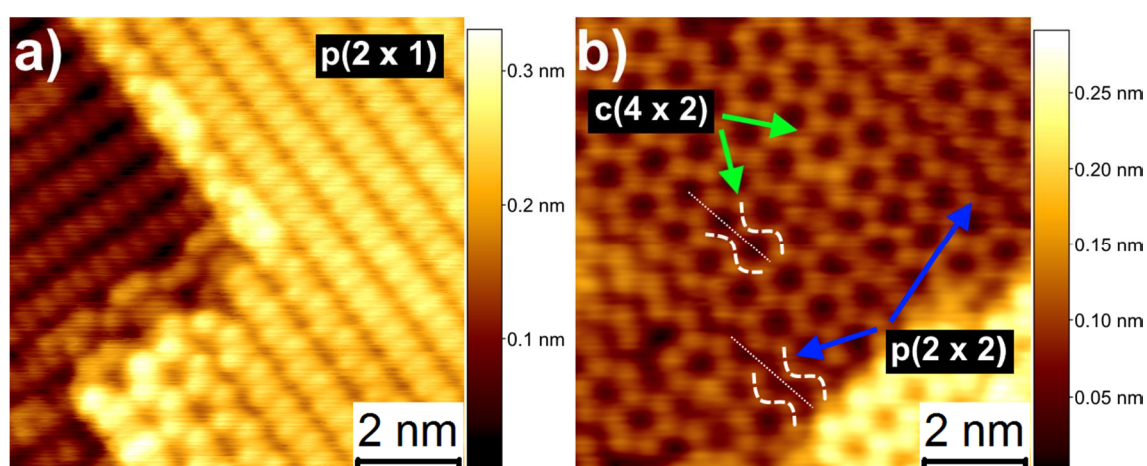


Figure 3.2 STM images of very clean Ge(001) showing local  $p(2 \times 1)$ ,  $p(2 \times 2)$ , and  $c(4 \times 2)$  type of Ge surface reconstruction: a)  $9 \times 9 \text{ nm}^2$ ,  $V_s = -2 \text{ V}$ ,  $I = 80 \text{ pA}$ ; b)  $9 \times 9 \text{ nm}^2$ ,  $V_s = 2 \text{ V}$ ,  $I = 1 \text{ nA}$ .

## 3.2. Cobalt germanide nanostructures on Ge(001) surface

This chapter presents a systematic study on the growth and evolution of  $\text{Co}_x\text{Ge}_y$  nanostructures as a function of subsequent annealing treatments at increasing temperature. Please note that subsequent thermal annealing treatments were realized *in-situ* at different temperatures (150 °C, 250 °C, 400 °C, 500 °C, 600 °C for 60 min using radiative heating mode and 700 °C for 30 min by direct heating mode). Temperatures were measured by means of a thermocouple type K and an infrared pyrometer (above 500 °C range) with an accuracy of  $\pm 10$  °C and  $\pm 5$  °C, respectively. For XPS study the samples were prepared nominally identical like for the STM study. After RT deposition of the same amount of Co on clean Ge(001) substrate, the sample was immediately transferred to the XPS UHV system to perform temperature dependent XPS studies.

### **Characterization of the Co-Ge system**

The search for low resistance metal-germanide contact schemes benefits from the gained scientific expertise on the formerly investigated corresponding silicides [208] [209] but fundamental materials science differences in terms of thermal budgets, crystal phases etc. exist and must be considered with great care to achieve stable low resistance metal contacts to Ge. In particular, as shown in Figure 3.3, the Co-Ge system exhibits a complex bulk-phase diagram, containing seven equilibrium stable phases with a wide range of different physical properties [210] [211]. Please note that in general the bulk phase diagrams are only of limited use for nanoscience. For instance, it was found in thin films that not all bulk metal-germanide phases occur, and that, contrary to bulk systems, simultaneous nucleation of different phases were observed [211]. Consequently, the Co/Ge thin and ultra-thin film systems have recently been investigated using different experimental methods such as: TEM [212] [213], XRD [214] [215], XPS [216] and STM studies also supported by theoretical calculations [217] [218] [219] [220] [221] [222] [223].

The interest in cobalt germanides, in particular  $\text{CoGe}_2$  stems from the fact that this phase shows the lowest resistivity and good thermal stability, and as such is best suited for ohmic metal contact formation in Ge-based devices [224] [225] [226].  $\text{CoGe}_2$  phase crystallizes in an orthorhombic structure with unit cell dimensions  $a=b = 5.68$  Å,

$c = 10.82 \text{ \AA}$  [227]. A schematic structure of the  $\text{CoGe}_2$  unit cell is shown in Figure 3.3 b) [217]. The resistivity of  $\text{CoGe}_2$  is approximately  $69 \mu\Omega\text{cm}$  [211]. In addition, Figure 3.3 c) shows a typical phase sequence, for 30 nm-thin film  $\text{Co}/\text{Ge}(001)$  system. In contrast to binary bulk phase diagrams, which present system stabilities of a given alloys at a certain temperature, the phase sequence shown here describes the effect of increasing temperature to the  $\text{Co}_x\text{Ge}_y$  phase due to diffusion. The  $\text{CoGe}_2$  phase occurs around  $650 \text{ }^\circ\text{C}$ , while at lower temperature the  $\text{CoGe}$  and  $\text{Co}_5\text{Ge}_7$  phases dominate.

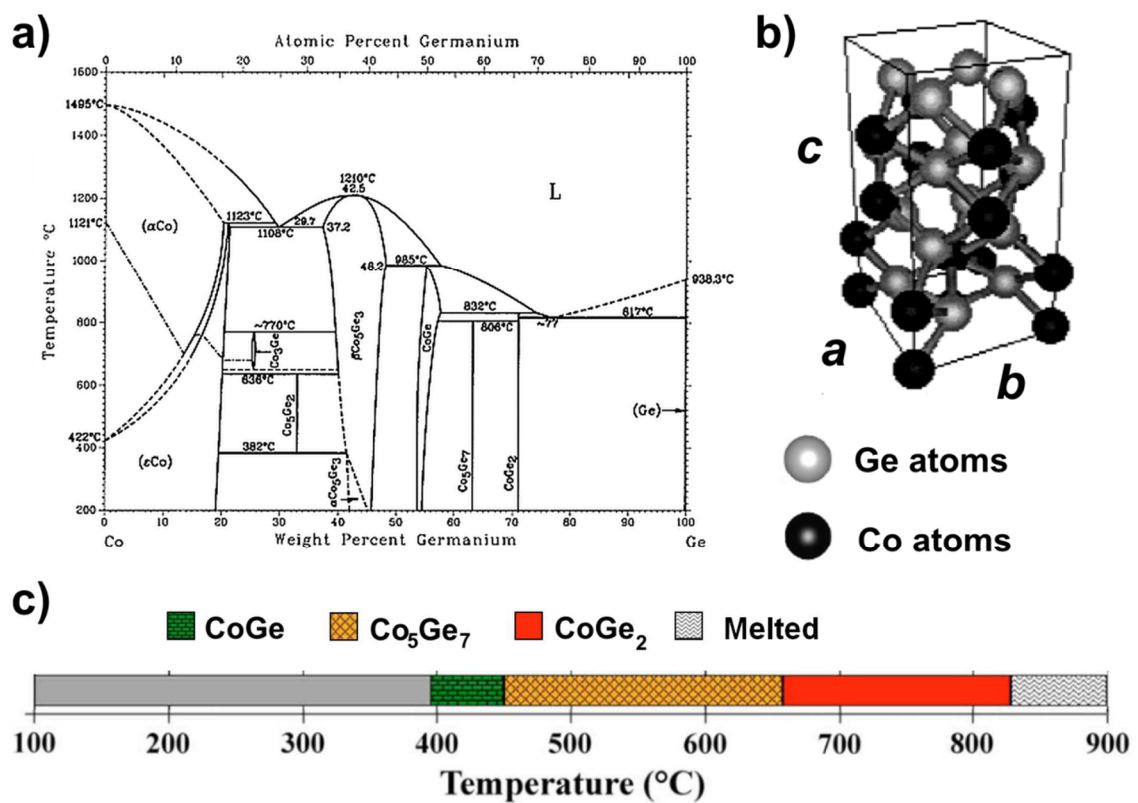


Figure 3.3 Characterization of the Co-Ge system: a) the binary bulk phase diagram for the Co-Ge system (after [210]); b)  $\text{CoGe}_2$  unit cell structure (after [217]); and c) typical phase sequence for the reaction of 30 nm thick Co film deposited on Ge(001) (after [211]).

## STM study

Results presentation in Chapter 3.2 begins with a general description of the evolution of the surface structure of RT-deposited Co on Ge(001) as a function of subsequent annealing treatments at increasing temperature, by means of STM technique.

Figure 3.4 shows a STM topographic image of Ge(001) surface after deposition of approximately 4(1) ML of Co atoms at RT. The Co surface coverage was estimated from STM images for low coverage and extrapolated to high coverage (shown in next section titled “Low coverage STM study”). The terrace structure of the underlying Ge substrate is clearly visible. Quantitative analysis shows that the average height between two neighbouring terraces is  $\sim 0.14(1)$  nm (height profile in Figure 3.4 a)), which corresponds to monoatomic high Ge(001) step edges. However, closer inspection shows that the Ge(001) surface reconstruction is no longer observed by STM at this coverage (Figure 3.4 b)). After Co deposition, the STM images show a high density of Co metal nano-sized clusters covering the surface. The average size of the Co metal cluster is: 0.8(4) nm (radius), 3.1(8) nm<sup>2</sup> (cluster area), and 0.12(2) nm (apparent height). The RMSR of single terraces was estimated to be 0.07(4) nm. These observations strongly suggest that evaporation of a few MLs of Co on the Ge(001) substrate at RT results in a VW growth mode.

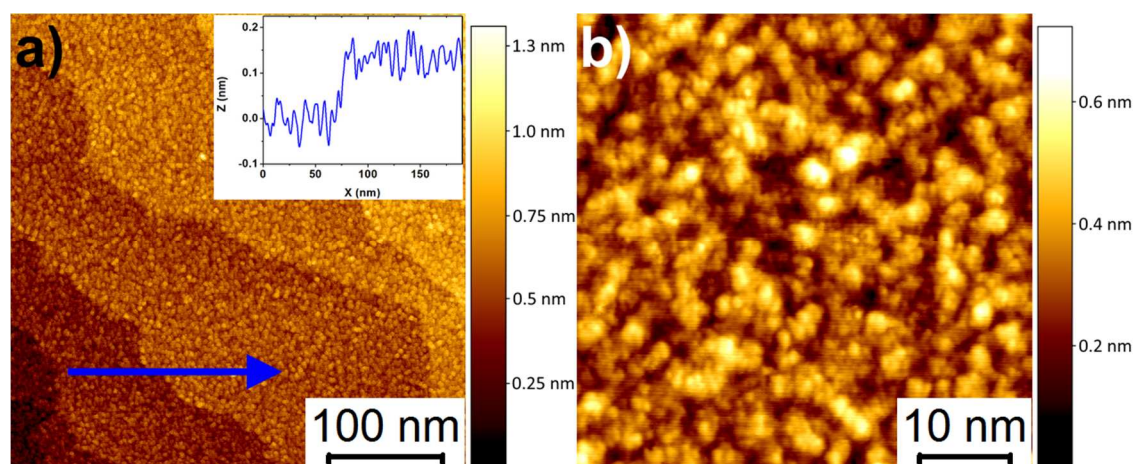


Figure 3.4 STM images: a) sample surface after Co deposition ( $400 \times 400$  nm<sup>2</sup>,  $V_s = -2$  V,  $I = 120$  pA), inset depicts an example of height profile along the marked blue line; b) enlarged view on the sample surface which is coated with nanometer-sized metal clusters ( $50 \times 50$  nm<sup>2</sup>,  $V_s = 2$  V,  $I = 220$  pA). All image sides aligned on the  $\langle 010 \rangle$  equivalent directions.



In addition, in line with a VW growth mode, LEED data clearly demonstrates the Ge(001)-p(2 x 1) type of reconstruction in Co-free surface regions (Figure 3.5). Please note that these apparently conflicting results from STM and LEED clearly indicate the VW growth mode. LEED, which is a very surface sensitive technique, can easily “see” the Ge(001) surface reconstruction in Co-free surface regions between Co clusters. Although STM theoretically allows sub-atomic resolution, one is not able to resolve the p(2 x 1) reconstruction of clean Ge between the high density Co clusters, due to the strongly corrugated sample surface morphology (i.e. high difference between the STM tip curvature and the dimensions of Co metal clusters).

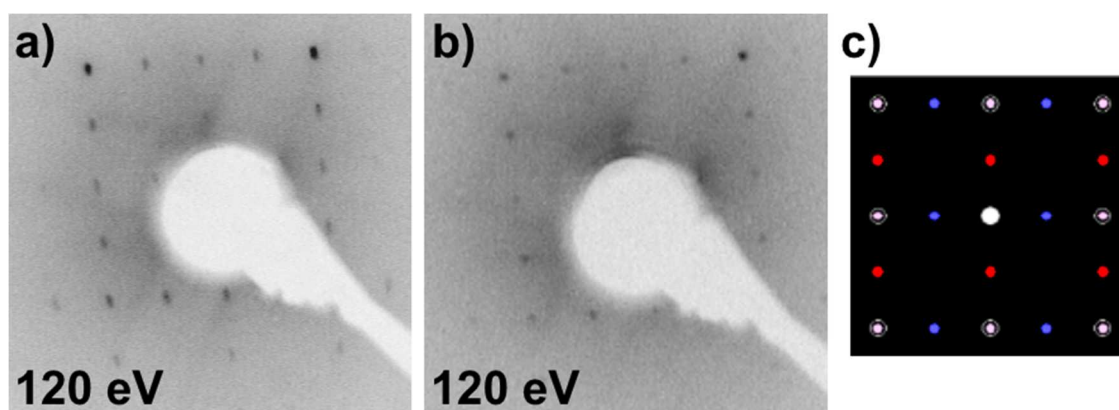


Figure 3.5 LEED images taken at 120 eV for: a) clean Ge(001) surface; b) sample after deposition of approximately 4(1) ML of Co atoms at RT. To help the analysis of LEED results, part c) depicts simulated LEED pattern of 90° rotated p(2 x 1) surface domains.

First sample annealing treatment at 150 °C for 1 hour caused a slight change in the morphology of the surface (see Figure 3.6). The terraced character of the surface morphology was retained. The morphological analysis showed only a slight increase of the RMSR value from 0.07(4) nm (as-deposited) to 0.09(2) nm. The metal clusters are still visible, however it seems that they start to wet the surface and merge each other. In consequence, a clear border between single clusters disappears, which creates difficulties in estimating the global statistics for metal clusters.

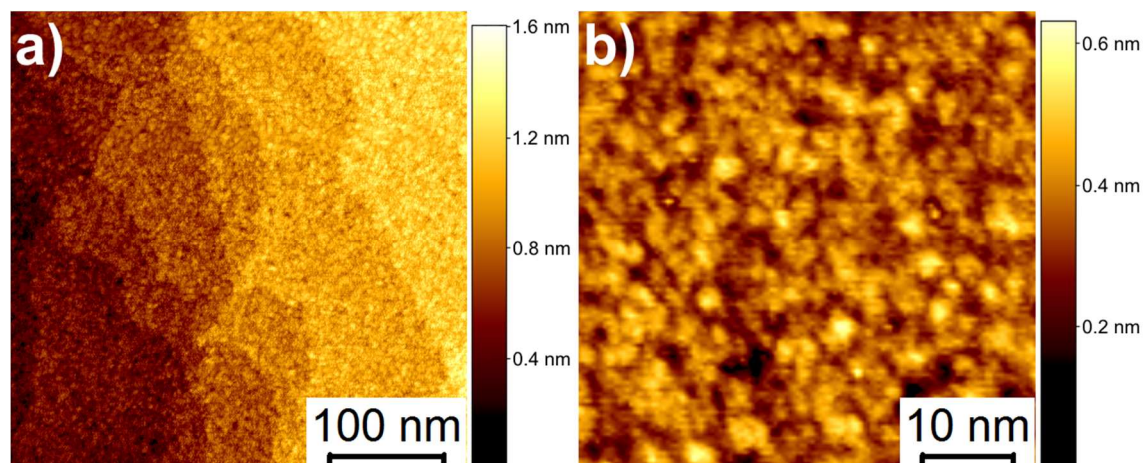


Figure 3.6 Sample surface after annealing at 150 °C for 1 hour: a) 400 x 400 nm<sup>2</sup>,  $V_s = 2$  V,  $I = 120$  pA; b) 50 x 50 nm<sup>2</sup>,  $V_s = -1.6$  V,  $I = 60$  pA. All image sides aligned on the  $\langle 010 \rangle$  equivalent directions.

Subsequent annealing at 250 °C for 1 hour caused a significant change in surface morphology (Figure 3.7). The Ge terrace structure morphology is not visible anymore. Instead of typical Ge-terraced morphology, an inhomogeneous layer of probably  $\text{Co}_x\text{Ge}_y$  phase is clearly visible. A detailed analysis of flat areas shows that on the atomic scale, the top layer sometimes is characterized by presence of surface order (Figure 3.7 b)). From a global perspective, on the inhomogeneous  $\text{Co}_x\text{Ge}_y$  top layer, local voids are present. In addition, ordered islands of rectangular shape start to nucleate and grow at randomly located places on the surfaces (Figure 3.7 c)). In consequence, the surface roughness increases (RMSR  $\sim 0.16(2)$  nm).

In short summary, annealing at 250 °C drives the nucleation of ordered nanocrystals. A significant rearrangement of the surface morphology in the Co/Ge system was observed. These changes in the surface morphology are caused probably due to the fact that atoms in the Ge terraces are interacting with the Co metal clusters. The de-wetting phenomenon plays also an important role, however as it turned out, its relevance is more pronounced after next annealing steps. The hypothesis about the onset of Co-Ge interaction during this annealing step is based on STM studies on the oxidation of metal surfaces where a similar reaction scheme was observed: namely the onset of oxide formation starts by consuming the more reactive metal terrace atoms first (missing row reconstructions etc.) [228].

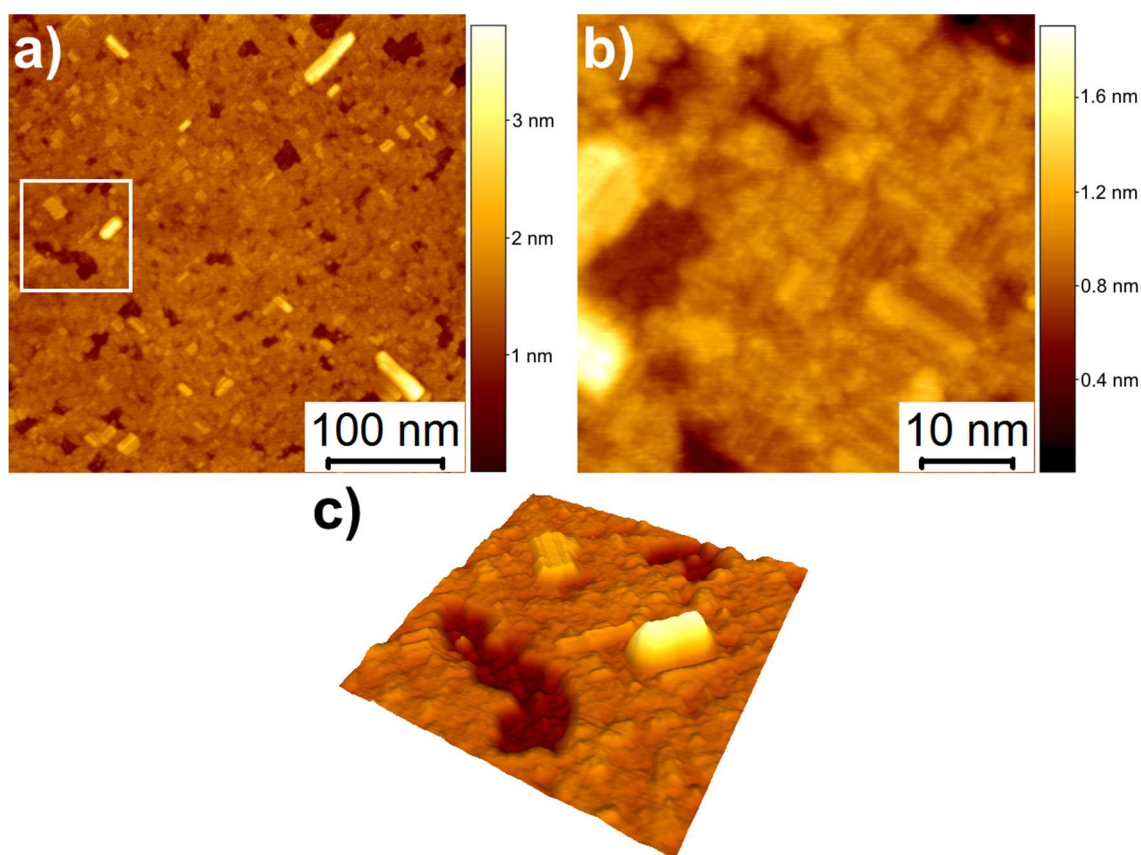


Figure 3.7 Sample surface after annealing at 250 °C for 1 hour: a) 400 x 400 nm<sup>2</sup>,  $V_s = 2$  V,  $I = 80$  pA; b) 50 x 50 nm<sup>2</sup>,  $V_s = -1.8$  V,  $I = 80$  pA; and c) 3D rendering of marked area in panel a) 100 x 100 nm<sup>2</sup>,  $V_s = 1$  V,  $I = 200$  pA. For a) and b) all image sides aligned on the  $\langle 010 \rangle$  equivalent directions.

Figure 3.8 shows the derivative of STM images recorded after annealing the sample at temperatures between 400 °C and 700 °C. Because all images represent the same scanning scale, Figure 3.8 provides a simple comparison of the surface morphology changes after subsequent annealing treatments at a relatively high temperature range. It is clearly shown that during annealing significant changes in surface morphology occurred. Starting from annealing at 400 °C the occurrence of well ordered, three-dimensional nanostructures is evident. A clear increase of the size/volume of the larger nanostructures as a function of annealing temperature was visible. In addition, a decrease in the density of the smallest nanoislands in favor to bigger ones was observed. This scenario most probably results from the Ostwald ripening phenomenon, driving the merging of smaller clusters thanks to their enhanced surface diffusion. Next paragraphs give a short description of each of these annealing treatment steps.

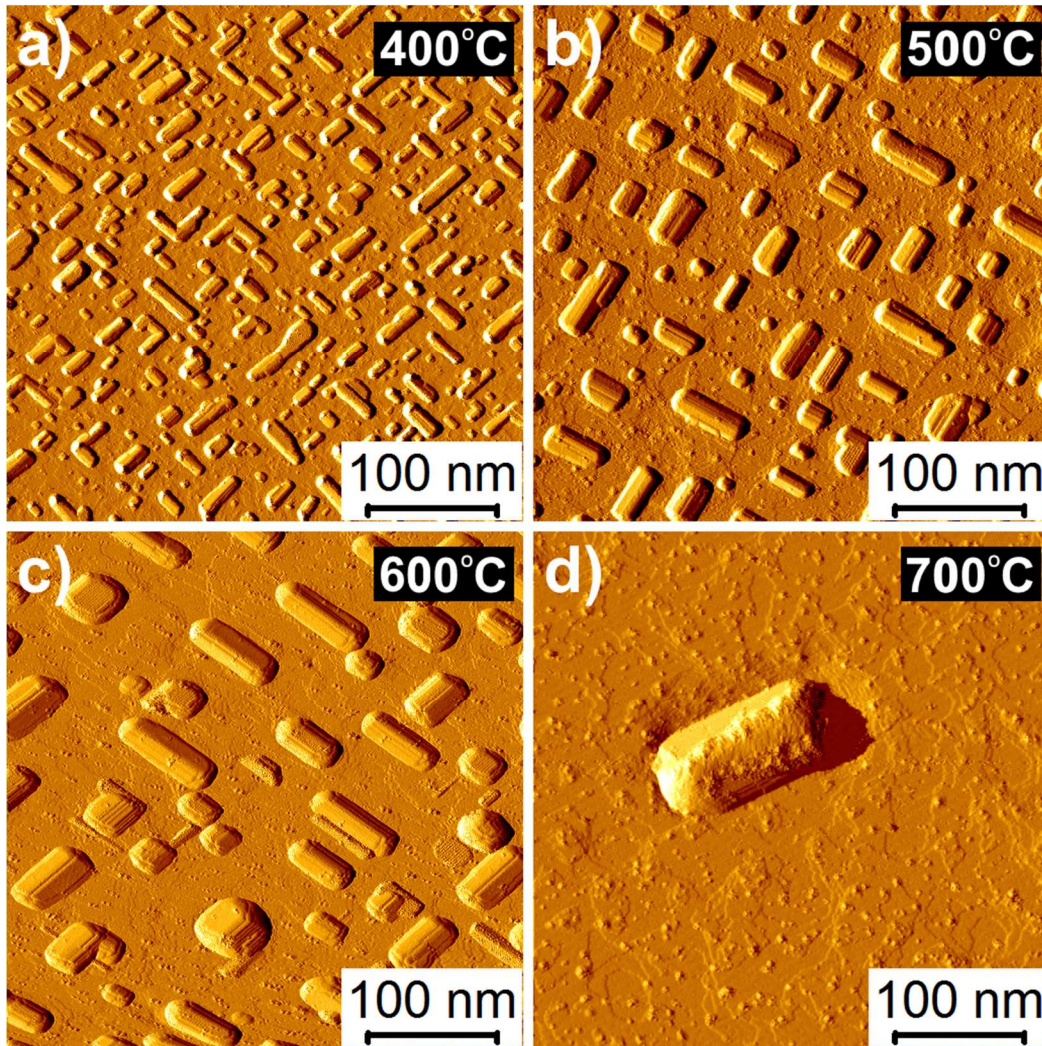


Figure 3.8 Scanning tunneling topographic derivative images of annealed samples at: a) 400 °C for 1 hour (400 x 400 nm<sup>2</sup>, V<sub>s</sub>= 2 V, I= 100 pA); b) 500 °C for 1 hour (400 x 400 nm<sup>2</sup>, V<sub>s</sub>= 2 V, I= 80 pA); c) 600 °C for 1 hour (400 x 400 nm<sup>2</sup>, V<sub>s</sub>= 1.6 V, I= 50 pA); and d) 700 °C for 30 minutes (400 x 400 nm<sup>2</sup>, V<sub>s</sub>= -1.6 V, I= 100 pA).

Figure 3.9 illustrates STM results obtained for sample annealing at 400 °C for 1 hour. Once again, with reference to the previous annealing step (at 250 °C), annealing at 400 °C leads to a significant change in surface morphology. The Co<sub>x</sub>Ge<sub>y</sub> layer tends to agglomerate, which leads to the growth of well ordered, three-dimensional nanostructures, exposing the underlying Ge(001) surface. The majority of these structures has rectangular, elongated shapes and preferentially grows along two orthogonal Ge directions [110];[-110]. It could be noticed that several nanostructures

exhibit more complex L- or T-beams-like shapes, which might result from coalescence at  $90^\circ$  of two or more rectangular shaped nanostructure islands. Quite often, the flat top surface of such nanostructures is characterized by complicated, locally ordered surface arrangements (inset in Figure 3.9 a)). A short description as well as possible explanation for the presence of this type of super-structures is given below in the description of the next annealing step. In addition, a large number of very small, more square than slightly elongated nanoislands, distributed between the larger structures were also observed.

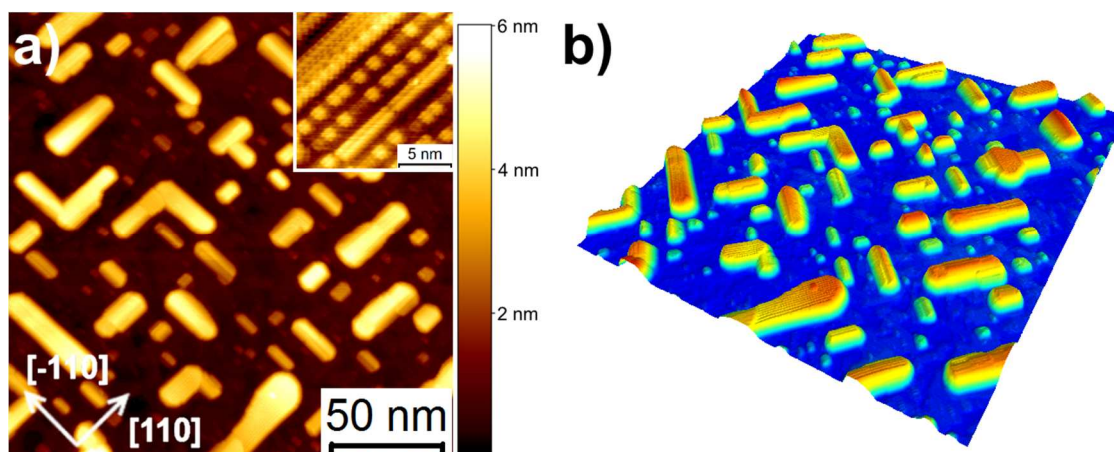


Figure 3.9 Sample surface after annealing at  $400^\circ\text{C}$  for 1 hour: a) STM and b) 3D rendering ( $200 \times 200 \text{ nm}^2$ ,  $V_s = 2 \text{ V}$ ,  $I = 100 \text{ pA}$ ). Inset in panel a) depicts the one-dimensional super-structures found often on top surface of nanostructures ( $15 \times 15 \text{ nm}^2$ ,  $V_s = -0.8 \text{ V}$ ,  $I = 100 \text{ pA}$ , Z-Range:  $500 \text{ pm}$ ).

Further annealing at higher temperature ( $500^\circ\text{C}$  for 1 hour) tremendously improves the surface structure ordering processes. Figure 3.10 shows well separated and organized nanostructures. The nanostructures prefer to adopt an elongated shape and preferentially run along the two orthogonal  $[110]$ ;  $[-110]$  directions of the  $\text{Ge}(001)$  substrate. The number of structures with more complex shapes strongly decreased. It was found that due to the Gibbs-Thomson mechanism [229], the population of the smallest nanoislands clearly decreases in favour of the larger ones. Moreover, simultaneous increase of the size/volume of the larger nanostructures was observed. A more quantitative analysis of nanostructure dimensions including all annealing steps is given in the following of this thesis, however at this point other important findings related to annealing at  $500^\circ\text{C}$  are shortly presented.

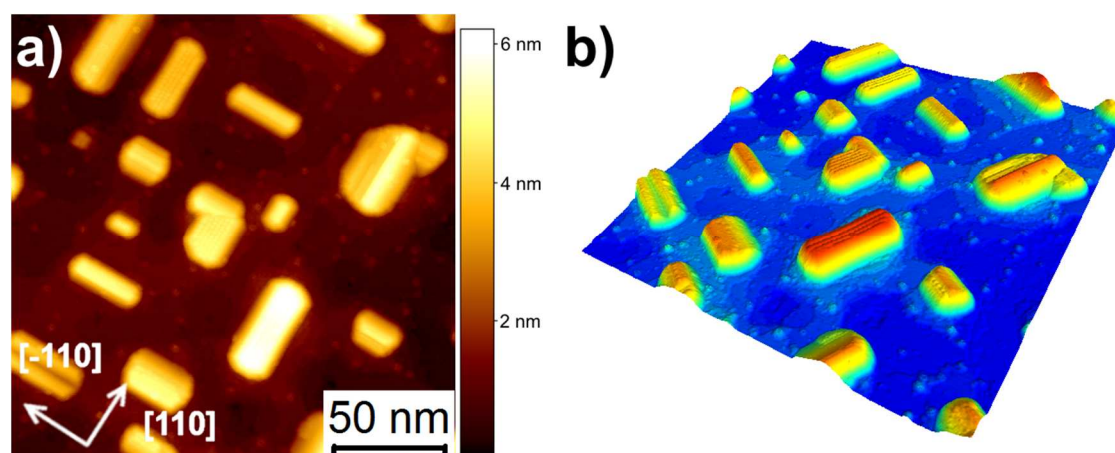


Figure 3.10 Sample surface after annealing at 500 °C for 1 hour: a) STM and b) 3D rendering (200 x 200 nm<sup>2</sup>, V<sub>s</sub>= 1.8 V, I= 80 pA).

Figure 3.11 depicts STM investigations of the surface area between nanoislands recorded after annealing at 500 °C. Figure 3.11 a) illustrates that the surface between nanoislands exhibits a terraced morphology. Closer inspection clearly shows the reconstructed Ge(001) surface, which was confirmed by e.g. monoatomic terrace step height of 0.15(2) nm and by the presence of typical types of Ge(001) surface reconstructions (inset in Figure 3.11 a) and Figure 3.11 b)). It is important to note that the nanostructures influence the terrace width distribution as compared to the clean reconstructed Ge(001) surface - the average terrace width decreases near the nanostructures. This effect is understandable and it can be explained as a result of Ge consumption near the nanostructure and/or step pinning due to locally induced strain fields by the nanostructure. In addition, a significant increase in DVC to ~6(2)% was observed. This effect is very likely related to the Co-Ge interaction. Choi *et al.* reported that for Ge(001)-p(2 x 1) surfaces, subsurface diffusion of Co atoms results in the creation of surface strain which is partially compensated by a DVC increase which allow for more effective elastic relaxation of the surface strain [223]. This phenomenon was predicted using theoretical calculations and confirmed by STM measurements. Finally, Figure 3.11 distinctly illustrates that Ge(001)-c(4 x 2) reconstructed surface areas are more frequently visible near the nanostructures, suggesting again that this behaviour can be triggered by a changed strain balance on the Ge surface in the vicinity of the Co-Ge nanostructure islands.

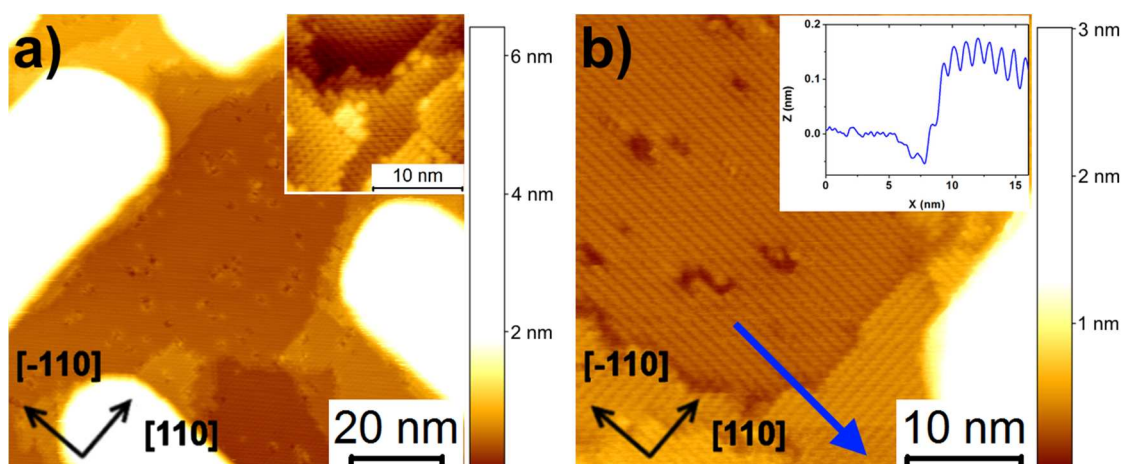


Figure 3.11 Detailed STM analysis of the surface area between nanoislands for sample after annealing at 500 °C: a) 100 x 100 nm<sup>2</sup>, V<sub>s</sub>= -0.4 V, I= 100 pA; a) Inset 20 x 20 nm<sup>2</sup>, V<sub>s</sub>= 0.8 V, I= 30 pA, Z-Range: 600 pm; b) 40 x 40 nm<sup>2</sup>, V<sub>s</sub>= 0.8 V, I= 80 pA.

Further analysis of the surface morphology for samples after annealing at 400 °C and 500 °C reveals that the observed nanostructures can be divided into two different morphology classes, namely flattop-type and ridge-type nanostructures, with the ridge-type nanostructures observed more frequently. Figure 3.12 depicts a more detailed analysis of ridge- (panel (a)) and flattop-type (panel (b)) nanostructures, which were found on the sample surface after annealing at 500 °C. Line profiles along (blue lines) and across (red lines) the nanostructure longitudinal axes x and y are presented in panels (c), (d) and (e), (f), respectively. Side walls for both types of nanostructures have an inclination of ~35° with respect to the Ge(001) surface, corresponding to four equivalent {112} facets. The top surface of the flattop-type nanoislands is parallel to the Ge(001) surface. The ridge-type nanostructures have a surface structure which is entirely characterized by inclined facets, contrary to the flattop-type islands.

As shown on insets in Figure 3.12 a) and b), the top surface of the investigated flattop- as well as ridge-type nanoislands reveals the existence of one-dimensional super-structures. In the case of ridge-type islands, the structure is made of a single one-dimensional chain, whereas in the case of the flattop islands, the top surface area is composed of multiple one-dimensional chains in a staggered arrangement. Detailed analysis of these super-structures shows that each segment of one-dimensional chain consists of small features with a size of ~1 nm<sup>2</sup>. For a single feature the average width is

1.1(2) nm (FWHM value) and apparent height is 100(25) pm. Additionally, the most common distance between nearest features is given by 1.8(2) nm. However, quite often deviations from this periodicity occur. Namely the periodicity of 2.6(3) nm, which is a value around 1.5 times greater than the basic periodicity (1.8(2) nm), was seen very often for flatter-type nanostructures. Interestingly, such lateral periodicity breaks were not observed for features on ridge-type nanostructures. Understanding of the origin of this type of super-structures is still under investigation. However, the hypothesis that this regular arrangement is stabilized by strain relaxation at the island edge, while the flat top facet could indicate a plastic strain relaxation occurring in this type of islands appears to be most appropriate assumption. Please note that results presented above perfectly corroborate and extend previous work reported by Mocking *et al.* [222], where for similar conditions of Co/Ge(001) sample preparation two types of nanostructures were observed (called by them: peaked nano-crystals (equivalent to ridge-type nanoislands) and flat-topped nanocrystals (equivalent to flatter-type nanostructures)). In addition, close-up of the one-dimensional structures were also observed. However, in contrast to results presented in this dissertation, one-dimensional super-structures were observed only on top surface of flat-topped nanocrystals.

Finally, the STM image obtained after further annealing at 600 °C for 1 hour is presented in Figure 3.13. In comparison to the previous annealing steps, annealing at 600 °C causes a clear and significant increase of the nanostructure area and height. Interestingly, the ridge-type nanostructures clearly dominate in the nanoisland population. These trends are even more pronounced after annealing at 700 °C for 30 minute. Figure 3.14 shows the growth of fairly big ridge-type nanoisland. It is relevant that after annealing at 700 °C flatter-type nanostructures were not observed anymore.



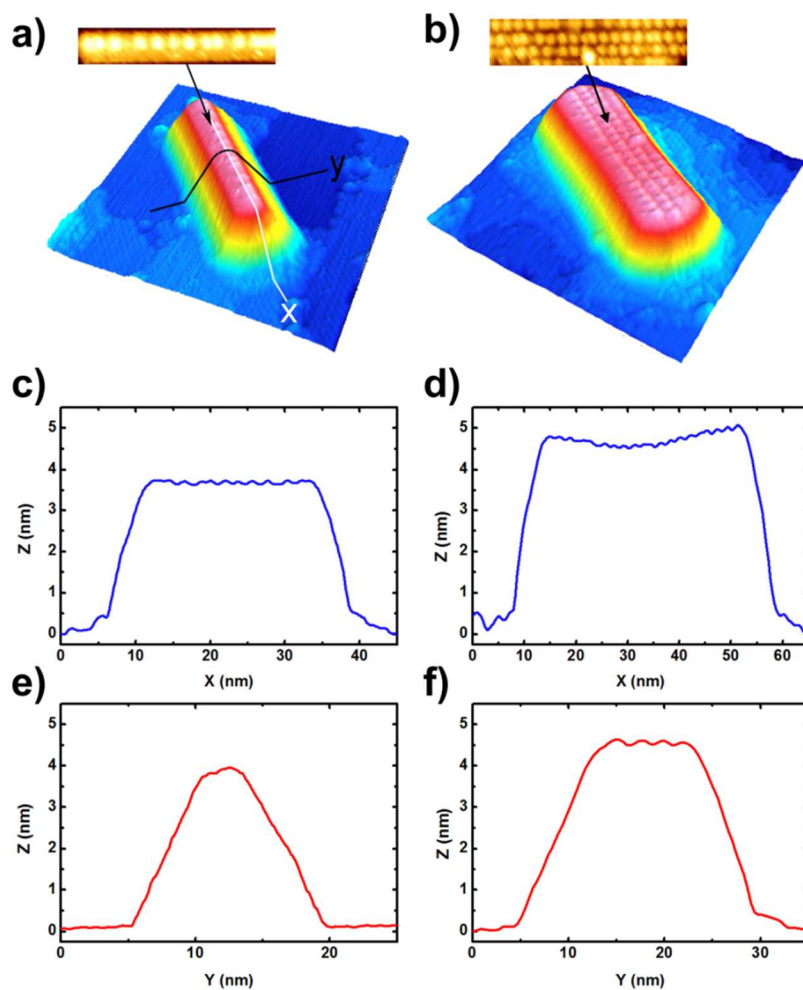


Figure 3.12 3D rendering of a) ridge-type island and of a b) flat-top-type island found on the surface of the sample after annealing at 500 °C for 1 hour; cross sectional profile obtained along (x-direction, c-d) and across (y-direction, e-f) the main nanostructure axis, respectively.

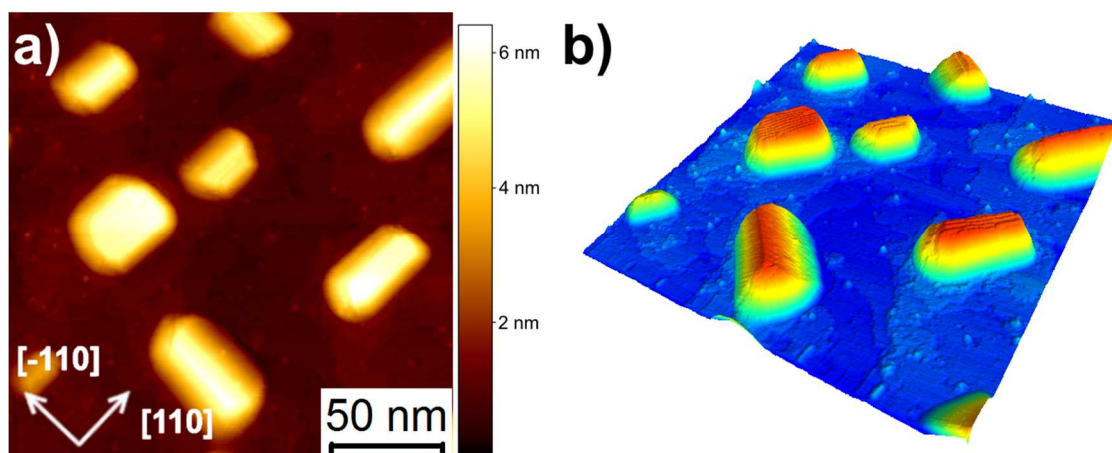


Figure 3.13 Sample surface after annealing at 600 °C for 1 hour: a) STM and b) 3D rendering ( $200 \times 200 \text{ nm}^2$ ,  $V_s = 1.6 \text{ V}$ ,  $I = 60 \text{ pA}$ ).

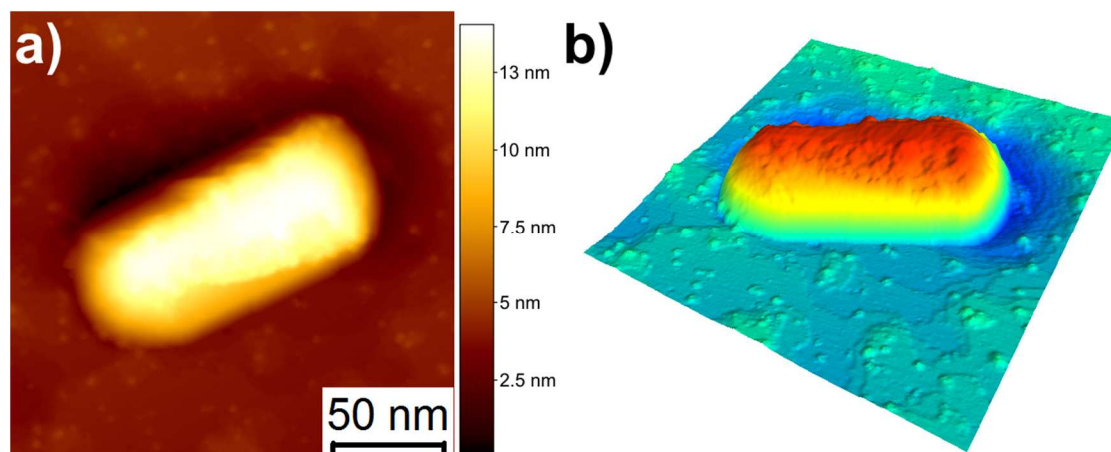


Figure 3.14 Sample surface after annealing at 700 °C for 30 minutes using direct heating mode: a) STM and b) 3D rendering ( $200 \times 200 \text{ nm}^2$ ,  $V_s = -1.6 \text{ V}$ ,  $I = 100 \text{ pA}$ ).

Figure 3.15 shows a quantitative analysis of the morphological parameter evolution as a function of the sample annealing. This overview is based on analysis of: 200 (50 flattop-type) nanoislands for 400 °C and 500 °C, 200 (30 flattop-type) nanoislands for 600 °C and 30 nanoislands for 700 °C. At the beginning, the so-called effective thickness  $t_{\text{eff}}$  was analyzed. The  $t_{\text{eff}}$  is defined as the ratio of the total volume of nanostructures found on top of the sample surface to the scan area. Figure 3.15 a) depicts the  $t_{\text{eff}}$  parameter as a function of the anneal temperature. It is clearly visible that by the annealing treatments, the total amount of nanostructure material was diminished. The effective thickness decreasing from  $t_{\text{eff}} = 0.53(2) \text{ nm}$  ( $T_{\text{ann}} = 400 \text{ °C}$ ) to  $t_{\text{eff}} = 0.25(6) \text{ nm}$  ( $T_{\text{ann}} = 700 \text{ °C}$ ). Such behaviour can be explained by two phenomena during the annealing treatment: re-evaporation or diffusion into the substrate. Because STM measurements alone cannot discriminate between these two hypotheses, additional measurements based on for example (S)TEM and/or XPS are necessary to further unveil the origin of the growth behavior. Figure 3.15 b) illustrates the variation of the nearest neighbor distance  $d_{\text{nn}}$  between nanostructures with annealing temperature. In the 400 °C-600 °C range an almost linear increase of neighbor distance from  $d_{\text{nn}} = 24.9(8) \text{ nm}$  to  $d_{\text{nn}} = 43(2) \text{ nm}$  was observed, which is in contrast to last annealing step at 700 °C, where a rapid, clearly non-linear increase was observed ( $d_{\text{nn}} = 364(5) \text{ nm}$ ). As anticipated by commenting the derivative STM images in Figure

3.8, this behavior is due to an Ostwald ripening phenomenon on the surface, leading to the consumption of the smallest nanoislands in favor of the larger ones.

The average nanostructure length, width and the length/width ratio ( $L/W$ ) as a function of the annealing temperature, is displayed in Figure 3.15 c), d) and e), respectively. The two types of nanostructures exhibit a different growth dynamics. Therefore, it is important to describe the evolution of the nanostructures under the annealing process in a separate way:

*i)* In case of the flattop-type nanostructures, a slight decrease in average nanostructure length from  $L=60(8)$  nm at  $400\text{ }^{\circ}\text{C}$  to  $L=38(4)$  nm at  $600\text{ }^{\circ}\text{C}$  and slight increase in average island width  $W=24(2)$  nm at  $400\text{ }^{\circ}\text{C}$  to  $W=32(3)$  nm at  $600\text{ }^{\circ}\text{C}$  was observed. As a consequence, the  $L/W$  ratio decreased from  $1.9(2)$  to  $1.2(1)$ , which means that the flattop nanostructures changed slightly from an initially elongated towards a more “square” shape. As was already mentioned, beyond  $600\text{ }^{\circ}\text{C}$  flattop nanostructures were not observed anymore in STM.

*ii)* In case of the ridge-type nanostructures, the annealing treatment resulted in an increase of both lateral dimensions. The average nanostructures length grew exponentially from  $L=5(1)$  nm at  $400\text{ }^{\circ}\text{C}$  to  $L=124(9)$  nm at  $700\text{ }^{\circ}\text{C}$ . Simultaneously a similar behavior was observed for the average nanostructures width, which increased from  $W=10(1)$  nm at  $400\text{ }^{\circ}\text{C}$  to  $W=70(3)$  nm at  $700\text{ }^{\circ}\text{C}$ . In consequence, the  $L/W$  ratio did not substantially change during annealing treatments and remained at a level  $\sim 1.8$ .

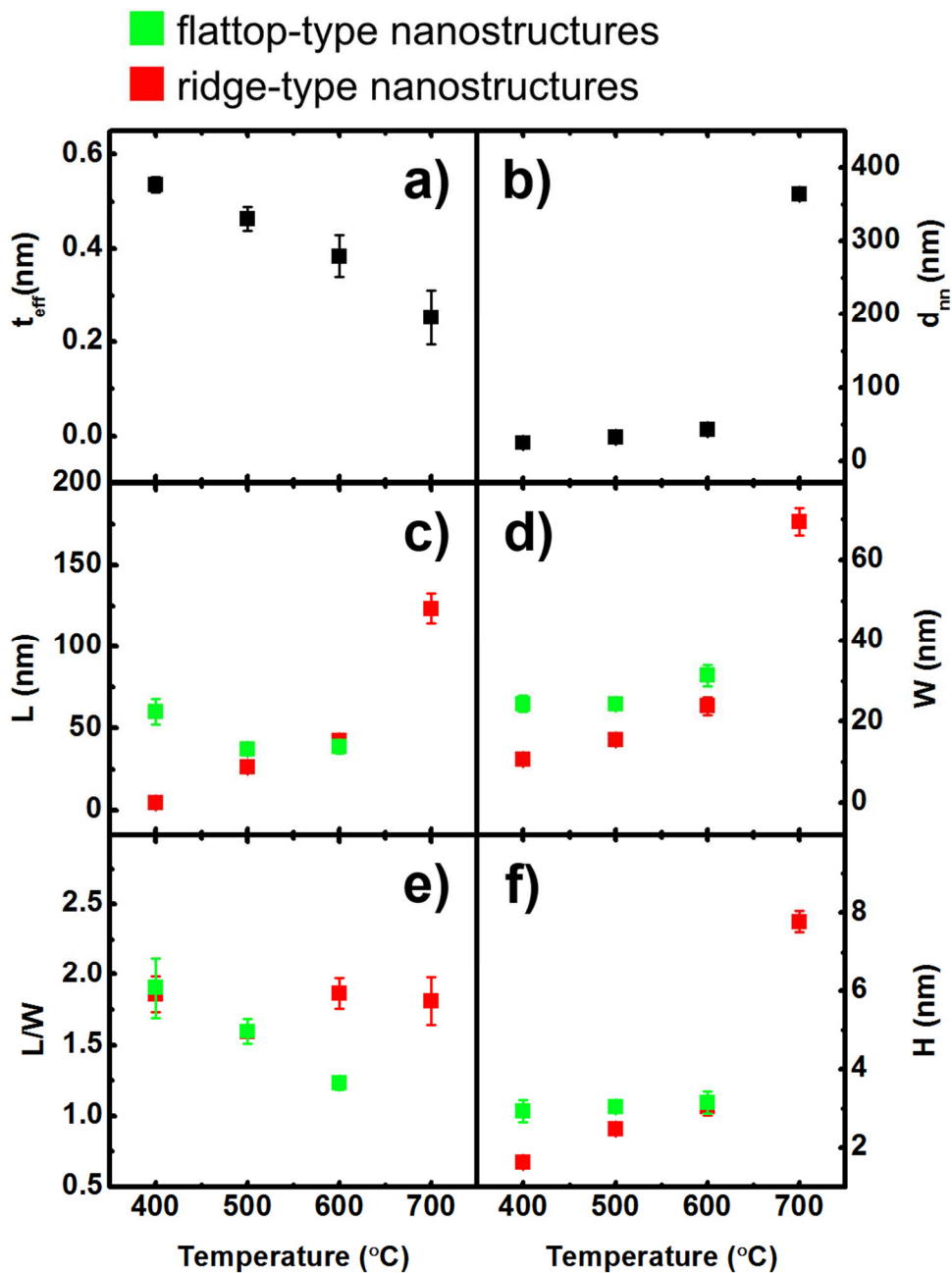


Figure 3.15 Quantitative analysis of nanostructure morphological data: a) effective thickness; b) nearest neighbor distance; c) length; d) width; e) aspect ratio (length/width) and f) height as a function of the annealing temperature. Red symbols are for ridge-type structures while green for flattop-type structures.

In conclusion, quantitative analysis of nanostructures lateral dimension points out that the ridge-type nanostructures show larger shape stability than the flattop nanostructures in the observed annealing temperature range. Both types of

nanostructures show an elongated shape (see L/W ratio). However, this ratio is preserved in ridge-type nanostructures up to 700 °C, while the flattop nanostructures develop a more squared shape at 600 °C, and then disappear at 700 °C.

Finally, in Figure 3.15 f) the analysis of the influence of the annealing temperature on the average height of the flattop- and the ridge-type nanostructures is given. As shown, the flattop nanostructures exhibited a constant average height of about  $h=3$  nm up to 600 °C. In contrast, the average height of the ridge-type nanostructures increased slightly from  $h=2.9(3)$  nm at 400 °C to  $h=3.1(3)$  nm at 600 °C, and then substantially increased to  $h=7.8(3)$  nm at 700 °C. In other words, upon increasing the annealing temperature from 600 °C to 700 °C, a substantial change in surface morphology was induced. In fact, not only the flattop nanostructures disappeared, but the ridge-type nanostructures showed the most substantial increase in lateral as well as height dimensions.

### Low coverage STM study

In order to shed more light on the initial nucleation of the  $\text{Co}_x\text{Ge}_y$  nanostructures, a low coverage STM study was performed. The main results associated with low coverage STM studies are briefly presented in this sub-chapter. What is also important and as was already mentioned, the Co surface coverage was estimated using STM images for low coverage and a simple model proposed by Zandvliet *et al.* [221]. Based on these findings, the coverage was further extrapolated to high coverage cases.

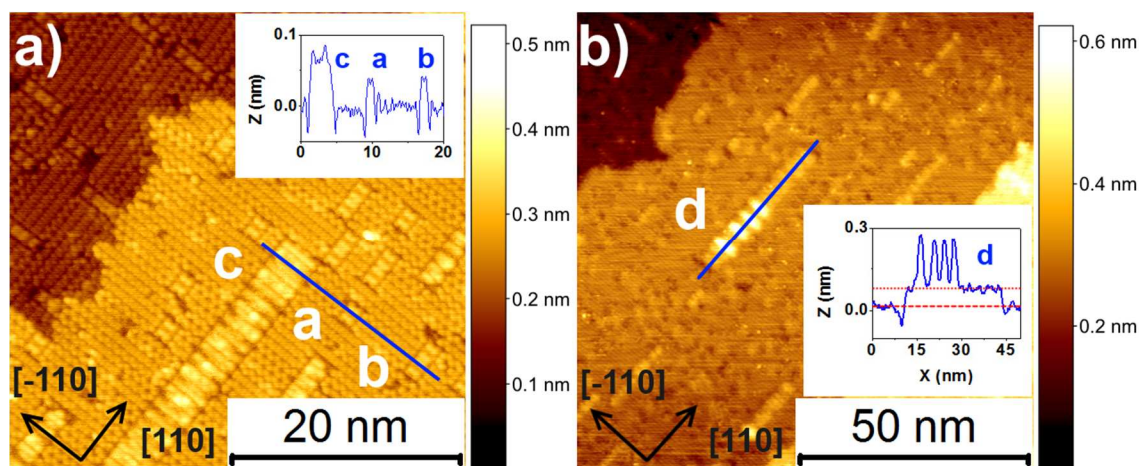


Figure 3.16 STM topographic images of Ge(001) surface after the deposition of small Co coverage and annealing at 500 °C for 1 hour and Z profiles obtained along blue lines as insets: a) 40 x 40 nm<sup>2</sup>,  $V_s = -1.2$  V,  $I = 250$  pA; b) 100 x 100 nm<sup>2</sup>,  $V_s = -2$  V,  $I = 150$  pA.

Figure 3.16 shows two STM topographic images of the Ge(001) surface after the RT deposition of a small Co coverage of about 0.23(5) ML (around 16 times less than the coverage so far discussed and presented in previous Figs.), additionally annealed at 500 °C for 1h. The filled state STM image (Figure 3.16 a)) clearly shows that after deposition of small amount of Co and additionally annealing treatment at 500 °C for 1h, Co has ordered into regular shaped, small units. These low-coverage, atomic-scale 2D structures can be grouped into three main types, which are described more precisely in paragraphs below.

The height-profile in Figure 3.16 a) passes through three low-coverage structures, namely: elementary building block or elementary unit – denoted (*a*), a small 2D stripes – (*b*), and large 2D nanostructure stripe – (*c*).

- **Elementary unit (*a*)** is the smallest Co structure, found in the low coverage STM measurements. These structures have rectangular shape and are embedded within the topmost layer of the Ge(001) surface. Most of the elementary units have dimensions of 1.59(2) nm in width and 2.27(4) nm in length, while a height of about 0.04(1) nm is measured with respect to the Ge surface level. These findings are consistent with earlier studies from 2011. Namely professor's Zandvliet research group also reported that the deposition of sub-monolayer amounts of Co (0.1 ML) on Ge(001) and subsequent annealing at 275 °C for 5 min results in the creation of small, well-ordered Co structures, which are embedded within the topmost layer of the Ge (001) surface [221].
- **Small 2D stripes (*b*)** also occur frequently. It seems that these structures consist of several elementary building blocks. Precise analysis revealed that the elementary unit (*a*) and small 2D stripes (*b*) nearly exhibit the same values of height and width (which for structure (*b*) amount to 0.05(2) nm and 1.60(2) nm, respectively). The length of small 2D stripes (*b*) across the dimer rows instead, is about 1.67 times bigger (3.79(2) nm) than the elementary unit cell (*a*). Figure 3.16 a) clearly shows that the length of the elementary unit cell (*a*) is extended over 3 Ge dimer rows while structure (*b*) is clearly placed over 5 Ge dimer rows.
- And finally **large 2D nanostructure stripe (*c*)**. These nanostructures also show an elongated 2D structure of their shape, where the length of the nanostructures

is determined by nanostructure growth across the dimer rows. Analyzing precisely the dimensions of these structures, it can be concluded that height and width of the broad 2D nanostructure stripe (*c*) is determined by multiple – but not necessarily integer - numbers of the elementary unit cell dimensions, namely a height of 0.07(2) nm (2x bigger) and a width of 3.89(2) nm (2.5x bigger) is determined.

On the other hand, Figure 3.16 b) highlights the onset of 3D nanostructure growth behavior. The 2D growth for nanostructures typically proceeds up to a critical size where nucleation of the next layer becomes statistically and energetically possible and nanostructure growth in the third dimension is thus initiated. An elongated 2D nanostructure stripe (*d*) featuring protrusions on its top is clear visible in Figure 3.16 b). The additional inset shows the height profile along the described nanostructures. In this inset the dashed red line represents the level of the Ge substrate while the dotted red line corresponds to the height of the investigated nanostructure stripe without protrusions. Interestingly, the height-profile analysis demonstrates that the vertical distance between Ge substrate (dashed red line) and nanostructure without protrusion (dotted red line) is 0.07(2) nm, which is nearly the same of what was obtained in the large 2D nanostructure stripe (*c*) in Figure 3.16 a). The total height of nanostructure stripe (*d*) is 0.26(2) nm (height measured with respect to Ge and taking into account nanostructure's protrusion). Also noteworthy is the fact that the three bright protrusions on the right side demonstrate the same periodicity of around 3.34(4) nm. However, the distance between the first protrusion on the left side and the nearest entity is larger, namely 4.32(4) nm. This irregularity could point to a lateral symmetry break in the 2<sup>nd</sup> layer nucleation process. And finally, the total length of the imaged nanostructure is 34.7(2) nm and its width is 4.7(2) nm which corresponds to the sum of 15 elementary unit blocks (15 x 2.3 nm) in length and of three columns in width (3 x 1.6 nm).

In short conclusion, findings related to the low coverage STM study of Co on Ge(001) shown in Figure 3.16 allow to gain insights on the anisotropic growth mechanisms in the early stage. It is hypothesized that the elongated shape of the 3D nanostructure observed at high coverage (presented in previous sub-chapter) is thus

related to an anisotropic spatial correlation of unit building blocks which is very pronounced perpendicular to the Ge dimer rows but very limited along the Ge dimer rows. The elongated shape of the nanostructures can therefore result from an attractive force of basic unit building blocks across adjacent dimer rows. The structural similarities of the elongated nanostructure morphology at high coverage and low coverage 2D structures are clearly evident and points to the fact that similar growth mechanisms are active here.

### (S)TEM-EDX study

This sub-section contains additional *ex-situ* (S)TEM-EDX results of selected Co/Ge(001) samples. (S)TEM-EDX measurements gave an opportunity to validate findings based on STM study and report a clear evidence for the formation of Co germanide nanostructures.

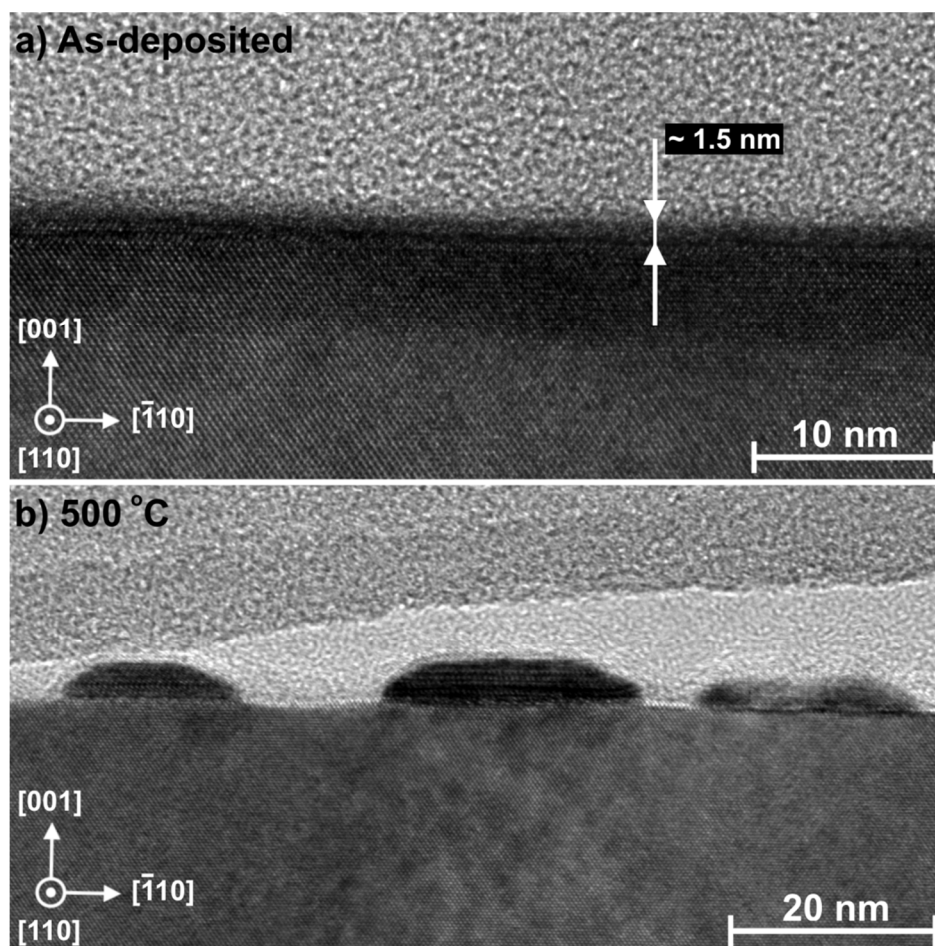


Figure 3.17 HR-TEM measurements on Co/Ge(001) samples for: a) “as-deposited” sample; and b) sample after annealing at 500 °C.



Figure 3.17 a) and b) shows two HR-TEM images for two samples: “as-deposited” and annealed at 500 °C for 1h, respectively. In addition Figure 3.18 depicts (S)TEM-EDX analysis of three samples: “as-deposited” at RT, annealed at 500 °C and annealed again at 700 °C. After RT metal deposition a thin Co layer on top of Ge substrate is clearly noticeable (Figure 3.17 a) and Figure 3.18-top panel). It seems that the Co layer fully covers the Ge surface, however this result is due to the projection of the (S)TEM-EDX study along the surface and thus that the observation of continuous Co layer is not in contradiction to the Volmer-Weber growth behavior reported earlier based on STM-LEED study. The approximate thickness of the deposited Co layer, estimated by means of HR-TEM as well as EDX profiles, is about 1.5(3) nm. A further annealing at 500 °C for 1 hour leads to tremendous changes of sample morphology. The formation of faceted  $\text{Co}_x\text{Ge}_y$  nanostructures with a sharp, plane nanostructure/Ge interface was observed (Figure 3.17 b)). By means of EDX analysis (Figure 3.18 b)) it is clearly visible that the nanostructures undoubtedly consist of a Co germanide phase. We noticed that between the  $\text{Co}_x\text{Ge}_y$  nanostructures, only a signal from the Ge substrate is observed, which perfectly matches to STM observations. Taking into account this EDX analysis and STM observations after thermal annealing steps in the range between 250 °C and 500 °C, the formation of  $\text{Co}_x\text{Ge}_y$  nanostructure can be attributed to a chemical reaction between Co and Ge which is characterized by two growth stages. First, according to STM, surface diffusion of Co and Ge results at 250 °C in the formation of a continuous  $\text{Co}_x\text{Ge}_y$  wetting layer along with a substantial change in Ge terrace morphology. Secondly, according to the STM and EDX study, at around 400 °C, the  $\text{Co}_x\text{Ge}_y$  wetting layer becomes instable due to Ge bulk diffusion into the  $\text{Co}_x\text{Ge}_y$  wetting layer, resulting in the formation of the discontinuous  $\text{Co}_x\text{Ge}_y$  nanostructure islands with no major Co diffusion into the bulk of the Ge substrate. This onset of Ge diffusion into the continuous wetting  $\text{Co}_x\text{Ge}_y$  - without noticeable Co diffusion into the Ge substrate - is potentially related to the significantly lower melting temperature of Ge ( $T= 938$  °C) in comparison to Co ( $T= 1495$  °C), providing Ge atoms with a higher diffusion into the bulk at the given temperature. Finally, annealing at 700 °C for 1 hour results in a strong enhancement of the interface reaction between the Co germanide nanostructures and the underlying Ge substrate. The (S)TEM-EDX image clearly shows

that the formerly planar Co germanide nanostructure/Ge substrate interface evolves into a strongly faceted interface structure. In contrast to previous annealing step, where Ge bulk diffusion into the  $\text{Co}_x\text{Ge}_y$  nanostructure was considered, here EDX analysis clearly reveals a strong Co diffusion into the Ge substrate. This result confirms previous Co diffusion studies on Ge substrates, which showed similar types of diffusion behavior [225] [216] [230].

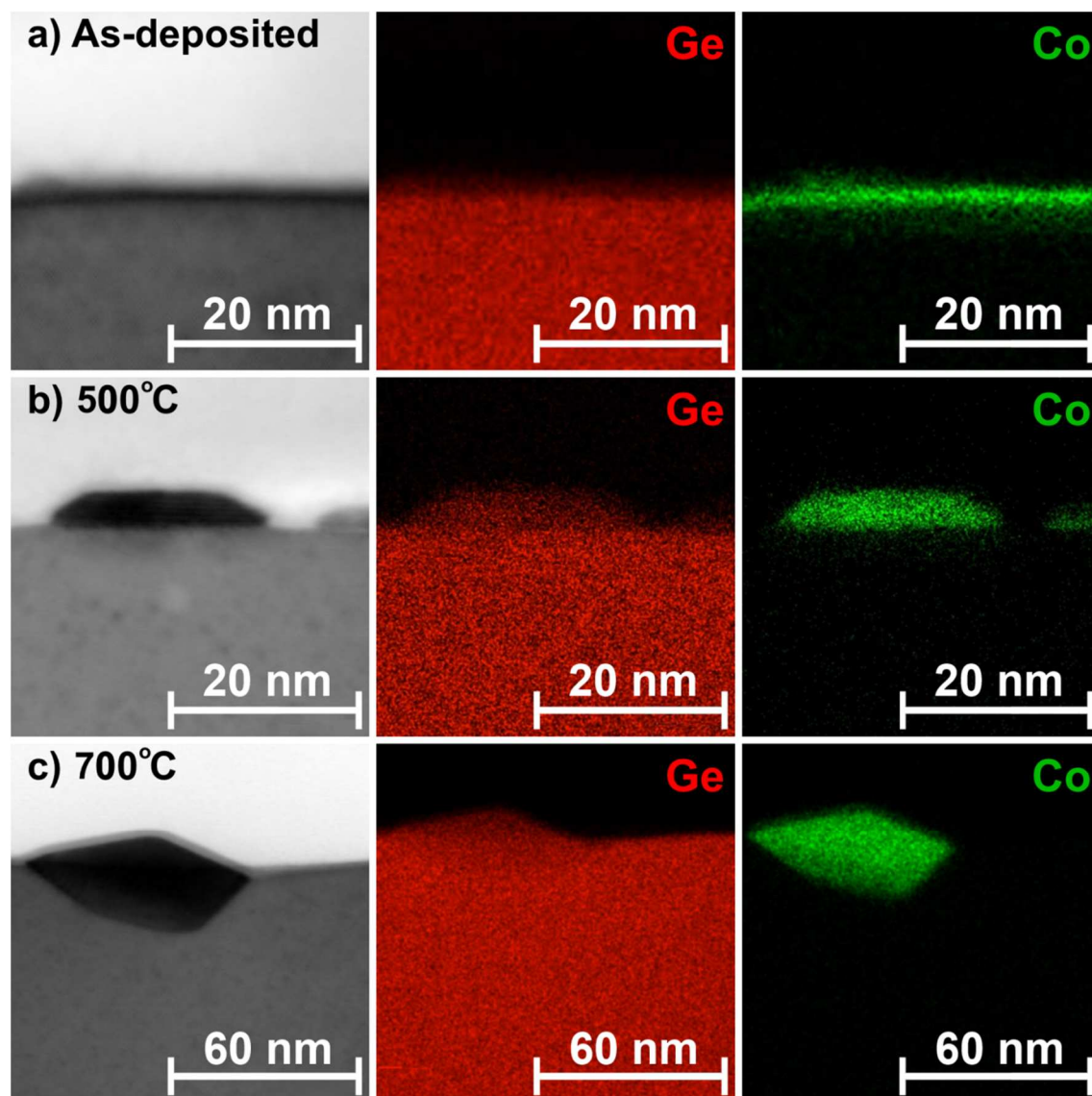


Figure 3.18 (S)TEM-EDX measurements on Co/Ge(001) samples. Scanning mode TEM images with corresponding EDX analysis for: a) “as-deposited” sample, b) sample after annealing at 500 °C, and c) sample after annealing at 700 °C.

In conclusion, (S)TEM-EDX results are in line with findings based on STM-LEED study and report a clear evidence for the formation of Co germanide nanostructures. It can furthermore be stated that the Co-Germanide nanostructures develop as a function of annealing temperatures from a Co-rich towards a Ge-rich  $\text{Co}_x\text{Ge}_y$  phase but a detailed determination of the Co germanide nanostructure stoichiometry is however not accessible by (S)TEM-EDX studies alone.

### XPS study

To further validate observations presented in previous sections, this part shows and discusses the results based on *ex-situ* XPS measurements. The sample was prepared in STM UHV system in the same way as for measurements discussed so far (about 4 ML Co deposited on Ge substrate at RT) and then *ex-situ* transferred to the XPS UHV system where the sample was *in-situ* annealed in the 200 °C to 500 °C range. To check the quality of the deposited Co layer, a survey scan was recorded (data not shown).

Figure 3.19 presents the evolution of Co  $2p_{3/2}$ , Ge  $2p_{3/2}$  and Ge 3d XPS spectra measured for the as-deposited case (RT) and after each 1 hour long annealing step. The insets highlight peak position shifts as a function of annealing temperature.

The analysis of the evolution of the Co  $2p_{3/2}$  XPS peak gives two main conclusions. In this case, the peak intensity increases as a function of annealing and can be explained by the change in surface morphology, namely evolution from 2D wetting layer towards 3D nanostructures. Given the surface sensitivity of the XPS signal, such behavior is typical for thin film morphology evolution from 2D towards 3D if the continuous layer thickness is larger than the photoelectron inelastic mean free path before the dewetting. Secondly, a clear Co  $2p_{3/2}$  peak shift by up to 0.2 eV as a function of annealing towards higher binding energy, clearly bigger than experimental error in binding energy determination (0.1 eV), was observed (inset in Figure 3.19 a)). Based on (S)TEM-EDX results, this peak shift can be attributed to a chemical reaction towards Co-germanide formation. In this most probable scenario, the chemical reaction between Co and Ge leads to a decrease in space charge around the Co atoms, resulting in a higher binding energy for the Co  $2p_{3/2}$  photoemission process ( $\text{Co}^{\delta+}$  -  $\text{Ge}^{\delta-}$  bonding scenario).

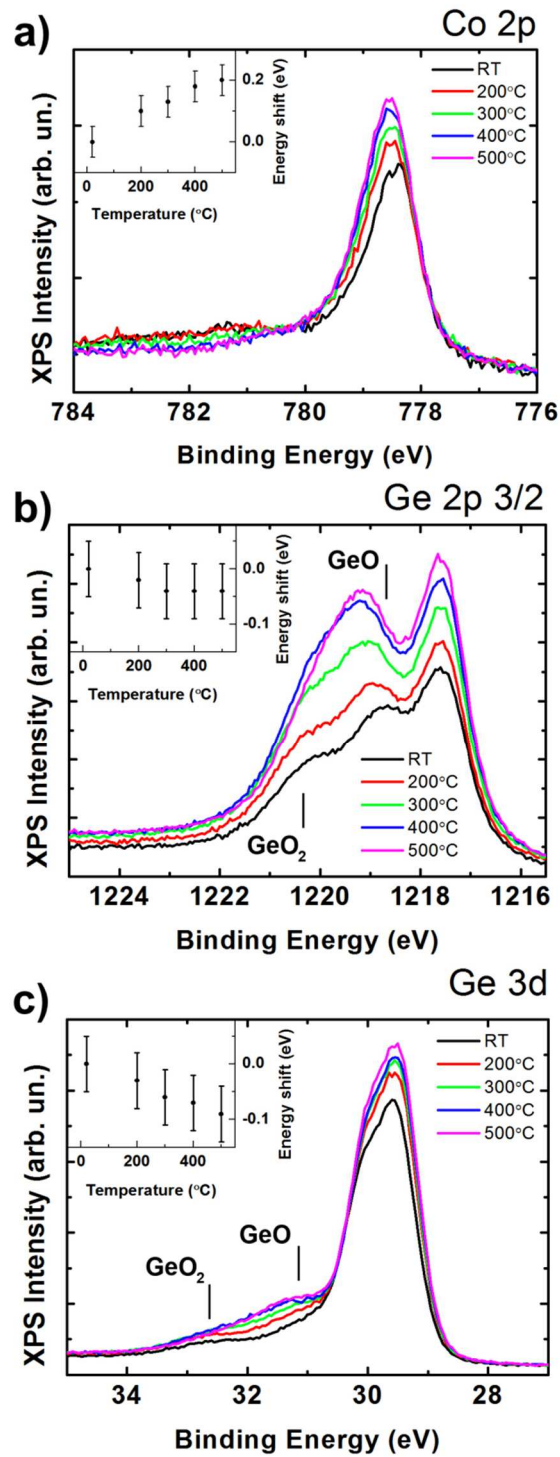


Figure 3.19 Co 2p, Ge 2p<sub>3/2</sub> and Ge 3d core spectra of Co/Ge sample recorded after RT deposition of ~4 ML of Co and annealed to various temperatures represented as different colored lines (see legend on top). Peak position shift as a function of annealing temperature presented in insets. Data were not normalized.

Figure 3.19 b) and c) illustrates that both Ge core levels (Ge 2p<sub>3/2</sub> and Ge 3d) feature an intensity increase as a function of annealing. Before continuing the XPS analysis, please note that the Ge 2p<sub>3/2</sub> and Ge 3d signals, due to the large difference of their corresponding photoelectron escape depth, result in higher surface sensitivity of the Ge 2p<sub>3/2</sub> with respect to the Ge 3d level. Detailed analysis shows that the intensity increase is much more pronounced for the Ge 2p<sub>3/2</sub> XPS signal. Once again, this behaviour can be attributed to the evolution of the surface morphology going from an initial 3D metal cluster layer over a 2D wetting layer towards 3D Co-germanide nanostructure islands, with major uncovered clean Ge(001) surface areas, as the annealing temperature is increased. Please also note that the presence of Ge native oxide, formed during the *ex-situ* transfer from the deposition chamber to the XPS tool, undoubtedly may influence the recorded Ge peaks and may prevent the observation of the initial transformation from VW cluster to the Co<sub>x</sub>Ge<sub>y</sub> wetting layer. The energy shifts of the Ge 2p<sub>3/2</sub> and Ge 3d core levels are reported in the insets. The Ge 2p<sub>3/2</sub> binding energy decreases by ~0.05 eV while the Ge 3d by ~0.1 eV. Such a peak shift towards lower binding energy is in principle in line with a partial Ge reduction in the course of Co-germanide formation.

Furthermore, it must be noted that these peak shift values are close to the limits of the experimental resolution and need thus to be interpreted with care. The reason for the small peak shifts of the Ge XPS peak is partly attributed to the fact that the Ge signal from Co-Ge islands is strongly superimposed by the bulk Ge surface contributions. Furthermore, the interpretation of the Ge XPS signals is complicated by the fact that Ge oxide signals become visible in the Ge 2p<sub>3/2</sub> as well as Ge 3d signal towards the high binding energy side.

In summary, the temperature depended XPS study allows to complement other surface science techniques by additional structural and chemical information. Findings based on XPS results are in agreement with previously discussed STM and (S)TEM-EDX studies.

## Summary

In summary, the presented combined STM, LEED, (S)TEM-EDX and XPS study were performed to investigate the evolution of  $\text{Co}_x\text{Ge}_y$  nanostructures after RT Co thin film deposition, followed by subsequent thermal annealing. These studies present the relevant structural and chemical processes taking place during Co-germanide formation on Ge(001).

Schematically the main results of this study can be summarized as follows:

- i)* The RT deposition of few Co MLs on the Ge(001) substrate results in a Volmer-Weber growth mode. Due to limitations of STM, this technique allowed to observe only 3D metallic clusters on the unchanged sample terraced morphology. However, by LEED the (2 x 1) Ge surface reconstruction from areas not covered by Co clusters was observed. Furthermore, Co and Ge core level binding energies confirm the non-reacted nature of the Co/Ge system after RT deposition.
- ii)* Annealing at relatively low temperature range results in the first reaction between Co and Ge. First annealing treatment at 150 °C results in only small changes in surface morphology. This leads to the conclusion that Volmer-Weber Co islands are stable up to 150 °C. However, XPS measurements exhibit first changes in Co and Ge peak positions which is the proof for the onset of a low temperature reaction. Similar XPS findings in this temperature range were reported by Prabhakaran *et al.* [216].

Next annealing was realized at 250 °C. This step results in relevant surface morphology changes: the Co VW clusters are not visible anymore. Co clusters react in particular with the Ge terrace atoms and form a continuous  $\text{Co}_x\text{Ge}_y$  wetting layer. What is important, no Ge terraces were visible anymore. First instabilities of this flat  $\text{Co}_x\text{Ge}_y$  are visible in terms of the formation of elongated  $\text{Co}_x\text{Ge}_y$  nanostructures. Changes in XPS peak intensities and positions support the STM findings. It is interesting to note that thin film XRD studies by Gaudet *et al.* report the formation of the CoGe phase in the temperature range from 300 °C to 400 °C so that the Co-Germanide continuous wetting layer is probably related to the CoGe phase [211].

*iii*) Annealing at high temperature (400 °C to 500 °C) initiates the dewetting of the  $\text{Co}_x\text{Ge}_y$  layer. This process is accompanied by the formation of two types of well-ordered, elongated 3D Co-germanide nanostructures (flattop- and ridge-type), and simultaneously expose of the clean, reconstructed Ge(001) surface areas between nanostructures. Based on (S)TEM-EDX study, it can be concluded that Ge diffusion from bulk into the  $\text{Co}_x\text{Ge}_y$  nanostructures is the main driving force towards creation of  $\text{Co}_x\text{Ge}_y$  nanostructures. Probably, the Co-germanides formed during this high temperature annealing state are related to  $\text{Co}_5\text{Ge}_7$ , as this phase was found to dominate in the temperature regime from 400 °C to 600 °C [211].

*iv*) Finally, annealing above 600 °C demonstrates Ostwald ripening. Statistical analysis of the 3D  $\text{Co}_x\text{Ge}_y$  nanostructures evolution as a function of higher annealing treatments shows that flattop-type nanostructures are less stable than ridge-type nanostructures. Flattop nanostructures disappear completely whereas ridge-type nanostructures grow in size. The (S)TEM-EDX study presents a change of the Co/Ge interface structure away from a planar towards a faceted interface morphology and reveals Co diffusion into the Ge substrate. It is noted that the Ostwald ripening occurs in the temperature regime where Gaudet *et al.* report the formation of the  $\text{CoGe}_2$  phase to start above 600 °C [211].

### 3.3. Nickel germanide nanostructures on Ge(001) surface

This chapter presents systematic study on the growth and evolution of  $\text{Ni}_x\text{Ge}_y$  nanostructures as a function of subsequent annealing treatments at increasing temperature. In order to ease the comparison between two investigated systems, the sample preparation procedure, the amount of deposited material and the duration as well as temperature of annealing treatments were very similar. However, it should be pointed out that due to the strong low temperature Ni diffusion and limitations associated with current state-of-the-art Si photonics in CMOS technology, the annealing temperature has been limited to 500 °C. All subsequent thermal annealing steps were performed *in-situ* at temperatures ranging from 100 °C up to 500 °C for 60 min using radiative heating. The sample temperature was controlled by means of a type K thermocouple in direct contact with the sample holder (T measurement accuracy of  $\pm 10$  °C).

#### **Characterization of the Ni-Ge system**

Figure 3.20 a) depicts that Ni-Ge system exhibits a complex phase diagram with a wide range of different physical properties [227]. However, it must be noted that in general the bulk phase diagrams are only of limited use for nanoscience owing to the strongly increased surface/volume ratio and to the influence of the nanostructure/substrate interface at the nm-scale. Consequently, the Ni–Ge thin and ultra-thin film systems have recently been re-investigated using different experimental methods (such as transmission electron microscopy (TEM) [231] [232]; X-ray diffraction (XRD) [233] [234]; electrical characterization [235] [236]; and X-ray photoelectron spectroscopy (XPS) [237]) as well as theoretical calculations [238] [239]. According to the best knowledge of the author of this thesis, there is a clear lack of STM studies on Ni-Ge system, which is extremely important from the point of view of ultimate nano-scale growth control. The STM studies were reported insofar for the Ni/Ge(111) system only, and have been dated to the years 2013-2014 [240] [241]. However, it should be emphasized that as the scalability of Ni-germanide formation becomes more and more important in nano-scaled Ge-based devices (the ohmic phase has to be achieved in ever smaller nanostructures [118]), studies without nano-scale resolution are thus of limited use for future process development guidance. Therefore, it is crucial to perform STM



studies on Ni-Ge systems, because it gives an opportunity to unveil the atomistic mechanisms of the formation of metal contacts in nano-scaled Ge-based devices. Certainly, Ni germanide contacts on photonic Ge microstructures also require nano-scale control, as nano-scale defects might result in inhomogeneous SBH with detrimental effects.

Among all stable stoichiometric Ni-Ge phases, it is generally acknowledged that the NiGe phase is best suited for ohmic metal contact formation, due to low sheet resistance, good stability under heat treatment and low forming temperature [211] [224]. The NiGe phase crystallizes in a MnP-type orthorhombic structure with unit cell dimensions  $a= 5.381 \text{ \AA}$ ,  $b= 3.428 \text{ \AA}$ ,  $c= 5.811 \text{ \AA}$  [233]. A schematic structure of the NiGe unit cell is shown in Figure 3.20 b). The resistivity of NiGe is approximately  $22 \mu\Omega\text{cm}$  [211], which is comparable to that of NiSi (one of the materials commonly used in the manufacturing of electrical contacts in Si-CMOS technology).

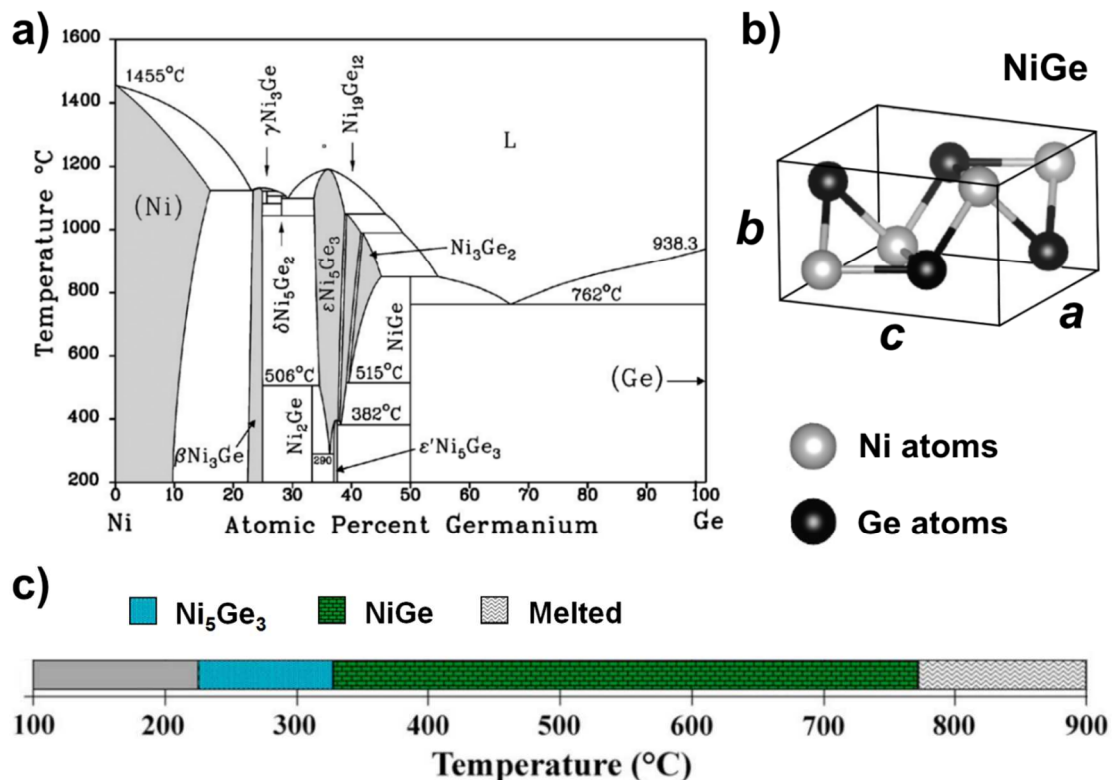


Figure 3.20 Characterization of the Ni-Ge system: a) the binary bulk phase diagram for the Ni-Ge system (after [227]); b) schematic of the NiGe structure (after [239]); and c) unusual phase sequence for the reaction of 30 nm thick Ni film deposited on Ge(001) (after [211]). Typically, the observed phase sequence for most of investigated thin film Ni/Ge(001) system is as follows:  $\text{Ni}_2\text{Ge} \rightarrow \text{NiGe} \rightarrow \text{Melted}$ . This example shows how important are further investigations of this system on the nano-scale.

For such complex systems like Ni-Ge, it is important to determine the phase formation sequence. According to the Walser and Benè (WB) rule (explained in detail in Chapter 4.2.1) proposed in the '70s, which describes the bulk metal-semiconductor solid-phase reactions [242] [243], first compound to nucleate in binary Ni-Ge reaction is the Ni<sub>2</sub>Ge phase, which then passes into NiGe. Many scientific papers demonstrate the compliance of the mentioned rule and predicted phase sequence. For example, Wittmer *et al.* confirmed the WB rule for the Ni/Ge system and demonstrated the presence of NiGe above 250 °C, following the initial appearance of a Ni<sub>2</sub>Ge phase [243]. However, Nemouchi *et al.* [244] and Gaudet *et al.* [211] [234] presented another Ni<sub>x</sub>Ge<sub>y</sub> growth scenario where, based on TEM and XRD, the initial formation of Ni<sub>5</sub>Ge<sub>3</sub> and NiGe germanides phases was reported to simultaneously occur; further annealing resulted in the growth of NiGe while Ni<sub>5</sub>Ge<sub>3</sub> was completely consumed. In addition, Nath *et al.* reported, based on *in-situ* TEM studies, that the NiGe phase can be grown directly on Ge(001) – without the metal rich phase Ni<sub>x</sub>Ge<sub>y</sub> phase ( $x > y$ ) – when Ni is deposited on Ge at a substrate temperature of 300 °C [232]. In summary, the formation of good quality NiGe phase occurs around 300 °C. However, it was also demonstrated that NiGe formation can occur at lower temperatures (around 250 °C) [245] [246] and even at RT [244]. In conclusion, the various studies agree on the formation of NiGe around 300 °C but disagree on the initially formed, metal rich phase.

### **STM study**

This sub-section presents the main part of results on the studied Ni/Ge(001) system, namely the STM study on the surface morphology evolution of RT-deposited Ni thin layer as a function of subsequent annealing steps at increasing temperature.

Figure 3.21 shows a series of STM images of the Ge(001) surface after ~1 nm Ni deposition at RT. To determine the thickness of the coating, other techniques like HR-TEM and angle-resolved XPS were used, which is described in next sub-chapters. Here, STM results clearly show that after RT Ni deposition, the Ge(001) surface is closely covered by high density metal nano-sized clusters. However, the terrace structure of the underlying Ge substrate is preserved. Quantitative analysis shows that the average height between two neighbouring terraces is ~0.16(2) nm (e.g. height profile in Figure

3.21 b)), which corresponds to monoatomic high Ge(001) step edges. Closer inspection shows that the Ge(001) surface reconstruction is no longer observed by STM at this coverage (Figure 3.21 c) and d)). This can either be attributed to limited STM resolution on this strongly corrugated system or to a change of surface energy by the metal/Ge induced interface strain. The average size of the Ni metal cluster is: 1.79(8) nm (radius), 10.6(6) nm<sup>2</sup> (cluster area), and 0.08(1) nm (apparent height).

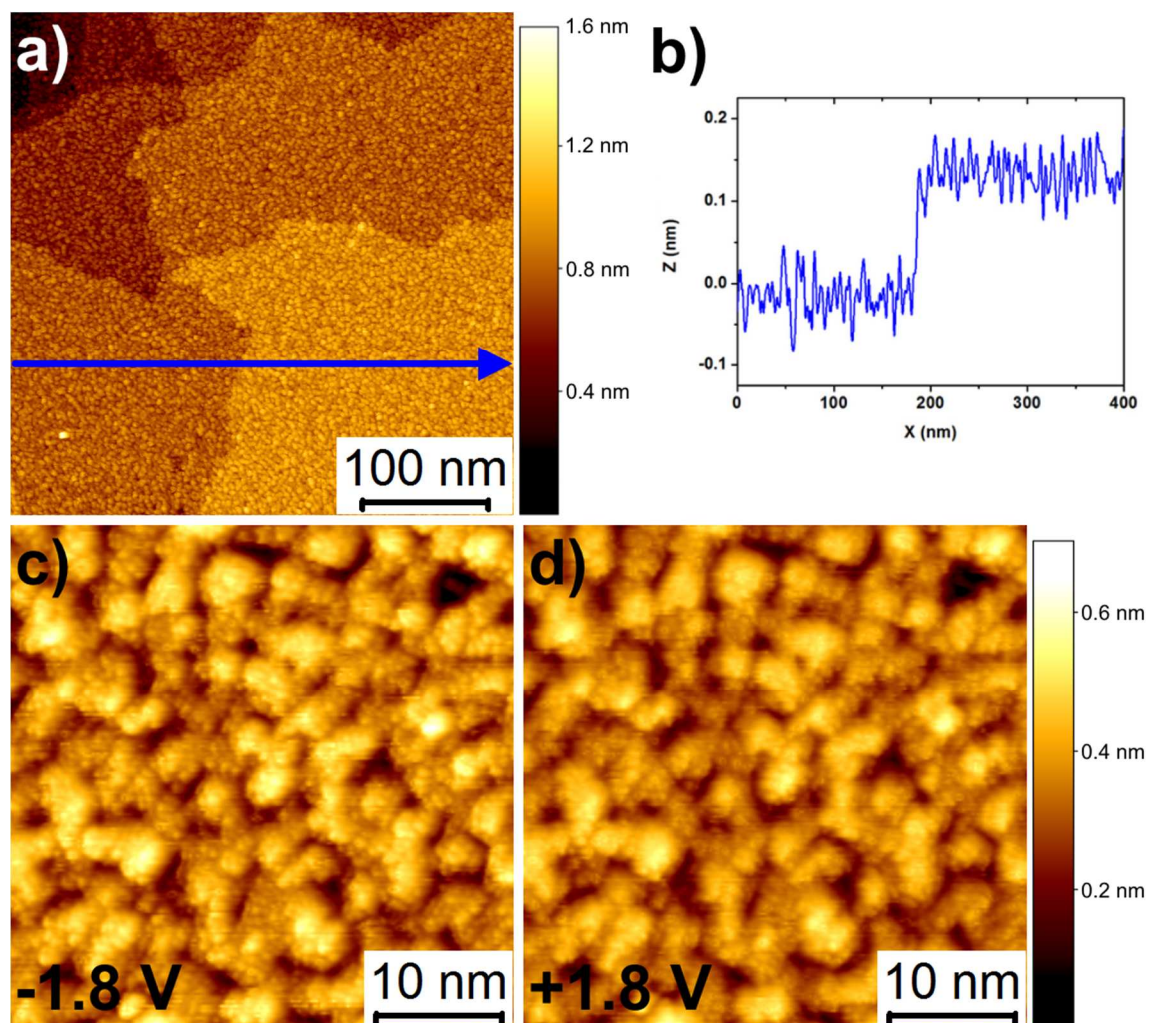


Figure 3.21 STM topographic images of sample surface after Ni deposition: a) 400 x 400 nm<sup>2</sup>,  $V_s = -2$  V,  $I = 80$  pA; b) an example of height profile along the marked blue line; c) and d) enlarged view on the sample surface which is coated with nanometer-sized metal clusters at two opposite polarities (40 x 40 nm<sup>2</sup>,  $I = 80$  pA,  $V_s = -1.8$  V and 1.8 V, respectively). All STM image sides aligned on the  $\langle 010 \rangle$  equivalent directions.

The RMSR of single terraces was estimated to be 0.09(1) nm and is only little bit higher than for clean Ge(001) surface. No difference between two opposite bias high resolution images also proves the metallic character of the observed nanoclusters. These observations lead to the conclusion that evaporation of a few MLs of Ni on the Ge(001) substrate at RT results in a Volmer-Weber growth mode.

This conclusion about a VW growth mode is also confirmed by the results derived from the LEED study. Figure 3.22 depicts an example of the LEED images recorded directly before (clean Ge (001)) and right after the deposition of about 1 nm of Ni at RT, carried out on the same sample and at the same electron beam energy (120 eV). LEED clearly demonstrates that on clean Ge(001) surface, the Ge(001)-p(2 x 1) type of reconstruction occupies the widest surface area. After Ni deposition the signal to noise ratio has changed, however the weak spots, which correspond to Ge(100)-p(2 x 1) surface reconstruction from Ni-free surface regions, are preserved. These observations are in line a) with the conclusion based on STM study that evaporation of few ML of Ni on the Ge(001) substrate at RT results in a VW growth mode and b) that limited STM resolution fails to resolve the (2 x 1) reconstruction of clean Ge between the high density Ni metal clusters.

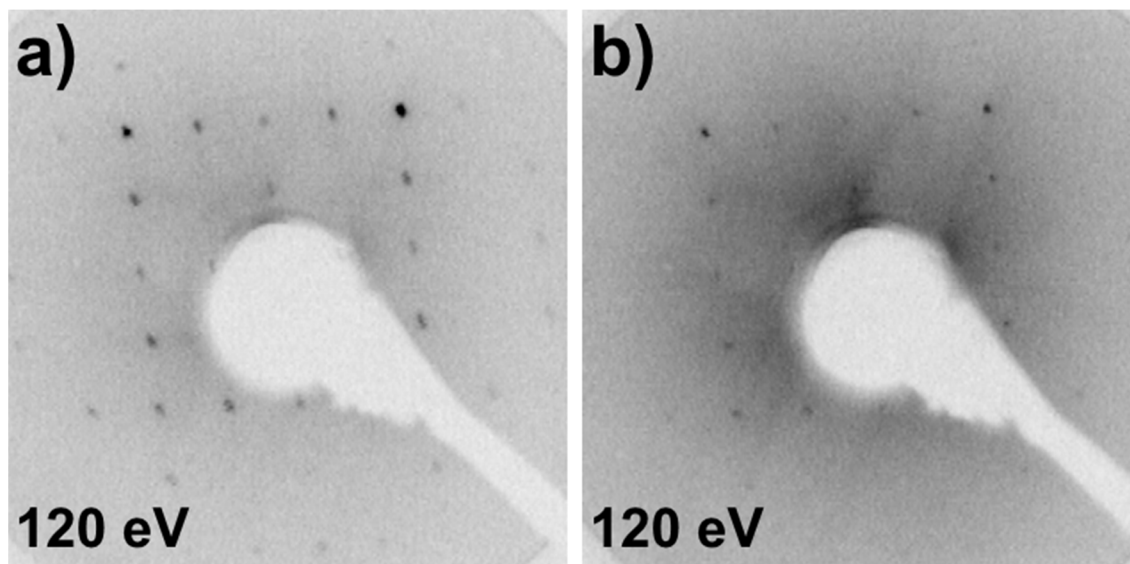


Figure 3.22 LEED images taken at 120 eV for: a) clean Ge(001) surface, and b) sample after deposition of about 1 nm Ni at RT.

Annealing the sample at 100 °C for 1 hour caused significant changes of the surface morphology (Figure 3.23). The sample surface still manifests a terrace morphology with an average step height of 0.17(4) nm, compatible with the Ge(001) step edges height. However, metallic nanoclusters are no longer visible. During the annealing treatment, Ni clusters coalesce to form an inhomogeneous  $\text{Ni}_x\text{Ge}_y$  layer. On each single terrace, the presence of a large number of small (by means of occupied area,  $10(4) \text{ nm}^2$ ), but relatively deep (0.20(6) nm) voids is observed. These voids occupy about 15(1)% of the total surface area of the terraces. The RMSR value measured on top of  $\text{Ni}_x\text{Ge}_y$  layer on the single terrace (voids are not included) did not change and still equals  $\sim 0.09(1) \text{ nm}$ .

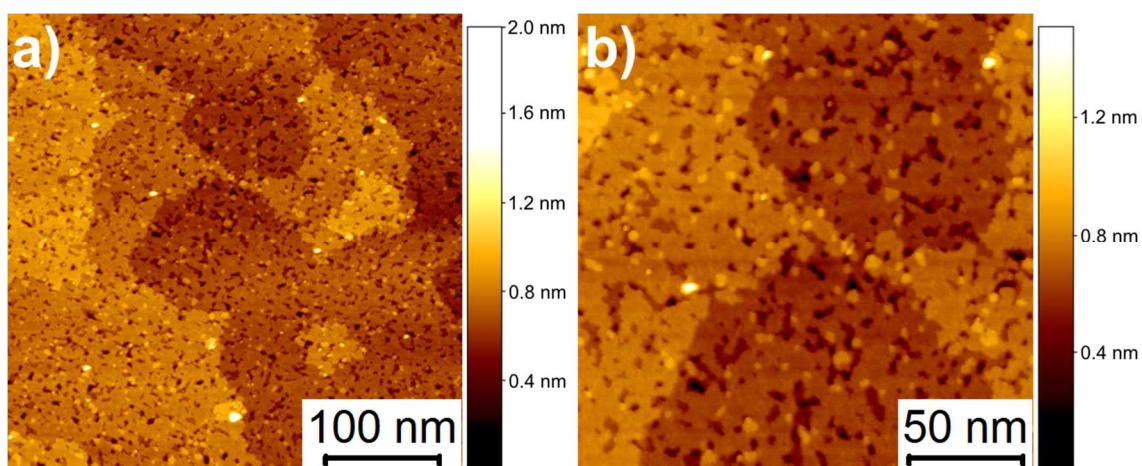


Figure 3.23 Sample surface after annealing at 100 °C: a)  $400 \times 400 \text{ nm}^2$ ,  $V_s = -2 \text{ V}$ ,  $I = 120 \text{ pA}$ ; b)  $200 \times 200 \text{ nm}^2$ ,  $V_s = -1.8 \text{ V}$ ,  $I = 80 \text{ pA}$ . All image sides aligned on the  $\langle 010 \rangle$  equivalent directions.

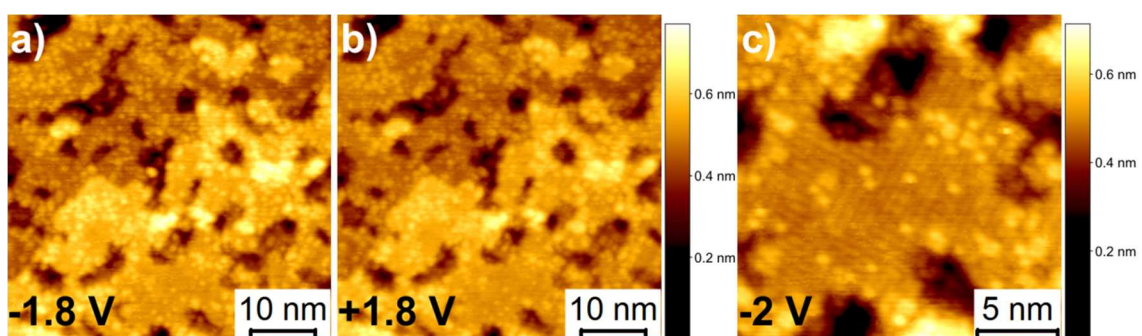


Figure 3.24 STM topographic images of sample surface after annealing at 100 °C: a) and b)  $50 \times 50 \text{ nm}^2$ ,  $I = 80 \text{ pA}$ ,  $V_s = -1.8 \text{ V}$  and  $1.8 \text{ V}$ , respectively; c) sporadic manifestations of top layer periodicity,  $15 \times 15 \text{ nm}^2$ ,  $V_s = -2 \text{ V}$ ,  $I = 80 \text{ pA}$ . All image sides aligned on the  $\langle 010 \rangle$  equivalent directions.

A close inspection of the STM images shows that imaging in different values of bias voltage did not present significant differences, which could suggest the Ni-rich character of the inhomogeneous top-layer (Figure 3.24 a) and b)). In addition, the top layer is not reconstructed for the most of the analyzed areas. However, for a very small number of images and for small scanning areas it can be seen that the top-layer begins to exhibit some signs of periodicity. It is manifested by the presence of periodic rows, which are preferentially running along two orthogonal  $[110]$ ;  $[-110]$  Ge surface directions. The average interval between periodic rows is on the scale of around  $0.65(3)$  nm (Figure 3.24 c)).

These results suggest that the Ni atoms from the metallic Ni VW clusters start to interact first with the Ge atoms – probably in kink positions - of the top Ge terrace layers. Basically, it can be concluded that annealing at  $100$  °C causes first the formation of a continuous  $\text{Ni}_x\text{Ge}_y$  wetting layer and then initiates the de-wetting process, characterized by the appearance of voids on the  $\text{Ni}_x\text{Ge}_y$  terraces, as well as initiating simultaneous surface ordering processes. A more detailed description of the observed periodic structures is still under investigation. In short summary, presented observations are consistent with earlier non STM-based studies, e.g. Nemouchi *et al.*, where Ni germanide formation was reported to occur at a similarly relatively low temperatures range [244].

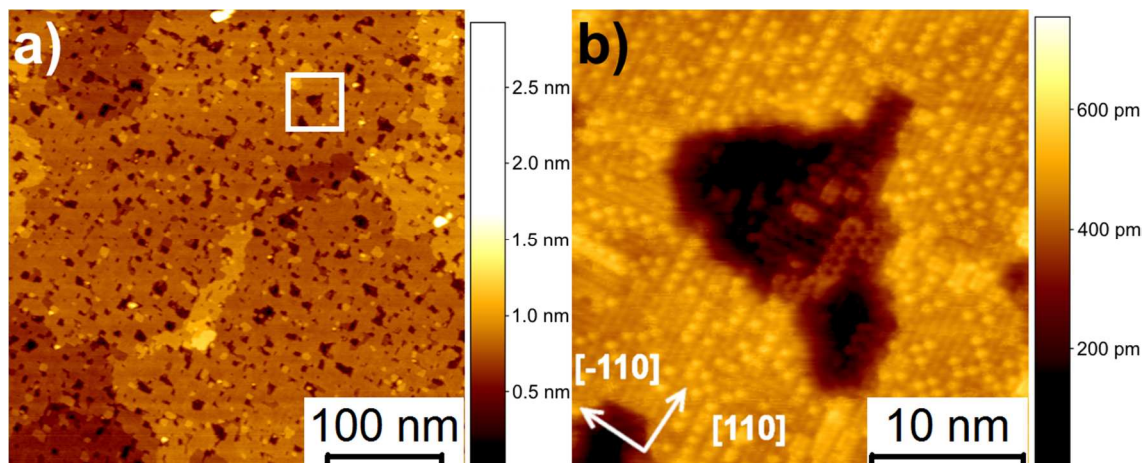


Figure 3.25 STM topographic images of sample surface after annealing at  $200$  °C: a)  $400 \times 400$  nm<sup>2</sup>,  $V_s = -2$  V,  $I = 80$  pA; b) magnified image of the area marked with a white square,  $30 \times 30$  nm<sup>2</sup>,  $V_s = -2$  V,  $I = 80$  pA.

Subsequent sample annealing at 200 °C for 1 hour leads to further changes in surface morphology through the enhancing of de-wetting and surface ordering processes (Figure 3.25). The terraced character of surface morphology was retained. The step edge height is given by 0.15(2) nm. An increase in average surface area of a single void and the percentage void area coverage relative to single terrace was observed. These values increase to 38(6) nm<sup>2</sup> and 21(4)%, respectively. Furthermore the terrace RMSR value also increased and reached the value of 0.14(6) nm. As shown in Figure 3.25 b) in some voids, regions with the characteristic Ge buckled dimer structure are observed again. This observation clearly points to the retransformation of areas of the surface to clean Ge(001), due to the onset of a de-wetting phenomenon.

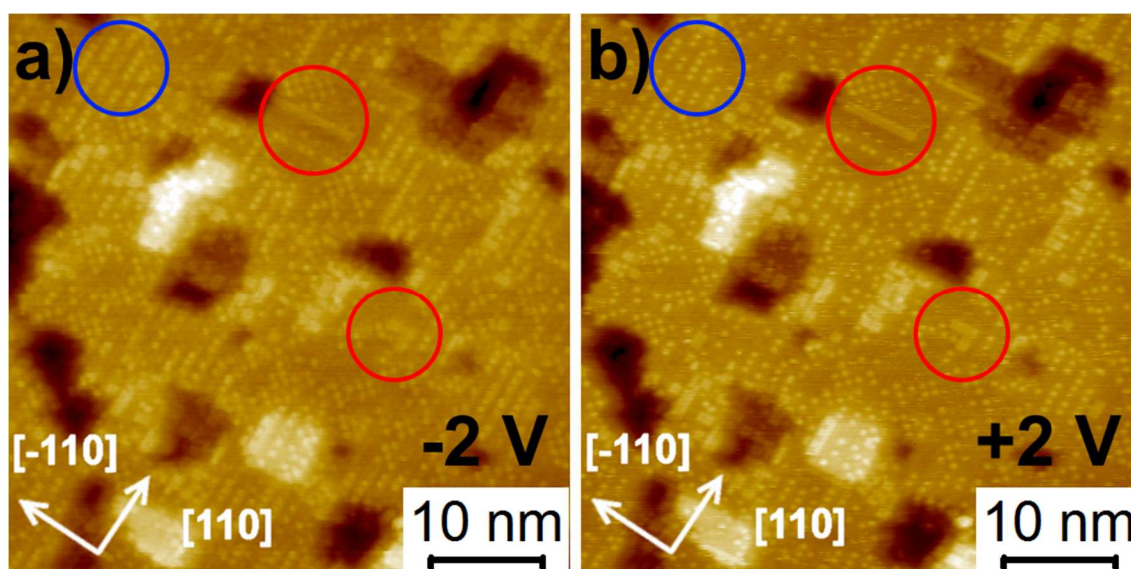


Figure 3.26 The complicated formation of ordered features at 200 °C observed on the top layer (50 x 50 nm<sup>2</sup>, I= 80 pA, Vs= -2 V and 2 V, respectively). The Z scale was modified in order to facilitate the observation of features on top layer. Colour circles present different types of top layer features (information in text).

Furthermore, in contrast to the previous annealing step, where only occasionally some origins of top layer arrangement were observed, here it is clearly visible that the top layer itself shows complex, ordered features (Figure 3.26). Except that the top layer itself is characterized by the presence of regular rows, an additional variation of structure types is also present e.g.: bright protrusions which are arranged in regular rows (blue circle) or single square unit blocks which can create bigger units by simple multiplication (red circle). Unfortunately, the detailed investigation of these ordered

structures is currently undergoing by means of further STM studies as well as theoretical calculations, and will not be discussed further in the framework of this dissertation. It should be also emphasized that most edges, whether voids edge or terrace edge, start to run along two orthogonal  $[110]$ ;  $[-110]$  Ge surface directions.

In conclusion, annealing at  $200\text{ }^{\circ}\text{C}$  points to the occurrence of a de-wetting behaviour of the  $\text{Ni}_x\text{Ge}_y$  layer (i.e. density of voids clearly increases) and, as will be discussed in the following, this process is strongly enhanced at higher annealing temperatures.

The derivative of STM images acquired after annealing the sample at higher temperatures, namely  $300\text{ }^{\circ}\text{C}$ ,  $400\text{ }^{\circ}\text{C}$  and  $500\text{ }^{\circ}\text{C}$  are displayed in Figure 3.27. It is clear that in comparison to the previous annealing steps, here a significant change in surface morphology occurred. The reconstructed, terraced type  $\text{Ni}_x\text{Ge}_y$  layer evolved into well ordered, three-dimensional nanostructures. In addition, as these three images have been prepared on the same scale, the thermal evolution of  $\text{Ni}_x\text{Ge}_y$  nanostructures can be immediately seen. A decrease of the density of the smallest nanoislands, and the increase of the size/volume of the larger ones was observed. This scenario most probably results from the Ostwald ripening phenomenon, driving the merging of smaller clusters thanks to their enhanced surface diffusion. However, before a further discussion about the thermal evolution of surface morphology, a short description of each this annealing treatment steps is given below.

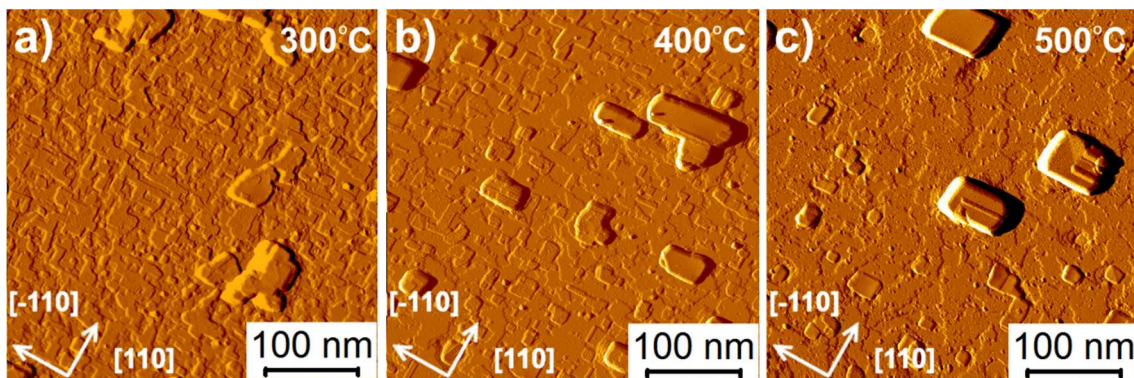


Figure 3.27 Scanning tunneling topographic derivative images of annealed samples at: a)  $300\text{ }^{\circ}\text{C}$  ( $400 \times 400\text{ nm}^2$ ,  $V_s = -2\text{ V}$ ,  $I = 80\text{ pA}$ ); b)  $400\text{ }^{\circ}\text{C}$  ( $400 \times 400\text{ nm}^2$ ,  $V_s = -2\text{ V}$ ,  $I = 80\text{ pA}$ ); and c)  $500\text{ }^{\circ}\text{C}$  ( $400 \times 400\text{ nm}^2$ ,  $V_s = -2\text{ V}$ ,  $I = 120\text{ pA}$ ).



Annealing at 300 °C for 1 hour leads to a significant change in surface morphology (Figure 3.28). The  $\text{Ni}_x\text{Ge}_y$  layer tends to agglomerate into well ordered, three-dimensional nanostructures. As clearly visible, the observed nanostructures feature in general a rather complex shape, but most of their side walls run along the two orthogonal  $[110]$ ;  $[-110]$  directions of the Ge(001) substrate. It is also very characteristic that the side walls of these nanostructures are very steep (e.g. see 3D image and/or height profile in Figure 3.28 a)). Profiles analysis of randomly chosen nanostructures and also facet analysis of entire images show that the average inclination angle of nanostructures side walls, with respect to the Ge(001) surface is only a few degrees (max.  $5^\circ$  to  $8^\circ$ ). The mean height of the nanostructures is  $h = 0.22(2)$  nm.

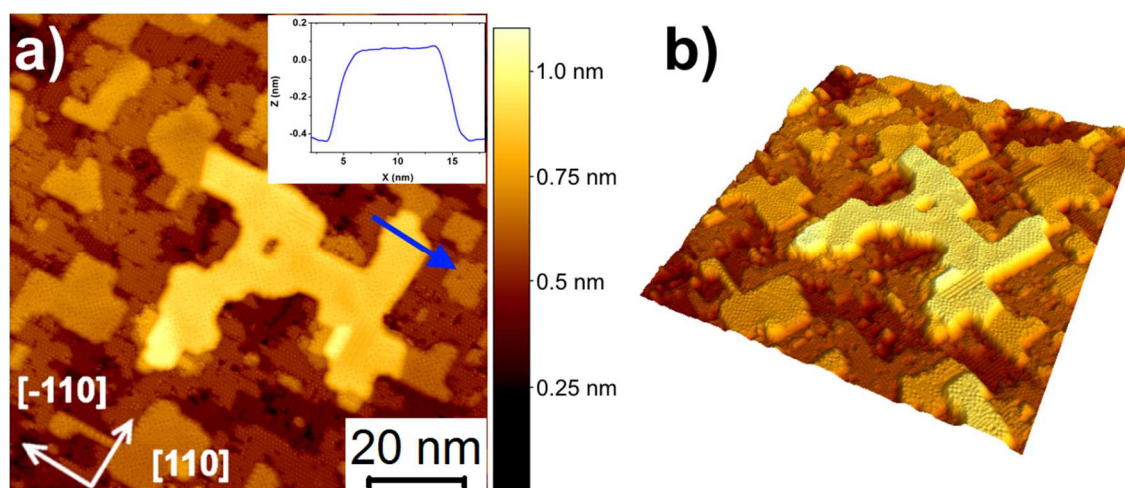


Figure 3.28 Sample surface after annealing at 300 °C: a) STM and Z profile obtained along blue lines as insets; and b) 3D rendering image ( $100 \times 100 \text{ nm}^2$ ,  $V_s = 2 \text{ V}$ ,  $I = 80 \text{ pA}$ ).

As a result of the agglomeration process of the  $\text{Ni}_x\text{Ge}_y$  layer, and consequently the formation of  $\text{Ni}_x\text{Ge}_y$  nanostructures, a reappearance of the underlying clean Ge(001) surface occurs (Figure 3.29 a)). In average, more than half of the scanned area was recognized as clean Ge(001) (variable from 45% to 65%, depending on the area selection). Again, both types of Ge(001) surface reconstruction,  $p(2 \times 1)$  and  $c(4 \times 2)$ , were observed, albeit the contribution of the latter is now much more relevant. In the light of this corrugated  $\text{Ni}_x\text{Ge}_y$  nanostructure morphology, this is to be expected as the  $c(4 \times 2)$  reconstruction is known to be stabilized by the presence of step edges when imaged at room temperature. An average distance between  $p(2 \times 1)$  type dimer rows

was measured to be 0.82(2) nm (e.g. blue Z-profile in Figure 3.29 a)). Finally, flat top surfaces of the nanostructures are observed with some locally ordered surface arrangements. Figure 3.29 b) depicts that the top surface of the nanostructure presents an ordered character in the form of perpendicular rows. The spacing between neighbouring rows is 0.66(3) nm.

In short summary, it seems that annealing at 300 °C is the starting temperature above which the agglomeration process of  $\text{Ni}_x\text{Ge}_y$  layer allows the formation of well-ordered nanostructures. Since this step, the co-existence of  $\text{Ni}_x\text{Ge}_y$  nanostructures and clean Ge(001) surface areas are easily recognizable. In presented STM results, this de-wetting phenomenon is clearly visible. However, it is noted that the same de-wetting phenomenon is possible to investigate by other technique. For example, Huang *et al.* observed similar results by SEM measurements on continuous  $\text{Ni}_x\text{Ge}_y$  layers annealed at similar temperature: these authors attributed the origin of the de-wetting to the higher  $\text{Ni}_x\text{Ge}_y$  interface/surface energy as compared to the reconstructed Ge(001) surface energy [247].

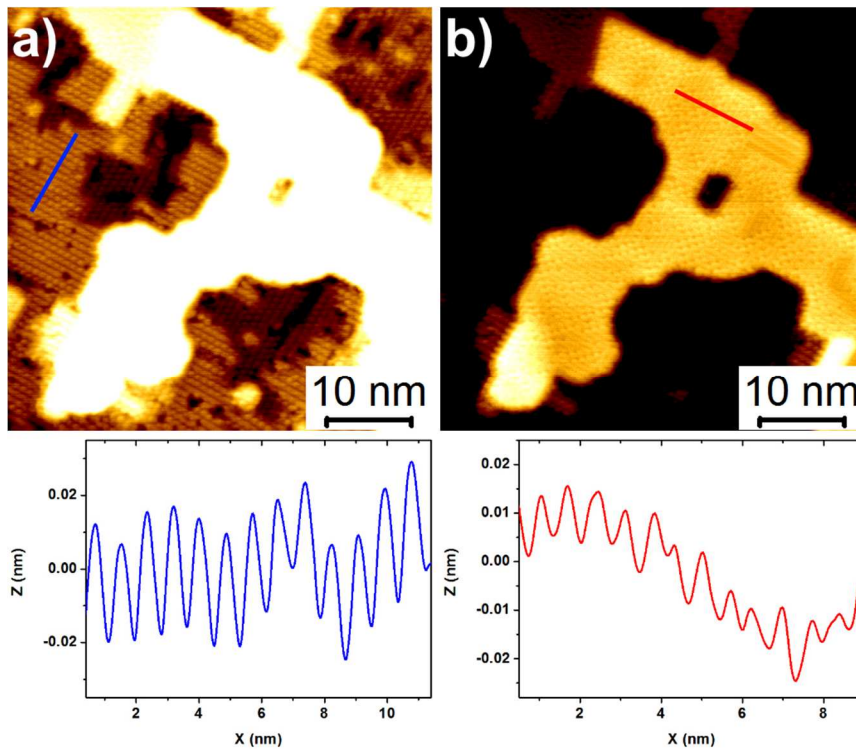


Figure 3.29 Detailed analysis of  $\text{Ni}_x\text{Ge}_y$  nanostructure and its close neighbourhood: a) underlying Ge(001) surface, and b) surface arrangements on the top surfaces of the nanostructures. Below STM images appropriate Z-profiles are shown. The colour scale in STM images has been artificially matched to show the discussed structures ( $50 \times 50 \text{ nm}^2$ ,  $V_s = -2 \text{ V}$ ,  $I = 80 \text{ pA}$ ).

STM images obtained after further annealing at 400 °C for 1 hour are presented in Figure 3.30. This annealing step results in a further evolution of the surface morphology. A slight increase of the nanostructure area and height is observed, most probably as a result of the ongoing Ostwald ripening phenomenon, driving the merging of smaller clusters thanks to their enhanced surface diffusion. The average height of nanostructures increased to  $h = 1.1(2)$  nm. It can be seen that the largest nanostructures are found to have a more regular shape of mostly square and rectangular form.

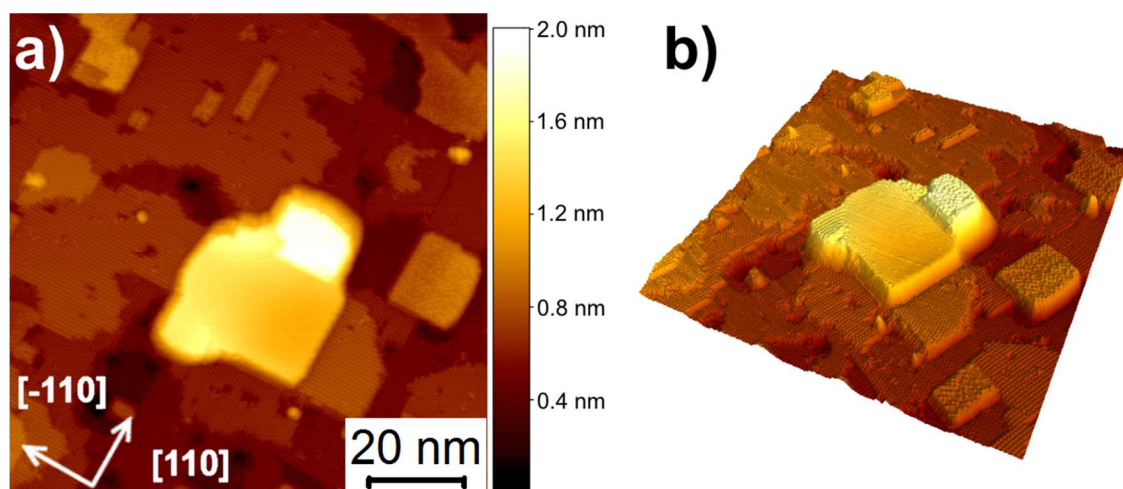


Figure 3.30 Sample surface after annealing at 400 °C: a) STM and b) 3D rendering image ( $100 \times 100 \text{ nm}^2$ ,  $V_s = -2 \text{ V}$ ,  $I = 160 \text{ pA}$ ).

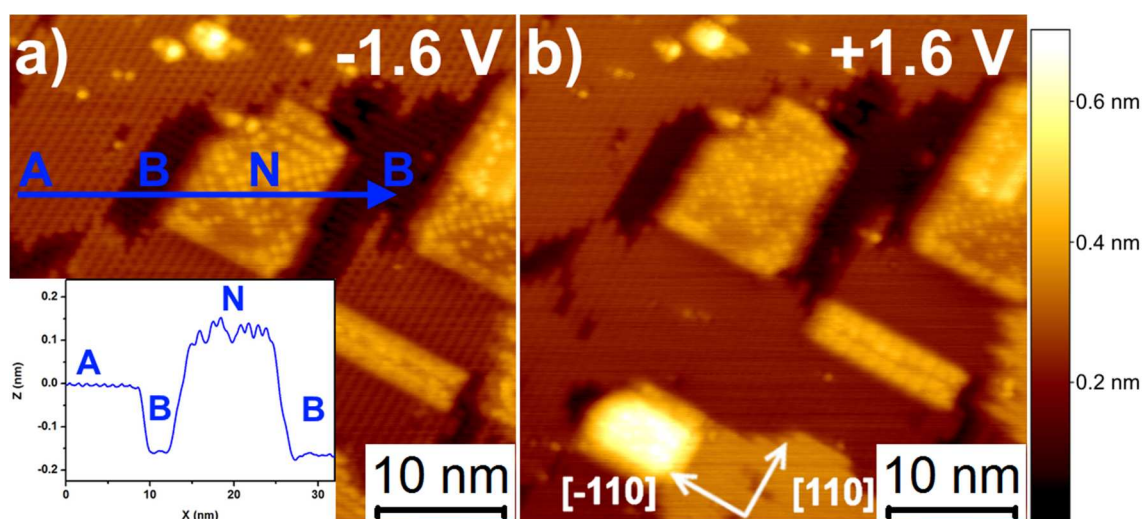


Figure 3.31 Sample surface after annealing at 400 °C. Here attention is focused on smaller nanostructures – see text ( $40 \times 40 \text{ nm}^2$ ,  $I = 80 \text{ pA}$ ,  $V_s = -1.6 \text{ V}$  and  $1.6 \text{ V}$ , respectively).

In average, almost three fourth of scanned area was identified as pure Ge(001) surface (variable from 70% to 85%, depending on the area selection). The Ge(001)-c(4 x 2) type of surface reconstruction was visible more frequently. It is also important to note that, besides the large  $\text{Ni}_x\text{Ge}_y$  nanostructure, other much smaller structures (in means of height) were frequently visible. They were located quite often in local troughs, and what is also important their height was only slightly higher than surrounded clean Ge terraces. As shown in the inset in Figure 3.31 a), the height profile goes along terrace A, lower terrace B, then through nanostructure N and returns back to the terrace B level. The height difference between nanostructure top surface N and terrace A is around (100-120) pm. In addition, the nanostructures' top surface reconstruction reminds the arrangement of the  $\text{Ni}_x\text{Ge}_y$  top layer for the sample after annealing at 200 °C.

Finally, the tendency of  $\text{Ni}_x\text{Ge}_y$  nanostructures to adopt more regular - rectangular and square - shape as well as the increase in nanostructures height is even more pronounced after annealing at 500 °C for 1 hour. Here, a clear increase in average height, area, and volume of the rectangular nanostructures was observed, with the average height increasing from  $h= 1.1(2)$  nm (400 °C) to  $h= 1.7(3)$  nm (500 °C).

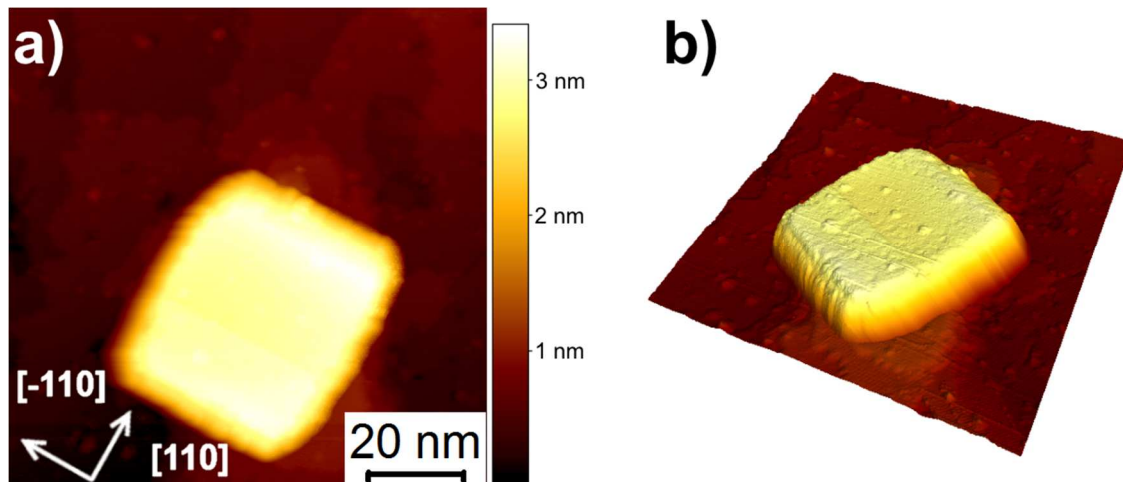


Figure 3.32 Sample surface after annealing at 500 °C: a) STM and b) 3D rendering image ( $100 \times 100 \text{ nm}^2$ ,  $V_s = -2 \text{ V}$ ,  $I = 70 \text{ pA}$ ).

And similarly as in the previous step, the tendency that many of the smaller nanostructures started to be positioned in local troughs, surrounded by clean Ge terraces

placed higher than the nanostructure itself was observed (nanostructures marked by green circles in Figure 3.33). The height profile illustrated in Figure 3.33 c) clearly shows that the nearest neighbour Ge terrace (B) corresponds to the top surface of nanostructure (N). And correspondingly, next Ge terrace (A) is located around 0.14 nm higher than terrace B and nanostructure. These STM findings clearly give an indication that nanostructures grow not only as 3D structures outwards the surface but also inwards, accompanied by a strong Ni diffusion into the Ge(001) substrate, as confirmed by (S)TEM-EDX study (see next subchapter).

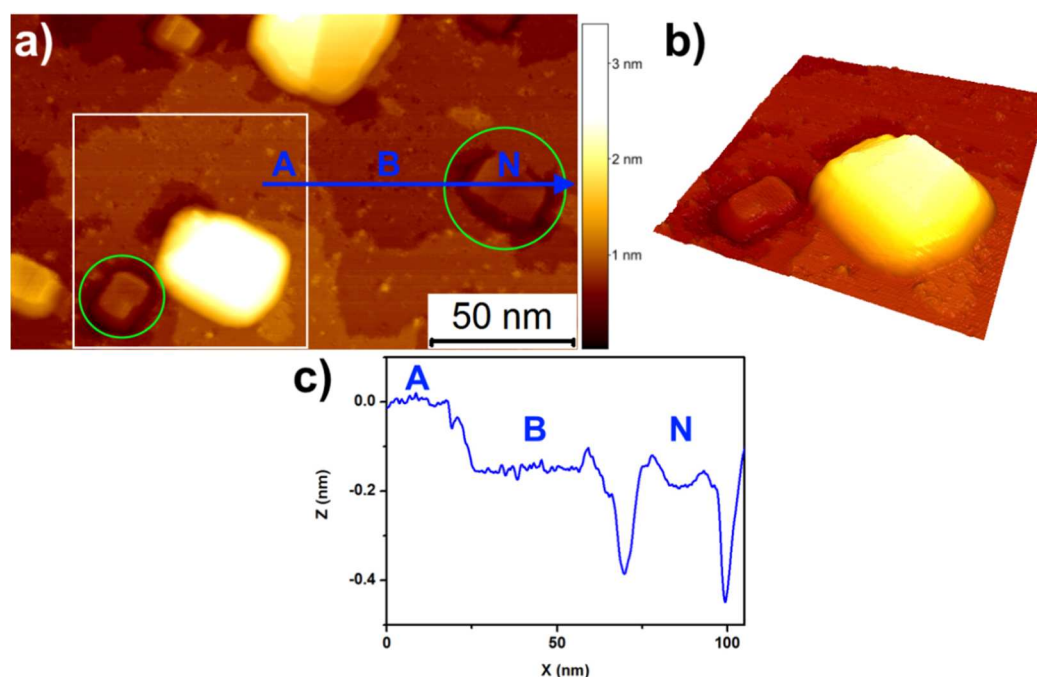


Figure 3.33 Sample surface after annealing at 500 °C: a) STM ( $200 \times 120 \text{ nm}^2$ ,  $V_s = -2 \text{ V}$ ,  $I = 120 \text{ pA}$ ); and b) 3D rendering image of area marked by white square ( $85 \times 85 \text{ nm}^2$ ); c) height profile along blue line. Green circles present nanostructures which are dug in the top surface layers– see text.

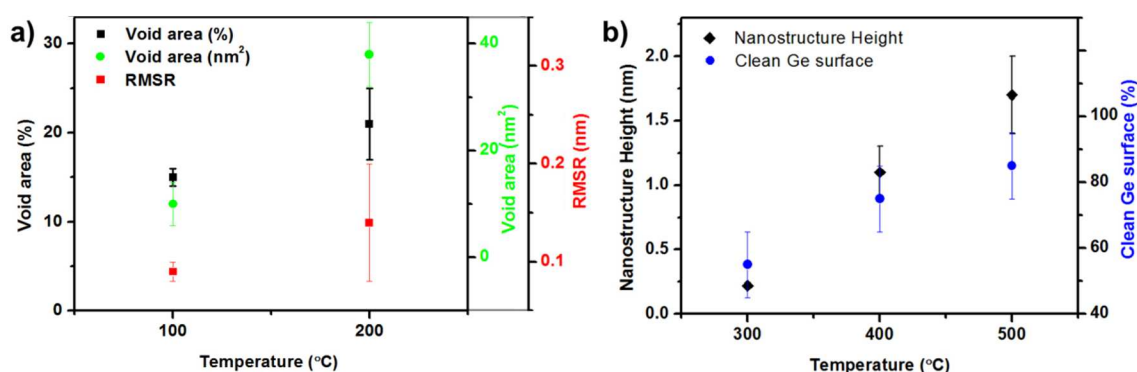


Figure 3.34 Quantitative analysis: a) parameters which describe the de-wetting  $\text{Ni}_x\text{Ge}_y$  layer below 300 °C; b) parameters which describe the  $\text{Ni}_x\text{Ge}_y$  nanostructures in the range of 300 °C-500 °C.

In conclusion, STM results clearly show the surface morphology evolution from 3D VW metallic clusters after RT deposition, through the creation of wetting  $\text{Ni}_x\text{Ge}_y$  top layer at 100 °C and finally creation of  $\text{Ni}_x\text{Ge}_y$  top nanostructures as a result of dewetting at 300 °C. In addition, the evolution of  $\text{Ni}_x\text{Ge}_y$  nanostructures due to Ostwald ripening was shown in the range from 300 °C to 500 °C. To summarize this chapter, Figure 3.34 gives a quantitative analysis: part a) presents the most important parameters, which are describing the  $\text{Ni}_x\text{Ge}_y$  top layer, while part b) is focused on the evolution of  $\text{Ni}_x\text{Ge}_y$  nanostructures.

### **(S)TEM-EDX study**

In order to monitor the reaction between Ni and Ge, as well as to report clear evidence for the formation of Ni germanide nanostructures, additional *ex-situ* measurements were performed. This sub-chapter briefly presents main results obtained by the (S)TEM-EDX technique.

Figure 3.35 shows the *ex-situ* HR-TEM measurements of three samples: a) “as-deposited” at RT, b) annealed at 300 °C, and c) at 500 °C. After metal deposition at RT a very thin continuous Ni layer on top of Ge substrate is clearly noticeable. The approximate thickness of the deposited metal layer is about 1 nm (Figure 3.35 a)). Please note that observation of a continuous Ni layer is not in contradiction to the Volmer-Weber growth behaviour reported earlier based on STM-LEED study. It is the result from the projection of the HR-TEM study along the surface. Annealing at 300 °C for 1 hour leads to significant changes of the sample structure. The continuity of the Ni layer was broken. It is clearly visible that at random locations on the surface, deposited Ni material starts to agglomerate and diffuse into the bulk Ge substrate, which is demonstrated and discussed in detail in the next paragraph about the EDX study (Figure 3.35 b)). Finally, annealing at 500 °C for 1 hour results in a strong enhancement of the interface reaction between these Ni aggregation centers and the underlying Ge substrate and leads to the formation of well-ordered, faceted  $\text{Ni}_x\text{Ge}_y$  nanostructures (Figure 3.35 c)). As clearly shown in the figure, the interfaces between the  $\text{Ni}_x\text{Ge}_y$  nanostructures and the surrounding Ge(001) substrate is very sharp and is also

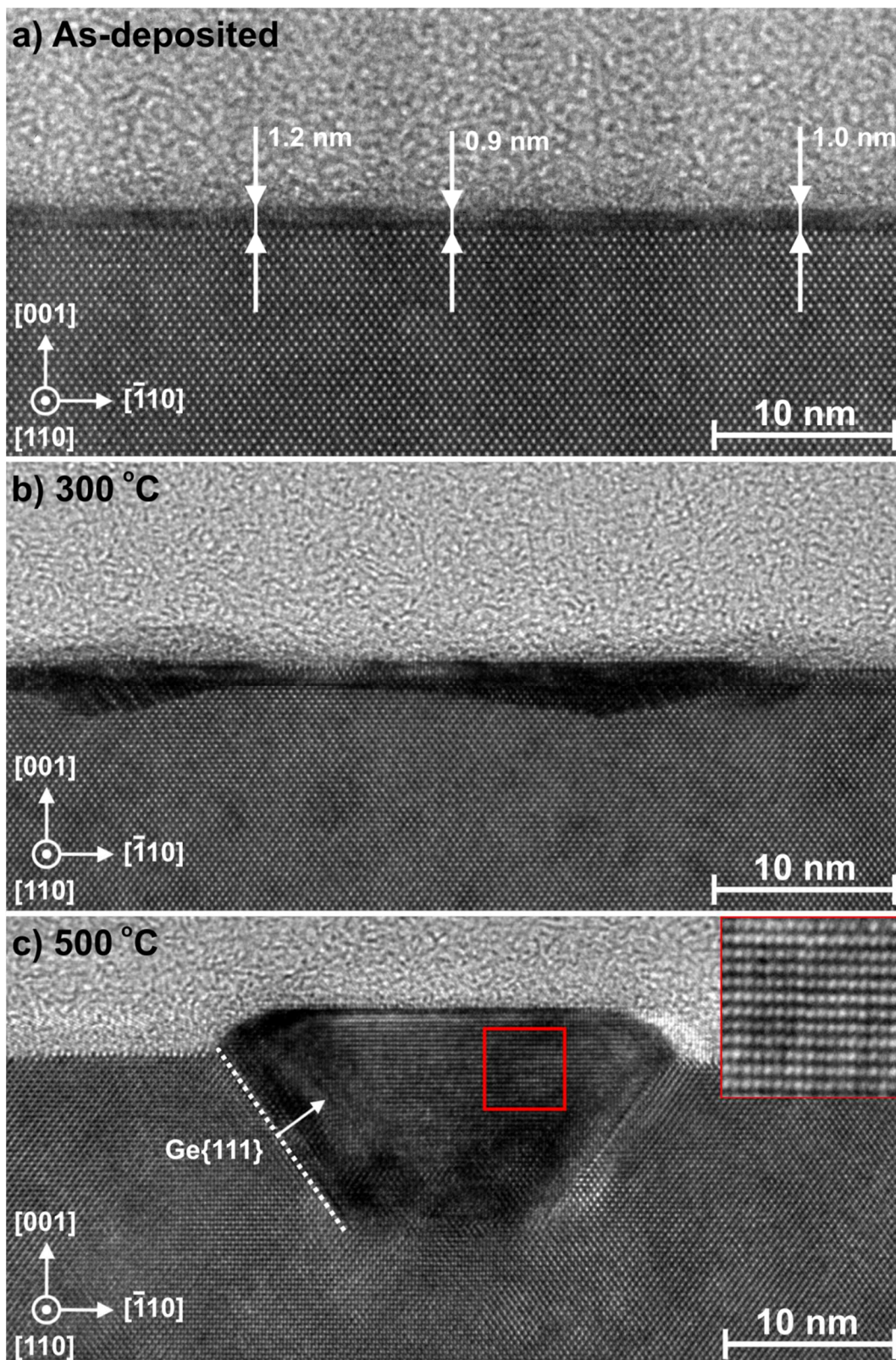


Figure 3.35 HR-TEM measurements on Ni/Ge(001) samples for: a) “as-deposited” sample; b) sample after annealing at 300 °C; and c) sample after annealing at 500 °C.

characterized by facets having an inclination of  $\sim 54.6(6)^\circ$  with respect to the Ge(001) surface, corresponding to equivalent Ge{111} facets.

In addition, a detailed analysis presented in the inset in Figure 3.36 c) shows that the  $\text{Ni}_x\text{Ge}_y$  nanostructure is composed of crystalline planes which are parallel to the Ge(001) surface. The distance between these planes is 0.27(2) nm, a value close to lattice spacing of the orthorhombic NiGe phase in the [101] direction (0.29 nm) [248]. At this point, it should be noted that all previous studies, focused on thin layer Ni-Ge system (known to the author of this dissertation) show that only the NiGe phase can occur and is stable in the temperature range around 500 °C (e.g. [211]). In addition, recently Niranjana *et al.*, based on theoretical calculations, namely density-functional theory for various surface terminations, showed that for the NiGe orthorhombic structure, the NiGe(101) surface presents the lowest surface energy [238]. Literature and presented experimental findings thus strongly suggest that the observed nanostructures present the NiGe phase, with a NiGe(101); (010) || Ge(001); (110) epitaxial relationship towards the Ge(001) substrate.

The panel of images presented on Figure 3.36 presents the (S)TEM-EDX measurements performed on these same samples, namely: a) “as-deposited” at RT, b) annealed at 300 °C, and c) annealed at 500 °C. The left side part of Figure 3.36 presents the (S)TEM bright field images of the investigated area, and the middle and right side of panel present the EDX measurements, which are focused on the presence of Ge and Ni, respectively. After deposition at RT, an about 1 nm-thick continuous layer of Ni on top of the Ge substrate is clearly visible (Figure 3.36 a)). Please note that EDX measurements show also some low content of Ni below the surface (deeper than 1 nm). However, this might be an artefact due to slight heating and polishing during TEM lamella preparation. The annealing step at 300 °C for 1 hour leads to a disruption of the continuous Ni film (Figure 3.36 b)). Agglomeration of Ni at randomly located places and its diffusion into the bulk Ge substrate is clearly visible. In light of the previously discussed STM results, we suggest that these Ni aggregation centers can be attributed to the formation of a  $\text{Ni}_x\text{Ge}_y$  phase. Finally, last annealing at 500 °C results in the formation of faceted NiGe nanostructures. The accompanying EDX analysis clearly reveals that these nanostructures undoubtedly consist of a Ni germanide phase. The Ni



signal was observed only within the nanostructures. Outside the nanostructures the signal from Ge substrate was only observed. These findings are consistent with the dewetting behaviour suggested on the basis of the STM study discussed earlier. It is well known that Ni diffuses strongly in chemical reactions with Si and with Ge [209] [244]. Therefore, the strong Ni diffusion into bulk Ge is the driving force for the formation of NiGe nanostructures. This is in contrast to previously presented study on Co-Ge system, where Ge diffusion was established as major driving force to enable Co germanide formation in this same temperature range.

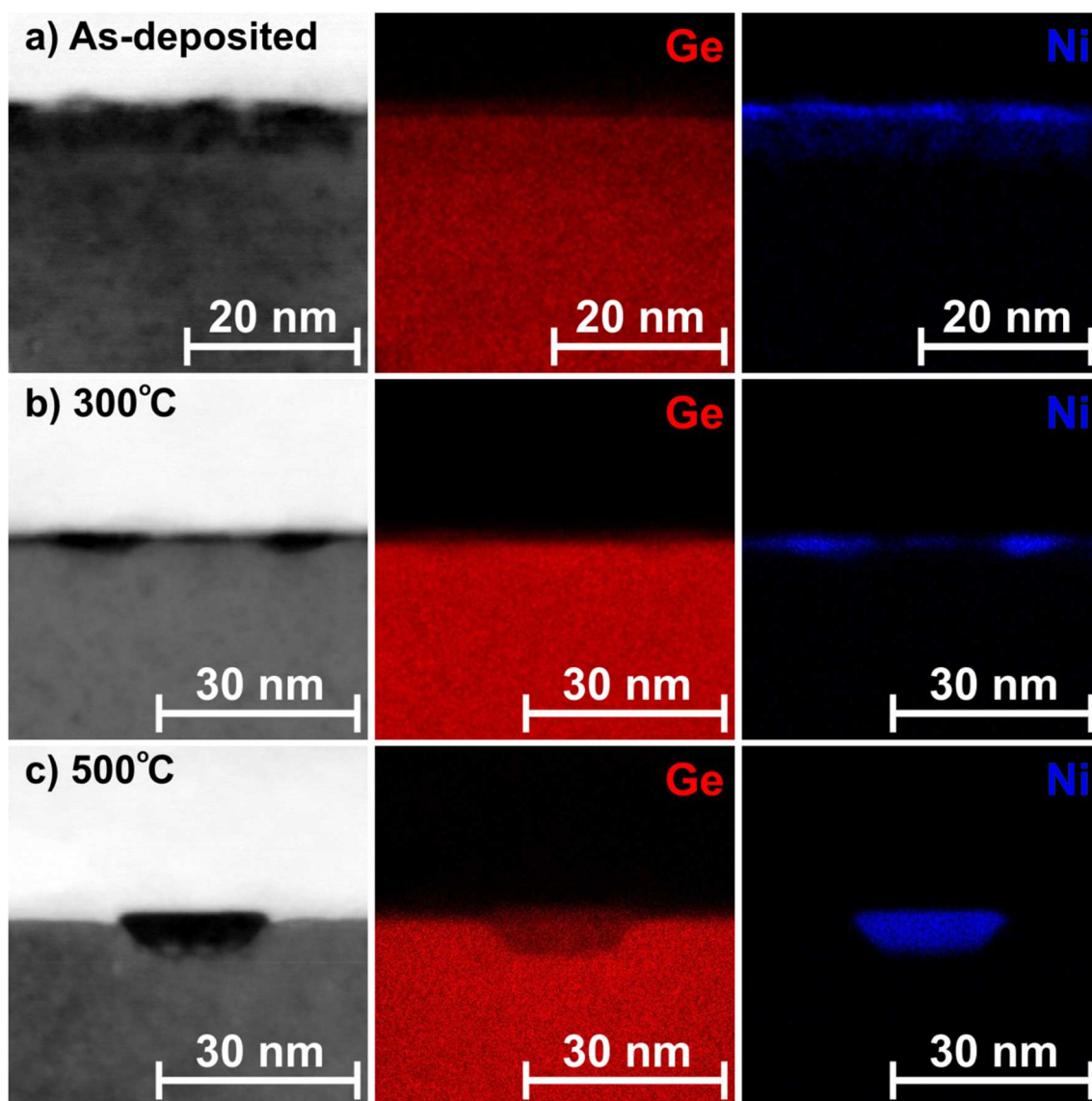


Figure 3.36 (S)TEM-EDX measurements on Ni/Ge(001) samples. Scanning mode TEM images with corresponding EDX analysis for: a) “as-deposited” sample, b) sample after annealing at 300 °C, and c) sample after annealing at 500 °C.

In summary, the (S)TEM-EDX study corroborates the STM-LEED results and brings evidence for the formation of orthorhombic Ni germanide nanostructures characterized by a faceted growth inward the Ge substrate.

### XPS study

This section contains the results based on *ex-situ* XPS measurements. Basically, the temperature dependent XPS studies were intended to shed more light into structural, morphological, and compositional aspects of Ni germanide nanostructure formation on Ge(001).

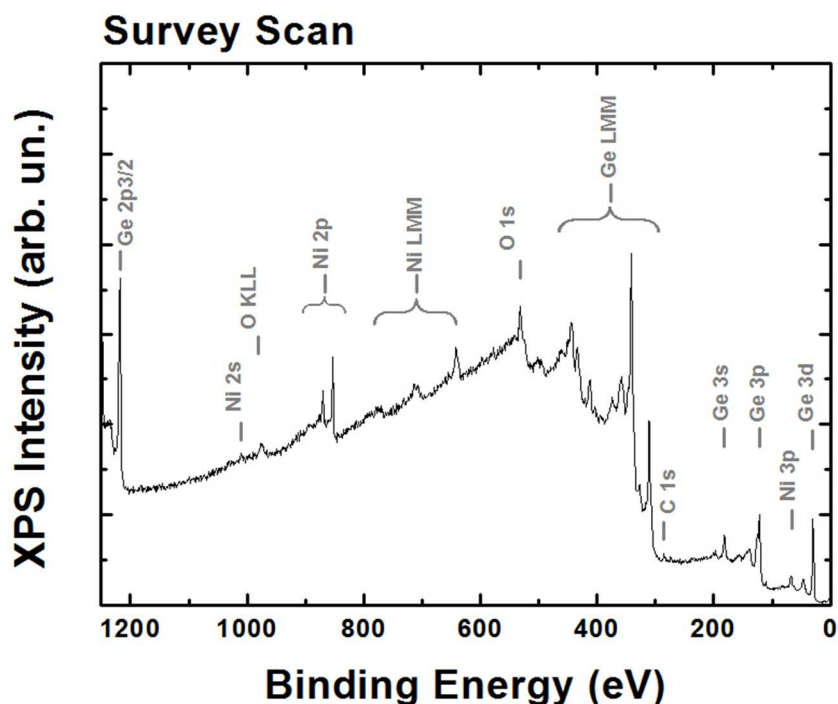


Figure 3.37 An example of survey scan taken for 1 nm thick Ni/Ge(001) sample right after transfer from STM UHV system to XPS UHV system.

The samples for the XPS study were prepared nominally identical to that discussed so far. The same amount of Ni was deposited at RT on clean Ge(001) substrate in the STM UHV system. After metal deposition, the sample was immediately *ex-situ* transferred to the XPS UHV system. To check the quality and thickness of the deposited Ni layer, a survey scan and angle-dependent XPS spectra were recorded. The survey scan is shown in Figure 3.37. It is obvious that, as a result of the vacuum break during the transfer of the samples between the two UHV systems, a thin adsorbate film will

cover the sample surface. Therefore, signals coming from oxygen and carbon can be seen in the survey scan. Despite these peaks, the survey spectra indicate a sufficient quality of the deposited layer to perform the T-dependent XPS study on the Ni/Ge system. In addition, an angle-dependent XPS measurement confirmed that a layer of  $\sim 1$  nm Ni was deposited on the Ge surface (data not shown).

To complement presented study by additional structural and chemical information, a temperature dependent XPS study was performed. Figure 3.38 presents the evolution of Ni  $2p_{3/2}$ , Ge  $2p_{3/2}$ , and Ge 3d XPS spectra measured for the as-deposited case (RT) and after each 1 hour long annealing step in the 100 °C to 500 °C range. It is clearly visible that both Ge peaks (Ge  $2p_{3/2}$  and Ge 3d) feature an intensity increase as a function of annealing (illustrated schematically by arrows in Figure 3.38 a) and b)). Besides the desorption of Ge native oxide, formed during the transfer from the deposition chamber to the XPS tool, this behaviour can be attribute to the evolution of the  $Ni_xGe_y$  surface layer morphology going from an initial 3D metal cluster layer over a 2D wetting layer towards 3D nanostructure islands, with major uncovered clean Ge(001) surface areas, as the annealing temperature is increased. Please note that initial transformation from metallic 3D VW clusters to 2D wetting layer is not seen by Ge  $2p_{3/2}$  and Ge 3d XPS peaks binding energy evolution (a slight decrease should be expected). This effect probably was related to the native oxide influence (GeO, GeO<sub>2</sub>). This explanation is in line with previously discussed STM studies, where the de-wetting process is manifested in the increase in size and number of voids in the top layer and the final formation of 3D nanostructures. Therefore, the de-wetting process results in the higher surface of the exposed clean Ge area and, consequently, in the increase of the corresponding XPS signal. Please also keep in mind that Ge  $2p_{3/2}$  core level is characterized by a much shorter electron escape depth ( $\lambda \sim 0.5$  nm) as compared to the Ge3d level ( $\lambda \sim 2.4$  nm) and it is thus more surface-sensitive [249]. Consequently, a significant increase of the Ge  $2p_{3/2}$  peak as a function of annealing temperature compared to the only moderate increase of the Ge 3d peak is also understandable and in line with the given scenario. Interestingly, a significant increase of the Ge  $2p_{3/2}$  peak for annealing at 400 °C clearly shows that the presence of Ni strongly enhances the Ge surface cleaning process.

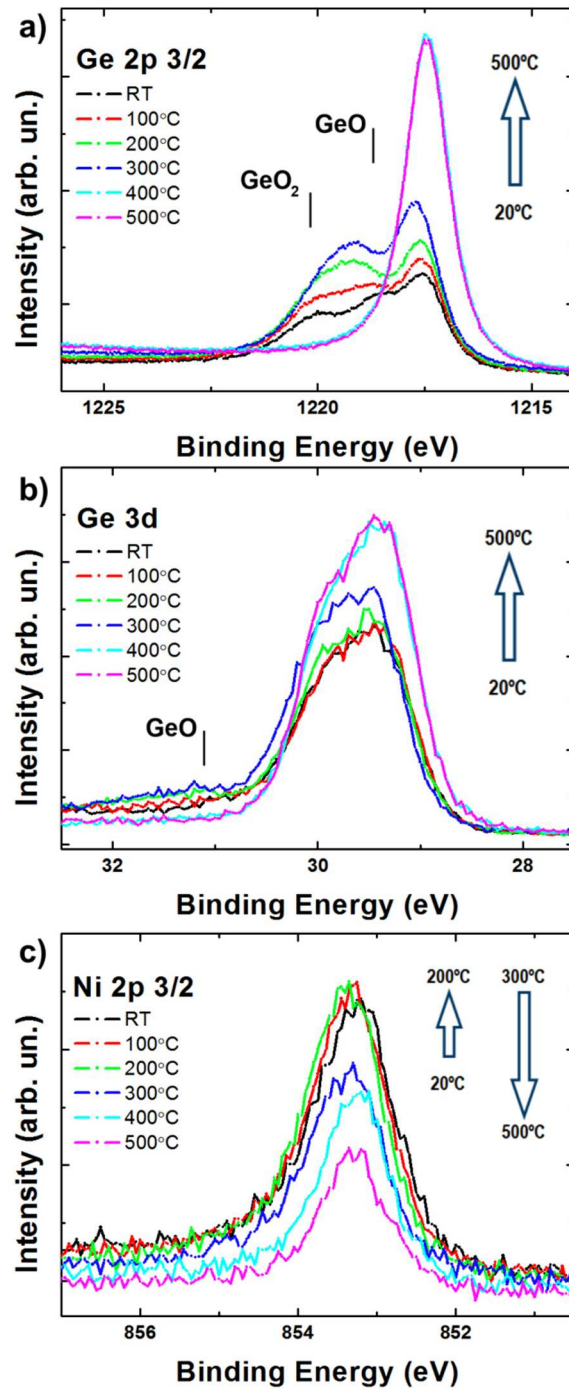


Figure 3.38 Ge  $2p_{3/2}$ , Ge 3d and Ni  $2p_{3/2}$  core spectra of a Ni/Ge sample recorded after RT deposition of 1 nm of Ni and subsequent annealing at different temperatures (see legend on top). The arrows schematically indicate changes in the intensity of the peaks. Data were not normalized.

Again, changes in the surface morphology from a 2D layer towards 3D islands are supported by the spectral analysis of the Ni 2p<sub>3/2</sub> core level (Figure 3.38 c)). The first two annealing steps cause a slight increase in Ni 2p<sub>3/2</sub> peak intensity which is in line with a higher exposed Ni surface area when the system evolves from isolated metallic VW islands to a complete 2D, terraced wetting layer morphology. This dependency is changing completely for annealing treatment above 300 °C. In this case, a significant decrease in the Ni 2p<sub>3/2</sub> peak intensity is observed. Such a behaviour can be explained by the combination of two effects: i) Ni diffusion into the Ge substrate and ii) Ostwald ripening of Ni<sub>x</sub>Ge<sub>y</sub> nanostructures towards bigger clusters with decreased surface/volume, as the one observed in particular by STM during the formation of Ni germanide nano-clusters.

Furthermore, it must be noted that similar to our XPS study on Co-Ge system, peak shift values are close to the limits of the experimental resolution and need thus to be interpreted with care. Unfortunately, here the observed XPS peak shifts were near the tool spectral resolution (~0.1 eV). Consequently, Ni and Ge XPS peak position analysis did not allow to gain further insights into electronic effects/chemical reactions during the Ni-germanide formation. Future *in-situ* synchrotron-based XPS studies are planned to overcome these resolution limits and avoid the detrimental influence of *ex-situ* contamination.

## Summary

In conclusion, these combined STM, LEED, (S)TEM-EDX and XPS study unveils the relevant structural and chemical processes taking place during Ni germanide nanostructure formation on a Ge(001).

Schematically the main results of this study can be summarized as follows:

- i)* The evaporation of ~1 nm of Ni on Ge(001) substrate results in a Volmer-Weber growth. The Ni/Ge system is chemically inert under these deposition condition, as can be argued observing the unchanged terraced morphology of the underlying Ge and the observation of metallic Ni clusters.
- ii)* Annealing treatments at relatively low temperatures (100 °C – 200 °C) results in a significant change in the surface morphology. After annealing at

100 °C the Ni VW clusters are not visible any more. Ni clusters wet the Ge surface by reacting with the Ge terrace atoms (probably at kink positions), which result in the creation of a  $\text{Ni}_x\text{Ge}_y$  continuous layer with multiple terrace levels featuring small, randomly located voids.

Then, after annealing at higher temperature (200 °C), the de-wetting phenomena starts, and consequently the voids area in the wetting layer increases. In addition, the top wetting layer shows that clear surface arrangement surface ordering processes were initiated.

*iii)* Finally, annealing in the high temperature range (300 °C - 500 °C), induces the breakup of the layer in isolated 3D NiGe nanoclusters undergoing an Ostwald ripening phenomenon accompanied by Ni-germanide diffusion into the Ge substrate. This results in the formation of rectangular 3D Ni-germanide nanostructures often in form of truncated inverted pyramids with a  $\text{NiGe}(101); (010) \parallel \text{Ge}(001); (110)$  epitaxial relationship towards the  $\text{Ge}(001)$  substrate.

# Chapter 4

## Summary and Outlook

In the following Section 4.1, the key findings of this PhD dissertation are briefly summarized. Next, in Section 4.2 the thermal evolution of Co and Ni germanide nanostructures on Ge(001) substrates is presented in detail and main findings related to both metal/Ge systems are compared. As previously mentioned, the growth scenario observed for the investigated nanostructures is in line with main characteristics of the Walser and Benè rule. In consequence, the description of the investigated systems growth scenario shall start with a detailed presentation of the principles of the WB rule. Finally, an outlook of possible future research is given in Section 4.3.

### 4.1. Summary

This thesis presents a multi-technique experimental nano-scale study on the formation processes of Co and Ni germanide nanostructures on Ge(001) substrate after few MLs metal deposition at RT followed by subsequent annealing treatments. Motivated by their high potential for ohmic contact formation on the nano-scale towards future Ge device modules integrated into mainstream Si-based integrated circuit platform, the growth studies on Co and Ni germanide nanostructures on Ge(001) were discussed here. The insights gained provide crucial information on the nanostructure characteristics of epitaxial Co/Ge and Ni/Ge and assist future theoretical physics description of Schottky barrier formation (SBH).

The study indicates that metal deposition at RT results in a Volmer-Weber (VW) growth mode for both investigated systems. Low temperature annealing treatment results in a significant surface morphology change from 3D metal clusters to 2D wetting layers. A very flat wetting layer is observed for the Co/Ge(001) after annealing at about 250 °C for 1 hour, which is slightly different to Ni/Ge system where inhomogeneous 2D wetting domains are formed in lower temperature range, namely 100 °C. Furthermore, annealing at higher temperatures leads to the growth of well-ordered 3D nanostructures, surrounded by clean, reconstructed Ge(001). (S)TEM-EDX results reveal that 3D nanostructures formed after annealing in high temperature ranges are undoubtedly metal germanide phases. In addition, analysis of these Co- and Ni-germanide structures shows that the growth mechanism is different: in particular, the Ni/Ge system is more reactive and results in nanostructures which show a strong tendency to be embedded into the Ge(001) substrate; in contrast, the Co-germanide nanostructures are situated on top of the Ge(001) substrate for the investigated temperature range. In addition, it was found that in case of Co/Ge system, Ge diffusion from bulk into the  $\text{Co}_x\text{Ge}_y$  nanostructures was the main driving force behind the formation of nanostructures, which is in contrast to Ni/Ge system, where it was demonstrated that Ni was a strong surface and bulk diffusing species into the Ge(001) substrate.

Overall, the thesis presented sets the groundwork for future research on metal/Ge interaction required for the future development of high performance Ge-based device. In particular, chemical phase identification is undoubtedly one of the key aspects that require further studies. Taking into account the fact that, among many stable stoichiometric phases, only some may have an ohmic character, it is relevant to complete the understanding of the chemical composition of the  $\text{Metal}_x\text{Ge}_y$  wetting layer as well as the 3D metal germanide nanostructures. Finally, the electrical characterization of nanocontact (e.g. electrical characterization of 3D nanostructure/Ge(001) substrate interface) is also a major challenge in the coming future.



## 4.2. Thermal evolution of Co and Ni germanides

### 4.2.1. Walser and Benè rule

The results presented in this PhD thesis by combined STM, LEED, (S)TEM-EDX and XPS studies reveal that in general, for both investigated systems, the formation process of metal germanide nanostructures is very similar and can be described using a similar scenario. In particular, it was found out that the growth scenario is in line with main characteristics of the so-called Walser and Benè (WB) rule, giving thus microscopic insights into the origins of the WB rule established about 40 years ago for macroscopic metal-semiconductor interaction.

The WB rule was proposed in the '70s to describe on the macroscopic scale bulk metal-semiconductor solid-phase reactions [242] [243]. Literally, the WB rule tells that: *“The first compound nucleated in planar binary reaction couples is the most stable congruently melting compound adjacent to the lowest-temperature eutectic on the bulk equilibrium phase diagram”* [242]. The main task of the WB rule is thus to predict which phase will nucleate as first one in planar solid silicon-transition-metal binary couple reactions at subeutectic temperatures. In case of metal-silicide as well as metal-germanide systems, the correctness of the WB rule has been confirmed by many research groups for different material systems. For example, it was predicted and confirmed that the first compounds formed in Co/Ge and Ni/Ge binary systems are  $\text{Co}_2\text{Ge}$  and  $\text{Ni}_2\text{Ge}$ , respectively [243]. However, please note that WB describes macroscopic scale bulk metal-semiconductor solid-phase reactions, and for that reason exceptions to the WB rule are expected, especially in case of thin film or nano-scale nanostructure reactions. In addition, the nucleation process is certainly very sensitive to the initial state of the metal/semiconductor interface in terms of impurities as well as crystalline defects. It is thus not too surprising that inconsistencies in the literature were reported, in particular with respect to the exact nature of the metallic germanide phase nucleating first. For example, it was shown that in thin film reaction of Co with Ge quite often the first stable phase which nucleates is CoGe [211]. In case of Ni/Ge system the matter is more complicated. Wittmer *et al.* confirmed the WB rule and demonstrated the presence of NiGe above 250 °C, following the initial appearance of a

Ni<sub>2</sub>Ge phase [243]. However, Nemouchi *et al.* [244] and Gaudet *et al.* [234] presented another Ni<sub>x</sub>Ge<sub>y</sub> growth scenario where, based on TEM and XRD, the initial formation of Ni<sub>5</sub>Ge<sub>3</sub> and NiGe germanides phases was reported to simultaneously occur; further annealing resulted in the growth of NiGe while Ni<sub>5</sub>Ge<sub>3</sub> was completely consumed. In addition, Nath *et al.* reported, based on *in-situ* TEM studies, that the NiGe phase can be grown directly on Ge(001) – without the metal rich phase Ni<sub>x</sub>Ge<sub>y</sub> phase ( $x > y$ ) – when Ni is deposited on Ge at a substrate temperature of 300 °C [232].

However coming back to the main considerations about WB rule it must be mentioned that besides the main aspects of the WB rule, namely the predictions of the first stable phase, the work of Walser and Benè includes also the microscopic growth scenario on which the WB rule is based. As shown schematically in Figure 4.1 the growth scenario presented by the WB rule can be divided into three main stages (assuming that our semiconductor is Ge):

- i)* Figure 4.1 a): At first, the metal is deposited on the semiconductor surface. According the WB growth scenario, it is envisaged that metal deposition leads to the formation of only a thin interface region as a result of the presence of supercooled metal structure for fast metal deposition or presence of a stable metal structure for slow metal deposition on a cold substrate. In general, in both paths there is no reaction (or very weak reaction) between the metal and the semiconductor surface. The VW growth of 3D metal clusters on a semiconductor surface after metal deposition is in line with this situation, as semiconductor and metal surface as well as metal/semiconductor interface energies support this growth behaviour.
- ii)* Figure 4.1 b): Next, upon increasing the annealing temperature, the interface between metal clusters/semiconductor increases as a result of diffusion phenomena. This leads to the wetting of the semiconductor surface by the metallic cluster, driven by the chemical reaction between metal and semiconductor towards a formation of so-called “metallic glass” layer. This evolution stage is characterized by the presence of an amorphous or poorly ordered metallic layer. Given the local excess of metal, the first nucleating

phase is predicted to be a metal rich  $\text{Metal}_x\text{Ge}_y$  phase ( $x > y$ ). Please note that this state goes along with a change of the semiconductor surface morphology.

iii) Figure 4.1 c): And finally, the transition from amorphous “metallic glass” state to crystalline phase takes place. The WB rule predicts the nucleation of the crystalline  $\text{Metal}_x\text{Ge}_y$  phase which is characterized by the lowest energy path for the transition from amorphous to crystalline. The congruently melting path is favored in contrast to non-congruently melting pathways, owing to the relative energy barriers for long range rearrangement in a crystalline state from the short range ordered amorphous state.

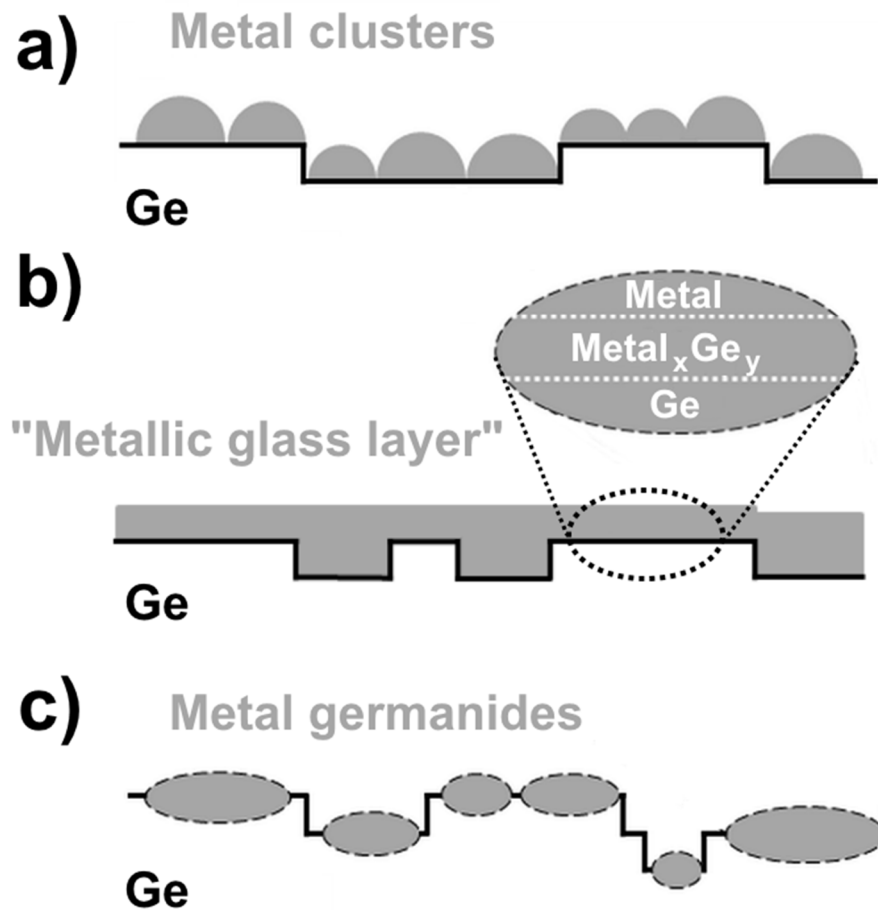


Figure 4.1 Important states in the growth scenario presented by the WB rule: a) metallic 3D VW clusters; b) transformation to 2D “metallic glass”; and c) crystallization of metal germanides.

#### 4.2.2. Growth scenarios of Co/Ge(001) and Ni/Ge(001)

In general, for the Co/Ge(001) as well as Ni/Ge(001) system, the growth and evolution of metal germanide nanostructures on a Ge(001) reconstructed surface is very similar and can be described using the WB rule. However, as presented in this thesis, the combined STM, LEED, (S)TEM-EDX and XPS studies unveil the relevant differences regarding the structural and chemical processes taking place during Co-germanide formation compared to Ni-germanide nanostructures on a microscopic point of view. Please note that both investigated systems are not yet fully understood on the same level as the corresponding metal silicide systems investigated for decades.

An overview and schematic summary of the main results of the work performed in this thesis is schematically depicted in Figure 4.2.

##### **Volmer-Weber growth of Ni and Co on Ge(001)**

At first, the RT deposition of few metal MLs (nominal metal thickness was ~1.5 nm and ~1 nm for Co/Ge and Ni/Ge samples, respectively) on atomically clean, reconstructed Ge(001) substrate results in a VW growth. The metal/Ge(001) system is chemically inert under these deposition condition, as can be argued observing the unchanged terraced morphology of the underlying Ge. The Ge-p(2 x 1) surface reconstruction is preserved in areas not covered by metal clusters. This same scenario is observed for both investigated system (Figure 4.2 a) and e)).

##### **Co germanide nanostructures growth and evolution**

Next, due to significant differences in surface morphology evolution as a function of annealing steps at increasing temperature, each of the investigated system must be described separately. The description begins with the presentation of the growth dynamics of the Co germanide nanostructures (left side in Figure 4.2):

- i) *Low temperature annealing* (Figure 4.2 b)): STM results have shown that the first annealing treatment at 150 °C for 1 hour results in only small changes in surface morphology. The terraced Ge surface morphology and presence of metallic clusters are preserved. This leads to the conclusion that VW Co clusters are stable up to 150 °C. However, XPS measurements depict first

changes in Co and Ge peak positions, which can be interpreted as the onset of a low temperature reaction, as also reported by Prabhakaran *et al.* in this temperature range [216]. Next annealing step at 250 °C results in a substantial surface morphology change. The observed surface lost its terraced character (no Ge terraces observed anymore). The Co clusters react in particular with the Ge terrace atoms, forming a continuous  $\text{Co}_x\text{Ge}_y$  wetting layer. Probably, surface diffusion of Co (dark arrow) and Ge (bright arrow) atoms is the major mechanism, enabling the formation of this continuous  $\text{Co}_x\text{Ge}_y$  wetting layer. In addition, first instabilities of this flat  $\text{Co}_x\text{Ge}_y$  are visible in terms of the formation of elongated  $\text{Co}_x\text{Ge}_y$  nanostructures. Findings related with STM measurements are in line with further changes in XPS peak intensities and positions which are sensitive to surface morphology and electronic interface bonding changes, respectively. Based on thin film XRD studies by Gaudet *et al.* it can be assumed that the Co-Germanide continuous wetting layer is probably related to the CoGe phase [211].

*ii) High temperature annealing* (Figure 4.2 c)): Annealing at higher temperature range (400 °C to 600 °C) results in the de-wetting of the  $\text{Co}_x\text{Ge}_y$  layer and surface ordering process. The formation of two types of 3D Co-germanide nanostructures, namely flattop- and ridge-type, was observed. These nanostructures are well-ordered, have an elongated shape and run along equivalent  $\langle 110 \rangle$  Ge surface direction. In addition, the reappearance of clean, reconstructed Ge surface areas in the uncovered parts of the sample surface was observed. Based on a complementary (S)TEM-EDX study it is assumed that the Ge diffusion from bulk into the  $\text{Co}_x\text{Ge}_y$  nanostructures is the main driving force. According to Gaudet *et al.*'s work, the Co-germanides formed during this high temperature annealing state are probably related to  $\text{Co}_5\text{Ge}_7$ , as this phase was found to dominate in the temperature regime from 400 °C to 600 °C [211].

*iii) Additional - Ostwald ripening at higher temperatures* (Figure 4.2 d)): (S)TEM-EDX measurements show that annealing treatment at 700 °C results in a change of the Co/Ge interface structure away from a planar towards

faceted interface morphology. In addition, it is clearly visible that this change is characterized by an interface reaction comprising strong Co diffusion into the Ge substrate. Statistical analysis of the 3D Co germanide nanostructure evolution by STM studies as a function of annealing temperature, demonstrates that flattop-type nanostructures are less stable than ridge-type nanostructures: flattop nanostructures disappear completely whereas ridge-type nanostructures grow in size. This significant increase of nanostructure volume unambiguously argues for the presence of the Ostwald ripening phenomena. Based on the paper by Gaudet *et al.*, it follows that the Ostwald ripening occurs in the temperature regime where this group reported the formation of the  $\text{CoGe}_2$  phase (the ohmic phase in the Co/Ge system), namely above 600 °C [211].

### **Ni germanide nanostructures growth and evolution**

Finally, the attention is focused on the study of the Ni/Ge(001) system and the list below summarizes the main results of the growth dynamics of the Ni germanide nanostructures (right side in Figure 4.2):

*i) Low temperature annealing* (Figure 4.2 f): In contrast to the previously discussed Co/Ge system, annealing treatments at relatively low temperatures result in a tremendous change in the surface morphology of the Ni/Ge system. After the first annealing at 100 °C, the Ni VW clusters wet the Ge surface by reacting with the Ge terrace atoms. In the Ni-Ge system, Ni is the main diffusing species at low temperature. This leads to the formation of a  $\text{Ni}_x\text{Ge}_y$  continuous layer with multiple terrace levels. Additionally, terraces are characterized by the presence of small, randomly located voids. It is noted that none of any type of Ge surface reconstruction was resolved inside the voids. Generally, no local order was detected on top of single  $\text{Ni}_x\text{Ge}_y$  terraces, however very occasionally some signs of local order in the form of ordered rows with constant periodicity were observed. Annealing at higher temperature (200 °C) entails the onset of a de-wetting with the voids area in the wetting layer increasing. In addition, the top of single  $\text{Ni}_x\text{Ge}_y$  terraces clearly exhibits a local, complex surface arrangement of currently unknown origin.

ii) *High temperature annealing* (Figure 4.2 g): Annealing in the high temperature range (300 °C – 500 °C) enhances the de-wetting process and causes the breakup of the layer in isolated  $\text{Ni}_x\text{Ge}_y$  nanoclusters. Furthermore, an Ostwald ripening phenomenon accompanied by Ni-germanide diffusion into the Ge substrate was also observed.

iii) *Additional epitaxy assignment* (Figure 4.2 h): STM results supported by (S)TEM-EDX show that well-ordered 3D nanostructures are observed after annealing at 500 °C. These 3D nanostructures were tentatively assigned to the NiGe phase. It was found that 3D NiGe nanostructure morphologies can be described by the epitaxial relationship  $\text{NiGe}(101);(010) \parallel \text{Ge}(001);(110)$ , resulting in rectangular pyramids which appear either in form of truncated pyramid structures on top of the Ge(001) surface or embedded into the Ge(001) substrate.

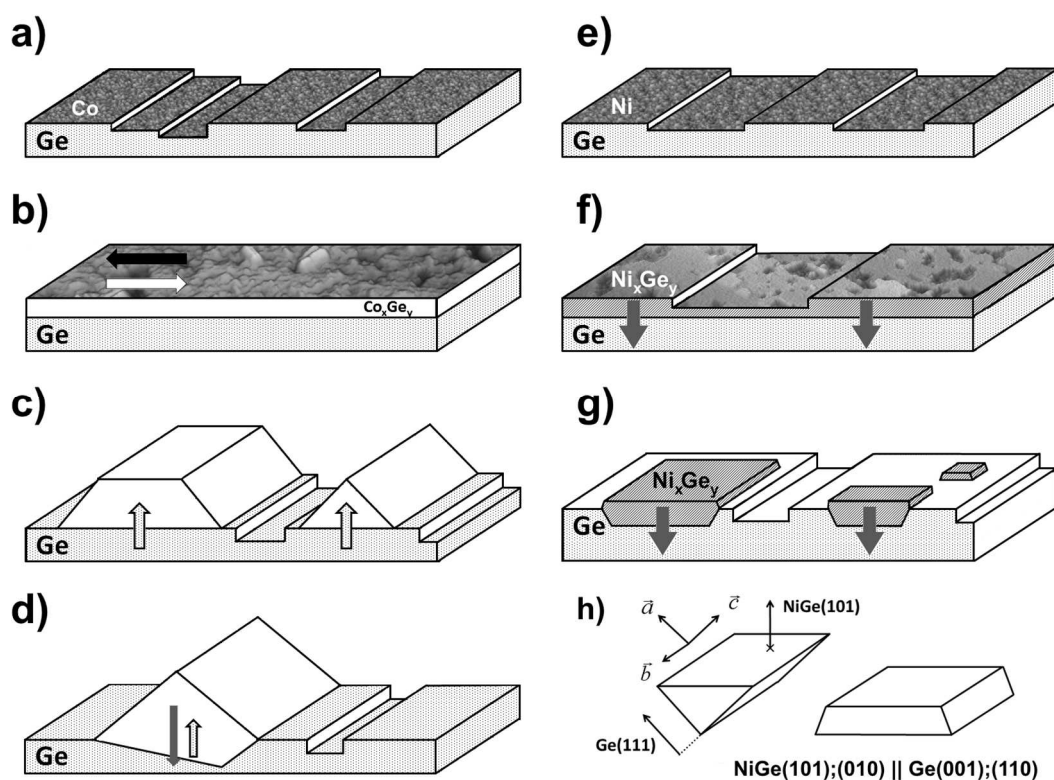


Figure 4.2 Important growth states of metal germanide nanostructures evolution on Ge(001) as a function of annealing: left-hand side presents growth scenario for Co germanides (a-d), and right-hand side depicts growth scenario for Ni germanides (e-h). VW metal clusters on Ge(001) surface after RT metal deposition (a,e); Low temperature continuous  $\text{Metal}_x\text{Ge}_y$  wetting layer formation (b,f); High temperature  $\text{Metal}_x\text{Ge}_y$  nanostructure formation (c,g); and additional findings associated with the investigated systems (d,h). More information in text.

### 4.3. Outlook

The results presented in this PhD thesis by a multi-technique surface science approach on the *in-situ* growth of Co and Ni germanides by evaporation of few metal MLs on Ge(001) at RT and subsequent annealing succeed to unveil on the nano-scale the various structural growth mechanisms at work. However, these results do not explain all aspects of the growth process and still some questions remain unanswered. In consequence, in order to complete the understanding of the Co and Ni germanide formation, additional studies need to be performed. This sub-chapter briefly comments on the possible way to extend the approach presented in this thesis by additional future experiments. In addition, the growing interest not only on Ge but also on germanium-tin (GeSn) alloys, as e.g. potential material candidate for Ge-based laser device production, strongly suggests that in near future an atomic-level study on the formation of metal germanides on Ge surfaces with incorporated Sn-atoms will be also of high academic and technological interest.

#### **Future PEEM/LEEM experiments**

It is clear that in this PhD dissertation the scientific interest was focused on the physical and chemical properties of solid surfaces, thin metal films, and metal germanide nanostructures. However, the STM technique, the main base of this PhD work, cannot itself provide compelling information about chemical properties of the investigated nanostructures directly. It is natural that in this case, STM must be supported by other experimental techniques. In this dissertation, complementary techniques like XPS and (S)TEM-EDX were performed, which gave general chemical insights into the metal germanide nanostructures growth process. However, please note that this approach is not the ideal solution due to *ex-situ* sample transfer between UHV chambers, and what is most important, the XPS technique does not provide spatial resolution on the nano-scale regime. In consequence, additional *in-situ* photoelectron emission/low energy electron microscopy (PEEM/LEEM) studies are planned in order to complete the understanding of the Co and Ni germanide formation. In general, PEEM/LEEM technique enables time-resolved *in-situ* physical and chemical characterization of surface structure on the micro- and even down to the nanometre scale. What is



important, modern synchrotron radiation facilities give a possibility to achieve in PEEM/LEEM tools the needed spatially resolved chemical information resolution on the nano-scale. Such promising capabilities of Synchrotron PEEM/LEEM systems could be useful from the point of view of this thesis to identify e.g. the non-homogenous composition of flat-top- vs. ridge-type Co-germanide nanostructures or the real stoichiometry of the  $\text{Metal}_x\text{Ge}_y$  wetting layers in both investigated systems. Currently, such measurements on Co/Ge and Ni/Ge system are carried out in cooperation with Th. Schmidt *et al.* from University of Bremen also using the PEEM/LEEM system at ALBA Synchrotron facility in Spain. More information about these techniques, including the presentation of modern, advanced PEEM/LEEM operating modes and also the theoretical description of physical phenomena observed in these techniques can be found in Refs. [250] [251].

From a point of view of further experiments, it should be noted that correlation between structure and chemical information on the nano-scale will be even more required when metal contact formation control is mandatory to chemically more complex GeSn functional layer systems, currently discussed for CMOS as well as group IV photonics applications, as mentioned in the next subsection.

### **GeSn system**

As was already mentioned in the introduction, currently besides Ge also GeSn is considered as a strong alternative to silicon e.g. as stressor channel material in MOSFET as well as gain medium for laser applications. It was shown that a small amount of Sn can strongly improve the electronic properties of Ge. However, a problem associated with the fabrication of low resistance, thermally stable metal contacts to GeSn surface, which is particularly important for high-current applications, remains unresolved. As a result, the Transition metal/GeSn systems will be extensively studied. This certainly refers also to the Ni/GeSn system (by analogy, the first candidate for ohmic contact formation on GeSn substrates, which need to be checked). This also suggests that similar studies on Ni/GeSn system, to those described in this PhD, namely surface science study on the nano-scale regime will soon be performed. For example, the STM approach can be used to investigate the impact of surface-strain and of

incorporated Sn-atoms on the nucleation behaviour of Ni(GeSn) nanocontact structures on GeSn(001) surfaces.

Finally, apart from basic material research, other important measurements focusing more on the technological aspects are necessary. This refers primarily to current–voltage characteristics of Schottky barriers for Ni/Ge and Ni/GeSn contacts. A lot of work has been dedicated to electrical measurements, trying to understand and control the mechanism of SBH formation. In particular, much attention was paid to study the impact of doping and impurities near the metal-semiconductor (MS) interface on the electrical properties of MS contacts. For example, it was shown that slight incorporation of platinum (Ref. [252]) or carbon (Refs. [253] [254]) can distinctly improve the MS contact properties (cited papers are focused on Ni/GeSn(Pt), Ni/SiGe(C) and NiSi/Si(C) systems, respectively). It is obvious that in order to reduce and stabilize the SBH of Ni/(GeSn) contacts, similar experiments need to be performed. More information about electrical measurements on Ni/Ge as well as Ni/GeSn contacts can be found in Refs. [112] [255] [256].

# Chapter 5

## Scientific visibility during the PhD

### 5.1. Publications in peer-reviewed journals

1. **T. Grzela**, G. Capellini, W. Koczorowski, M.A. Schubert, R. Czajka, N.J. Curson, I. Heidmann, Th. Schmidt, J. Falta, and T. Schroeder, *Growth and evolution of nickel germanide nanostructures on Ge(001)*, *Nanotechnology* **26**, 385701 (2015)  
<http://dx.doi.org/10.1088/0957-4484/26/38/385701>
2. W. Koczorowski, A. Puchalska, **T. Grzela**, M.W. Radny, L. Jurczynszyn, S.R. Schofield, R. Czajka, and N.J. Curson, *Initial growth of Ba on Ge(001) – an STM and DFT study*, *Physical Review B* **91**, 235319 (2015)  
<http://journals.aps.org/prb/abstract/10.1103/PhysRevB.91.235319>
3. W. Koczorowski, **T. Grzela**, M.W. Radny, S.R. Schofield, G. Capellini, R. Czajka, T. Schroeder, and N.J. Curson, *Ba termination of Ge(001) studied with STM*, *Nanotechnology* **26**, 155701 (2015)  
<http://dx.doi.org/10.1088/0957-4484/26/15/155701>
4. **T. Grzela**, W. Koczorowski, G. Capellini, R. Czajka, M.W. Radny, N.J. Curson, S.R. Schofield, M.A. Schubert, and T. Schroeder, *Interface and nanostructure evolution of Cobalt Germanides on Ge(001)*, *J. Appl. Phys.* **115**, 074307 (2014)  
<http://dx.doi.org/10.1063/1.4865955>

5. L. Tarnawska, J. Dabrowski, **T. Grzela**, M. Lehmann, T. Niermann, R. Paszkiewicz, P. Storck, and T. Schroeder, *Interface science of virtual GaN substrates on Si(111) via Sc2O3/Y2O3 buffers: Experiment and theory*, J. Appl. Phys. **113**, 213507 (2013)  
<http://dx.doi.org/10.1063/1.4807907>

## 5.2. Presentations at conferences and courses

1. 7<sup>th</sup> International Conference on Scanning Probe Spectroscopy and Related Methods (SPS'15), *Comparative study of thermal evolution of Co and Ni germanide nanostructures on Ge(001)*, oral presentation, June 2015, Poznan (Poland)
2. 9<sup>th</sup> International Conference of Silicon Epitaxy and Heterostructures (ICSI-9), *Thermal evolution of Co and Ni germanide nanostructures on Ge(001): Comparative STM, LEED, TEM-EDX & XPS study*, oral presentation, May 2015, Montreal (Canada)
3. 79<sup>th</sup> Annual Meeting of the DPG and DPG Spring Meeting, *Comparative study of Co and Ni germanides growth on Ge(001) substrates*, oral presentation, March 2015, Berlin (Germany)
4. 10<sup>th</sup> Interregional Workshop on Advanced Nanomaterials (IWAN 2014), *Characterization of Co and Ni germanide nanostructure growth on Ge(001) substrate: comparative STM, LEED, TEM-EDX and XPS study*, oral presentation, November 2014, Wroclaw (Poland)
5. E-MRS Fall Meeting 2014, *Comparative STM, LEED, TEM-EDX and XPS study of Co and Ni germanide growth on Ge(001)*, oral presentation, September 2014, Warsaw (Poland)

6. 9<sup>th</sup> Interregional Workshop on Advanced Nanomaterials (IWAN 2013), *Characterization of Cobalt Germanide Nanostructures on Ge(001) Substrate: an STM Investigation on the Initial Phase of Metal Contact Formation to Ge*, oral presentation, November 2013, Prague (Czech Republic)
7. JSPS Core-to-Core Advanced Research Network "International Collaborative Research Center on Atomically Controlled Processing for Ultralarge Scale Integration", *Cobalt Germanide nanostructures on Ge(001): A combined STM, LEED, XPS and TEM study on the initial phase of metal contact formation to Ge*, oral presentation, October 2013, Frankfurt Oder (Germany)
8. E-MRS Fall Meeting 2013, *Formation and characterization of cobalt germanide structures on Ge(001) substrate – an STM study*, oral presentation, September 2013, Warsaw (Poland)
9. Doktorandenforum der Sektion D der Leibniz-Gemeinschaft, *Room-Temperature STM study of cobalt germanides growth on Ge(001)*, poster presentation, June 2013, Berlin (Germany)
10. 22<sup>nd</sup> Materials for Advanced Metallization Conference (MAM 2013), *Early growth studies of cobalt germanides on Ge(001) surface by means of SPM technique*, poster presentation (**Best poster award**), March 2013, Leuven (Belgium)
11. 7<sup>th</sup> Workshop on Applications of Scanning Probe Microscopy STM/AFM, *STM study of growing  $Co_xGe_y$  structures on Ge(001) substrate*, poster presentation, November 2012, Zakopane (Poland)
12. 8<sup>th</sup> Interregional Workshop on Advanced Nanomaterials (IWAN 2012), *STM study of growing  $Co_xGe_y$  structures on Ge(001) substrate*, oral presentation, November 2012, Frankfurt Oder (Germany)
13. E-MRS Fall Meeting 2011, *Structural and dielectric properties of  $CeO_2/Pr_2O_3/Si(111)$  heterostructures as a function of oxygen content in the buried Pr oxide layer*, oral presentation, September 2011, Warsaw (Poland)



# Appendix A

## Tunneling theory

The operating principle of the STM is based on the quantum mechanical phenomenon of tunneling. Tunneling is an important mechanism of transport in condensed matter and across artificial junctions, which plays a significant role in some aspects of solid state physics, nuclear physics and chemical physics, as well as in biology. However, in contrast to other type of transport mechanism, like e.g. diffusion, the tunneling effect can be understood only in terms of quantum theory. In order to gain a basic understanding of obtained STM results, this appendix introduces the reader to the basics of a quantum mechanical description of the tunneling effect.

### **Elastic tunneling through a one-dimensional rectangular potential barrier**

As simplest case, the tunneling effect through a one-dimensional rectangular potential barrier is considered (Figure A.1). In classical mechanics an electron with mass  $m$  and a kinetic energy  $E$  impinging from area **I** cannot pass a barrier of height  $V_0$  in region **II**. However, in accordance with quantum theory, the wave-particle dualism may in fact allow this electron to traverse the barrier and a finite probability of the emergence of electron in area **III** exists. The incident electron wave function is oscillatory. In the barrier, the wave function decays exponentially. However, when the electron passed through the barrier the wave function is once again oscillatory. For a quantitative description of the tunneling effect for each region, the time-independent Schrödinger equations and an ansatz for the corresponding wave functions  $\psi_j$  ( $j = 1,2,3$ ) must be solved ( $\hbar$  is Planck's constant divided by  $2\pi$ ).

For region **I**:  $V = 0$

$$-\frac{\hbar^2}{2m} \cdot \frac{d^2\psi_I}{dz^2} = E\psi_I \quad (\text{A.1})$$

$$\psi_I = A_1 e^{ikz} + B_1 e^{-ikz}, \text{ with } k^2 = 2mE/\hbar^2 \quad (\text{A.2})$$

For region **II**:  $V = V_0$

$$-\frac{\hbar^2}{2m} \cdot \frac{d^2\psi_{II}}{dz^2} + V_0\psi_{II} = E\psi_{II} \quad (\text{A.3})$$

$$\psi_{II} = A_2 e^{ik'z} + B_2 e^{-ik'z} = A_2 e^{-\kappa z} + B_2 e^{\kappa z}, \quad (\text{A.4})$$

$$\text{with } \kappa^2 = -k'^2 = 2m(V_0 - E)/\hbar^2$$

For region **III**:  $V = 0$

$$-\frac{\hbar^2}{2m} \cdot \frac{d^2\psi_{III}}{dz^2} = E\psi_{III} \quad (\text{A.5})$$

$$\psi_{III} = A_3 e^{ikz}, \text{ with } k^2 = 2mE/\hbar^2 \quad (\text{A.6})$$

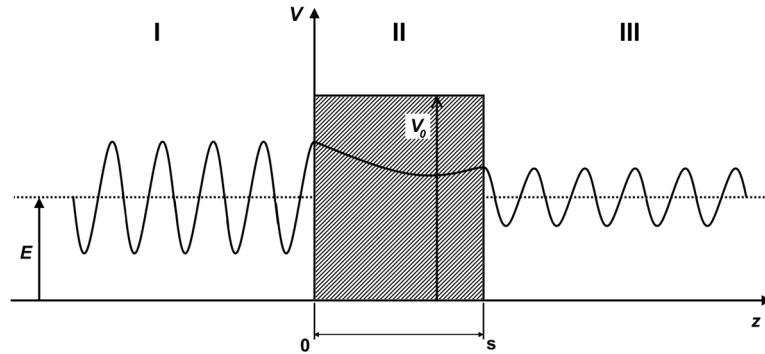


Figure A.1 The electron is incident from the left side on the one-dimensional rectangular potential barrier with height  $V_0$  and width  $s$ . In regions I and III the electron wave function is oscillatory. Within the barrier, the wave function decays exponentially.

Most interesting is the barrier transmission coefficient  $T$ , which is defined by the ratio between the transmitted current density  $j_t$  and the incident current density  $j_i$  given by:

$$T = \frac{j_t}{j_i} = \left| \frac{A_3}{A_1} \right|^2 \quad (\text{A.7})$$

By matching the boundary conditions, at the discontinuities of the potential  $V(z)$  at  $z = 0$  and  $z = s$ , for each  $\psi_j$  as well as their derivatives of first order, all coefficients  $A_j$



and  $B_j$  can be derived. Therefore, after simple but laborious calculations, the barrier transmission coefficient  $T$  is given by Eq. (A.8).

$$T = \frac{1}{1 + (k^2 + \kappa^2)^2 / (4k^2 \kappa^2) \sinh^2(\kappa s)} \quad (\text{A.8})$$

In case of a strongly attenuating barrier ( $\kappa s \gg 1$ ) the transmission coefficient can be approximated by:

$$T \approx \frac{16k^2 \kappa^2}{(k^2 + \kappa^2)^2} \cdot e^{-2\kappa s} \quad (\text{A.9})$$

with a decay rate

$$\kappa = [2m(V_0 - E)]^{1/2} / \hbar \quad (\text{A.10})$$

The dominant contribution of equation (A.9) comes from the factor  $\exp(-\kappa s)$ , so that the probability for tunneling through a barrier is an exponential function of the barrier width. This physical dependence allowed Binnig, Rohrer and co-workers the construction of the scanning tunneling microscope, which provides extremely high spatial resolution. In addition, the transmission probability also depends on the square root of the effective barrier height  $(V_0 - E)^{1/2}$ , which is independent of the exact shape of the barrier and typical for tunneling. In this part, elastic tunneling was considered since the energy of the electron is conserved during the tunneling process. In other words, the electron energy is equal in the initial and final state.

### **Elastic tunneling through barrier of arbitrary shape between two conductors**

An extension to potential barriers of arbitrary shape can be made by using the WKB approximation developed in 1926 by Wentzel, Kramers and Brillouin [257]. In general, the WKB procedure allows to approximate the solution of a differential equation whose highest derivative is multiplied by a small parameter, in this case Planck's constant  $\hbar$ . In accordance with the WKB approximation, the expression (A.11) describes the probability that an electron will penetrate a potential barrier  $V(z)$  of arbitrary shape, where  $s_1$  and  $s_2$  are the distances from the first surface to the place where the potential energy equals the Fermi energy near the surfaces 1 and 2, respectively, and  $s_2 - s_1$  is thus the width of the barrier (Figure A.2).

$$D(E) = \exp\left\{-\frac{2}{\hbar} \int_{s_1}^{s_2} [2m(V(z) - E)]^{1/2} dz\right\} = \exp\left\{-2 \int_{s_1}^{s_2} \kappa(z, E) dz\right\} \quad (\text{A.11})$$

This approximation refers to the one-dimensional case, although it can be evolved to a multidimensional space [258] [259].

In 1963 Simmons [260] calculated the tunnel current through a generalized barrier between two metal electrodes and obtained the following expression for the current density  $J$  at zero temperature:

$$J = \frac{e}{4\pi^2 \hbar (\Delta s)^2} \cdot \left\{ \bar{\phi} \exp\left(-A \bar{\phi}^{1/2} \Delta s\right) - (\phi + eU) \exp\left(-A(\bar{\phi} - eU)^{1/2} \Delta s\right) \right\} \quad (\text{A.12})$$

where:  $e$  is the charge of electron,  $\Delta s = s_2 - s_1$ ,  $A = 2(2m)^{1/2}/\hbar$  and  $\phi$  is a mean potential barrier height above Fermi level  $E_F$ , while  $\bar{\phi}$  is given by

$$\bar{\phi} = \frac{1}{\Delta s} \int_{s_1}^{s_2} \phi(z) dz \quad (\text{A.13})$$

The first term in (A.12) is related with a current density flowing from the left to the right metal electrode, while the second term represents the opposite current density flow. The difference between these both expressions results in a net current density. In Simmons work, different initial limits of barrier height or bias range were considered. For example, an expression for the tunnel current density in the low bias voltage range ( $U \approx 0$ ,  $eU \ll \bar{\phi}$ ) is given by:

$$J = \frac{e^2}{4\pi^2 \hbar^2} \cdot \frac{(2m\bar{\phi})^{1/2}}{\Delta s} \cdot U \exp\left(-A \bar{\phi}^{1/2} \Delta s\right) = \frac{e^2}{8\pi^2 \hbar} \cdot \frac{A \bar{\phi}^{1/2}}{\Delta s} \cdot U \exp\left(-A \bar{\phi}^{1/2} \Delta s\right) \quad (\text{A.14})$$

Eq. (A.14) shows clearly the characteristic exponential dependence of the tunneling current on the barrier width  $\Delta s$  and the square root of the mean barrier height  $\phi$ . In addition, in the low bias limit a linear dependence of the tunneling current as a function of applied bias voltage is observed.

In another work by Simmons, a metal-isolator-metal tunnel junction with dissimilar metal electrodes (having different work functions) was analyzed [261]. In this work the polarity dependent I-U characteristic was presented. An intrinsic electric field came from the contact potential that exists between two dissimilar electrodes

$((\phi_2 - \phi_1)/e)$ . As a consequence, the dependence of the tunneling current on the applied bias voltage becomes polarity dependent. For the lower voltages range, the major current flows when the electrode of lower work function is positively biased. For the high voltage case, opposite flow direction of rectification is observed; i.e., greater current flows when the electrode of lower work function is negatively biased.

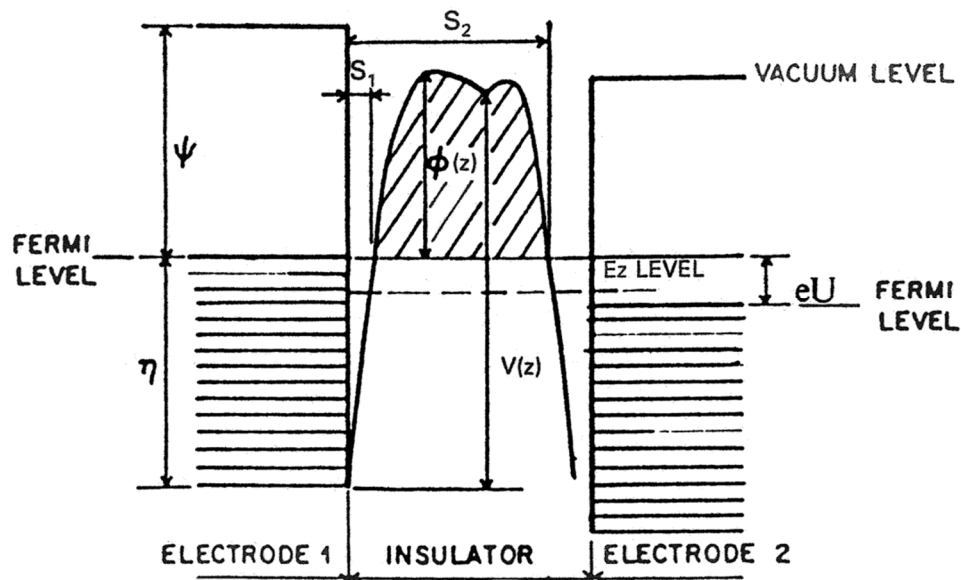


Figure A.2 General tunnel barrier between two metal electrodes of different work function (after [260]).

Please note that all above mentioned theoretical approximations were considered for temperature  $T = 0$  K. Following Stratton [262] the temperature-dependence of the tunneling current can be given by the equation (A.15):

$$\frac{j(T)}{j(T=0)} = \frac{\pi c k_B T}{\sin(\pi c k_B T)} \approx 1 + \frac{1}{6} (\pi c_1 k_B T)^2 + \dots \quad (\text{A.15})$$

where:  $k_B$  is the Boltzmann constant and  $c$  is a function of the applied voltage  $U$ .

In summary, this chapter gives some basic information about the quantum mechanic description of the tunneling effect, showing the simplest cases and first historically theoretical works on this phenomenon. Please note that nowadays many complicated theoretical models describing the tunneling effect, as well as different aspects of this phenomenon, exist and may concern sophisticated topics like e.g.: Josephson tunneling, spin-polarized tunneling, inelastic tunneling etc. More information about the broad range of topics on tunneling phenomena can be found in Ref. [145]



# Appendix B

## Abbreviations

(S)TEM	(scanning) transmission electron microscope/microscopy
2D	two-dimensional
3D	three-dimensional
AC	alternating current
ACh	analysis chamber
AES	Auger electron spectroscopy
APD	avalanche photodiode
ARC	anti-reflection coating
ATS	adsorbate-terminated semiconductor surface
BiCMOS	bipolar complementary metal oxide semiconductor
BioMEMS	Bio-Micro-Electro-Mechanical System
BSE	back-scattered electrons
CCD	charge-couples device
CITS	current imaging tunneling spectroscopy
CMOS	complementary metal oxide semiconductor
CNL	charge neutrality level
DC	direct current
DH	direct heating
DV	dimer vacancy
DVC	dimer vacancy concentration
EA	electro-absorption (modulators)

EBE	electron beam evaporation
EBPVD	electron beam physical vapour deposition
EDX	energy dispersive X-ray spectroscopy
EPIC	electronic-photonic integrated circuit
ESCA	electron spectroscopy for chemical analysis
FinFET	fin-shaped field effect transistor
GBT	graphene base transistor
HAADF	high angle annular dark field
HBT	hetero-bipolar transistor
i	intrinsic layer
IC	integrated circuits
IHP	Innovations for High Performance Microelectronics
IMFP	inelastic mean free path
ITRS	International Technology Roadmap for Semiconductors
LED	light-emitting diode
LEED	low energy electron diffraction
LEEM	low energy electron microscopy
LL	load lock chamber
MIS	metal-interlayer-semiconductor
MOSFET	metal-oxide semiconductor field-effect transistor
MQW	multi quantum wells
MS	metal-semiconductor
MSM	metal-semiconductor-metal
PBN	pyrolytic boron nitride
PCh	preparation chamber
PEEM	photoelectron emission electron microscopy
PG	pyrolytic graphite
QCL	quantum cascade lasers
QCSE	quantum confined Stark effect
R&D	research and development
RF	radio frequency

---

RFA	retarding field analyser
RH	radiative heating
SAW	surface acoustic wave
SBH	Schottky barrier height
SE	secondary electrons
SEM	scanning electron microscope/microscopy
SIP	System-In-Package
SOC	System-On-Chip
SOI	Silicon-on-insulator
SPM	scanning probe microscope/microscopy
SRH	Shockley-Read-Hall recombination
STM	scanning tunneling microscope/microscopy
TDD	threading dislocations density
TSV	through silicon via (technology)
UHV	ultra-high vacuum
UPS	ultraviolet photoelectron spectroscopy
VW	Volmer-Weber
WB	Walser and Benè rule
WKB	Wentzel, Kramers and Brillouin approximation
XPS	X-ray photoelectron spectroscopy





# Appendix C

## Glossary of symbols

$A$	area
$A^*$	effective Richardson constant
Al	aluminium
CH <sub>3</sub> COOH	acetic acid
Co	cobalt
$D_{GS}$	density of semiconductor surface states
$e$	charge of electron
$eD_{int}$	interface dipole
$e\phi$	work function
$-e\overline{V}_M$	average electrostatic potential energy per unit cell of the metal
$-e\overline{V}_S$	average electrostatic potential energy per unit cell of the semiconductor
$E$	kinetic energy of electron / external electric field
$E_a$	characteristic activation energy
$E_B$	binding energy
$E_C$	conduction band
$E_F$	Fermi Level
$E_g$	energy gap / semiconductor band gap
$E_{kin}$	kinetic energy of photoemitted electron
$E_V$	valence band
GaAs	gallium arsenide
Ge	germanium

GeSn	germanium-tin
$h$	Planck constant
$\hbar$	reduced Planck constant
$h\nu$	photon energy
H <sub>2</sub> SO <sub>4</sub>	sulphuric acid
H <sub>3</sub> PO <sub>4</sub>	phosphoric acid
HF	hydrogen fluoride
$I_0$	intensity from an infinitely thick uniform substrate
$I$	tunneling current
$I_{XPS}$	intensity of photoelectrons
InAs	indium arsenide
InGaAs	indium gallium arsenide
InP	indium phosphide
InSb	indium antimonide
$J$	current density
$j_i$	incident current density
$j_t$	transmitted current density
$k$	effective ionization ratio
$k_B$	Boltzmann constant
KCN	potassium cyanide
KOH	potassium hydroxide
$kT$	thermal energy
LiNbO <sub>3</sub>	lithium niobate
$m$	mass of particle / mass of electron
$m^*$	effective mass
Mg	magnesium
Mo	molybdenum
$N$	doping concentration
NaCl	sodium chloride
NaNO <sub>3</sub>	sodium nitrate
NH <sub>4</sub> OH	ammonium hydroxide

---

Ni	nickel
Pt-Ir	platinum-iridium
$q\phi_B$	Schottky barrier height
$R$	total contact resistance
$R_C$	contact resistance
$s$	distance sample-tip
$s_1, s_2$	distances from the first surface to the place where the potential energy equals the Fermi energy near the surfaces 1 and 2, respectively
$s, \Delta s$	barrier width
$S$	S-parameter, interface behaviour parameter
Si	silicon
SiGe	silicon-germanium
SiO <sub>2</sub>	silicon dioxide
Sn	tin
$T, T(E, eU)$	transmission coefficient
Ta	tantalum
TaN	tantalum nitride
$T_s$	substrate temperature
$v$	velocity of particle / electron
$\nu$	probability per unit time of thermally activated processes
$V$	voltage
$V_0$	barrier height
$V(z)$	potential barrier
$x$	depth
W	tungsten

---

$\chi_s$	electron affinity of the semiconductor
$\delta$	gap distance
$\delta_{gap}$	dielectric gap thickness

$\epsilon_{\text{int}}$	dielectric constant of the gap material
$\epsilon_S$	permittivity of semiconductor
$\lambda$	wavelength, inelastic mean free path
$\mu_M$	internal chemical potential of the metal
$\mu_S$	internal chemical potential of the semiconductor
$\rho_s(E)$	density of states of the sample
$\phi$	spectrometer work function
$\phi$	mean potential barrier height above Fermi level
$\phi_M$	metal work function
$\phi_{B,n}$	n-type Schottky barrier height
$\phi_{B,p}$	p-type Schottky barrier height
$\phi_{\text{CNL}}$	energy of the CNL measured with respect to the $E_V$
$\psi_j$	wave function

# Bibliography

- [1] IHP Annual Report 2014
- [2] G. E. Moore, *Electronics* **38**, 114 (1965).
- [3] ITRS Roadmap [Online]. Available: <http://public.itrs.net/> .
- [4] ITRS Roadmap 2012 White paper (2012).
- [5] B. Schaller, The Origin, Nature, and Implications of ‘Moore’s Law in *The Benchmark of Progress in Semiconductor Electronics* (1996).
- [6] P. Chevalier, T. F. Meister, and B. Heinemann, *Proc. 25th IEEE Bipolar/BiCMOS Circuits and Technology Meeting (BCTM)*, 57 (2011).
- [7] W. Mehr, J. Dabrowski, J. C. Scheytt, G. Lippert, Y. H. Xie, M. C. Lemme, M. Ostling, and G. Lupina, *IEEE Electron Device Lett.* **33**, 691 (2012).
- [8] R. Wang, Y. Sun, M. Kaynak, S. Beer, J. Borngräber, and J. C. Scheytt, *Proc. International Microwave Symposium (IMS 2012)* (2012).
- [9] C. Knochenhauer, J. C. Scheytt, and F. Ellinger, *IEEE J. Solid-State Circuits* **46**, 1137 (2011).
- [10] M. Ko, D. Kim, H. Rücker, and W.-Y. Choi, *J. Semicond. Technol. Sci.* **11**, 256 (2011).
- [11] M. Birkholz, K. E. Ehwald, T. Basmer, P. Kulse, C. Reich, J. Drews, D. Genschow, U. Haak, S. Marschmeyer, E. Matthus, K. Schulz, D. Wolansky, W. Winkler, T. Guschauski, and R. Ehwald, *J. Appl. Phys.* **113**, 244904 (2013).
- [12] U. Kaletta, P. V. Santos, D. Wolansky, A. Scheit, M. Fraschke, C. Wipf, P. Zaumseil, and C. Wenger, *Semicond. Sci. Technol.* **28**, 065013 (2013).
- [13] A. Gajda, L. Zimmermann, M. Jazayerifar, G. Winzer, H. Tian, R. Elschner, T. Richter, C. Schubert, B. Tillack, and K. Petermann, *Opt. Express* **20**, 13100, 2012.
- [14] S. Lischke, D. Knoll, L. Zimmermann, Y. Yamamoto, M. Fraschke, A. Trusch, A. Kruger, M. Kroh, and B. Tillack, *IEEE Photonics Conf. (IPC 2012)*, 628 (2012).

- [15] T. Arguirov, M. Kittler, M. Oehme, N. V. Abrosimov, O. F. Vyvenko, E. Kasper, and J. Schulze, *Solid State Phenom.* **205–206**, 383 (2013).
- [16] G. Capellini, C. Reich, S. Guha, Y. Yamamoto, M. Lisker, M. Virgilio, a. Ghrib, M. El Kurdi, P. Boucaud, B. Tillack, and T. Schroeder, *Opt. Express* **22**, 399 (2014).
- [17] R. R. Tummala and S. Madhavan, *System on Package: Miniaturization of the Entire System*. McGraw-Hill Education (2008).
- [18] R. Wilson, “The Great Debate: SOC vs. SIP” (2005). [Online]. Available: <http://www.eetimes.com/electronics-news/4052047/The->
- [19] J. Bardeen and W. Brattain, *Phys. Rev.* **74**, 230 (1948).
- [20] H. Shang, M. M. Frank, E. P. Gusev, J. O. Chu, S. W. Bedell, K. W. Guarini, and M. Jeong, *IBM J. Res. Dev.* **50**, 377 (2006).
- [21] Y. Kamata, *Mater. Today* **11**, 30 (2008).
- [22] R. Pillarisetty, *Nature* **479**, 324 (2011).
- [23] J. Mitard, B. De Jaeger, F. Leys, G. Hellings, K. Martens, G. Eneman, D. Brunco, R. Loo, D. Shamiryan, T. Vandeweyer, G. Winderickx, E. Vrancken, K. De Meyer, M. Caymax, L. Pantisano, M. Meuris, and M. Heyns, *Technical Digest International Electron Devices Meeting - IEDM*, 873 (2008).
- [24] R. Pillarisetty, B. Chu-Kung, S. Corcoran, G. Dewey, J. Kavalieros, H. Kennel, R. Kotlyar, D. Lionberger, and M. Metz, *Technical Digest of the International Electron Devices Meeting*, 671 (2010).
- [25] S. M. Sze and K. K. Ng, *Physics of Semiconductor Devices* (3rd ed.), John Wiley & Sons, Inc., (2007).
- [26] F. Jia, R. Woo, C. Shulu, L. Yaocheng, P. B. Griffin, and J. D. Plummer, *IEEE Electron Device Lett.* **28**, 637 (2007).
- [27] N. Collaert, A. Alian, H. Arimura, G. Boccardi, G. Eneman, J. Franco, T. Ivanov, D. Lin, R. Loo, C. Merckling, J. Mitard, M. a. Pourghaderi, R. Rooyackers, S. Sioncke, J. W. Sun, A. Vandooren, A. Veloso, A. Verhulst, N. Waldron, L. Witters, D. Zhou, K. Barla, and A. V.-Y. Thean, *Microelectron. Eng.* **132**, 218 (2015).
- [28] J. E. Roth, O. Fidaner, R. K. Schaevitz, Y.-H. Kuo, T. I. Kamins, J. S. Harris, and D. a. Miller, *Opt. Express* **15**, 5851 (2007).

- 
- [29] J. Liu, M. Beals, A. Pomerene, S. Bernardis, R. Sun, J. Cheng, L. C. Kimerling, and J. Michel, *Nat. Photonics* **2**, 433 (2008).
- [30] S. Assefa, F. Xia, S. W. Bedell, Y. Zhang, T. Topuria, P. M. Rice, and Y. A. Vlasov, *Opt. Express* **18**, 4986 (2010).
- [31] J. Wang and S. Lee, *Sensors (Basel)* **11**, 696 (2011).
- [32] R. E. Camacho-Aguilera, Y. Cai, N. Patel, J. T. Bessette, M. Romagnoli, L. C. Kimerling, and J. Michel, *Opt. Express* **20**, 11316 (2012).
- [33] Purdue University, "Purdue News - Germanium comes home to Purdue for semiconductor milestone," [Online]. Available: <http://www.purdue.edu/newsroom/releases/2014/Q4/germanium-comes-home-to-purdue-for-semiconductor-milestone.html>
- [34] L. Pavesi, *J. Phys. Condens. Matter* **15**, R1169 (2003).
- [35] R. Kirchain and L. Kimerling, *Nat. Photonics* **1**, 303 (2007).
- [36] A. Grill, S. M. Gates, T. E. Ryan, S. V. Nguyen, and D. Priyadarshini, *Appl. Phys. Rev.* **1**, 011306 (2014).
- [37] D. A. B. Miller, *IEEE J. Sel. Top. Quantum Electron.* **6**, 1312 (2000).
- [38] G. Q. Lo, S. H. G. Teo, M. B. Yu, T. Y. Liow, A. Lim, J. F. Song, D. Liang, X. G. Tu, X. S. Luo, N. Duan, L. X. Jia, and D. L. Kwong, *Conference on Lasers and Electro-Optics (CLEO)*, CM4A.3 (2012).
- [39] P. J. Carrington, V. A. Solov'ev, Q. Zhuang, A. Krier, and S. V. Ivanov, *Appl. Phys. Lett.* **93**, 091101 (2008).
- [40] S. I. Tsintzos, N. T. Pelekanos, G. Konstantinidis, Z. Hatzopoulos, and P. G. Savvidis, *Nature* **453**, 372 (2008).
- [41] W. Zhou, P. Bhattacharya, and O. Qasaimeh, *IEEE J. Quantum Electron.* **37**, 48 (2001).
- [42] D. J. Paul, *Semicond. Sci. Technol.* **19**, R75 (2004).
- [43] J. Michel, J. Liu, and L. C. Kimerling, *Nat. Photonics* **4**, 527 (2010).
- [44] P. H. Lim, Y. Kobayashi, S. Takita, Y. Ishikawa, and K. Wada, *Appl. Phys. Lett.* **93**, 041103 (2008).

- [45] B. E. A. Saleh and M. C. Teich, *Fundamentals of Photonics*, John Wiley & Sons, Inc., (1991).
- [46] Y. Yacoby, *Phys. Rev.* **142**, 445 (1966).
- [47] A. Frova and P. Handler, *Phys. Rev.* **137**, A1857 (1965).
- [48] S. Jongthammanurak, J. Liu, K. Wada, D. D. Cannon, D. T. Danielson, D. Pan, L. C. Kimerling, and J. Michel, *Appl. Phys. Lett.* **89**, 16 (2006).
- [49] A. E.-J. Lim, T.-Y. Liow, F. Qing, N. Duan, L. Ding, M. Yu, G.-Q. Lo, and D.-L. Kwong, *Opt. Express* **19**, 5040 (2011).
- [50] D. Miller, D. Chemla, T. Damen, A. Gossard, W. Wiegmann, T. Wood, and C. Burrus, *Phys. Rev. Lett.* **53**, 2173 (1984).
- [51] Y.-H. Kuo, Y. K. Lee, Y. Ge, S. Ren, J. E. Roth, T. I. Kamins, D. a B. Miller, and J. S. Harris, *Nature* **437**, 1334 (2005).
- [52] Y.-H. Kuo, Y. K. Lee, Y. Ge, S. Ren, J. E. Roth, T. I. Kamins, D. A. B. Miller, and J. S. Harris, *IEEE J. Quantum Electron.* **12**, 1503 (2006).
- [53] S. Klinger, M. Berroth, M. Kaschel, M. Oehme, and E. Kasper, *IEEE Photonics Technol. Lett.* **21**, 920 (2009).
- [54] Y. Kang, H.-D. Liu, M. Morse, M. J. Paniccia, M. Zadka, S. Litski, G. Sarid, A. Pauchard, Y.-H. Kuo, H.-W. Chen, W. S. Zaoui, J. E. Bowers, A. Beling, D. C. McIntosh, X. Zheng, and J. C. Campbell, *Nat. Photonics* **3**, 59 (2008).
- [55] J. Wang, W. Y. Loh, H. Zang, M. B. Yu, K. T. Chua, T. H. Loh, J. D. Ye, R. Yang, X. L. Wang, S. J. Lee, B. J. Cho, G. Q. Lo, and D. L. Kwong, *4th IEEE International Conference on Group IV Photonics*, 1 (2007).
- [56] M. Jutzi, M. Berroth, G. Wohl, M. Oehme, and E. Kasper, *IEEE Photonics Technol. Lett.* **17**, 1510 (2005).
- [57] J. Liu, J. Michel, W. Giziewicz, D. Pan, K. Wada, D. D. Cannon, S. Jongthammanurak, D. T. Danielson, L. C. Kimerling, J. Chen, F. O. Ilday, F. X. Kärtner, and J. Yasaitis, *Appl. Phys. Lett.* **87**, 103501 (2005).
- [58] R. B. Emmons, *J. Appl. Phys.* **38**, 3705 (1967).
- [59] H. Zang, S. J. Lee, W. Y. Loh, J. Wang, M. B. Yu, G. Q. Lo, D. L. Kwong, and B. J. Cho, *Appl. Phys. Lett.* **92**, 051110 (2008).



- 
- [60] C. O. Chui, A. K. Okyay, and K. C. Saraswat, *IEEE Photonics Technol. Lett.* **15**, 1585 (2003).
- [61] L. Chen, P. Dong, and M. Lipson, *Opt. Express* **16**, 11513 (2008).
- [62] Q. Mi, X. Xiao, J. C. Sturm, L. C. Lenchyshyn, and M. L. W. Thewalt, *Appl. Phys. Lett.* **60**, 3177 (1992).
- [63] H. Presting, T. Zinke, A. Splett, H. Kibbel, and M. Jaros, *Appl. Phys. Lett.* **69**, 2376 (1996).
- [64] M. H. Liao, T.-H. Cheng, and C. W. Liu, *Appl. Phys. Lett.* **89**, 261913 (2006).
- [65] T.-H. Cheng, M. H. Liao, L. Yeh, T.-L. Lee, M.-S. Liang, and C. W. Liu, *J. Appl. Phys.* **103**, 016103 (2008).
- [66] S.-L. Cheng, J. Lu, G. Shambat, H.-Y. Yu, K. Saraswat, J. Vuckovic, and Y. Nishi, *Opt. Express* **17**, 10019 (2009).
- [67] B. Dutt, D. S. Sukhdeo, D. Nam, B. M. Vulovic, Z. Yuan, and K. C. Saraswat, *IEEE Photonics J.* **4**, 2002 (2012).
- [68] J. Liu, J. Michel, and L. C. Kimerling, *2010 IEEE Photonic Society's 23rd Annual Meeting*, 325 (2010).
- [69] M. V. Fischetti and S. E. Laux, *J. Appl. Phys.* **80**, 2234 (1996).
- [70] J. Liu, X. Sun, D. Pan, X. Wang, L. C. Kimerling, T. L. Koch, and J. Michel, *Opt. Express* **15**, 11272 (2007).
- [71] J. R. Sánchez-Pérez, C. Boztug, F. Chen, F. F. Sudradjat, D. M. Paskiewicz, R. B. Jacobson, M. G. Lagally, and R. Paiella, *Proc. Natl. Acad. Sci. U. S. A.* **108**, 18893 (2011).
- [72] M. de Kersauson, M. El Kurdi, S. David, X. Checoury, G. Fishman, S. Sauvage, R. Jakomin, G. Beaudoin, I. Sagnes, and P. Boucaud, *Opt. Express* **19**, 17925 (2011).
- [73] D. S. Sukhdeo, D. Nam, J.-H. Kang, M. L. Brongersma, and K. C. Saraswat, *Photonics Res.* **2**, A8 (2014).
- [74] D. Jenkins and J. Dow, *Phys. Rev. B* **36**, 7994 (1987).
- [75] K. Lu Low, Y. Yang, G. Han, W. Fan, and Y.-C. Yeo, *J. Appl. Phys.* **112**, 103715 (2012).

- [76] S. Gupta, B. Magyari-Köpe, Y. Nishi, and K. C. Saraswat, *J. Appl. Phys.* **113**, 073707 (2013).
- [77] S. Wirths, R. Geiger, N. von den Driesch, G. Mussler, T. Stoica, S. Mantl, Z. Ikonic, M. Luysberg, S. Chiussi, J. M. Hartmann, H. Sigg, J. Faist, D. Buca, and D. Grützmacher, *Nat. Photonics* **9**, 88 (2015).
- [78] R. F. Kazarinov and R. A. Suris, *Fiz. i Tekhnika Poluprovodn.* **5**, 797 (1971).
- [79] J. Faist, F. Capasso, D. L. Sivco, C. Sirtori, A. L. Hutchinson, and A. Y. Cho, *Science* **264**, 553 (1994).
- [80] G. Ciasca, M. De Seta, G. Capellini, F. Evangelisti, M. Ortolani, M. Virgilio, G. Grosso, A. Nucara, and P. Calvani, *Phys. Rev. B* **79**, 085302 (2009).
- [81] M. De Seta, G. Capellini, Y. Busby, F. Evangelisti, M. Ortolani, M. Virgilio, G. Grosso, G. Pizzi, A. Nucara, and S. Lupi, *Appl. Phys. Lett.* **95**, 051918 (2009).
- [82] C. Jirauschek and T. Kubis, *Appl. Phys. Rev.* **1**, 011307 (2014).
- [83] Y. Yamamoto, P. Zaumseil, T. Argyurov, M. Kittler, and B. Tillack, *Solid. State. Electron.* **60**, 2 (2011).
- [84] Z. Huang, J. Oh, and J. C. Campbell, *Appl. Phys. Lett.* **85**, 3286 (2004).
- [85] A. Giussani, P. Rodenbach, P. Zaumseil, J. Dabrowski, R. Kurps, G. Weidner, H.-J. Müssig, P. Storck, J. Wollschläger, and T. Schroeder, *J. Appl. Phys.* **105**, 033512 (2009).
- [86] G. Kozlowski, Y. Yamamoto, J. Bauer, M. a. Schubert, B. Dietrich, B. Tillack, and T. Schroeder, *J. Appl. Phys.* **110**, 053509 (2011).
- [87] Y. Yamamoto, G. Kozlowski, P. Zaumseil, and B. Tillack, *Thin Solid Films* **520**, 3216 (2012).
- [88] M. Koike, Y. Kamata, T. Ino, D. Hagishima, K. Tatsumura, M. Koyama, and A. Nishiyama, *J. Appl. Phys.* **104**, 023523 (2008).
- [89] A. Chroneos and H. Bracht, *Appl. Phys. Rev.* **1**, 011301 (2014).
- [90] G. Capellini, W. M. Klesse, G. Mattoni, M. Y. Simmons, and G. Scappucci, *ECS Journal of Solid State Science and Technology*, **64**, 163 (2014).
- [91] A. Dimoulas, P. Tsipas, A. Sotiropoulos, and E. K. Evangelou, *Appl. Phys. Lett.* **89**, 252110 (2006).

- 
- [92] T. Nishimura, K. Kita, and A. Toriumi, *Appl. Phys. Lett.* **91**, 123123 (2007).
- [93] R. R. Lieten, S. Degroote, M. Kuijk, and G. Borghs, *Appl. Phys. Lett.* **92**, 022106 (2008).
- [94] R. T. Tung, *Mater. Sci. Eng. R Reports* **35**, 1 (2001).
- [95] F. Braun, “Ueber die Stromleitung durch Schwefelmetalle,” *Ann. der Phys. und Chemie*, **229**, pp. 556–563 (1875).
- [96] W. Schottky, *Zeitschrift für Phys.* **113**, 367–414 (1939).
- [97] R. T. Tung, *Appl. Phys. Rev.* **1**, 011304 (2014).
- [98] Y. Yang, Y. Lin, P. Xiang, M. Liu, W. Chen, X. Han, G. Hu, G. Hu, W. Zang, X. Lin, Z. Wu, Y. Liu, and B. Zhang, *Appl. Phys. Express* **7**, 042102 (2014).
- [99] P. Calka, M. Sowinska, T. Bertaud, D. Walczyk, J. Dabrowski, P. Zaumseil, C. Walczyk, A. Gloskovskii, X. Cartoixa, J. Suñé, and T. Schroeder, *ACS Appl. Mater. Interfaces* **6**, 5056 (2014).
- [100] N. F. Mott, *Proc. R. Soc. A Math. Phys. Eng. Sci.* **171**, 27 (1939).
- [101] R. T. Tung, *J. Vac. Sci. Technol. B Microelectron. Nanom. Struct.* **11**, 1546 (1993).
- [102] S. Kurtin, T. McGill, and C. Mead, *Phys. Rev. Lett.* **22**, 1433 (1969).
- [103] M. Schlüter, *Phys. Rev. B* **17**, 5044 (1978).
- [104] W. Mönch, *Phys. Rev. Lett.* **58**, 1260 (1987).
- [105] J. Bardeen, *Phys. Rev.* **71**, 717 (1947).
- [106] A. M. Cowley and S. M. Sze, *J. Appl. Phys.* **36**, 3212 (1965).
- [107] J. R. Heath and M. A. Ratner, *Phys. Today* **56**, 43 (2003).
- [108] A. Vilan, A. Shanzer, and D. Cahen, *Nature* **404**, 166 (2000).
- [109] T. Nishimura, K. Kita, and A. Toriumi, *Appl. Phys. Express* **1**, 051406 (2008).
- [110] R. R. Lieten, V. V. Afanas’ev, N. H. Thoan, S. Degroote, W. Walukiewicz, and G. Borghs, *J. Electrochem. Soc.* **158**, H358 (2011).

- [111] Z. Wu, W. Huang, C. Li, H. Lai, and S. Chen, *IEEE Trans. Electron Devices* **59**, 1328 (2012).
- [112] M. Mueller, Q. T. Zhao, C. Urban, C. Sandow, D. Buca, S. Lenk, S. Estévez, and S. Mantl, *Mater. Sci. Eng. B* **154–155**, 168 (2008).
- [113] W. Long, Y. Li, and R. T. Tung, *Thin Solid Films* **557**, 254 (2014).
- [114] C. Y. Chang, Y. K. Fang, and S. M. Sze, *Solid. State. Electron.* **14**, 541 (1971).
- [115] A. Y. C. Yu, *Solid. State. Electron.* **13**, 239 (1970).
- [116] V. L. Rideout, *Solid. State. Electron.* **18**, 541 (1975).
- [117] J. P. Gambino and E. G. Colgan, *Mater. Chem. Phys.* **52**, 99 (1998).
- [118] J. A. Kittl, K. Opsomer, C. Torregiani, C. Demeurisse, S. Mertens, D. P. Brunco, M. J. H. Van Dal, and A. Lauwers, *Mater. Sci. Eng. B* **154–155**, 144 (2008).
- [119] H. Geng, *Semiconductor Manufacturing Handbook*, McGraw-Hill Education (2005).
- [120] J. D. Cressler, *The Silicon Heterostructure Handbook: Materials, Fabrication, Devices, Circuits, and Applications of SiGe and Si Strained-Layer Epitaxy*, CRC Press Taylor & Francis Group (2005).
- [121] H. Fujitani and S. Asano, *Phys. Rev. B* **42**, 1696 (1990).
- [122] R. Stadler and R. Podloucky, *Phys. Rev. B* **62**, 2209 (2000).
- [123] G. Binnig and H. Rohrer, *Helv. Phys. Acta* **55**, 726 (1982).
- [124] G. Binnig, H. Rohrer, C. Gerber, and E. Weibel, *Appl. Phys. Lett.* **40**, 178 (1982).
- [125] G. Binnig, H. Rohrer, C. Gerber, and E. Weibel, *Phys. Rev. Lett.* **49**, 57 (1982).
- [126] G. Binnig and H. Rohrer, *Surf. Sci.* **126**, 236 (1983).
- [127] Nobel Foundation, “The Nobel Prize in Physics 1986” [Online]. Available: [http://www.nobelprize.org/nobel\\_prizes/physics/laureates/1986/](http://www.nobelprize.org/nobel_prizes/physics/laureates/1986/)
- [128] IBM, “IBM News room - Image gallery” [Online]. Available: <http://www-03.ibm.com/press/us/en/photos.wss?rN=141&topic=8>
- [129] H. Rohrer, *Jpn. J. Appl. Phys.* **32**, 1335 (1993).

- 
- [130] J. Tersoff and D. R. Hamann, *Phys. Rev. B* **31**, 805 (1985).
- [131] Burleigh Instruments Inc., “Inchworm Motor Controller Instruction Manual.” Burleigh Park, Fishers,.
- [132] S. Park and C. F. Quate, *Rev. Sci. Instrum.* **58**, 2010 (1987).
- [133] D. W. Pohl, *Surf. Sci.* **181**, 174 (1987).
- [134] D. W. Pohl, *Rev. Sci. Instrum.* **58**, 54 (1987).
- [135] C. J. Chen, *Appl. Phys. Lett.* **60**, 132 (1992).
- [136] K. Besocke, *Surf. Sci.* **181**, 145 (1987).
- [137] R. G. Carr, *J. Microsc.* **152**, 379 (1988).
- [138] D. Berlincourt, “Important Properties of vernitron piezoelectric ceramics”, Vernitron Piezoelectric Division.
- [139] H. Kuzmany, *Solid-State Spectroscopy*, Springer, (2009).
- [140] J. A. Kubby and J. J. Boland, *Surf. Sci. Rep.* **26**, 61 (1996).
- [141] A. J. Nam, A. Teren, T. A. Lusby, and A. J. Melmed, *J. Vac. Sci. Technol. B Microelectron. Nanom. Struct.* **13**, 1556 (1995).
- [142] A. J. Melmed, *J. Vac. Sci. Technol. B Microelectron. Nanom. Struct.* **9**, 601 (1991).
- [143] A. J. Melmed, *J. Vac. Sci. Technol. B Microelectron. Nanom. Struct.* **16**, 3077 (1998).
- [144] A.-S. Lucier, “Preparation and Characterization of Tungsten Tips Suitable for Molecular Electronics Studies” (Thesis), McGill University, (2004).
- [145] R. Wiesendanger, *Scanning Probe Microscopy and Spectrometry: Methods and Applications*, Cambridge University Press, (1994).
- [146] L. de Broglie, *Phil. Mag.* **47**, 446 (1924).
- [147] P. Weinberger, *Phil. Mag. Lett.* **86**, 405 (2006).
- [148] C. Davisson and L. H. Germer, *Phys. Rev.* **30**, 705 (1927).

- [149] H. Lüth, *Solid Surfaces, Interfaces and Thin Films* (5th ed.), Springer-Verlag, (1993).
- [150] S. R. Morrison, *The Chemical Physics of Surfaces* (2nd ed.), Plenum Press, (1990).
- [151] D. Tabor, *J. Vac. Sci. Technol.* **9**, 695 (1972).
- [152] J. M. Cowley, *Diffraction Physics* (3rd ed.), Elsevier Science B.V., (1995).
- [153] G. Ertl and J. Küppers, *Low energy electrons and surface chemistry* (2nd ed.), Verlag Chemie, (1974).
- [154] Specs GmbH, “ErLEED 100/150 - Product Brochure.” [Online]. Available: <http://www.specs.de/>
- [155] SPECS GmbH, *User manual for the ErLEED optics and power supplies* (Ver. 1.2.), (2002).
- [156] D. H. Narumand and K. D. Childs, *Appl. Spectrosc. Rev.* **34**, 139 (1999).
- [157] R. E. Weber, *J. Appl. Phys.* **38**, 4355 (1967).
- [158] J. C. Vickerman and I. S. Gilmore, Eds., *Surface Analysis – The Principal Techniques* (2nd ed.), John Wiley & Sons, Inc., (2009).
- [159] A. Einstein, *Ann. Phys.* **17**, 1 (1905).
- [160] K. Siegbahn, C. Nordling, A. Fahlman, K. Hamrin, J. Hedman, R. Ndberg, C. Johansson, T. Bergmark, S.-E. Karlsson, I. Lindgren, and B. Lindberg, *Nov. Acta Regiae Soc. Sci. Ups.* **1** (1967).
- [161] J. F. Watts and J. Wolstenholme, *An Introduction to Surface Analysis by XPS and AES*, John Wiley & Sons, Inc., (2003).
- [162] C. J. Powell and A. Jablonski, *Surf. Interface Anal.* **29**, 108 (2000).
- [163] S. Tanuma, C. J. Powell, and D. R. Penn, *Surf. Interface Anal.* **43**, 689 (2011).
- [164] L. Meitner, *Zeitschrift für Phys.* **9**, 131 (1922).
- [165] P. Auger, *C.R.A.S.* **177**, 169 (1923).
- [166] W. Spicer, *Phys. Rev.* **112**, 114 (1958).

- 
- [167] D. B. Williams, *Transmission Electron Microscopy: A Textbook for Materials Science* (2nd. ed.), Springer, (2009).
- [168] R. W. Kelsall, I. W. Hamley, and M. Geoghegan, Eds., *Nanoscale Science and Technology*, John Wiley & Sons, Inc., (2005).
- [169] I. Chorkendorff and J. W. Niemantsverdriet, *Concepts of Modern Catalysis and Kinetics*, WILEY-VCH Verlag GmbH, (2003).
- [170] H. J. W. Zandvliet, *Phys. Rep.* **388**, 1 (2003).
- [171] R. E. Schlier and H. E. Farnsworth, *J. Chem. Phys.* **30**, 917 (1959).
- [172] C. R. Bayliss and D. L. Kirk, *Thin Solid Films* **38**, 183 (1976).
- [173] J. A. Kubby, J. E. Griffith, R. S. Becker, and J. S. Vickers, *Phys. Rev. B* **36**, 6079 (1987).
- [174] G. J. Russell, *Surf. Sci.* **19**, 217 (1970).
- [175] L. Y. L. Shen, *Surf. Sci.* **47**, 685 (1975).
- [176] B. Z. Olshanetsky, S. M. Repinsky, and A. A. ShklyaeV, *Surf. Sci.* **64**, 224 (1977).
- [177] D. J. Chadi, *Phys. Rev. Lett.* **43**, 43 (1979).
- [178] M. Needels, M. Payne, and J. Joannopoulos, *Phys. Rev. B* **38**, 5543 (1988).
- [179] S. D. Kevan, *Phys. Rev. B* **32**, 2344 (1985).
- [180] R. J. Culbertson, Y. Kuk, and L. C. Feldman, *Surf. Sci.* **167**, 127 (1986).
- [181] R. G. Musket, W. Mclean, W. J. Siekhaus, A. Colmenares, and D. M. Makowiecki, *Appl. Surf. Sci.* **10**, 143 (1982).
- [182] S. J. Jung, J. Y. Lee, S. Hong, and S. Kim, *J. Phys. Chem. B* **109**, 24445 (2005).
- [183] H. J. W. Zandvliet, B. S. Swartzentruber, W. Wulfhekel, B. J. Hattink, and B. Poelsema, *Phys. Rev. B* **57**, 6803 (1998).
- [184] G. Schulze and M. Henzler, *Surf. Sci.* **73**, 553 (1978).
- [185] Y. Takagi, M. Yamada, K. Nakatsuji, and F. Komori, *Appl. Phys. Lett.* **84**, 1925 (2004).

- [186] L. H. Chan, E. I. Altman, and Y. Liang, *J. Vac. Sci. Technol. A Vacuum, Surfaces, Film.* **19**, 976 (2001).
- [187] W. M. Klesse, G. Scappucci, G. Capellini, and M. Y. Simmons, *Nanotechnology* **22**, 145604 (2011).
- [188] S. Gan, L. Li, T. Nguyen, H. Qi, R. F. Hicks, and M. Yang, *Surf. Sci.* **395**, 69 (1998).
- [189] G. Scappucci, G. Capellini, W. C. T. Lee, and M. Y. Simmons, *Nanotechnology* **20**, 495302 (2009).
- [190] J. S. Hovis, R. J. Hamers, and C. M. Greenlief, *Surf. Sci.* **440**, L815 (1999).
- [191] H. Okumura, T. Akane, and S. Matsumoto, *Appl. Surf. Sci.* **125**, 125 (1998).
- [192] K. Prabhakaran, T. Ogino, R. Hull, J. C. Bean, and L. J. Peticolas, *Surf. Sci.* **316**, 7 (1994).
- [193] T. Akane, J. Tanaka, H. Okumura, and S. Matsumoto, *Appl. Surf. Sci.* **108**, 303 (1997).
- [194] K. S. S. Harsha, *Principles of Physical Vapor Deposition of Thin Films*, Elsevier Science & Technology, (2006).
- [195] D. M. Mattox, *Handbook of Physical Vapor Deposition (PVD) Processing* (2nd. ed.), Elsevier Science, (2010).
- [196] Omicron NanoTechnology, "Instruction Manual UHV Evaporator EFM3/4 Triple Evaporator EFM3T" (1996).
- [197] C. Ratsch and J. A. Venables, *J. Vac. Sci. Technol. A Vacuum, Surfaces, Film.* **21**, S96 (2003).
- [198] J. A. Venables, G. D. T. Spiller, and M. Hanbucken, *Rep. Prog. Phys.* **47**, 399 (1984).
- [199] J. Venables, *Introduction to Surface and Thin Film Processes*, Cambridge University Press, (2000).
- [200] E. Bauer, *Zeitschrift für Krist.* **110**, 372 (1958).
- [201] W. Ostwald, *Zeitschrift für Phys. Chemie* **22**, 289 (1897).
- [202] N. C. Bartelt, W. Theis, and R. M. Tromp, *Phys. Rev. B* **54**, 11741 (1996).



- 
- [203] W. Thomson, *Philos. Mag.* **42**, 448 (1871).
- [204] J. W. Gibbs, "Transactions of the Connecticut Academy of Arts and Sciences" Vol.3, 108, (1876).
- [205] B. K. Chakraverty, *J. Phys. Chem. Solids* **28**, 2401 (1967).
- [206] B. K. Chakraverty, *J. Phys. Chem. Solids* **28**, 2413 (1967).
- [207] M. Zinke-Allmang, L. C. Feldman, and M. H. Grabow, *Surf. Sci. Rep.* **16**, 377 (1992).
- [208] E. D. Marshall, S. S. Lau, D. M. Scott, and T. F. Kuech, *Mat. Res. Soc. Symp. Proc.* **47**, 161 (1985).
- [209] J. Li, Q. Z. Hong, J. W. Mayer, and L. Rathbun, *J. Appl. Phys.* **67**, 2506 (1990).
- [210] K. Ishida and T. Nishizawa, *J. Phase Equilibria* **12**, 470 (1991).
- [211] S. Gaudet, C. Detavernier, a. J. Kellock, P. Desjardins, and C. Lavoie, *J. Vac. Sci. Technol. A Vacuum, Surfaces, Film.* **24**, 474 (2006).
- [212] Y. F. Hsieh, L. J. Chen, E. D. Marshall, and S. S. Lau, *Appl. Phys. Lett.* **51**, 1588 (1987).
- [213] H. P. Sun, Y. B. Chen, X. Q. Pan, D. Z. Chi, R. Nath, and Y. L. Foo, *Appl. Phys. Lett.* **87**, 211909 (2005).
- [214] A. Tsuruta, W. G. Chu, K. Tamura, H. Ishii, M. Owari, and Y. Nihei, *Surf. Interface Anal.* **37**, 230 (2005).
- [215] K. Opsomer, D. Deduytsche, C. Detavernier, R. L. Van Meirhaeghe, a. Lauwers, K. Maex, and C. Lavoie, *Appl. Phys. Lett.* **90**, 031906 (2007).
- [216] K. Prabhakaran and T. Ogino, *Appl. Surf. Sci.* **100–101**, 518 (1996).
- [217] I. Goldfarb and G. A. D. Briggs, *J. Mater. Res.* **16**, 744 (2001).
- [218] I. Goldfarb and G. A. D. Briggs, *J. Vac. Sci. Technol. B* **20**, 1419 (2002).
- [219] K. Sell, A. Kleibert, V. V. Oeynhausen, and K.-H. Meiwes-Broer, *Eur. Phys. J. D* **45**, 433 (2007).
- [220] J. Choi, D. K. Lim, Y. Kim, and S. Kim, *J. Phys. Chem. C* **114**, 8992 (2010).

- [221] H. J. W. Zandvliet, A. van Houselt, and P. E. Hegeman, *Surf. Sci.* **605**, 1129 (2011).
- [222] T. F. Mocking, G. Hlawacek, and H. J. W. Zandvliet, *Surf. Sci.* **606**, 924 (2012).
- [223] J. Choi, D. K. Lim, Y. Kim, D. H. Kim, and S. Kim, *Phys. Rev. B* **82**, 201305 (2010).
- [224] A. Chawanda, C. Nyamhere, F. D. Auret, W. Mtangi, M. Diale, and J. M. Nel, *Phys. Status Solidi* **7**, 248 (2010).
- [225] A. Chawanda, C. Nyamhere, F. D. Auret, W. Mtangi, T. T. Hlatshwayo, M. Diale, and J. M. Nel, *Phys. B Condens. Matter* **404**, 4482 (2009).
- [226] S. P. Ashburn, M. C. Öztürk, G. Harris, and D. M. Maher, *J. Appl. Phys.* **74**, 4455 (1993).
- [227] ASM International, *Alloy Phase Diagrams; Volume 3*. ASM International, (1992).
- [228] T. Schroeder, J. B. Giorgi, A. Hammoudeh, N. Magg, M. Bäumer, and H.-J. Freund, *Phys. Rev. B* **65**, 115411 (2002).
- [229] M. Perez, *Scr. Mater.* **52**, 709 (2005).
- [230] H. P. Sun, Y. B. Chen, X. Q. Pan, D. Z. Chi, R. Nath, and Y. L. Foo, *Appl. Phys. Lett.* **86**, 071904 (2005).
- [231] S.-L. Hsu, C.-H. Chien, M.-J. Yang, R.-H. Huang, C.-C. Leu, S.-W. Shen, and T.-H. Yang, *Appl. Phys. Lett.* **86**, 251906 (2005).
- [232] R. Nath, C. W. Soo, C. B. Boothroyd, M. Yeadon, D. Z. Chi, H. P. Sun, Y. B. Chen, X. Q. Pan, and Y. L. Foo, *Appl. Phys. Lett.* **86**, 201908 (2005).
- [233] B. Balakrisnan, C. C. Tan, S. L. Liew, P. C. Lim, G. K. L. Goh, Y. L. Foo, and D. Z. Chi, *Appl. Phys. Lett.* **87**, 241922 (2005).
- [234] S. Gaudet, C. Detavernier, C. Lavoie, and P. Desjardins, *J. Appl. Phys.* **100**, 034306 (2006).
- [235] D. Han, Y. Wang, D. Tian, W. Wang, X. Liu, J. Kang, and R. Han, *Microelectron. Eng.* **82**, 93 (2005).
- [236] A. Chawanda, J. M. Nel, F. D. Auret, W. Mtangi, C. Nyamhere, M. Diale, and L. Leach, *J. Korean Phys. Soc.* **57**, 1970 (2010).

- 
- [237] J. K. Patterson, B. J. Park, K. Ritley, H. Z. Xiao, L. H. Allen, and A. Rockett, *Thin Solid Films* **253**, 456 (1994).
- [238] M. Niranjana, L. Kleinman, and A. Demkov, *Phys. Rev. B* **75**, 085326 (2007).
- [239] D. Connétable and O. Thomas, *J. Phys. Condens. Matter* **25**, 355403 (2013).
- [240] T.-Y. Fu, A. Tomaszewska, X.-L. Huang, J.-H. Li, P.-I. Hsieh, and M.-K. Jhou, *Nanoscale Res. Lett.* **8**, 416 (2013).
- [241] A. Tomaszewska, J.-H. Li, X.-L. Huang, and T.-Y. Fu, *Mater. Sci.* **32**, 641 (2014).
- [242] R. M. Walser and R. W. Bené, *Appl. Phys. Lett.* **28**, 624 (1976).
- [243] M. Wittmer, M.-A. Nicolet, and J. W. Mayer, *Thin Solid Films* **42**, 51 (1977).
- [244] F. Nemouchi, D. Mangelinck, C. Bergman, G. Clugnet, P. Gas, and J. L. Lábár, *Appl. Phys. Lett.* **89**, 131920 (2006).
- [245] D. Z. Chi, R. T. P. Lee, S. J. Chua, S. J. Lee, S. Ashok, and D.-L. Kwong, *J. Appl. Phys.* **97**, 113706 (2005).
- [246] Y. Deng, O. Nakatsuka, N. Taoka, and S. Zaima, *Jpn. J. Appl. Phys.* **53**, 05GA06 (2014).
- [247] W. Huang, M. Tang, C. Wang, C. Li, J. Li, S. Chen, C. Xue, and H. Lai, *Appl. Phys. Express* **6**, 075505 (2013).
- [248] B. E. Warren, *X-Ray Diffraction*, Dover Publications (1990).
- [249] M. De Seta, G. Capellini, and F. Evangelisti, *Phys. Rev. B* **77**, 045431 (2008).
- [250] J. I. Flege, W. X. Tang, and M. S. Altman, “Low-energy electron microscopy” in *Characterization of materials* (2nd. ed.), John Wiley & Sons, Inc., (2012).
- [251] J. I. Flege and E. E. Krasovskii, *Phys. status solidi - Rapid Res. Lett.* **8**, 463 (2014).
- [252] L. Wang, G. Han, S. Su, Q. Zhou, Y. Yang, P. Guo, W. Wang, Y. Tong, P. S. Y. Lim, B. Liu, E. Y.-J. Kong, C. Xue, Q. Wang, B. Cheng, and Y.-C. Yeo, *Electrochem. Solid-State Lett.* **15**, H179 (2012).
- [253] S. Zaima, O. Nakatsuka, A. Sakai, J. Murota, and Y. Yasuda, *Appl. Surf. Sci.* **224**, 215 (2004).

- [254] O. Nakatsuka, K. Okubo, A. Sakai, M. Ogawa, Y. Yasuda, and S. Zaima, *Microelectron. Eng.* **82**, 479 (2005).
- [255] M.-H. Kang, Y.-Y. Zhang, K.-Y. Park, S.-G. Li, S.-Y. Jung, G.-W. Lee, J.-S. Wang, H.-D. Lee, J.-W. Oh, P. Majhi, R. Jammy, and K.-J. Park, *J. Korean Phys. Soc.* **55**, 221 (2009).
- [256] Z. Li, X. An, M. Li, Q. Yun, M. Lin, X. Zhang, and R. Huang, *IEEE Electron Device Lett.* **33**, 1687 (2012).
- [257] S. N. Elaydi, I. Gyori, and G. Ladas, Eds., *Advances in Difference Equations: Proceedings of the Second International Conference on Difference Equations*, CRC Press, (1998).
- [258] B. Das and J. Mahanty, *Phys. Rev. B* **36**, 898 (1987).
- [259] Z. H. Huang, *J. Vac. Sci. Technol. A Vacuum, Surfaces, Film.* **8**, 177 (1990).
- [260] J. G. Simmons, *J. Appl. Phys.* **34**, 1793 (1963).
- [261] J. G. Simmons, *J. Appl. Phys.* **34**, 2581 (1963).
- [262] R. Stratton, *J. Phys. Chem. Solids* **23**, 1177 (1962)